Surface functionalisation techniques for colloidal inorganic nanocrystals

by

Paul D. McNaughter

A thesis submitted in partial fulfilment for the
degree of Doctor of Philosophy

at the
University of East Anglia
School of Chemistry

May 2013

Abstract

Colloidally-stable inorganic nanocrystals have a wide range of envisaged applications in biological environments. To reach their potential, the nanocrystals need to be stable in aqueous environments and have pendant functionality available for attachment of biomolecules. In this thesis, new methods for the transfer of nanocrystals from organic to aqueous media are developed and the interaction of aqueous stabilised particles with serum proteins is investigated.

In Chapter 3, a new method for the synthesis of a thin silica layer upon the surface of nanocrystals is demonstrated. The method uses the hydrophobic interaction between an amphiphilic polymer and nanocrystal ligands to provide a foundation for growth of a silica layer. The coated nanocrystals are characterised using a wide range of techniques confirming that the presence and location of the silica shell.

In Chapter 4, custom-synthesised amphiphilic polymers for water transfer and functionalisation of nanocrystals are synthesised, characterised and tested. Commercially-available polymers used for this purpose are examined, leading to a rationale for custom-design. Partial water transfers were achieved using activated ester copolymers with styrene but no transfers were achieved the octadecylacrylate copolymers. Poly(ethylene glycol) containing monomers were also used but yielded no transfers. This suggests that behaviour of the polymer during the coating procedure is intimately linked to the structure of the polymer.

In Chapter 5, small-angle neutron scattering is used to elucidate structural information for the protein corona formed on nanocrystals and silica nanoparticles. Information on the packing of ligands on colloidal nanocrystals without a amphiphilic polymer coating was determined. The fitting of the protein corona upon silica nanoparticles was explored using core-shell form factors but was hampered by complexities within the scattering profiles which were not accounted for using simple form factors.

Table of Contents

List of Figures

List of Tables

List of Abbreviations

AIBN	azobisisobutyronitrile
APEGm	acryloyloxy poly(ethylene glycol) monomethyl ether
ATR	Attenuated Total Reflection
AuNP	Gold Nanoparticle
AuNR	Gold Nanorod
BSA	Bovine serum albumin
CRP	Controlled Radical Polymerisation
DLS	Dynamic Light Scattering
DLVO	Derjaguin, Landau, Verwey and Overbeek
DMF	dimethylformamide
DMSO	dimethylsulphoxide
EDC	1-ethyl-3-(3-diaminopropyl)carbodiimide
EDX	Energy-dispersive X-ray
EELS	Electron Energy-Loss Spectroscopy
EFTEM	Energy-filtered Transmission Electron Microscopy
FT-IR	Fourier Transform-Infra-Red
GPC	Gel Permeation Chromatography
HRTEM	High Resolution Transmission Electron Microscope
HSA	Human serum albumin
ICP-AES	Inductively-Coupled Plasma Atomic Emission Spectroscopy

NAS . . . . . .*N*-(acryloyloxy)succinimide

NMR . . . . . .Nuclear Magnetic Resonance

NP . . . . . .Nanoparticle

ODA . . . . . .octadecylacrylate

PBS . . . . . .Phosphate Buffered Saline

PDI . . . . . .polydispersity index

PEG . . . . . .poly(ethylene glycol)

PRE . . . . . .Persistant Radical Effect

QD . . . . . .Quantum Dot

QY . . . . . .Quantum Yield

RAFT . . . . . .Reversible Addition-Fragmentation Chain Transfer

SAED . . . . . .Selected-area Electron Diffraction

SANS . . . . . .Small-Angle Neutron Scattering

SEC . . . . . .Size Exclusion Chromatography

SLD . . . . . .Scattering Length Density

SPR . . . . . .Surface Plasmon Resonance

Sty . . . . . .styrene

TEM . . . . . .Transmission Electron Microscope

TEOS . . . . . .tetraethyl orthosilicate

THF . . . . . .tetrahydrofuran

UCN . . . . . .Up Converting Nanocrystal

XPS . . . . . .X-Ray Photoelectron Spectroscopy

Publications Associated With This Work

---

(1) **P. D. McNaughter**, J. C. Bear, D. C. Steytler, A. G. Mayes and T. Nann, 'A thin silica-polymer shell for functionalising colloidal inorganic nanoparticles', *Angew. Chem. Int. Ed.*, 2011, **50**, 10384–10387, DOI: 10.1002/anie.201103954.

(2) J. Bear, G. Charron, M. T. Fernández-Argüelles, S. Massadeh, **P**. **McNaughter** and T. Nann, In Vivo Applications of Inorganic Nanoparticles, in *BetaSys: Systems Biology of Regulated Exocytosis in Pancreatic ß-Cells*, ed. B. Booß-Bavnbek, B. Klösgen, J. Larsen, F. Pociot and E. Renström, Springer New York, New York, NY, 2011, pp. 185–220, ISBN: 978-1-4419-6955-2, DOI: 10.1007/978-1-4419-6956-9_9.

Acknowledgements

My primary supervisor, Dr Andrew Mayes, has been a pillar of support during the course of my studies. His wisdom, knowledge and patience has been crucial to getting me through my PhD.

My secondary supervisors have provided many opportunities to learn about the subjects I've encountered through them. The early years working with Prof Thomas Nann allowed me to explore the field of nanocrystals, without which this thesis would be very different. I owe Dr David Steytler a large debt as without him I would not have been doing a PhD at the University of East Anglia. Dr Francesca Baldelli Bombelli has shared much experience about neutron scattering and bio-nano interface without which I would not have been able to do my last experimental chapter. Andrew and Francesca had the difficult task of seeing me over the finishing line for which I'm very grateful.

None of this would have been possible without the ongoing support of my parents, David and Amanda. My parents have endured more than should be reasonably expected with my strange working hours, emotions and, in later years, general lack of money.

My girlfriend, Amy, has been very supportive during the course of the PhD even though I've been testing. I can't recall how many times Amy has waited for me to leave the lab, normally later than expected, and jumped in my car to zoom to dancing, arriving with moments to spare.

I'm very fortunate to have had the support and love from of all of my grandparents, Brian, Dianne, Derek and Ivorine, during my PhD. I'd like to thank my brother, Robert, for his guidance on note taking in the lab.

All the way through the PhD, Mr Jamie Peck has been a good friend and by sharing the experiences with him I'm sure the PhD was easier. A young undergraduate, by the name of Mr Joseph Bear, arrived in the lab in my second year. He grew in to a great friend and his support and friendship over the years has been, in a word he might use, marvellous. In every situation over the years, Dr Abdirahman Saeed has known exactly what to say to me to keep me going. In the months writing in the office at the weekends, Abdirahman was the best companion I could ask for.

Quotation

When Sir Patrick Moore was asked if he still found the study of astronomy as interesting as he did when inspired at the age of six, despite all the discoveries in his lifetime, Sir Patrick responded;

> *"More so, every problem we solve raises a whole host of new ones. I remember a remark made to me by a Sir Arthur Eddington, the great pioneer of astrophysics. He knew all about the composition of the sun in 1930, rather less in 1932 and nothing at all in 1936."*

Sir Patrick Moore CBE FRS FRAS

CHAPTER 1

Introduction

"What could we do with layered structures with just the right layers? What would the properties of materials be if we could really arrange the atoms the way we want them? They would be very interesting to investigate theoretically. I can't see exactly what would happen, but I can hardly doubt that when we have some control of the arrangement of things on a small scale we will get an enormously greater range of possible properties that substances can have, and of different things that we can do."

From "There's Plenty of Room at the Bottom" by Richard P. Feynman, 1959[1]

1.1 Nanomaterials

Materials allow us to construct various structures to develop tools to perform tasks. A group of materials that have emerged over the past decades are designed and constructed with dimensions in the region of between one and a hundred nanometers, nm. These materials have been coined as nanomaterials. Although these materials are relatively new the concept of increasingly smaller materials and devices was brought to public attention by Richard P. Feynman in a talk entitled "There's Plenty of Room at the Bottom" to the American Physical Society in December 1959.[1] Decades before Feynman gave his 1959 talk, the imagination of scientists was already fuelled. The development of new techniques allowed the characterisation of structures smaller than previously achieved. A key event leading to the envisioning of nanometer sized structures was the development of the electron microscope in 1931. This allowed the visualisation of nanometer sized structures making the region feel more tangible and fired the imagination of scientists for years to follow.

Although Feynman had identified the potential for the materials with dimensions in the range of nanometers there was already a well established field of interface and col-

loid chemistry. The synthesis of "gold sols", spherical gold colloids, had been achieved by Michael Faraday in 1857 who attributed their unusual colours to the nature of finely divided gold.[2] In 1925 Richard A. Zsigmondy was awarded the Nobel prize in Chemistry for his work into the characterisation of gold colloids performed in 1909 using his ultramicroscope.[3]

It was in the 1980s that modern "nanotechnology" was born with discoveries such as the Buckminsterfullerene by Harold W. Kroto and coworkers[4] and the scanning tunnelling microscope at IBM. The manipulation of xenon atoms with a scanning tunnelling microscope to spell "IBM" earned Binnig and Rohrer the 1986 Nobel prize in Physics. Since the 1980s the wide reaching research area of nanomaterials has formed. Developing nanomaterials is an interdisciplinary exercise and requires work between chemists, physicists, biologists and other disciplines. The size of the materials fits between the realms of the physicist and chemist. Coincidentally, the smaller nanomaterials are on the order of magnitude of proteins. This allows the introduction of nanomaterials to biological systems and therefore a range of applications is possible due to the unique properties of nanomaterials.

1.2 Colloidal nanocrystals

Nanoparticles are a large family of nanomaterials. Spherical nanoparticles are zero-dimensional and can vary in diameter from one nanometer to hundreds of nanometers. As the size of a nanoparticle is decreased the properties they possess change from that of the bulk to atomic / molecular properties. Large nanoparticles ($>$20 nm) have properties which show a smooth scaling with size that derives from the properties of the bulk. Below 20 nm nanoparticles become more similar to their atomic / molecular counterparts and may show more erratic changes in properties which no longer scale smoothly. Properties which vary include surface reactivity, electronic structure, interactions with light and magnetic characteristics. Nanoparticles can be made from a wide variety of materials and can be either amorphous or crystalline. If crystalline the nanoparticle can also be described as a nanocrystal.[5]

1.2.1 Noble metal nanocrystals

As previously described in Section 1.1, nanoparticles have been studied for over 150 years by colloidal chemists. In fact some of the earliest nanoparticles studied were gold nanocrystals by Michael Faraday.[2] One of the observations that was made by Faraday was that the finely divided gold had colours of red and purple and not the typical yellow colour of bulk gold. This observation was a consequence of the interesting absorption profile that nanocrystals of metals such as gold and silver possess.

These metal nanocrystals have a strong absorption feature which is dependent on the size of the nanocrystal known as the Surface Plasmon Resonance (SPR), Figure 1.1. The electrons in the conduction band undergo a collective oscillation across the particle

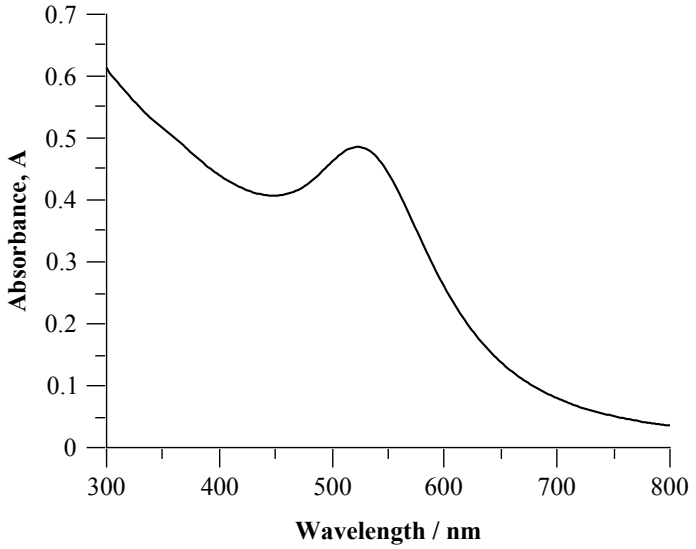

Figure 1.1: The absorption profile of AuNP showing the characteristic surface plasmon resonance

when excited by the appropriate wavelength of light.[6] In 1908 Gustav Mie modelled the conditions required for the SPR to occur by solving Maxwell's equations for a sphere interacting with light using a quasi-static approximation, *i.e*. the change in electric field of light experienced across the particle is approximately zero.[7,8] This can only be the case when the particle is much smaller than the wavelength of light. Mie's model for the extinction coefficient of a small particle is shown in Equation 1.1.

$$C_{\text{ext}}(\lambda) = \frac{24\pi r^3 \varepsilon_{\text{m}}^{3/2}}{\lambda} \frac{\varepsilon_2(\lambda)}{(\varepsilon_1(\lambda)+2\varepsilon_{\text{m}})^2+\varepsilon_2(\lambda)^2} \tag{1.1}$$

Where $C_{\text{ext}}(\lambda)$ is the wavelength dependent extinction coefficient, r is the radius of the particle, λ is the wavelength of the light, ε_{m} is the dielectric constant of the surroundings and $\varepsilon_{\text{Au}}(\lambda) = \varepsilon_1(\lambda) + i\varepsilon_2(\lambda)$ is the dielectric constant of gold, which has real and imaginary components. The plasmon resonance occurs when $\varepsilon_1(\lambda) = -2\varepsilon_{\text{m}}$. This condition is met in the visible region for gold and silver. Due to the sensitivity of the SPR to changes in the dielectric constant of the surroundings, metal nanoparticles which experience the SPR can be used in sensing applications where the particle surface is changed.[9] The plasmon resonance is observed in metal nanocrystals between 2 and approximately 100 nm in diameter.[10]

1.2.2 Semiconductor nanocrystals

Metals are able to conduct electricity due to the presence of easily accessible unoccupied energy levels, called the conduction band, found above the Fermi level of the metal. If the gap between the valence and conduction bands, known as a band gap (E_{gap}), is large the electrons cannot enter the conduction band and the material is an insulator. Semiconductors have a band gap which is small enough that it can be overcome by exciting the system, *e.g*.

by heating the material, allowing some conduction to occur.

When an electron is excited from the valence band to the conduction band a positive electron hole is created in the valence band. The promoted electron and the electron hole act as a quasiparticle with a hydrogenic wavefunction known as an *exciton*. Consequently, the spatial separation of the electron and the hole can be determined using a modified Bohr model. The binding energy between the electron and the electron hole is much weaker than that of the proton and electron in a hydrogen atom due to shielding of the electron hole by other electrons and the small effective masses involved. The resulting size of the exciton is much larger than that of a hydrogen atom. For most semiconductors the electron-hole pair separation is approximately 1 to 10 nm.

Once the semiconductor nanocrystal is smaller than this size the exciton is confined in the same way as the quantum mechanical "particle in a box" and quantum confinement occurs within the nanocrystal. Semiconductor nanocrystals that are small enough to undergo quantum confinement are known as Quantum Dots (QDs). The effect of this confinement is that the band gap of the nanocrystal, E_{gap}^{NC}, becomes related to the size of the nanocrystal and the observed result is the band gap increasing with decreasing size. This behaviour was modelled by Brus and coworkers where the band gap of the nanocrystal, E_{gap}^{NC}, was described as the band gap of the bulk semiconductor, E_{gap}^{B}, plus the internal energy of the exciton, E_{ex}, resulting in Equation 1.2[11–13]

$$E_{\text{gap}}^{NC} = E_{\text{gap}}^{B} + \frac{h^2}{8r^2}\left(\frac{1}{m_{\text{e}}} + \frac{1}{m_{\text{h}}}\right) - \frac{1.8e^2}{4\pi\varepsilon_0\varepsilon_{\text{B}}r} \tag{1.2}$$

where E_{gap}^{NC} is the band gap of the nanocrystal, E_{gap}^{B} is the energy of the band gap in the bulk semiconductor, m_{e} is the effective mass of an electron in the bulk material, m_{h} is the effective mass of the hole, ε_{B} is the dielectric constant for the bulk semiconductor, ε_0 is the vacuum permittivity, e is the elementary charge, h is Planck's constant and r is the radius of the nanocrystal. The Brus equation shows as the nanocrystal radius, r, increases the contribution from the exciton decreases and E_{gap}^{NC} will tend to E_{gap}^{B}.

As the band gap widens it allows visible light to be used to excite electrons to the conduction band. When the electron relaxes a lower energy photon of visible light is released from the QD, Figure 1.2 (top). The QDs act in the same manner as organic dyes except the excitation and emission wavelengths, which are intimately linked to the band gap, are tunable with nanocrystal size, Figure 1.2 (bottom). The semiconductor used, particle size, size distribution and chemical nature of the surface all influence the optical properties of QDs.[14,15] The molar absorption coefficients for QDs are between 100,000 and 1,000,000 $\text{M}^{-1}\,\text{cm}^{-1}$ which is approximately four times that of most dyes. The fluorescence Quantum Yields (QYs) are typically between 0.65 and 0.85 for CdSe.[16]

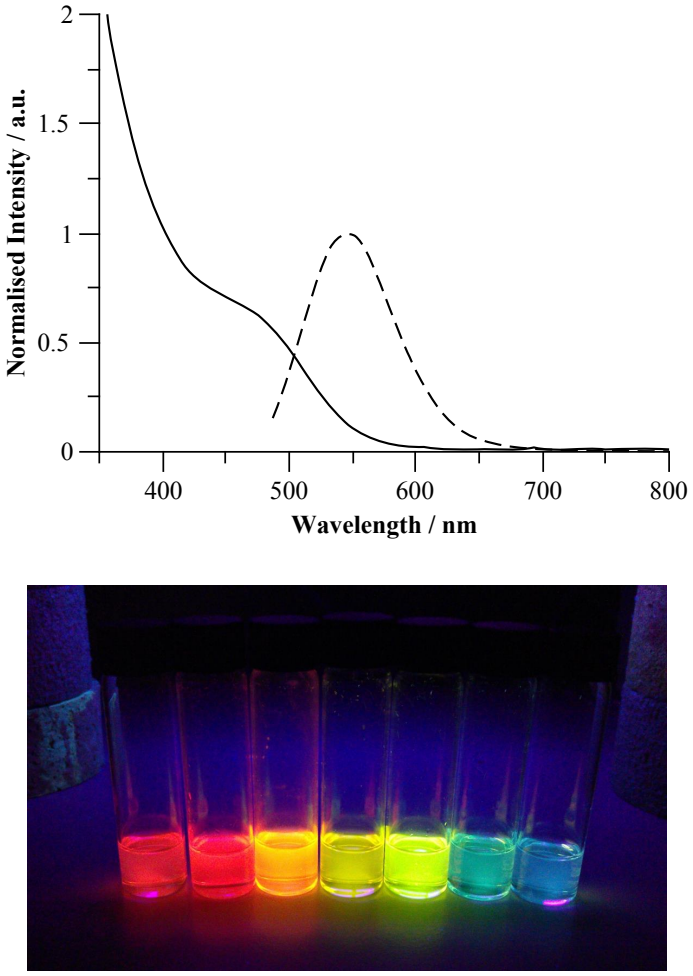

Figure 1.2: The optical properties of Quantum Dots with the absorption profile, full line, and emission profile, dashed line, for an InP@ZnS sample (top) and a photo showing the range of emission colours for InP@ZnS of different sizes synthesised during the course of this work. The size of the Quantum Dots decreases from left to right. A typical InP core diameter is 3.2 nm.

To improve the optical properties a shell of a second semiconductor can be grown on the surface of the QD to form a core-shell nanocrystal.[17] If the shell semiconductor has a wider band gap than that of the core the exciton is confined to the core resulting in a type-I system. A common type-I core-shell combination is CdSe@ZnS. The shell also provides a barrier which physically protects the core which results in reduced photobleaching and fluorescence quantum yield.

1.2.3 Magnetic nanocrystals

The properties of magnetic materials also vary with size and exhibit special properties when reduced to the size of a small nanocrystal, $d < 10\,\text{nm}$. Iron can form a range of oxides each with interesting magnetic properties. The three main stoichiometric forms of iron oxide are FeO (wüstite), Fe_2O_3 and Fe_3O_4 (magnetite). Fe_2O_3 commonly exists as two crystal forms: γ-Fe_2O_3 (maghemite) and α-Fe_2O_3 (hematite).[18] Fe_3O_4 and γ-Fe_2O_3 are commonly used as nanocrystal cores.[19] γ-Fe_2O_3 is ferromagnetic in the bulk, *i.e.* the

individual magnetic moments are of equal magnitude and aligned in the same direction. In the bulk Fe_3O_4 is a ferrimagnetic material, *i.e.* neighbouring magnetic moments are opposed and unequal so a net moment is present. There comes a point in a magnetic material where the ongoing alignment of moments becomes energetically unfavoured and domains, which are regions containing moments of a uniform direction, form which oppose one another. Many domains exist in the bulk forming a random pattern in the material. Above the Néel temperature the thermal energy is enough to make the moments to fluctuate randomly, causing order of the magnetic moments to disappear and the long range order collapses resulting in the material becoming paramagnetic.

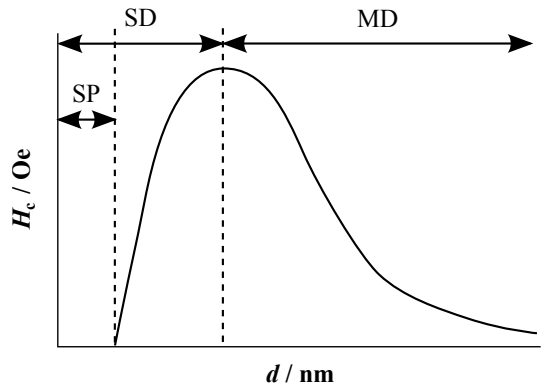

Figure 1.3: Illustration of the change of coercivity with nanocrystal size. The size regions for multidomain (MD), and single domain (SD) iron oxide are shown as well as the superparamagnetic region (SP). Adapted from [20].

As a particle of Fe_3O_4 or γ-Fe_2O_3 is made smaller the magnetic properties change. The magnetic coercivity, H_c, increases with smaller particle size till it reaches a maximum. This maximum coincides with the particle size becoming so small that the particle contains only a single domain, $d \approx 40\,\text{nm}$ depending on the material. Below this size H_c decreases till it becomes zero, Figure 1.3.[5,20] Particles below this size are superparamagnetic as they are small enough that thermal energy is enough to overcome the magnetic anisotropy barrier. This causes the random distribution of magnetic moments to be restored after a saturating applied field is removed, *i.e.* $H_c = 0$. Thus the domains have no memory of the applied field. Particles above this threshold do have a memory and exhibit hysteresis when taken to saturation resulting in a characteristic H_c.[21]

1.3 Methods of stabilising / functionalising colloidal nanocrystals

As mentioned in Section 1.2 many of the syntheses that produce the highest quality colloidal nanocrystals result in nanocrystals, which are stabilised by hydrophobic ligands. Typically, ligand used during synthesis contain alkyl chains between 12 and 18 carbons: for instance oleic acid, dodecanethiol, hexadecylamine, stearic acid, trioctylphosphine and trioctylphosphine oxide. The ligand is bound to the surface by the interaction between

the ligand head group and the surface of the nanocrystal. The best known example being the interaction of a thiol and a gold surface. The alkyl chain points outwards into the solvent providing stability in non-polar solvents. Often the ligands used for nanocrystal synthesis do not have any pendant functionality to perform further chemistry. If the ability to chemically connect a nanocrystal to a molecule, biomolecule, surface or another colloid is desired the nanocrystal surface needs to be modified to allow this to occur.

Each potential application will have criteria about the solvent the nanocrystals are required in, their total size and what functional groups are present on the surface. For instance, biological applications require that the particles are compatible with environments found in organisms, *i.e*. aqueous solutions with appropriate salt concentrations. A small size also is desirable as the ability to migrate in biological environments is hindered. Methods to modify the surface of nanocrystals are required to allow nanocrystals to be applied to these environments.

A range of different techniques now exist to modify the surfaces of nanocrystals. Largely these techniques fall into two categories: ligand exchange based and amphiphilic molecule bi-layers. An overview of this wide ranging field has recently been published by Sperling and Parak.[22]

If the nanocrystal has been synthesised with an aqueous method the particle can have pendant functionality on the surface. For instance iron oxide particles can have OH on the surface which can be directly reacted with another molecule to bestow new functionality to the nanocrystal.

1.3.1 Colloidal stability of nanocrystals

The initial surface adsorbed ligand has two roles. Firstly, the affinity of the ligand to the growing crystal has a large influence on shape and size of the resulting particle. Secondly, after the crystal has grown the surface ligand provides colloidal stability to the nanocrystal. Also, it is important that the nanocrystal is still colloidally stable after the surface has been modified for an application. Colloidal particles are attracted to each other through van der Waals interactions. Unlike van der Waals interations between molecules the interaction energy decays over a longer distance. To prevent the van der Waals forces causing nanocrystal aggregation, a repulsive force between particles is required. This can be provided electrostatically or sterically.

If charge is located at the surface of particles, Coulombic repulsion occurs. The balance between van der Waals and Coulombic forces is described by Derjaguin, Landau, Verwey and Overbeek (DLVO) theory.[23] In the presence of an electrolyte, an electrical double layer of ions is formed at the particle surface. This comprises of a strongly attracted layer of an ion of the opposite charge, the inner layer, followed by a less tightly bound layer of ions and counter ions of decreasing electric potential. Provided there is enough charge at the surface the attractive van der Waals forces will be overcome by repulsion between the electric bilayer of approaching nanocrystals. The influence of the surface charge can be

minimised to the point where it is weaker than the van der Waals forces by increasing the ionic strength of the electrolyte. Under such conditions the particles will aggregate.

Particles can also be stabilised by using sterically bulky groups, typically macromolecules, at the surface. Steric interactions are not incorporated into the DLVO model. These interactions are thought to work for a number of reasons upon approach of particles including an entropic decrease of the stabilising macromolecule, osmotic forces and the free energy cost being too high. Consequently sterically stabilised particles are immune to changes in ionic strength. This may have particular benefits in biological systems where the ionic strength if often high and electrostatic stabilisation is less effective.

1.3.2 Nanocrystal functionalisation

As already described, a nanocrystal surface may not have the correct properties after synthesis to be used for a desired application. The largest challenge is changing the solvent in which the nanocrystals are dispersed. Introducing points of attachment to allow the construction of more complicated structures can also be achieved by modifying the nanocrystal surface. The main themes of nanocrystal surface modification and functionalisation will be reviewed in this section.

1.3.2.1 Ligand exchange

The *ligand exchange* strategy is based on the replacement of the ligands that are on the surface of the particle from the synthesis with a new ligand. The driving force for the ligands to exchange is the stronger ability of the new ligand to bind to the surface. Ligand exchange can be used to change the pendant functionality or preferred solvent of nanocrystals. Simple ligands are small molecules, which contain two parts: a group which has an affinity to the surface and another part that provides stability in the desired medium. The region providing colloidal stability may also have functional groups for further attachment, Figure 1.4.

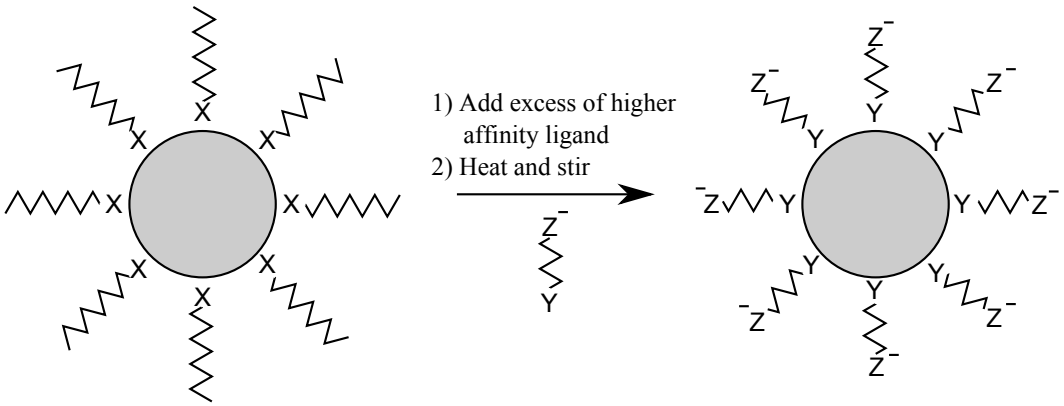

Figure 1.4: The ligands on a nanocrystal are stabilised with a ligand which is anchored by group X (left). The ligand is exchanged/displaced by a ligand with a higher affinity anchoring group, Y (right). The new ligand can also bestow the nanocrystal with new functionality or solubility, Z.

The best known example of a ligand that binds strongly to a surface is thiols and gold surfaces. AuNP synthesised using the Turkevich method use citrate as the reducing agent and final stabiliser and are thus electrostatically stabilised.[24] These nanocrystals are colloidally stable and can be for years. Citrate stabilised AuNPs are prone to irreversible aggregation when concentrated. If the nanocrystals are mixed with compounds containing sulphur, such as thiols, dithiocarbamates, disulphides *etc*., the citrate will be displaced by the new ligand. Popular ligands include short aliphatic compounds terminated with thiols and carboxylic acids such as mercaptoundecanoic acid, mercaptopropanoic acid and mercaptoacetic acid.

Ligand exchange, or ligand place exchange reactions, have also been studied on AuNP synthesised *via* the Brust method by the group of Royce W. Murray.[25] The AuNP synthesised by the Brust method are typically formed in the presence of alkanethiols (C > 3), which control the size of the resulting particles and stabilise the final nanocrystal.[26,27] If another thiol is introduced to the dispersion with the original ligand, the introduced ligand will compete for the surface, Equation 1.3. This can be used to develop mixed ligand systems or totally replace the initial ligand.

$$x(\mathrm{R_aSH}) + (\mathrm{R_bS})_m\mathrm{AuNP} \longrightarrow x(\mathrm{R_bSH}) + (\mathrm{R_aS})_x(\mathrm{R_bS})_{m-x}\mathrm{AuNP} \tag{1.3}$$

The binding of a ligand to the surface of a nanocrystal has a slightly different relationship with the various parts of the crystal. The crystal has many different exposed faces and edges and it has been shown that the ligand binding affinity is different depending on which part of the crystal it is interacting with.[28]

With the advent of QDs, similar requirements for functionalisation and phase transfer were found for envisaged applications. In the case of CdSe or CdSe@ZnS the most common syntheses result in nanocrystals stabilised with trioctylphosphine or trioctylphosphine oxide. The ligand is bound by the phosphorous or oxygen respectively to the Cd or Zn at the surface. Depending on the type of QD and the method used fatty acids and alkylamines can also be used as ligands during synthesis.[29] These can be exchanged with thiols, in a similar manner to AuNPs, in a ligand exchange reaction to bestow the nanocrystals with new functionality or solubility. The affinity of a thiol to a QD surface is lower than that for a AuNP resulting in the bound and unbound ligand being in equilibrium.[30,31] As with AuNPs, the optical properties of QDs are affected by the nature of the ligand that binds to the surface.[32,33]

QD ligands have received much attention in the literature with the development of different methods of anchoring the ligand such as dithiocarbamate[34] or polydentante ligands.[35,36] Multifunctional ligands have been designed where the ligand contains a region for anchoring, solubility and attachment for biomolecules.[37,38]

In the case of metal oxides, the ligands that are used during synthesis are typically fatty acids such as oleic acid. The ligand exchange procedure on metal oxide surfaces is not widely used as compared to AuNPs or QDs. Iron oxide particles have been studied

the most extensively due to their potential in therapy and imaging. The design of ligands for metal oxides and a discussion of their binding has been covered in recent reviews by Neouze and Schubert[39] and Amstad *et al.*[40]

For iron oxide nanocrystals the most common ligand exchange is the exchange of the carboxylic acid for another carboxylic acid.[41–43] Exchange for citric acid allows water transfer of the particles and potential further modification of the outward pointing groups. Another popular anchoring group is the catechols, which have a mode of interaction similar to a bridging carboxylate.[44–46] This has also been extended to derivatives of catechols which also show strong binding to iron oxide surfaces.[46,47] Other less common ligands for iron oxide particles include phosphonates[43,48] and silanes.[49]

Due to the range of affinities of ligands to surfaces, the ligand exchange approach is complex and it is hard to develop a universal coating procedure for all hydrophobic colloidal nanocrystals. Oxidation of the ligand, through chemical or photophysical processes, is an issue particularly for QDs where the colloidal stability is compromised after prolonged illumination.[50,51] Ligands without high affinities are in equilibrium with the unbound ligand. This results in multiple washings or increased dilution compromising colloidal stability. For AuNPs and QDs, the interaction of the ligand can significantly alter the absorption and emission profiles, changing the desired properties of the nanocrystals.

1.3.2.2 Amphiphile intercalation

Amphiphilic molecules have two regions, one of which prefers aqueous, or hydrophilic environments and the other which prefers hydrophobic environments. Classic examples of amphiphiles include compounds such as phospholipids, sodium dodecyl sulphate and dioctyl sodium sulphosuccinate where there is a head group, which is hydrophilic, and hydrophobic tails. These compounds can self-assemble in solvents to form regular structures due to the hydrophobic effect, *i.e.* solvent entropy driven assembly. For instance, in water the surfactants can assemble to minimise the exposure of the hydrophobic groups to water causing the formation of spheres, called micelles, with the hydrophobic region of the surfactant pointing inwards and the hydrophilic region pointing toward the solvent.

This ability for amphiphilic molecules to assemble can be used to create assemblies with the ligands on the surface of a nanocrystal.[52] The interaction of the surfactant and the nanocrystal is driven by the hydrophobic ligand and the hydrophobic part of the surfactant assembling preferentially. A bilayer is formed upon the surface of the nanocrystal with the ligand resulting from synthesis bound to the particle and an intercalated surfactant molecule which points the hydrophilic head group outwards, Figure 1.5. As a consequence this removes the strict requirements that the surface of a nanocrystal provides through the chemistry of the core material. In principle the methodology could be applied to any nanocrystal stabilised with hydrophobic ligands. Additionally, the exterior surface of all the nanocrystals would have the same chemical character making future functionalisation also more uniform across nanocrystals.

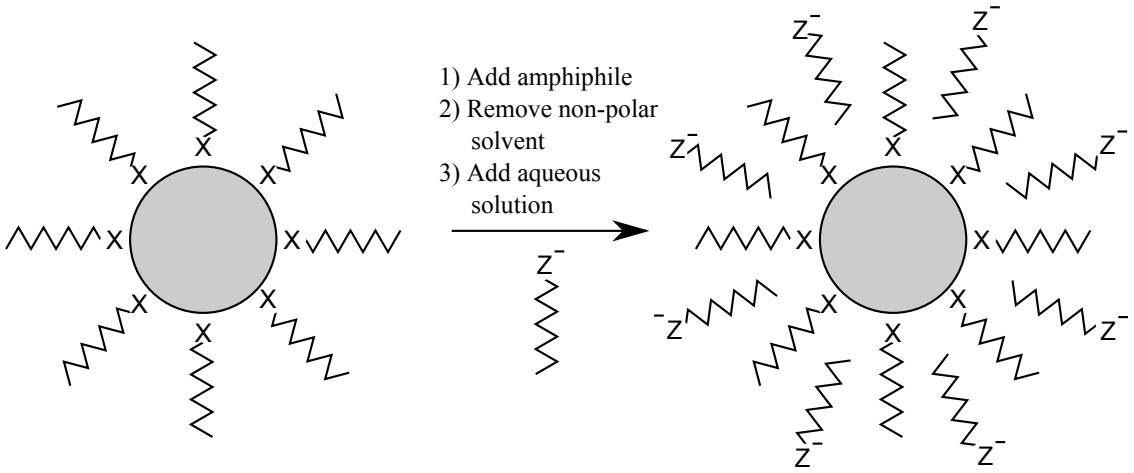

Figure 1.5: Ligand stabilised nanocrystals (left) are mixed with an amphiphile and the solvent is removed. A hydrophobic interaction occurs between the ligands and amphiphiles resulting in a bilayer forming around the nanocrystal. After addition of aqueous media the nanocrystals redisperse (right).

The amphiphiles most commonly used to transfer nanocrystals to the aqueous phase are fatty acids,[53–56] cetyltrimethylammonium bromide,[57–61] phospholipids,[62–64] gemini surfactants,[65–67] organo silanes[68] and poly(ethylene oxide)-poly(propylene oxide)-poly(ethylene oxide) triblock copolymers.[69] Of these fatty acids and phospholipids are found in nature and have potential for biological uses of nanocrystals.

Even though there is a great deal of scope for a "one amphiphile for all" approach much of the work done with a given amphiphile has been performed largely on one nanocrystal type. Much of the work on metal oxides, particularly iron oxides, has been achieved using fatty acids as the amphiphile.[53,55,56] This is presumably to maintain high compatibility with the surface bound ligand which, is typically a fatty acid, and to encourage biocompatibility. AuNPs and Gold Nanorods (AuNRs) have largely been transferred using cetyltrimethylammonium bromide[57–60] and QDs with phosphlipids.[62–64] This is probably not due to the surfactants not being compatible with a particular nanocrystal but more due to the research interests of the researchers being focussed on a particular nanocrystal or subsequent application.

A concern with surfactant stabilised nanocrystals is that the surfactant is in equilibrium with free surfactant, which is the case with traditional surfactant assemblies. This concern has not prevented amphiphile stabilised nanocrystals being used *in vivo* but has likely contributed to ligand exchange being the more popular method of interacting with a nanocrystal surface.

A closely related alternative is to use amphiphilic polymers. The term amphiphilic polymer covers many families of polymers but the polymers referred to are random or alternating copolymers that have a subunit which branches from the backbone, providing a hydrophilic component, and another subunit that has a branch which provides the hydrophobic component.[70,71] Hence, these polymers do not include poly(ethylene oxide)-poly(propylene oxide)-poly(ethylene oxide) triblock copolymers. The hydrophilic pendant

functionality is typically a carboxylate group and the hydrophobic group is normally an alkyl chain. The pendant alkyl group is able to form a bilayer with the nanocrystal surface ligands in the same manner as a traditional surfactant. The polymer can be thought of as a "poly-surfactant" in essence being a chain of amphiphiles.

Amphiphilic polymers are more attractive when compared to individual amphiphiles. Having multiple points of interaction with the nanocrystal means that once wrapped the desorption of the polymer would be an unfavourable process. A proportion of the outward facing carboxylic groups can undergo reactions to attach a desired compound to the surface without compromising the colloidal stability. Cross-linking between polymer chains has also been achieved with the aim of further reducing the likelihood of polymer detachment, although the majority of polymers are used without cross-linking. The structural features of amphiphilic polymers are discussed in detail in Chapter 4.

1.3.2.3 Ligand modification

The final option for adjusting the properties of an as-synthesised nanocrystal with hydrophobic ligands is to modify the ligand that is on the surface. This option is typically not available as the ligands used in the nanocrystal synthesis are chosen with tolerance to high temperatures and other chemical reactions in mind. In the case of octadecanethiol it has been shown that cyclodextrin rings can complex with the alkyl chain of octadecanthiol rendering the particle hydrophilic.[72] Complexing of cyclodextrin to nanocrystals stabilised by oleic acid has also been demonstrated.[73] If the nanocrystal was synthesised in an aqueous environment and has carboxylic acid functionality it can be transferred using coupling chemistry. For instance mercaptoacetic acid functionalised AuNPs have been transferred to organic solvent by coupling dicyclohexylamine.[74] Ligand modification is not widely used to transfer hydrophobic nanocrystals to water due to the limited options.

1.3.2.4 Methods that descend from ligand exchange and amphiphilic intercalation

There are many techniques that descend from the three aforementioned themes for interacting with nanocrystal surfaces. Encapsulating the nanocrystal in a shell of a protective material is very attractive. By encapsulating the nanocrystal it can be shielded from the chemically active environment it resides in, potentially prolonging the functional lifetime of the particle. Some nanocrystals contain elements that are well known for their toxic effects, *e.g*. QDs containing Cd. Adding a shell can protect the environment from the nanocrystal as well as the nanocrystal from the environment. Unlike particles with only ligands and amphiphiles on the surface, a shell acts as a cage, which traps the nanocrystal within, removing any issues of equilibria. However, the addition of a shell inevitably increases the total size of the structure, which is a problem when biological applications are the target.

Silica shells around nanocrystals have been an attractive structure to produce due to their optical transparency, low toxicity and wealth of coupling options. The chemistry of

silanes to form silica is well understood and furthermore the synthesis of spherical colloidal silica Nanoparticles (NPs) is well established. However, both methods for synthesising silica NPs are performed in solvents that hydrophobically stabilised nanocrystals are incompatible with: ethanol in the case of Stöber methods[75] and water in reverse microemulsion methods.[76] To solve this the surface of the nanocrystal needs to be modified to allow the nanocrystal to be in the same solvent. The methods for silica coating of nanocrystals have been extensively reviewed in Chapter 3.

Combining polymers and nanocrystals allows for a large range of materials to be made.[77] Strategies to attach polymers include "grafting to", "grafting from" and "grafting through". In "grafting to" methods a polymer is synthesised that has an anchor group allowing ligand exchange to occur. "Grafting from" is where the polymerisation initiator is located on the surface, usually by ligand exchange, and the polymer grows from the surface. Finally, "grafting through" is where a monomer is attached to the surface and the initiator is in the surrounding solution. Once again, all the strategies depend on modifying the surface of the nanocrystal before the shell can be grown.

1.3.2.5 Comparison of techniques

Smith *et al.* compared how QD properties were effected by the type of coating.[78] All methods of transfer caused a decrease in QY with both the ligand exchanged and amphiphilic polymer coated experiencing 19 % decreases. Amphiphilic polymer coated QDs were more resistant to photobleaching than the mercaptopropanoic acid functionalised QDs which precipitated under prolonged irradiation. The bilayer provided some protection against chemical oxidation by hindering access to the particle surface.

The cytotoxicity of CdSe and CdSe@ZnS with different surface functionalisations were studied by Kirchner *et al.*[79] It was found that QDs which were stabilised using mercaptopropanoic acid were very poor at preventing the release of Cd^{2+}. The addition of a silica shell allowed the concentration at which toxic effects were observed to increase by a factor of six. Use of an amphiphilic polymer appeared to double the toxicity of the QDs as compared to mercaptopropanoic acid functionalised QDs. The unexpected pattern was attributed to the reduced ability of the amphiphilic polymer fuctionalised QD to migrate in the cell, through either being too big to pass or sticking to the cell wall.

1.4 Uses of colloidal inorganic nanocrystals

Nanocrystals have been envisaged to have many possible uses. These largely fall into two categories: biological and materials.

1.4.1 Biological uses

Nanocrystals that are smaller than 10 nm possess a range of unique physical properties. This size range is also relevant in biology as it is approximately the same size as a large protein. Being in the same size domain as proteins allows for the potential migration of a nanocrystal through a biological system. This, combined with a range of intrinsic nanocrystal properties and the potential for bio-conjugation through functionalisation, see Section 1.3, allows the development of nanomaterials with biological objectives *in vivo*. This very active field has been recently reviewed by Bear *et al.*[80]

1.4.1.1 Therapy

Traditional drugs are delivered in a non-specific manner, *i.e*. they reach many parts of the body. This means that the dose needs to be higher for the drug to have the required effect at the target location and also that it may have undesired interactions elsewhere. More sophisticated drug delivery techniques are being developed to release or localise the drug at the site where it is needed. Drug delivery nanomaterials come in two classes: capsule like structures, such as micelles and liposomes, and carriers with drugs attached to their surfaces. Nanocrystals have been used as drug carriers due to their large surface to volume ratio and the range of methodologies for the attachment of drugs. Gold nanoparticles have been used due to the low toxicity of gold and the ready attachment of thiols to the surface.[81,82] The high surface area allows for a high loading of the drug. The surface would typically have a mixed functionality with another component allowing targeting to occur. Iron oxide nanocrystals have also been investigated but the weaker binding to the surface causes greater drug loss whilst travelling to the target.[83]

Cells are very sensitive to their temperature. Elevated temperatures can interfere with the internal function of a cell to the point where cell death occurs. For instance, if the temperature of a human is raised to 42 °C it is potentially fatal. An excited nanocrystal will release much of this energy as heat. If localised, this effect can be used to trigger cell death and when targeted on a diseased region can be used therapeutically, particularly for the treatment of cancer. Use of magnetism or light external to the patient as an excitation source allows for non-invasive treatment. Nanocrystals that have weak luminescent pathways, *i.e*. Fe_3O_4 and Au, have the greatest potential for hyperthermia.

The deep penetration of magnetic waves through the human body combined with the efficient heating provided by iron oxide nanocrystals has allowed for the development of magnetic hyperthermia treatments.[84] Iron oxide nanocrystals below a certain size contain a single magnetic domain and are superparamagnetic. When placed in a magnetic field

the domain aligns with the external field. In a magnetic field that is oscillating faster than the relaxation time of the particles magnetic moment, the majority of the particles are being forced from one magnetic state to another each time passing over the energy barrier separating them. The energy that is taken in to change the magnetic moment is released thermally. The magnetic moment can relax through two mechanisms: within the particle (Néel) and rotation of the particle (Brownian). Iron oxide nanocrystals less than 20 nm in diameter have been used to perform magnetic hyperthermia.[84]

AuNPs have also been used for hyperthermia treatments by use of the SPR.[85] Plasmonic photothermal therapy is where the gold nanoparticles are excited in the SPR band and the energy leaves the particle through non-radiative pathways, *i.e*. as heat. This is hindered by the narrow absorption window in the near infra-red provided by haemoglobin and water in biological systems. The position of the SPR can be tuned by adjustment of the size of the particle to match the absorption minimum. A high intensity light source such as a pulsed near infra-red laser is used as the excitation source.

Photodynamic therapy is when a therapeutic material triggers cell death by the generation of singlet oxygen following excitation with light. Traditional photosensitisers are administered to the patient and light is applied to the region where the therapy is to occur. Due to their large absorption cross-section nanocrystals, such as gold, Up Converting Nanocrystals (UCNs) and QDs, can be used to harvest light. Nanocrystals functionalised with traditional photosensitisers, such as porphyrin derivatives, potentially can be used to significantly improve the yield of singlet oxygen produced, although the limiting step is the energy transfer process from the particle to the photosensitiser.[86] Also, biofunctionalisation of nanocrystals offers improved targeting of cancerous regions for photosensitisers potentially allowing lower doses to be used. This has been explored for various QDs,[87,88] UCNs[88,89] and AuNPs.[90]

1.4.1.2 Imaging

Non-invasive imaging of the body has huge potential for the diagnosis and discovery of a range of medical conditions. The main forms of imaging are based on the use of light, magnetic contrast and vibrations.

Due to their photostability, size and tuning of emission profile QDs have enormous potential in optical bioimaging as compared to organic dyes.[16] QDs have molar absorption coefficients and fluorescence QYs (≤ 0.85) much higher than that of organic dyes. The thermal and photochemical stability of surface passivated QDs is much better than that of organic dyes, such as fluorescein and tetramethyl rhodamine isothiocyanate, which bleach preventing long term imaging. The surface of a QD has a range of surface functionalisation techniques available allowing for biomolecules to be attached to the surface. Biomolecules allow targeting of the QD to a particular region of a body to occur.[91,92] The ability to tune the absorption and emission profiles by controlling the particle size allows the near infra-red window to be used with QDs.

UCNs are another family of fluorescent nanocrystals that have potential for nanocrystal based optical imaging.[89,92] Unlike QDs, light absorbed by UCNs undergoes anti-Stokes processes. Low energy light, typically multiple photons of near infra-red is absorbed and visible or UV light is released. The two photons are not simultaneously absorbed as in two-photon absorption processes and consequentially have higher efficiencies. High intensity near infra-red sources are used which is an advantage over QDs, eliminating non-specific autofluorescence.

AuNRs can undergo a plasmon-enhanced two-photon absorption resulting in luminescence.[93] The benefits of exciting in the near infra-red window are similar to that of UCNs. Gold has the advantage of a perceived low toxicity compared to QDs and UCNs.

Nanocrystals can also serve as contrast agents in magnetic resonance imaging. The relaxation times of water are observed in two dimensions to form an image. Contrast agents influence the T1 or T2 relaxation of protons in water, allowing enhancement of the image. In the case of superparamagnetic iron oxide the T2 relaxation is lengthened. In a T2 weighted image the iron oxide will produce a region of low intensity.[21]

AuNR have been used to perform imaging by photoacoustic tomography. In this the AuNRs absorb light and releases heat. When using a high intensity pulsed light source the rapid thermal expansion generated a sound wave that travels through the tissue, which can be imaged.[93,94]

1.4.2 Non-biological materials

The light harvesting properties of QDs allow their use in energy harvesting materials. The ability to tune the absorption profile through the quantum confinement effects allows materials that effectively absorb particular frequencies to be developed. QD-based solar cells are an attractive alternative third generation of solar cell. This is due to their extinction coefficients being much higher than that of the dyes used in dye sensitised solar cells. The lower cost of manufacture and the potential to exceed the current maximum efficiency available to previous generations of solar cells make QD based systems very attractive.[95,96]

The generation of H_2 from water offers a source of clean and potentially renewable fuel. QDs surface functionalised with catalysts for the reduction of water have been developed.[97] Once again the photostability and high molar decadic absorption coefficient make QDs a good alternative to organic compounds, which have been previously used.

The use of the ability to tune the emission colour through the size of QDs and a narrow full width at half maximum has resulted in light emitting diodes incorporating QDs being developed. QDs offer purer colours and a wider range closer to that of the human eye than current light emitting diode technologies provide.[98,99]

CHAPTER 2

Colloidal inorganic nanoparticle synthesis and characterisation techniques

---

2.1 Nanocrystal synthesis - Theories

2.1.1 Routes to monodisperse nanocrystals

The synthesis of nanocrystals can be categorised into two different approaches: "top-down" methods involve the physical destruction of a bulk material and "bottom-up" syntheses, which are based upon solution-phase chemistry starting from molecular precursors. Physical methods offer the possibility of making large quantities of nanocrystals but more complex structures such as core-shell particles would be difficult to synthesise. Bottom-up methods, employing the already established field of colloid chemistry, offer a more simple route to monodisperse spherical particles and greater flexibility towards more complex structures, but suffer from limitations of scale.

To date, the synthesis of nanocrystals using bottom-up methodologies follows two themes: high temperature thermal decomposition of metal precursors and reduction of metal salts.[100] Common to all methodologies is the requirement that the resulting particles are colloidally stable, according to DLVO theory,[23] see Section 1.3.1. Without colloidal stability, further modification or use of the nanocrystal for any potential application is difficult. Colloidal stabilisation can be provided electrostatically by ions produced during the particle synthesis or sterically by ligands added before or after the synthesis.

It is important to remember that the unique properties of nanomaterials are size dependent and as a consequence minimising the polydispersity of particle size is crucial. The synthesis of truly monodisperse colloids, where there is no variation in size, is synthetically challenging and as a consequence a relaxed definition of the term monodispese is widely accepted; Equation 2.1.[101] A monomodal system is to be considered monodisperse if 90 % of the population (1.645σ, where σ is the standard deviation) lie within ± 5 % of the mean

particle size, $\langle \mathbf{d} \rangle$. Otherwise the system is considered as polydisperse.

$$\frac{1.645\sigma}{\langle \mathbf{d} \rangle} \leq 0.05 \tag{2.1}$$

2.1.2 Nucleation and growth

To achieve greater control over the polydispersity of a nanocrystal suspension using "bottom-up" methods, a consideration of the formation of the suspension is required. As with bulk crystals, control over the final nanocrystal structure is thought to be governed largely by processes during the nucleation and growth phases.

It must be stated that the development of models and experimental data to thoroughly explain the nucleation and growth of nanocrystals is still ongoing. There have been a number of different studies on a range of types of nanocrystal materials and a single model does not fit all. The field has recently been reviewed by Finney and Finke.[102]

2.1.2.1 Nucleation

Classical nucleation theory treats the nucleus as a bulk phase, using the Gibbs capillary approximation.[103] Nucleus formation is described using two terms: a term for the favourable formation of a more thermodynamically stable new phase and a unfavourable term from the development of an interface between the old and new phases, Equation 2.2. The displayed relation assumes that the nucleus is spherical, as this minimises the surface area of the nucleus, where r is the radius of the nuclei, γ is the surface free energy per unit area and ΔG_v is the difference in free energy per unit volume between the new and old phases.

$$\Delta G = -\frac{4}{3}\pi r^3 |\Delta G_v| + 4\pi r^2 \gamma \tag{2.2}$$

Using Equation 2.2, a plot of ΔG against r will result in a curve with a maximum free energy at a radius known as the critical radius r^*; Figure 2.1. This is due to the stabilising influence of the formation of the thermodynamically stable new phase prevailing over the unfavourable interaction at the surface of the spherical nucleus. For nuclei with $r < r^*$ growth is unfavourable and the nuclei will dissolve, whereas, when $r \geq r^*$ the growth of the nuclei is favoured.

Although there are now many models for explaining the process of nucleation, LaMer's descriptions of the formation of sulphur sols from the 1950s are still widely quoted and have directed many studies into the formation of nanocrystals.[104] Since 1997 there has been a resurgence in interest in the mechanisms of nucleation and growth of nanocrystals where transition metal and semi-conductor systems have been investigated.[102]

LaMer's sulphur sol system works by the generation of S_2 from sodium thiosulphate in hydrochloric acid. As time progresses the concentration of S_2 increases; Phase I in Figure 2.2. When a critical supersaturation level is achieved, nucleation of the nanocrystal precursors occurs; Phase II. Nucleation is said to occur over a short period of time with the

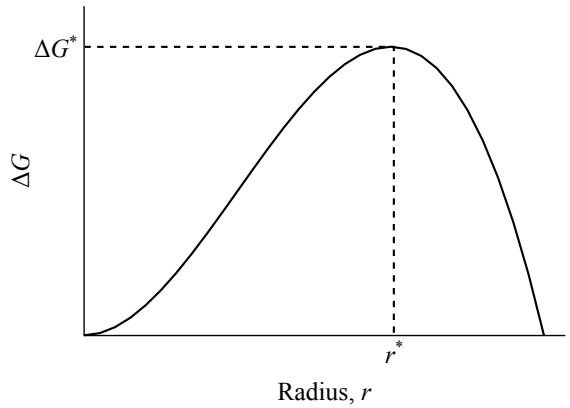

Figure 2.1: A plot showing the critical radius, r^*, in terms of free energy, ΔG.

generation of multiple nuclei resulting in a burst of nucleation. As nucleation occurs the concentration of the precursor falls resulting in no new nucleation events. The nanocrystals continue to grow by diffusion of the precursor to the surface, Phase III.

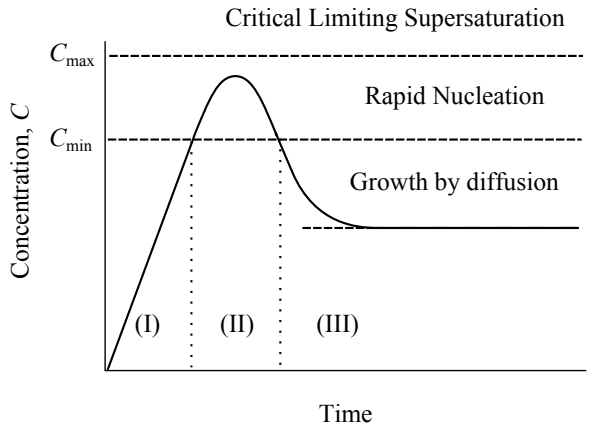

Figure 2.2: LaMer's mechanism for the nucleation and growth of sulphur sols. The phases shown are: I) concentration increase of precursor, II) supersaturation of precursor is achieved and nucleation occurs and III) growth of nuclei beneath the supersaturation concentration. Adapted with permission from [104]. Copyright (1950) American Chemical Society.

It is well known that LaMer's mechanism for nanocrystal formation is not applicable to most transition metal and semi-conductor nanocrystal systems.[102] Even so, the mechanism has served as a source of inspiration for the development of new methodologies for the synthesis of nanocrystals since it was the first where the processes of nucleation and growth were separated in time. By nucleation occurring over a short period of time it is possible to achieve greater control over the polydispersity of the final particles. This is known as "burst nucleation" and is generally thought of as a requirement for synthesising monodisperse nanocrystals.[105] As with the LaMer model, methods to synthesise nanocrystals use supersaturation and the subsequent concentration decrease to create the burst.

2.1.2.2 Growth

Ideally, once nucleation has finished growth occurs. This is a slow process in which the remaining precursors are consumed by the nuclei. There are many theoretical models for growth but all are focussed around the interplay between Fick's first law and the Gibbs-Thomson equation.[100,102]

Recently, Mulvaney described a model for growth and nucleation of nanocrystals.[106] In this model growth is assumed to occur in two steps. The precursor diffuses to the surface at a rate constant determined by the diffusion coefficient, D. Once at the interface the precursor may be taken up into the particle to become a part of the lattice, with a rate k_{up}, or precursor may be formed by the dissolution of the particle, with a rate k_{dis}.

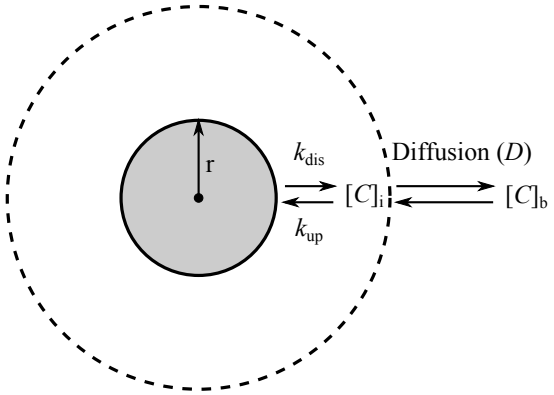

Figure 2.3: An illustration showing an isolated particle of radius r, the interfacial zone where the concentration is $[C]_i$ and the bulk solution where the concentration is $[C]_b$. The diffusion coefficient, D of precursor from the bulk solution to the interface is shown as well as the rate constants for uptake, k_{up} and dissolution of precursor, k_{dis}. Adapted with permission from [106]. Copyright (2009) American Chemical Society.

The flux, J_{dif}, of the monomer to and from the particle may be described using Fick's first law, Equation 2.3, where D is the diffusion coefficient and σ is the radius of the sphere of diffusion.

$$J_{dif} = 4\pi\sigma^2 D\frac{\mathrm{d}[C]}{\mathrm{d}\sigma} \tag{2.3}$$

Taking into account the flux of precursor diffusing to the particle surface, J_{dif}, the flux into the particle, J_{react}, and the limitation that monomer may not react faster than it can diffuse to the surface a steady state flux can be generated, J^{SS}. The steady state flux is intimately linked to the rate of particle growth, Equation 2.4, the bulk concentration of monomer, $[C]_b$, and the equilibrium concentration of monomer, $[C]_{eq} = k_{dis}/k_{up}$.

$$\frac{\mathrm{d}r}{\mathrm{d}t} = \left(\frac{3V_m J^{SS}}{4\pi r^3}\right) \tag{2.4}$$

The Gibbs-Thomson equation relates the particle radius, r, the surface free energy per unit area, γ, and the concentration of monomer with an infinitely flat surface, $[C]_\infty$, to the equilibrium concentration of monomer, $[C]_{eq}$, Equation 2.5.

$$[C]_{eq} = [C]_{\infty} \exp\left(\frac{2\gamma V_m}{rRT}\right) \tag{2.5}$$

To link Equation 2.4 to the surface free energy per unit area, γ, the Gibbs-Thomson equation is used along with expressions for J_{dis} and J_{up} from Fick's first law resulting in Equation 2.6.

$$\frac{\mathrm{d}r}{\mathrm{d}t} = \frac{DV_m\left([C]_b - [C]_{\infty}\exp\left(\frac{2\gamma V_m}{rRT}\right)\right)}{\left(r + \frac{D}{k_r}\right)} \tag{2.6}$$

Equation 2.6 has a strong dependence on r. As r increases the rate of particle growth decreases. Many different forms of a rate equation exist for the growth rate of nanocrystals depending on the assumptions made in a particular model. A common feature in all models is the inverse dependence on r.

2.1.2.3 Ostwald ripening

Once the monomer is depleted, $[C]_b = 0$, the new concentration between the particles is determined by their combined relative $[C]_{eq}$. Particles with a smaller r have a higher $[C]_{eq}$ due to the Gibbs-Thomson equation, Equation 2.5. A high $[C]_{eq}$ means that the value of k_{dis} is high relative to k_{up}, due to $[C]_{eq} = \frac{k_{dis}}{k_{up}}$. So particles with $r > r^*$ are decreasing in size. Likewise, a large particle has a lower $[C]_{eq}$. In the case of larger particles $[C]_{eq}$ is lower and k_{up} is larger.

When a mixture of particle sizes is created the difference in the $[C]_{eq}$ drives the movement of monomer from one particle to the other. The larger particle with the lower $[C]_{eq}$, $[C]_{eq(big)}$, combats the high $[C]_{eq}$ provided by the small particle $[C]_{eq(small)}$. The two equilibria result in the decrease in size of the small particle and the increase in size of the large particle.

This makes the resulting polydispersity worse due to larger particles growing faster than their slightly smaller counterparts, which are all taking up monomer from the small particles. The mean size of the particle distribution will also increase. This process is known as Ostwald ripening. Inhibiting Ostwald ripening is achieved by capping agents, lowering the temperature or addition of more monomer.

2.1.3 Bottom-up synthesis of colloidal nanocrystals

There is a wide range of bottom-up, or chemical, methods for the synthesis of nanocrystals. In this work nanocrystals have been formed using thermolysis, or thermal decomposition, and ambient temperature reduction methods. Other bottom-up techniques such as solvothermal, photochemical, electrochemical and arrested precipitation have been reviewed by Rao *et al.*[5]

2.1.3.1 Reduction of metal salt

Historically, the reduction of metal salts is thought to have been used since Egyptian times for the production of AuNPs. The resulting particles were used for the decoration of pottery due to the characteristic ruby red colour, which is a consequence of the SPR. In 1857 Michael Faraday described the reduction of gold(III) chloride to produce a gold sol. "If the solution -of chloride of gold- be weak and the phosphorus clean, part of the gold is reduced in exceedingly fine particles, which becoming diffused, produce a beautiful ruby fluid."[2] This was further advanced by Enüstün and Turkevich with the production of a stable dispersion of deep-red 13 nm gold nanocrystals where sodium citrate was used as the reducing agent and as a stabilising agent for the final particles.[107]

Sodium borohydride, $NaBH_4$, was used by Brust and co-workers in a two phase mixture of water and toluene.[26,27] In this method a solution of hydrogen tetrachloroaurate, $HAuCl_4 \cdot {}_3H_2O$, is added to a solution of tetraoctylammonium bromide, $(C_8H_{17})_4N^+Br^-$, in toluene, causing the formation of a Au-tetraoctylammonium bromide complex in toluene. This is reduced by an aqueous solution of sodium borohydride whist being vigorously stirred. Depending on the version of the synthesis, the stabilising thiol ligands are added prior to the reducing agent or after growth and size focussing has occurred. The "Brust" two phase method has been modified many times since the original publication. In this thesis a slightly modified protocol is used to produce AuNP with a diameter of approximately 7 nm. Ambient temperature reduction methods have been used largely to produce Au and Ag nanocrystals.

2.1.3.2 High temperature thermal decomposition of precursors

High temperature thermal decomposition of metal containing compounds in high boiling solvents in the presence of compounds that ligate to the surface allows the growth of nanocrystals. A wide range of inorganic nanocrystals have been synthesised using thermal decomposition covering metal oxides, metals and semiconductors. The two thermal decomposition strategies used in this work include the "hot injection" of precursors and "heating up" methods.[105]

The hot injection method was developed with the aim of temporally resolving the events of nucleation and growth. The hot injection method was pioneered by Murray *et al.* when synthesising cadmium chalcogenide nanocrystals.[108] In this work a room temperature solution containing both precursors, dimethyl cadmium and trioctylphosphine selenide, is rapidly injected into a rapidly stirred high boiling point solvent, which is at 300 °C under an inert atmosphere. The precursors decompose rapidly, causing supersaturation conditions to be reached. At supersaturation, the formation of nuclei occurs in the same vein as in the LaMer mechanism, Section 2.1.2.1. The mixture of the room temperature precursor solution with the hot solvent causes a rapid decrease in temperature which, in combination with the precursor concentration decreasing, results in nucleation stopping and the remaining precursor causing growth upon the nuclei. The trioctylphosphine acts as

the solvent and the coordinating ligand during synthesis. Variants of this technique have been used to make many different semiconductor nanocrystals.[109] The method used in this work for InP@ZnS is a hot injection-based method by Xu *et al.*[110]

Heating up methods have been used to synthesise highly monodisperse iron oxide nanocrystals with a strong degree of size control. The precursors used are typically iron pentacarbonyl,[111] iron(III) acetylacetonate[112] or iron oleate.[113] In contrast to hot injection methods the precursors, ligands and solvent are all in the initial reaction mixture. The mixture is slowly heated to a certain temperature, typically in the range of 200 to 230 °C and held at this temperature for approximately 1 h. This is thought to be to allow complete decomposition of the precursors. After decomposition is complete the solution is slowly heated to induce nucleation. It is thought that the temperature of decomposition is beneath the temperature for nucleation or that intermediate precursors are formed which decompose at higher temperatures. The mechanism is not fully understood and is still the subject of debate.[105] The method used in this work is a modification of the iron(III) acetylacetonate heating up synthesis by Sun and Zeng.[112]

2.2 Nanocrystal synthesis - Methods Used

2.2.1 Synthesis of InP@ZnS Quantum Dots

The procedure for the synthesis of InP@ZnS QDs was based on earlier publications by Xu *et al.*[110,114,115] Typically, indium chloride (0.1 mmol, Aldrich, 98 %) stearic acid (0.1 mmol, Fluka, >97 %), hexadecylamine (0.2 mmol, Aldrich, 98 %) and zinc undecylenate (0.1 mmol, Aldrich, 98 %) were added to 1-octadecene (2 ml, Aldrich, 90 %). The reaction mixture was repeatedly evacuated and refilled with nitrogen. Whilst stirring the reaction mixture was heated to 270 °C. Immediately after reaching 270 °C, 1 ml of 0.1 mol dm^{-3} tris(trimethylsilyl)phosphine (0.1 mmol, Aldrich, 95 %) in 1-octadecene was rapidly injected into the reaction mixture. The solution was heated at 240 °C for 20 min.

Subsequently, the reaction mixture was cooled to room temperature. Zinc diethyldithiocarbamate (0.2 mmol, Aldrich, 98.5 %) and zinc undecylenate (0.2 mmol, Aldrich, 98 %) were added to the reaction mixture. The reaction mixture was repeatedly evacuated and refilled with nitrogen. The solution was heated to 180 °C for 10 min and 240 °C for 20 min.

After cooling to room temperature, toluene (4 ml, Sigma-Aldrich, ≥99.9 %) was added. The diluted reaction mixture was centrifuged at 2200 × g for 5 min and the clear QD solution was collected.Ethanol was added until the solution became turbid and the precipitated nanocrystals were collected by centrifugation at 2200 × g for 15 min. The QDs were redispersed in toluene (7 ml, Fisher Scientific, >99 %).

Control of emission colour was achieved by varying the amount of ligand added during the formation of the core and of the shell. Higher amounts of ligand present when adding the phosphine precursor resulted in a greater number of smaller nuclei. For good colloidal stability of the resulting InP@ZnS nanocrystals the total amount of zinc undecylenate

added in the synthesis of the core and the shell must be constant regardless of the core size. The amounts used to produce particles of a particular emission colour are shown in Table 2.1.

Table 2.1: The quantities of zinc undecylenate used when producing the core and the shell to generate specific emission colours.

	Zinc undecylenate used / mg	
Emission colour	**Core**	**Shell**
Orange	43	87
Yellow/Green	86	44
Green/Blue	130	0

To achieve blue or red emission profiles the reaction conditions and times needed to be modified. Achieving small cores is the most difficult and requires a brief nucleation followed by a slow growth.

2.2.2 Synthesis of iron oxide particles

The procedure for the synthesis of Fe_3O_4 particles used was described by Lattuada and Hatton.[41] Briefly, iron(III) acetylacetonate (2 mmol, Aldrich, 99.9+ %), oleic acid (6 mmol, Aldrich, 90 %), oleylamine (6 mmol, Fluka, $\geq$70 %) and 1,2-tetradecanediol (10 mmol, Aldrich, 90 %) were dissolved in dibenzylether (20 ml, Aldrich, 99 %). This was stirred under a flow of nitrogen. The mixture was heated to 100 °C over 45 min.The temperature was further increased to 200 °C over 40 min and left to stir for 2 h.The flow of nitrogen was increased and the mixture heated to 300 °C for 1 h.

The resulting black solution was cooled to room temperature. The particles were precipitated by the addition of ethanol ($\approx$50 ml, Sigma-Aldrich, $\geq$99.8 %) and centrifuged at 2200 $\times$ *g* for 5 min.The resulting black precipitate was redispersed in the minimum amount of toluene (24 ml, Sigma-Aldrich, $\geq$99.9 %). For use in the preparation of the hybrid layer 1 ml of saturated Fe_3O_4 solution was precipitated using ethanol and redispersed in chloroform (100 ml, Fisher Scientific, >99 %) to give a 100$\times$ dilution.

2.2.3 Synthesis of gold nanocrystals

The procedure for the synthesis of Au nanocrystals described is a modification of the method developed by Brust *et al.*[26] A colourless solution of tetraoctylammonium bromide (2.2151 g, 4.051 mmol, Aldrich, 98 %) in toluene (80 ml, Sigma-Aldrich, $\geq$99.9 %) and a yellow solution of hydrogen tetrachloroaurate(III) trihydrate (302.2 mg, 0.767 mmol, Aldrich, $\geq$99.9 %) in distilled water (25 ml) were mixed and shaken. Upon shaking, the yellow aqueous phase became colourless and the organic phase turned red. The phases are separated and a solution of sodium borohydride (335.8 mg, 8.877 mmol, Aldrich, $\geq$98 %) in distilled water (25 ml) was added dropwise to the stirred organic phase over

1 min.During sodium borohydride addition the solution turned a strong purple colour. The solution was stirred for 30 min.Excess sodium borohydride was removed by repeatedly washing the reaction mixture with portions of HCl (aq) (0.1 mol dm^{-3}, 100 ml) until the release of H_2 stopped. The reaction mixture was washed with NaOH (aq) (0.1 mol dm^{-3}, 100 ml) once to remove any HCl (0.1 mol dm^{-3}, 100 ml) and three times with NaCl (aq) (0.1 mol dm^{-3}, 100 ml). The purple dispersion was stirred at room temperature to ripen over 24 h. 1-Dodecanethiol (10 ml, Aldrich, $\leq$98 %) was added and stirred for 2 h at 65 °C.

The dispersion was centrifuged at 900 $\times$ g for 10 min to remove any large structures.The nanocrystals were precipitated using an excess of ethanol and collected by centrifugation at 8900 $\times$ g for 20 min.The collected precipitate was redissolved in toluene $\approx$5 ml and precipitated using excess cold methanol. The aggregated nanocrystals were collected by centrifugation at 8900 $\times$ g for 20 min and re-dispersed in toluene (8 ml).An improved size distribution can be achieved by removing the larger nanocrystals. The larger nanocrystals are removed by the addition of cold methanol (80 µl) and a final centrifugation at 8900 $\times$ g for 5 min.

2.3 Nanocrystal characterisation

The characterisation of nanocrystals requires the use of a range of techniques each providing a piece of the puzzle. Many techniques originally intended for molecular or bulk characterisation can be used and the extension of these techniques can provide more information. The subject of characterisation has been recently reviewed by Rao and Biswas[116] and Hutchison and Kirkland.[117] The methods used in this thesis are briefly described in the following sections. Typical nanocrystal characterisation data is provided in Appendix A.

2.3.1 Electron microscopy & related techniques

An electron microscope provides a wealth of structural and chemical characterisation due to the available imaging and spectroscopies that it can potentially perform. The use of electrons to study materials has a number of beneficial consequences due to electrons being a type of ionising radiation. As a consequence a range of secondary signals are produced which take the form of X-rays, light, forward scattered electrons (elastic and inelastic) and backscattered electrons. These allow a range of measurements to be made on a single sample in a relatively short period of time by a single instrument.

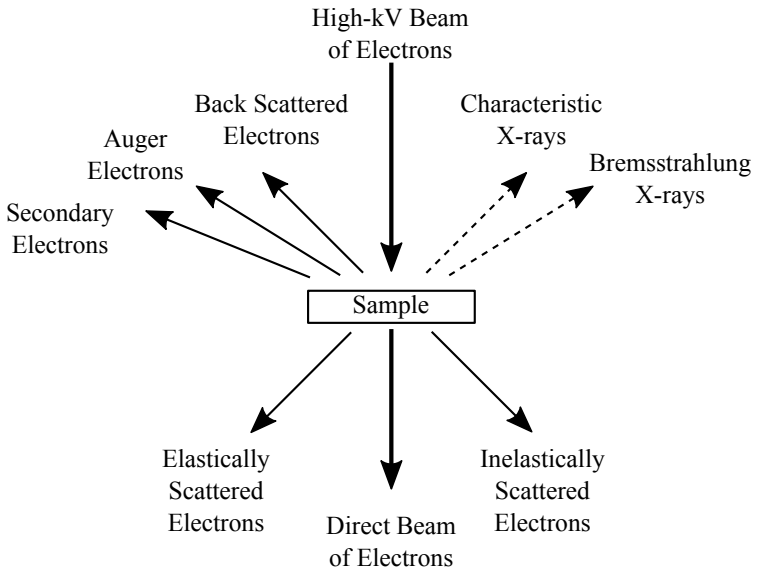

Figure 2.4: A simplified depiction of the incident beam of electrons being accelerated at a high voltage and the measurable signals that can be used for structural or chemical identification. Adapted from ref. [118].

2.3.1.1 Electron microscopy

The ability to form an image of an object smaller than the human eye can resolve is known as microscopy. Microscopy using visible light can at best resolve objects of approximately 300 nm, when using light of $\lambda = 550$ nm. To study objects with dimensions less than 100 nm microscopy using electrons is used. Electrons, as do other particles, exhibit properties of both a particle and a wave as described by de Broglie, $\lambda = h/(mc)$.[119] As electrons have a much smaller wavelength they can resolve structures that it is impossible to access with light. For instance, an electron accelerated by a voltage of 200 kV has a velocity of 2.086×10^8 m s^{-1} and a corresponding wavelength of 2.51 pm.

The most common form of electron microscope used in characterising nanocrystals is a Transmission Electron Microscope (TEM).[118] This is where the direct beam, also known as the transmitted beam, is imaged. Dark regions where scattering has occurred and light regions where the sample was transparent to the electrons are formed. The degree of scattering controls the intensity of an area of the image. As TEM is dependent on the transmission of electrons, a given sample can not be too thick as multiple scatterings will occur resulting in no direct beam.

A TEM consists of a series of lenses and apertures, which guide the beam of electrons down evacuated chambers to form a magnified image at the bottom. The lenses are in the form of magnetic fields, which act like convex glass lenses. Unlike light microscopy, the magnetic lenses do not change position but instead the strength of a magnetic lens can be adjusted. At the end of the tube are a range of options for the capture of an image: a phosphor screen, an electron sensitive film or a charge-coupled device. The resolution of a TEM is limited by spherical aberrations introduced by the magnetic lenses and chromatic aberrations introduced by interactions with the sample, although chromatic variations can

be useful, Section 2.3.1.4. Figure 2.5 shows that the two principle modes of operation involve the imaging of a diffuse direct beam to generate an image or the imaging of a concentrated direct beam along with the elastically scattered electrons giving rise to a diffraction pattern, Section 2.3.1.2.

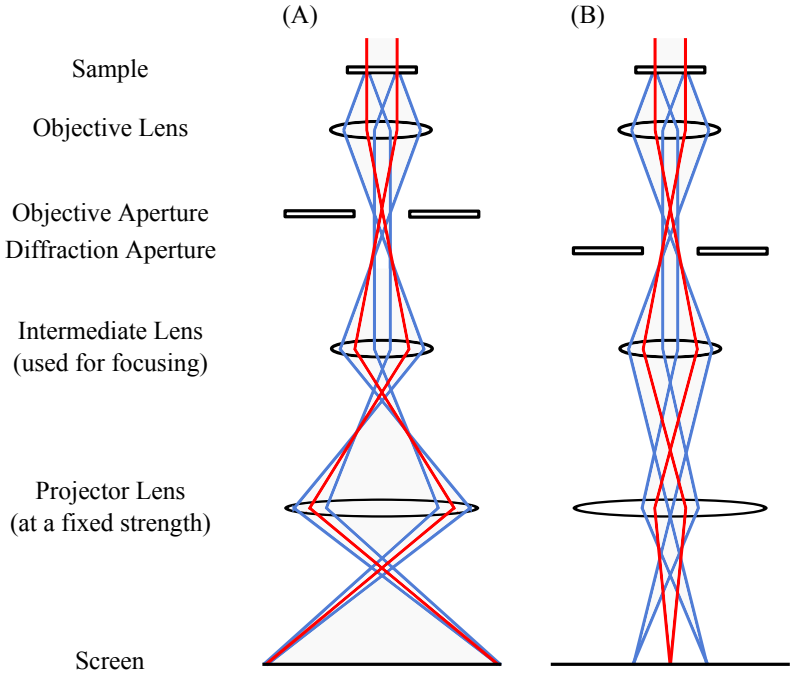

Figure 2.5: The two principle modes of operation of a TEM with the direct beam (red) and scattered beam (blue). (A) The direct beam is spread over a wide area and is focussed on the viewing screen to form a bright field image. (B) The direct and the elastically scattered beam are imaged together on the viewing screen resulting in a diffraction pattern. Adapted from ref. [118].

The image made from the direct beam is known as a bright field image. Alternatively, a dark field image can be formed using the scattered beam. In a dark field image the regions that causes the most scattering appear bright and the regions where little scattering occurs appear dark. The electrons, which form the image, have interacted with the sample and contain additional structural information, such as planar defects, stacking faults, *etc*., whilst offering better contrast, although dark field images suffer from low intensity.

Limitations of TEM include the poor sampling provided by an image. This is a natural consequence of observing an object so closely. As a consequence TEM should always be used in conjunction with other techniques, which provide information about the average properties of the sample, such as Dynamic Light Scattering (DLS). Weakly scattering materials, such as polymers, appear invisible as the elements contain relatively few electrons and small nuclei. The electron microscope is under a vacuum and as a consequence the sample is also. In the case of colloidal samples, any influences on the structure by the solvent will be absent in the observed image. Heating effects from the inelastically-scattered electrons may also cause sample distortion or destruction.

The instruments used were a Jeol 2000EX TEM with a tungsten filament and an acceleration voltage of 180 kV to 200 kV, at the University of East Anglia, and a Philips

CM200 field emission gun TEM, at the Leeds EPSRC Nanoscience and Nanotechnology Research Equipment Facility.

The sample grids used were 300 μm mesh copper grids with a carbon film as supplied by Agar Scientific. Samples in organic solvents were dropped onto the grid laid upon filter paper. Time was allowed for the organic solvent to evaporate between drops.

2.3.1.2 Selected area electron diffraction

The direct beam is used to form images but there may also be information within the elastically scattered beam depending on the composition of the sample. If the sample studied is crystalline the material acts as a diffraction grating for the scattered electrons. The electrons are deflected according to Bragg's Law. Lattice dimensions are often described in reciprocal space, typically $Å^{-1}$, by use of Bragg's Law in the form of Equation 2.7, where d is the interplanar distance within a crystal, θ is the angle of diffraction and n is an integer.[118] When n is an integer constructive interference occurs and when it is a non-integer destructive interference occurs. This results in the scattered beam containing a diffraction pattern.

$$\frac{n}{d} = \frac{2\sin\theta}{\lambda} \tag{2.7}$$

The diffraction pattern is produced from the direct beam and the elastically scattered electrons. The direct beam forms an intense spot in the centre of the pattern and the elastically scattered electrons form a pattern around the central spot. In the case of a crystalline material with many independent crystals, concentric rings are formed which form a diffraction pattern. This diffraction pattern can be used as a finger print for identification of the crystalline material being observed.

The pattern is directly comparable to an X-ray diffraction pattern but can be performed on a small area of a sample, 3.14×10^{-2} μm^2, allowing characterisation of different regions of a structure. Being able to choose the region of the sample from which the diffraction pattern is collected gives rise to the name of the technique, Selected-area Electron Diffraction (SAED). The selected area would contain many nanocrystals so characterisation results in a scattering pattern containing a series of concentric rings, as all the particles are orientated randomly. This pattern is directly comparable to an X-ray powder diffraction pattern, due to both incident X-rays and electrons interacting with the sample's electrons. The difference between the techniques is only the magnitude of the scattering angles.

The instruments used were a Jeol 2000EX TEM with a tungsten filament and an acceleration voltage of 180–200 kV, at the University of East Anglia, and a Philips CM200 field emission gun TEM, at the Leeds EPSRC Nanoscience and Nanotechnology Research Equipment Facility. Samples were prepared in accordance to Section 2.3.1.1 with the exception that more material is required so approximately five times more drops were used for a given sample.

2.3.1.3 Energy dispersive X-ray analysis

A range of X-rays are produced as secondary signals within the TEM. An X-ray is a photon with less energy than gamma rays and more energy than UV-light, between 100 eV and 10 eV. The X-rays that are created due to the inelastic scattering of electrons are known as characteristic X-rays and allow the identification and quantitation of elements in the sample.

Characteristic X-rays are formed due to a high energy electron from the beam causing an inner shell electron in the sample to be ejected. This results in an electron hole in a low energy orbital. The electrons rearrange to achieve the lowest energy configuration, resulting in an electron moving from a high energy orbital to the hole. An X-ray is emitted with an energy that is equal to the energy difference between the initial and final orbital of the electron that moved. The energy gaps between orbitals are characteristic of the element that it has been emitted from due to each nucleus having a different pull on the surrounding electrons. This process is depicted in Figure 2.6 with a K_α X-ray being emitted.

The production of a characteristic X-ray is only one of the potential routes of the excess energy being removed. The other major pathway is the ejection of an Auger electron due to transfer of the energy to another outer electron causing its ejection. As there are multiple pathways, a fluorescence QY, *i.e.* the proportion of electrons which relax in a certain manner, for the generation of K-line X-rays is considered.

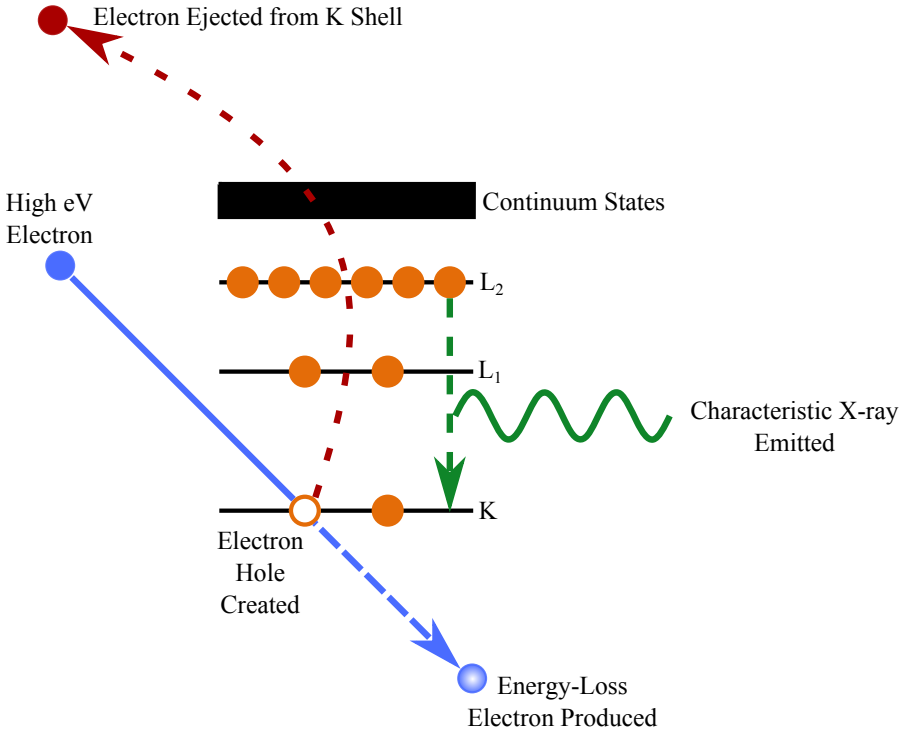

Figure 2.6: An energy level diagram showing the inelastic interaction of an electron with an atom within the sample. An energy-loss electron is produced and an inner shell electron is ejected. The system rearranges and the excess energy is released as a characteristic X-ray. Adapted from ref. [118].

Energy-dispersive X-ray (EDX) analysis across a range from 0 to 10 eV results in a

spectrum where most characteristic X-rays are observed.[120] An EDX analysis can also show a weak broad band across much of the spectrum. This is due to "Bremsstrahlung" X-rays being generated due to electrons that pass near to the nuclei being decelerated and emitting X-rays with an energy equal to the amount of deceleration.

The major weakness of EDX analysis is the poor sensitivity for lighter elements. This arises for two reasons: as Z decreases the K-line fluorescence yield falls, when $Z < 11$ the yield is below 2 % as opposed to above 50 % when $Z > 32$, and the EDX detector is protected from unwanted gasses in the microscope vacuum by a beryllium window which absorbs photons of less than 1000 eV.[121] Ultra-thin windows allow boron, $Z = 5$, and upwards to be detected.

The instrument used was a Oxford Instruments ultra-thin window EDX detector attached to a Philips CM200 field emission gun TEM. Samples were prepared in accordance with Section 2.3.1.1.

2.3.1.4 Electron energy-loss spectroscopy & Energy-filtered TEM

Electron Energy-Loss Spectroscopy (EELS) uses the electrons from the beam that have been elastically scattered.[121] These electrons have transferred some of their kinetic energy to the sample and are known as energy-loss electrons, Figure 2.6. The kinetic energy loss is characteristic of the element that the fast electron interacted with. A high resolution electron spectrometer is used to separate all the transmitted electrons by their kinetic energy. The result is an electron energy-loss spectrum where the intensity is proportional to the amount of electrons with a particular kinetic energy. The main characteristics are a zero-loss peak for inelastically scattered electrons, a plasmon band and a series of edges on a slowly decreasing slope, which are characteristic of the binding energy of an electron. As the binding energies of inner shell electrons are highly dependent on the atomic number of the element the ionisation edges allow identification of the elements within a sample.

The information in an energy-loss spectrum is complementary to the information acquired in an EDX analysis. Where EELS has an advantage is the characterisation and quantification of light elements. Firstly, after the energy-loss electron has created an electron hole there are a range of ways that the energy can be removed resulting in the aforementioned K-line fluorescence yield, which is low when $Z < 11$. Measurement of the energy-loss electron depends only on the primary interaction event whereas monitoring the characteristic X-ray is not solely dependent on the primary interaction, *i.e.* competing decay processes. Secondly, X-rays are produced isotropically and only a small fraction are collected to make a measurement, typically $\leq$10 %. Energy-loss electrons are created over a much narrower range allowing collection efficiencies of 20 to 50 %. This is because observing the energy-loss electron avoids the range of decay routes for the energy associated with electron rearrangement, see Figure 2.6.

The disadvantages of EELS as opposed to EDX are a very thin sample, 50 to 150 nm, is required to avoid multiple inelastic scattering events, performing a measurement is

much more difficult requiring a skilled TEM operator and a higher background makes interpreting the signal more difficult.

By separating electrons of particular kinetic energies it is possible to produce the equivalent of a band-gap filter in optical spectroscopy. By careful choice of electron energy it is possible to study electrons that have only interacted with a particular element. These electrons can be imaged to produce an elemental map. The technique is known as Energy-filtered Transmission Electron Microscopy (EFTEM).

The instrument used was a Gatan GIF200 Imaging Filter for EELS/EFTEM attached to a Philips CM200 field emission gun TEM. Samples were prepared in accordance with Section 2.3.1.1.

2.3.2 Scattering techniques

The scattering of radiation from matter is another route for characterising a material. Photons, electrons and neutrons can all be scattered but are indicative of different parts of a sample. The two different types of scattering experiments performed in this work are the 'static' scattering of neutrons, Section 2.3.2.1, which yields structural information and the 'dynamic' scattering of light, Section 2.3.2.2, which gives information about the dynamics, such as Brownian motion.[122]

The techniques that involve the scattering of electrons are addressed separately in Section 2.3.1.

2.3.2.1 Small-angle neutron scattering

Neutrons have no charge and possess an electron dipole moment near zero. The interaction with atoms is through nuclear and not electrical forces, unlike X-rays and electrons. These are typically short range interactions over the range of a few fermis (1 fermi = 10^{-15} metre). This means a neutron will perceive a solid as a largely empty space as the gap between atoms is approximately 100,000 times larger than the nucleus it could potentially interact with. As a consequence neutrons have a penetration depth much deeper than X-rays or electrons. The disadvantage is that the amount of scattering is very weak when compared to X-rays. To overcome the intense transmission signal long distances between the sample and detector are needed.

Scattering lengths

The strength of interaction between a scattering nucleus and a neutron is described by its scattering length, b. A positive value of b represents a repulsive interaction. The variation in strength of interaction between neutrons and the nuclei of elements follows what appears to be an erratic pattern and can even vary dramatically between isotopes, Table 2.2. For comparison, the equivalent values for X-rays are also shown in Table 2.2, showing the different opportunities for characterisation between X-rays and neutrons.

Table 2.2: A comparison of neutron scattering lengths and X-ray atomic scattering factors. Adapted from ref. [123].

Atom	Neutron b_{coh} / 10^{-12} cm	X-ray $f_{X\text{-}ray}$ / 10^{-12} cm
D^+	0.67	0.00
H	–0.37	0.28
D	0.67	0.28
C	0.67	1.69
N	0.94	1.97
O	0.58	2.25
S	0.29	4.48

A key parameter when designing Small-Angle Neutron Scattering (SANS) experiments is the contrast of the medium containing the scattering objects. The ability of an atom to scatter has already been described by the scattering length, b. The contrast of a medium is the density of atoms of a particular scattering length in a volume, known as the Scattering Length Density (SLD), is normal expressed in cm^{-2} or $Å^{-2}$. The SLD is described by Equation 2.8, where b_i is the coherent scattering length of nucleus i, x_i, is the number of i nuclei and v_m is the molecular volume.

$$\rho = \frac{\sum_i x_i b_i}{V_m} \tag{2.8}$$

Scattering vector

In SANS only coherent elastic scattering by matter is considered. Consequently the only change is the direction of movement of a neutron and not its energy. This is typically represented by the incident wave vector, $\mathbf{k_i}$ and the scattered wave vector, $\mathbf{k_s}$. The resultant vector, $\mathbf{Q}$, is used to describe the amount of scattering, Equation 2.9, and is depicted as a scattering triangle in Figure 2.7. Use of the magnitude of the wave vectors, $|\mathbf{k}| = 2\pi/\lambda$, and the scattering triangle allows $|\mathbf{Q}|$ to be derived, Equation 2.10. $|\mathbf{Q}|$ shall be represented as Q for the rest of this document.

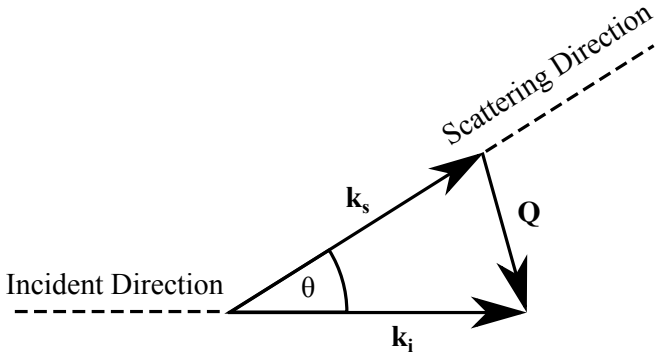

Figure 2.7: An illustration of how $\mathbf{Q}$, the scattering vector, is defined.

$$\mathbf{Q} = \mathbf{k_i} - \mathbf{k_s} \tag{2.9}$$

$$|\mathbf{Q}| = Q = \left(\frac{4\pi}{\lambda}\right) \sin\left(\frac{\theta}{2}\right) \tag{2.10}$$

The intensity function

In a SANS experiment the neutrons are scattered isotropically and are detected by a two dimensional detector. The distance from the centre of the scattering pattern is proportional to Q. The relationship between Q and the scattering pattern is shown in Figure 2.8. The intensity is radially averaged and a plot of $I(Q)$ against Q can be plotted. The resulting curve contains structural information of the sample, the interactions within the sample and information about the volume fraction. This is described in Equation 2.11 where $n_p v_p^2 \Delta\rho^2$ is the scale factor, $P(Q)$ is the form factor, $S(Q)$ is the structure factor and B_{inc} is the incoherent background.

$$\frac{\mathrm{d}\sigma(Q)}{\mathrm{d}\Omega} = I(Q) = n_p v_p^2 \Delta\rho^2 P(Q) S(Q) + B_{inc} \tag{2.11}$$

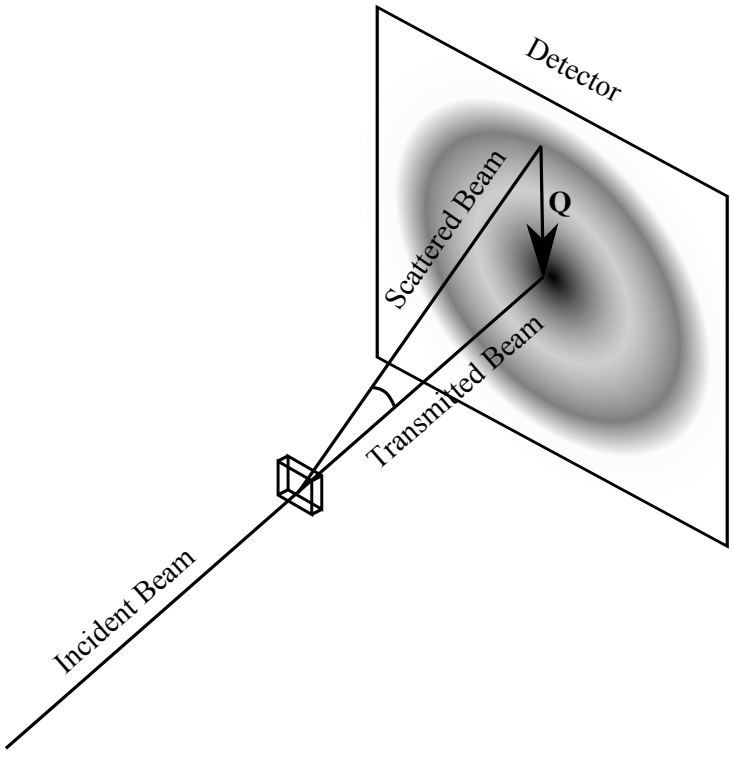

Figure 2.8: An illustration showing how the scattering vector generates a scattering profile.

The observed intensity $I(Q)$ is corrected by subtraction of the solvent background. As the solvent has no structure any scattering is from incoherent scattering and thus removes B_{inc} resulting in Equation 2.12. This contains information about the material dispersed in the solvent and is fitted to extract as much information as possible. Taking in to account a

volume fraction, ϕ_p, is related to the number of particles, n_p, and volume of a particle, v_p, $\phi_p = n_p v_p$ allows this to be simplified to form Equation 2.13.

$$I(Q) = n_p v_p^2 \Delta\rho^2 P(Q) S(Q) \tag{2.12}$$

$$I(Q) = \phi_p v_p \Delta\rho^2 P(Q) S(Q) \tag{2.13}$$

The scale factor

The first three terms of Equation 2.13, $\phi_p v_p \Delta\rho^2$, are directly linked to the magnitude of the scattering profile observed. This is intuitive as the amount of scattering material, given by ϕ_p, the size of the scattering object, which is linked to v_p, and the scattering contrast of the media, $\Delta\rho$, would all be connected to the amount of scattering that a sample would achieve.

Form factors

Information about the structure of a scattering object can be obtained by applying analytical expressions for scattering from objects with geometric shapes, such as spheres, cylinders, ellipsoids, *etc*.[124] Some knowledge of the sample is required so the correct expression can be applied. The functions, which describe the structure of the scattering object, are called form factors, $P(Q)$. The systems studied in this work are spherically symmetrical and the form factors for a sphere and a core-shell structure are given.

The form factor amplitude of a homogeneous sphere was first calculated by Lord Rayleigh in 1910.[125] Equation 2.14 is the expression for perfectly monodisperse spheres where R is the radius of the scattering object.

$$P(Q) = \left[\frac{3[\sin(QR) - QR\cos(QR)]}{(QR)^3}\right]^2 \tag{2.14}$$

Many colloids have uniform shells upon a core. The simplest of these is a sphere with a single shell. The form factor for a spherical particle consisting of a spherical core and a concentric shell is given in Equation 2.15 and the parameters are defined in Figure 2.9.

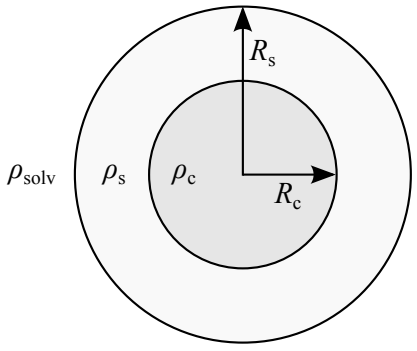

Figure 2.9: The parameters in the core-shell form factor

$$P(Q) = \Bigg[3V_c(\rho_c - \rho_s)\frac{3[\sin(QR_c) - QR_c\cos(QR_c)]}{(QR_c)^3} + 3V_s(\rho_s - \rho_{solv})\frac{3[\sin(QR_s) - QR_s\cos(QR_s)]}{(QR_s)^3} \Bigg]^2 \quad (2.15)$$

Structure factors

The structure factor, $S(Q)$, contains information about the interactions of particles and arises from the interference of scattering from different particles, *i.e*. interparticle scattering. Whereas, the form factor $P(Q)$ is an intraparticle scattering. For very dilute solutions, $S(Q) = 1$, particle interactions no longer occur and the structure factor can be neglected. As the concentration increases $S(Q)$ begins to contribute to the profile and functions for interactions and the form factor $P(Q)$ combined make the overall scattering profile.

Instrument details

The instruments used in this study are LOQ based at ISIS, Ruthorford Appleton Laboratory, Oxfordshire UK and D11 based at the Institut Laue-Langevin, Grenoble, France.

LOQ is a time-of-flight based SANS instrument. This allows for measurement of the entire Q range in a single measurement without needing to move the detector. The pulsed beam of neutrons is created by a spallation source based in Target Station 1, which operates at 50 Hz.

The D11 detector is based on a moveable trolley within an evacuated 40 m tube. The detector can be placed at any distance between 1.2 m and 39 m to access different parts of the Q range. The distances used in this study were 1.5, 8 and 39 m. D11 is supplied with neutrons from a nuclear reactor, which results in a continuous supply of neutrons.

At both instruments the samples were held in cylindrical "banjo" quartz cells. The path length of cell used was dependent on the hydrogen and deuterium content of the solvent. Samples that used hydrogen rich solvents were placed in a 1 mm path length cell and samples containing deuterium rich solvents were placed in a 2 mm path length cell. The samples were thermostated at 25 °C. Scattering profiles were corrected for pathlength, transmission and incoherent scattering using standard ISIS and ILL software respectively.

Analysis software

Modelling of the SANS data was performed using SasView.[126] The software is open source and developed by the major small angle scattering facilities, NIST, ILL, ISIS and others. This allows fitting with a range of form factors, $P(Q)$ and the introduction of structure factors, $S(Q)$. Parameters such as the volume fraction, SLDs and size can be fitted or floated. Polydispersity can also be introduced to allow for size distributions.

2.3.2.2 Dynamic light scattering

DLS is a technique that allows the determination of hydrodynamic size distributions of colloidal particles *in situ*.[127] A virtue of DLS is that the sample can be measured without any preparation, other than being within an appropriate concentration range, whereas other methods, such as TEM, require the sample to be dried before a measurement can be obtained. Thus, any potential corruptions to structure of the observed colloid are avoided when using DLS. In this respect DLS is similar to small angle X-ray scattering and small angle neutron scattering.

As mentioned, DLS techniques measure hydrodynamic quantities, usually diffusion coefficients, which can be used to extract size information by use of geometrical information of the predicted shape. DLS is built upon variations in the intensity of light scattered by particles undergoing Brownian motion. The intensity is dependent on the positions of the particles relative to one another, the incoming beam and the angle of observation. The result of this is that constructive and destructive interference can occur with light scattered off nearby particles. As the particles undergo Brownian motion their positions relative to one another change and consequently the intensity also changes. The scattered light intensity variations occur over a period of time that it takes for the particle to move over a significant fraction of the wavelength of the scattered light.

Scattered light intensity against time results in a stochastic signal related to the Brownian motion of the particles. To extract information from the signal a correlation function, $g^{(1)}(t)$, is created by comparing the signal to itself over time. This results in a function that decays with time as the signal becomes increasingly unlike the original intensity. For a dilute solution of monodisperse particles $g^{(1)}(t)$ has the form of a single exponential, Equation 2.16.

$$g^{(1)}(t) = \exp(-q^2 Dt) \tag{2.16}$$

The scattering vector, q, depends on the scattering angle, θ, and the wavelength of the light, λ, Equation 2.17.

$$q = \left(\frac{4\pi}{\lambda}\right) \sin\left(\frac{\theta}{2}\right) \tag{2.17}$$

Equations 2.16 and 2.17 show that using a measurement at a single angle the translational self diffusional coefficient, D, can be determined. Use of the Stokes-Einstein relationship, Equation 2.18, and assumption of a spherical shape allows the determination of the radius of the particles undergoing Brownian motion.

$$D = \frac{k_b T}{6\pi\eta R} \tag{2.18}$$

where D is the diffusion coefficient, k_b is the Boltzmann constant, T is the temperature, η is the viscosity of the medium and R is the radius of the particle. The radius from

Equation 2.18 is that of the entire moving object. Stabilised colloids have a shell of solvent molecules, which cause the observed radius, the 'hydrodynamic radius', to be different from that of the geometrical particle radius. In this sense DLS typically results in an over estimate of the particle size.

Polydisperse samples are much more common in practice and the resulting correlation function is more complex than a single exponential due to each size having a different translational diffusional coefficient. Fitting a single exponential, as in Equation 2.16, results in the mean diameter of the sample, Z_{ave}. The degree of polydispersity can be estimated by use of a cumulants analysis. This is where the correlation function is made of a number of different exponentials that are weighted according to their contribution, Equation 2.19. The reciprocal relaxation time is denoted as Γ, where $\Gamma_i = q^2 D_i$.

$$g^{(1)}(t) = \sum_i A_i \exp(-\Gamma_i t) \tag{2.19}$$

Expansion of $\ln(g^{(1)}(t))$, by use of a power series, results in,Equation 2.20. The cumulants are the coefficients of the expansion, K_n, where K_1 is the average reciprocal relaxation time, $\langle(\Gamma)\rangle$ and K_2 is a measure of the distribution of Γ around $\langle(\Gamma)\rangle$. K_2 is therefore a measure of the polydispersity of the system being observed. If $K_2 = 0$ the system is monodisperse and can be modelled with a single exponential.

$$\ln(g^{(1)}(t)) = -K_1 t + \frac{1}{2} K_2 t^2 + \ldots \tag{2.20}$$

The instruments used at the Univeristy of East Anglia was a Malvern Zetasizer ZS Nano with a HeNe 5 mW laser at 633 nm. The collection angle is fixed at 173°. At the Institut Laue-Langevin, Grenoble, France an ALV CGS-3 DLS with a HeNe 23 mW laser at 633 nm and an angular range between 25 and 155° was used.

2.3.3 Spectroscopy

Spectroscopic techniques can shed light on a wealth of information about nanocrystals. This can range from characterisation of surfaces to electronic structure and particle concentrations.

2.3.3.1 UV-vis spectroscopy

The absorption of light from the very near infrared or near ultraviolet regions of the electromagnetic spectrum, 1100 to 180 nm, deals with electronic transitions within a compound. This region is known as the 'UV-visible' range. Absorption of light in the UV-visible region causes electronic transitions to occur within an atom or compound. These transitions are excitations of electrons from a higher energy outer shell being excited to a energetically close unoccupied orbital.[128]

UV-visible spectra typically provide little structural information compared to other

types of spectroscopy but can be used to determine concentrations through use of the Beer-Lambert law and monitor changes in electronic transitions.

In this work UV-visible spectroscopy has been used for two purposes: determination of electronic information, *i.e*. location of the band edge for quantum dots or SPR location for AuNP, and relative concentration determination. The instrument used was a Hitachi U-3010 UV-vis spectrophotometer.

2.3.3.2 Fluorometry

Whilst UV-visible absorption techniques exploit the excitation of electrons by light, fluorometric techniques exploit the light emitted as the excited electron returns to the ground state. These techniques fall in two categories: steady-state and time resolved.[129]

In this work steady-state measurements of the luminescence of QDs were made to observe their quality, polydispersity and purity, and also for QY determination. Time-resolved measurements were used to determine the QD fluorescence lifetime, τ.

The instrument used was a Horiba Yobin FluoroLog-3 modular spectrophotometer for steady state and time correlated single photon counting measurements. The light source for time correlated measurements was a Horiba Yobin NanoLED laser with a wavelength of 369 nm.

2.3.3.3 Infra-red spectroscopy

Infra-red radiation, in the range of 4000 to 625 cm^{-1}, is absorbed by molecules and parts of molecules at specific frequencies, which allow structural elucidation. The absorption bands require that the functional group or bond undergoes a change in dipole moment. Fortunately, a large number of interesting functional groups and bonds meet these criteria allowing characterisation of a compound or material to occur. Reference tables of the typical absorption wavenumber and shape of common functional groups are used to characterise the peaks.[130]

In the case of nanocrystals, this can allow chemical changes of the organic material providing stabilisation on the surface to be confirmed. For instance, changing the functionalisation from one group to another could be confirmed by the appearance of the new group and the disappearance of the reacted group. As nanocrystals are typically suspended in a medium, and in this situation the signal is weak, it is best to remove the medium and perform the measurement as a powder using an Attenuated Total Reflection (ATR) Fourier Transform-Infra-Red (FT-IR) spectroscopy.

The instrument used was a Perkin Elmer Spectrum 65 FT-IR with an SensIR single pass diamond ATR attachment. Nanocrystal samples were prepared by drying particle suspensions using a Schlenk line. The powdered samples were placed directly on the ATR crystal.

2.3.3.4 Atomic Emission Spectroscopy

Atomic emission spectroscopy makes use of the characteristic radiation emitted from atoms when appropriately excited.[128] The result is a spectrum containing spectral lines for all the elements in the sample analysed. The peaks allow identification of the atoms present in a sample and also quantification of the elements. The measured spectrum contains no information about the relative configuration of the elements in the sample they originated from. Atomic emission spectroscopy is not an absolute technique and relies on the use of standards to determine the quantities of the atoms measured.

In this work Inductively-Coupled Plasma Atomic Emission Spectroscopy (ICP-AES) was used to determine the amount of metal in the core of the nanocrystals studied.[131] An ICP-AES instrument contains a plasma torch that can reach temperatures of 8000 K. The plasma is a gaseous cloud of Ar atoms, ions and their electrons formed by a Tesla discharge. The Ar plasma excites the nebulized sample causing the emission of photons and ionisation. The emitted light is passed through an optical grating to generate a spectrum.

The instrument used was a Varian Vista-PRO CCD Simultaneous ICP-AES Axial spectrometer with an SPS5 Sample Preparation System. The nanocrystal suspensions in toluene were digested in *aqua regia* using a microwave reaction vessel for 1 h.

2.3.3.5 X-ray photoelectron spectroscopy

In X-Ray Photoelectron Spectroscopy (XPS), electrons ejected from inner electron shells following excitation by X-rays are studied, allowing characterisation of a surface of a material.[132] The 'photoelectrons' are analysed by an electron spectrometer resulting in the production of a plot of intensity, in counts or counts per second, against electron energy. The process of photoemission in XPS is similar to the process in EELS and EDX, Figure 2.6, except that the excitation source is an X-ray and not an electron.

The kinetic energy, E_k, of the electron measured is not intrinsic to the material as it is dependent on the energy of the X-ray source used for excitation. The binding energy, E_b, of the electron is the property that is used for identification of elements within a material and is linked to E_k by taking into account the energy of the X-ray, $h\nu$, and the work function of the instrument. The depth of measurement is linked to the wavelength of the X-rays used but typically 95 % of the signal comes from a depth of less than 3λ.

The instrument used was a VG Escalab 250. It was equipped with an Al K_α source with a spot size of 120 to 600 µm in diameter. The spectra were processed using CasaXPS. The instrument was located at the Leeds EPSRC Nanoscience and Nantechnology Characterisation Facility at the University of Leeds.

CHAPTER 3

A thin silica-over-polymer shell for colloidal inorganic nanoparticles

---

3.1 Silica layers upon nanocrystals

3.1.1 Synthesis of silica colloids

SiO_2 NPs have huge potential in bioanalysis due to a wealth of bioconjugation methods and low toxicity. The ability to dope SiO_2 NP with dyes combined with bioconjugation methods allows optical analysis within biological systems to be performed. Fluorescent SiO_2 NP offer a higher optical intensity and optical photostability than their free molecular counterparts. This is is normally achieved using organic and inorganic dyes but with the emergence of QDs and upconverting nanocrystals the challenge of incorporating nanocrystals in silica particles has appeared. Fluorescent SiO_2 NP and core-shell nanocrystal/silica materials have potential applications in immunoassays, cellular imaging and multiplexed bioanalysis.[133] Nanocrystals have a range of properties depending on their material and other applications such as hyperthermia with magnetic nanocrystals can be envisaged.

The cytotoxicty of particles such as CdSe and CdSe@ZnS is already well known.[134] The high surface area of the small particles facilitates the leaching of Cd^{2+}. Cytotoxicity testing with different surface passivation techniques showed silica coating to be one of the most effective coatings to hinder Cd^{2+} leaching.[79]

Existing methodologies for silica coating nanocrystals are largely adapted from methods for the generation of SiO_2 NP. The most established methods for SiO_2 synthesis are known as the "Stöber" and "reverse microemulsion" methods. In all cases the same key steps are involved in the polymerisation of the alkoxysilanes, Figure 3.1. The first step is a hydrolysis of the Si−O bond of the silane to form Si−OH. This is followed by a condensation reaction of the silanol groups resulting in the formation of silica, Si−O−Si.

Silica provides a versatile surface which can be modified by taking advantage of the

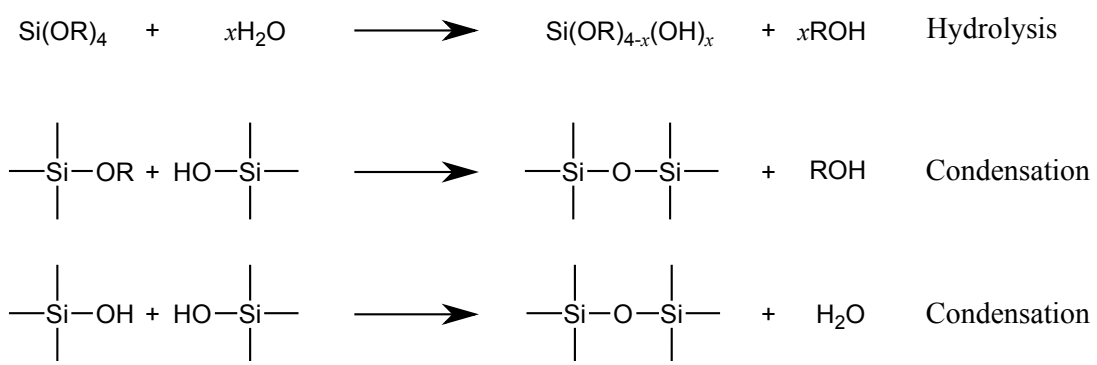

Figure 3.1: The base catalysed polymerisation of silanes to form silica.

pendant silanol groups.[135,136] Well established methods involve the reaction of the silanol groups with either alkoxy or monochlorinated silanes, Figure 3.2.[135] A range of new techniques for grafting on to silica surfaces have been developed and have been recently reviewed by Park *et al.*[136]

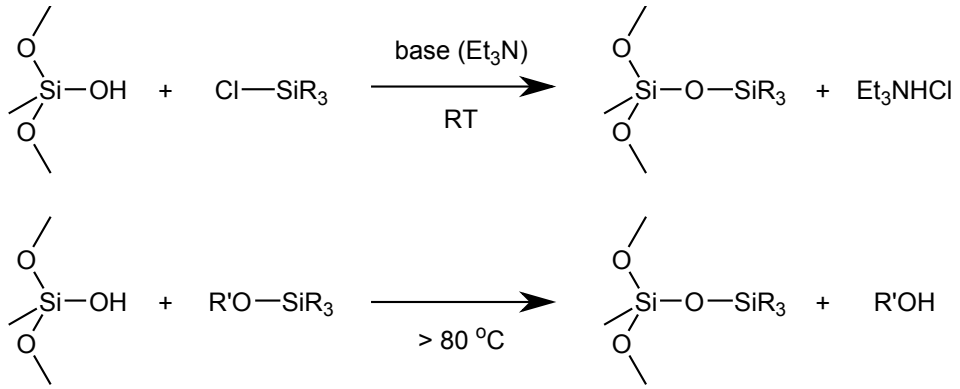

Figure 3.2: The two main reactions by which the silanol groups on the surface of silica are conventionally modified.

In the Stöber method tetraalkoxysilicates are polymerised in an alcohol, typically ethanol.[75] The reaction is catalysed by a base which, in the work of Stöber, is concentrated ammonia, NH_4OH. The resulting particles can be of a controlled diameter in the range of 20 to 1000 nm. The kinetics of nucleation and growth are thought to control the formation of particles instead of a silica gel.

The microemulsion method was developed by Osseo-Asare and Arriagada.[76,137] This method involves the use of water-in-oil microemulsions to encourage the separation of nucleation events using the oil phase as a barrier. The surfactant used was a non-ionic polyoxyethelene nonylphenyl ether with an average of five oxyethylene per molecule (NP-5, also known as Igepal CO-520). A microemulsion was formed using NP-5, cyclohexane and aqueous ammonium hydroxide. Tetraethyl orthosilicate (TEOS) is added and is hydrolysed to form $Si(OH)_4$ which is soluble in the aqueous domains. This nucleates to begin the process of nucleation and growth. It has been observed that at low R, where $R = [H_2O]/[\text{surfactant}]$), larger particles are formed and at high R smaller particles are formed.[137] NP-5 based microemulsions have been used to synthesise silica particles between 30 and 70 nm in diameter.

3.1.2 Routes to coating nanocrystals with silica

The formation of a layer of silica upon a nanocrystal or the incorporation of multiple nanocrystals within a silica particle allows a range of potential materials to be developed. This field has been reviewed at differing stages of development.[138–140]

3.1.2.1 Silica coating by adapted Stöber methods

High monodispersity colloidal nanocrystals are typically produced in organic solvents and the ligands used to control the formation of the nanocrystals result in particles which are dispersible in organic media due to their surface ligands, typically alkylamine, alkylthiols and alkylphoshines. As a consequence, the coating of metal nanocrystals with silica using the Stöber method is hindered by the lack of OH groups on the surface of most nanocrystals after synthesis. If the nanocrystal could be made compatible with Stöber reaction conditions it could act as a nucleus for silica growth. Early attempts to use the Stöber process were hindered by the poor dispersability of nanocrystals in basic alcohols and the lack of points of attachment, *i.e*. OH groups, for growing silica.[141]

Priming by ligand exchange

The problem of "vitreophilicity", *i.e*. how much a surface favours glass or silica, was addressed by Liz-Marzán *et al.* by performing a ligand exchange locating (3-aminopropyl)-trimethoxysilane on the surface of Au nanocrystals with the alkoxysilane pointing away from the particle, the first example of surface priming. The alkoxysilane is hydrolysed to form $Si(OH)_3$ on the surface ready for incorporation into a silica structure using the Stöber growth process in basic alcohol with TEOS.[142] Synthesising particles which are vitreophilic by virtue of the ligands used in synthesis has also been achieved for Ag nanocrystals[143] and Au nanocrystals.[144]

Priming using sodium silicate

An alternative to ligand exchange to allow a nanocrystal to partake in Stöber growth is to use sodium silicate to grow a thin layer of silica. Unlike the ligand exchange surface priming this method works best on nanocrystals which are already stable in aqueous or polar media. Surface priming with sodium silicate was first performed by Philipse *et al.* on ligand free Fe_3O_4.[145] The deprotonated nanocrystal surface OH groups allowed for direct reaction with the silicate. The resulting particles act as a nucleus to allow silica to grow from the surface using Stöber conditions.

The use of sodium silicate was combined with ligand exchange by Liz-Marzán *et al.* to allow citrate stabilised AuNPs to be used in the Stöber process.[146] The particles first underwent a ligand exchange with (3-aminopropyl)trimethoxysilane and then a thin layer was grown using sodium silicate. The sodium silicate solution (SiO_3^{2-}(aq)) was used at a pH low enough to allow polymerisation to occur slowly. Once the initial layer was

grown the shell was completed using Stöber conditions. This combined approach was later extended to CdS QDs[147] and Ag.[148]

3.1.2.2 Silica coating by use of microemulsions

Microemulsion based silica coating techniques are all founded on the methods of Osseo-Asare and Arriagada for the preparation of silica colloids.[76,137] Coating was first performed on CdS synthesised *in situ* in the same microemulsion that silica synthesis was subsequently performed in by Chang *et al.*[149] The electrostatically-stabilised CdS required no surface priming to allow the nanocrystals to exist in the water-in-oil microemulsion droplets. This approach has been extended to CdS@ZnS,[150] Au,[151] Ag,[152] Pd,[153,154] CdTe,[155] iron oxides[156,157] and FePt[158] nanocrystals synthesised and silica coated in microemulsions. The coating of pre-synthesised aqueous dispersed nanocrystals is reported far less.[159] This method relies on water-in-oil microemulsion based methods for synthesising nanocrystals.

As discussed in Chapter 2, many of the methods that produce the most monodisperse nanocrystals result in nanocrystals stabilised with hydrophobic ligands. Coating of nanocrystals synthesised with hydrophobic ligands falls into two categories: with and without surface priming. The incorporation of nanocrystals stabilised by hydrophobic ligands into silica shells based on a microemulsion method provides a clear challenge as the polymerisation of the silica occurs within the aqueous droplets. Both of the main methods to do this involve the modification of the surface to make the surface ligands hydrophilic.

The research group of Ying primed the surface of hydrophobic nanocrystals using aminopropyl trimethoxysilane.[160–162] The aminopropyl trimethoxysilane is thought to undergo a ligand exchange with the hydrophobic ligands belonging to the nanocrystal. The mechanism is likely to involve ligand exchange with the silane before hydrolysis and subsequent transfer to the aqueous domain after hydrolysis of the alkoxysilane. Afterwards a microemulsion is formed by addition of aqueous ammonia and polyoxyethyene nonylphenyl ether (Igepal CO-520). TEOS is added to form the silica shell. This was performed on CdSe QDs with trioctylphosphine oxide or with other weak ligands and PbSe QDs with oleic acid.[160,161] This method was adapted to coat heterodimers of CdSe and γ-Fe_2O_3 with a thin shell of silica by removal of the TEOS.[162] The resulting silica shell being made only from aminopropyl trimethoxysilane.

In 2005 Darbandi *et al.* developed a microemulsion based silica coating technique that lacked a priming step on CdSe@ZnS QDs.[163,164] In this work a microemulsion was formed using poly(ethylene glycol) nonylphenyl ether (NP-5), cyclohexane and aqueous ammonia. The CdSe@ZnS are introduced in chloroform and TEOS is the source of silicon and oxygen. Over the course of 24 h the particles had been taken up in to the microemulsion and a polymer shell formed around individual particles. The Nann group extended this methodology to PbSe,[165] InP@ZnS,[166] YF_3,[167] and doped $NaYF_4$ upconverting nanocrystals.[168] This method has no obvious surface priming step and the mechanism for the incorporation was later elucidated by Koole *et al.* to be dependent on

the ligand exchange of hydrolysed TEOS and surfactant with the hydrophobic surface ligands.[169] It was also found that QDs with thiol ligands bound were not incorporated into the silica spheres so this method is sensitive to the ligand binding strength. A very similar method was used earlier in 2005 to encapsulate both QDs and γ-Fe_2O_3 within a single sphere by the research group of Ying but is likely to follow the same mechanism.[170,171] The Ying group also encapsulated oleylamine functionalised Au and Ag nanocrystals in individual spheres by this method.[172] This method has been further refined with the relationship between size of the particle and conditions for various shell thicknesses on Fe_3O_4 particles being studied as well as improvements with respect to silica shell thickness control upon CdSe@ZnS.[173,174]

3.1.2.3 Reactions of trialkoxysilanes on nanocrystal surfaces

Reducing the thickness of silica shells is advantageous from the point of view of biological applications. Although some of the previously mentioned methods have controlled the thickness the total size can still be further reduced. Also the aforementioned methods produce plain silica surfaces, *i.e*. terminated with silanol groups. A thin shell that is functionalised with suitable reactive groups present would allow future attachment to the surface.

The following methods do not use a microemulsion or sodium silicate priming. They have been separated from Stöber-based methods because they are typically not performed in alcohols and do not depend on the nucleation and growth kinetics that are crucial to the Stöber process. These methods share the feature that the shells are thin and are made from trialkoxysilanes. One functional trialkoxysilane, 3-aminopropyltriethoxysilane or mercaptopropyltrimethoxysilane is exchanged with the typically hydrophobic surface ligands of the nanocrystal and a second is used to complete the shell whilst providing a functional group for further attachment.

This was first achieved for AuNP using, 3-mercaptopropyltrimethoxysilane as the surface ligand during the nanocrystal synthesis. Once the particles were synthesised 3-aminopropyltrimethoxysilane was added and the silanes polymerised to form the thin silica shell.[144] A similar approach was used later by Pastoriza-Santos and Liz-Marzán to make a thin shell upon Ag nanocrystals with 3-aminopropyltrimethoxysilane.[143]

The research group of A. Paul Alivisatos developed a similar method for CdSe@ZnS and CdSe@CdS. The nanocrystals were ligand exchanged with 3-mercaptopropyltrimethoxysilane after synthesis and were reacted with trialkoxysilanes possessing primary amide,[175] amine,[175,176] thiol[176] and phosphonate.[177] In the later publications the silanol surface was reacted with chlorotrimethylsilane to prevent reaction between silica shells.[176,177]

H. Weller and co-workers were developing similar shells using monomethoxysilanes, such as 3-aminopropyldimethoxysilane, to hinder silica cross-linking between nanocrystals and also provide outward pointing functionality.[178,179] This was achieved using AuNPs synthesised with 3-mercaptopropyltrimethoxysilane *in situ*[178] and with CdTe QDs.[179]

Chlorotrimethylsilane and TEOS were used to terminate the surface and further cross-link the shell respectively.

The use of trialkoxysilanes for the synthesis of thin shells was expanded by J. Y. Ying and coworkers. A bound trialkoxysilane and further polymerisation of a second outward pointing silane was used once more. The method was extended to also work for Fe_3O_4, ZnO and Ag nanocrystals and a wider range of silanes were explored to provide the outward pointing functionality.[180–182] In these works no silane was used to terminate the surface to prevent further polymerisation.

The use of trialkoxysilanes to form a thin layer using microemulsions to inhibit particle cross-linking has also been reported.[162]

3.1.2.4 Silica coating by use of surfactants and polymers as primers

Silica coating methods that do not involve ligand exchange include the use of amphiphiles or polyelectrolytes to allow the incorporation of nanocrystals. Amphiphiles have been used to form a bi-layer upon the surface of the nanocrystal and then TEOS polymerisation has been used to grow a shell. This has been achieved using cetyltrimethylammonium bromide stabilised Fe_3O_4,[183] AuNP,[59,61,184] AuNR[185] and CdSe@ZnS.[185] A more exotic surfactant containing a silane head group, octadecyldimethyl(3-trimethoxysilylpropyl)-ammonium chloride, has been used in a style similar to silane containing ligands, resulting in a vitrophilic surface. This has been used to synthesise a thin shell upon AuNPs[68] and thick shells around QDs.[186]

Poly(vinylpyrrolidone) wrapped around the surface of citrate stabilised Au and Ag nanocrystals has been used as a foundation for the growth of a silica shell.[187] The nanocrystals could then partake in Stöber silica growth once transferred to an alcohol. Wrapping of poly(vinylpyrrolidone) can be improved by using layers of polyelectrolytes in a layer by layer approach. This has been successfully used in the Liz-Marzán group to grow well controlled silica shells around cetyltrimethylammonium bromide stabilised AuNRs.[188]

3.1.3 Problems with existing methods for silica coating

The majority of methods described are based on methods that make relatively large silica colloids, *i.e.* Stöber and microemulsion methods, Sections 3.1.2.1 and 3.1.2.2. As a consequence the nanocrystal/SiO_2 core-shell particles made have shells greater than 10 nm. The techniques that make thin shells are largely based upon the reactions of ligand exchanged functional trialkoxysilanes on the nanocrystal surface or the use of silane containing amphiphiles, Sections 3.1.2.3 and 3.1.2.4. Alternatively, deposition of silicate on nanocrystal surfaces has been used to make thin shells of silica although these have been used immediately to grow a thicker shells using other methods, Section 3.1.2.1. The body of literature for thin silica shell techniques is relatively small in comparison to other techniques and has not been widely adopted.

The thin shell methods based on using functionalised trialkoxysilanes in organic solvents depend strongly on the amount of water present as it is required for the polymerisation of silanes. The organic solvents used in previous reports do not state whether or not solvents are dried and if air sensitive techniques have been used. The rate of reaction will be different depending on local temperature and humidity.

Secondly, the methods depend on ligand exchange procedures, which are strongly dependent on the surface in question. The thin shell techniques largely use thiol or amine based trialkoxysilanes, which work well for QDs and Au but will not be as effective on Fe_3O_4. A technique that is not dependent on the surface of the particles but instead takes advantage of the common feature of hydrophobic ligands would avoid the variable surface chemistry.

3.2 Proposed method for silica-over-polymer thin layer

In this work a new method for the creation of a thin layer of functionalised silica encasing individual nanocrystals is proposed. This method manages the aforementioned variable surface chemistry of the controlled formation of silica at the surface of nanocrystals, see Section 3.1.3. The proposed methodology separates the attachment of the silane to the surface from the polymerisation of silanes to form the thin shell, thus avoiding large silica structures containing many nanocrystals.

The nanocrystal surface is coated by a pro-amphiphilic polymer which provides activated esters in the form of acid anhydrides on the surface of the nanocrystal, Figure 3.3 reaction 1. The attraction of a pro-amphiphilic polymer to the ligands of a nanocrystal has been documented in the literature and has been used to stabilise particles in aqueous media, see Section 4.1. Once the polymer is bound, a nucleophilic silane is chosen to react with the acid anhydride causing the attachment of the silane to the surface, Figure 3.3 reaction 2. This reaction is thought to be fast in comparison to most ligand exchange reactions allowing the rapid attachment of the silane.

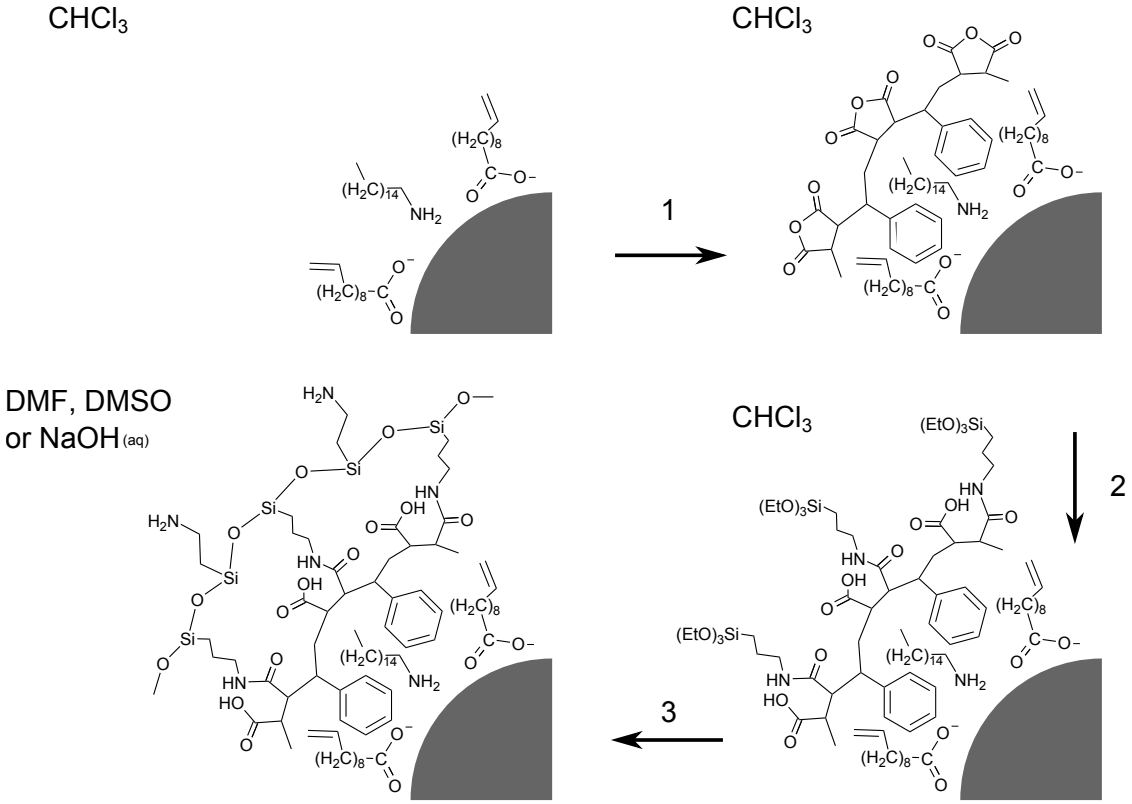

Figure 3.3: The proposed method for coating colloidal nanocrystals in a thin silica shell with a polymer foundation. The steps indicated are: 1) the wrapping of the pro-amphiphilic polymer around the nanocrystal, 2) the reaction of a nucleophilic ethoxysilane with the acid anhydride and 3) the continued polymerisation of bound and unbound silanes to form the silica shell.

In previous silica coating procedures where the silane is tethered to a surface the methoxysilane version of the molecule is normally used, Section 3.1.2. To increase the

discrepancy between the rate of hydrolysis and condensation reactions, as compared to the rate of surface attachment, ethoxysilanes were used, Figure 3.3 reaction 3. This causes the condensation reaction to slow and as a consequence the polymerisation of the surface tethered silanes and free silanes in solution.

The resulting structure has a polymer foundation and a thin shell of silica built upon it. The advantages of this structure over the amphiphilic polymer technique is that the silica layer is cross-linked resulting in the contained particle being trapped by a cage of silica. Any potential dynamic behaviour of the amphiphilic polymer is removed as the silica shell locks it in place. As compared to thicker silica shells this method offers a lower total size which is a benefit from a biocompatibility and application perspective.

3.3 Typical procedure for preparing a thin silica-polymer shell

3.3.1 Determination of quantity of polymer required

The concentration and size of nanocrystals varies between batches and as such the amount of poly(styrene-*co*-maleic anhydride) required also changes. To accommodate for this a water transfer protocol, as described by Lees *et al.*,[189] was used to determine the amount required. The minimum amount of polymer for a total transfer of particles from chloroform to water was then used as the amount required for the batch.

A series of water transfer experiments were undertaken where the amount of polymer and ethanolamine was varied. Typically, InP@ZnS (100 µl) is precipitated from the stock dispersion in toluene using ethanol (10 ml, Sigma-Aldrich, ≥99.8 %). The precipitated nanocrystals were redispersed in a solution of poly(styrene-*co*-maleic anhydride) in chloroform (0.9 mg ml^{-1}, 1 ml, Fisher Scientific, >99 %). An aqueous solution of ethanolamine (0.5 ml, 0.12 mol dm^{-3}), Sigma-Aldrich, ≤99.9 %) was added to the chloroform nanocrystal dispersion. This creates a two phase system with the water above the chloroform. Stirring overnight causes the nanocrystals to transfer from the chloroform to the aqueous phase.

3.3.2 Coating of InP@ZnS nanocrystals

InP@ZnS nanocrystals were precipitated from the stock dispersion in toluene (400 µl) with ethanol (≈10 ml, Sigma-Aldrich, ≥99.8 %). The precipitated nanocrystals were redispersed in $CHCl_3$ (2 ml, Fisher Scientific, >99 %). A solution of poly(styrene-*co*-maleic anhydride) in $CHCl_3$ (1.8 mg ml^{-1}) was added. The solution was stirred over night. 3-Aminopropyltriethoxysilane (56 µl, Sigma-Aldrich, 99 %) was added. The solution was stirred for 24 h at 18 °C. The nanocrystals were precipitated with toluene and redispersed in dimethylsulphoxide (DMSO) (4 ml, Sigma-Aldrich, ≤99.9 %), tetrahydrofuran (THF)

(4 ml, Sigma-Aldrich, $\leq$99.9 %) or NaOH (aq) (0.05 mol dm^{-3}, Fisher Scientific, $\geq$98 %).

3.3.3 Coating of Fe_3O_4 nanocrystals

Fe_3O_4 nanocrystals were precipitated from the stock dispersion in toluene (2.5 ml) with ethanol ($\approx$10 ml, Sigma-Aldrich, $\geq$99.8 %). The precipitated nanocrystals were redispersed in $CHCl_3$ (2 ml, Fisher Scientific, >99 %). A solution of poly(styrene-*co*-maleic anhydride) in $CHCl_3$ (1.8 mg ml^{-1}) was added. The solution was stirred over night. 3-Aminopropyltriethoxysilane (56 µl, Sigma-Aldrich, 99 %) was added. The solution was stirred for 24 h at 18 °C. The nanocrystals were precipitated with toluene and redispersed in DMSO (4 ml, Sigma-Aldrich, $\leq$99.9 %), THF (4 ml, Sigma-Aldrich, $\leq$99.9 %) or NaOH (aq) (0.05 mol dm^{-3}, Fisher Scientific, $\geq$98 %).

3.4 Characterisation of the silica-over-polymer thin layer

3.4.1 HRTEM images

The nanocrystals were characterised using a TEM, Figures 3.4 and 3.5. High Resolution Transmission Electron Microscope (HRTEM) images were collected at three stages: before coating, after being stirred with polymer and after growth of the silica layer.

In the case of InP@ZnS, Figure 3.4, the lower magnification images, (b), (d) and (f) indicate that the particles appear well dispersed at all stages of layer formation. At higher magnifications InP@ZnS are more difficult to observe as their low contrast combined with their small size results in faint images. Figure 3.4 (a), (c) and (e) show higher magnification images achieving lattice resolution. As the layer is formed no new features appear in the images. In Figure 3.4 (e) and (f) there is no distinctive shell around the particles from silica growth.

Figure 3.5 shows HRTEM images of the formation of the silica-over-polymer layer upon Fe_3O_4 nanocrystals. Figure 3.5 (b), (d) and (f) show that at all stages of coating the nanocrystals are well dispersed and there are no silica structures interconnecting the nanocrystals. Figure 3.5 (a), (c) and (e) allow for a more confident analysis of the surface of the nanocrystals due to the nanocrystals being more visible. As with the InP@ZnS, Figure 3.5 (e) shows no indication of a silica layer upon the Fe_3O_4 nanocrystal shown.

After coating with the thin silica over polymer layer the transmission electron micrographs showed no indication of a layer. At first this appeared a disappointing result as previous silica coating methodologies within the Nann group showed clearly visible silica shells.[163] Silica is an non-ideal material for characterisation by TEM due to weak scattering of electrons by silicon and oxygen as they both contain relatively few electrons. Secondly, silica is known to melt under observation within the TEM due to sample heating effects, Section 2.3.1.1.

From observations of changes in the solvent that the nanocrystals could be dispersed in it is clear that a change on the surface has occurred although HRTEM characterisation did not indicate the presence of a layer around the nanocrystals. If the material is as designed the layer would be thin and with a structure containing an organic polymer as well as the inorganic silica layer, *i.e.* a small amount of a weakly scattering material. The combination of these potential structural features makes characterisation by conventional electron microscopy non-trivial or not possible due to very weak scattering from the layer.

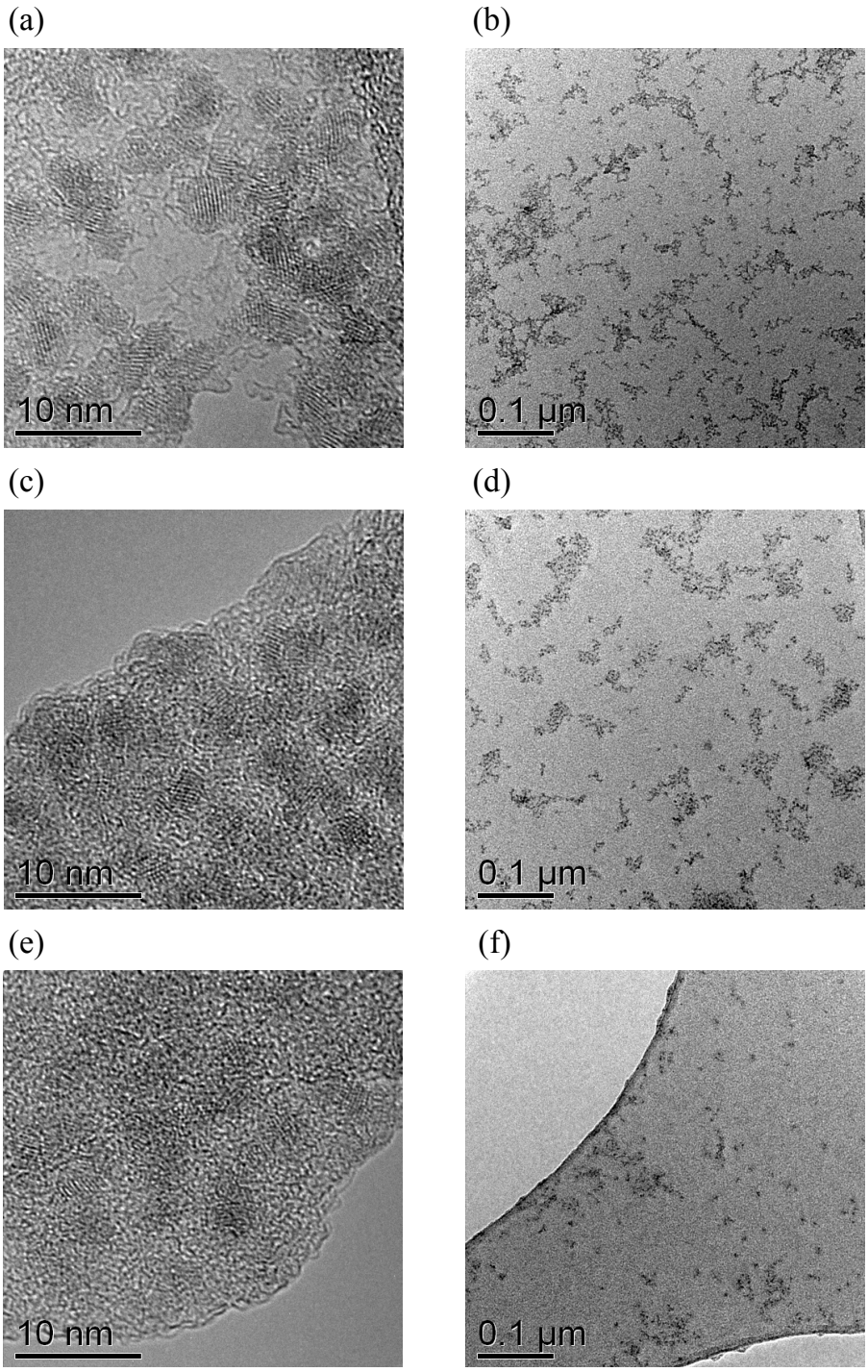

Figure 3.4: HRTEM images showing InP@ZnS particles at three stages of coating: uncoated particles (a & b), polymer coated InP@ZnS (c & d) and silica-over-polymer coated InP@ZnS (e & f)

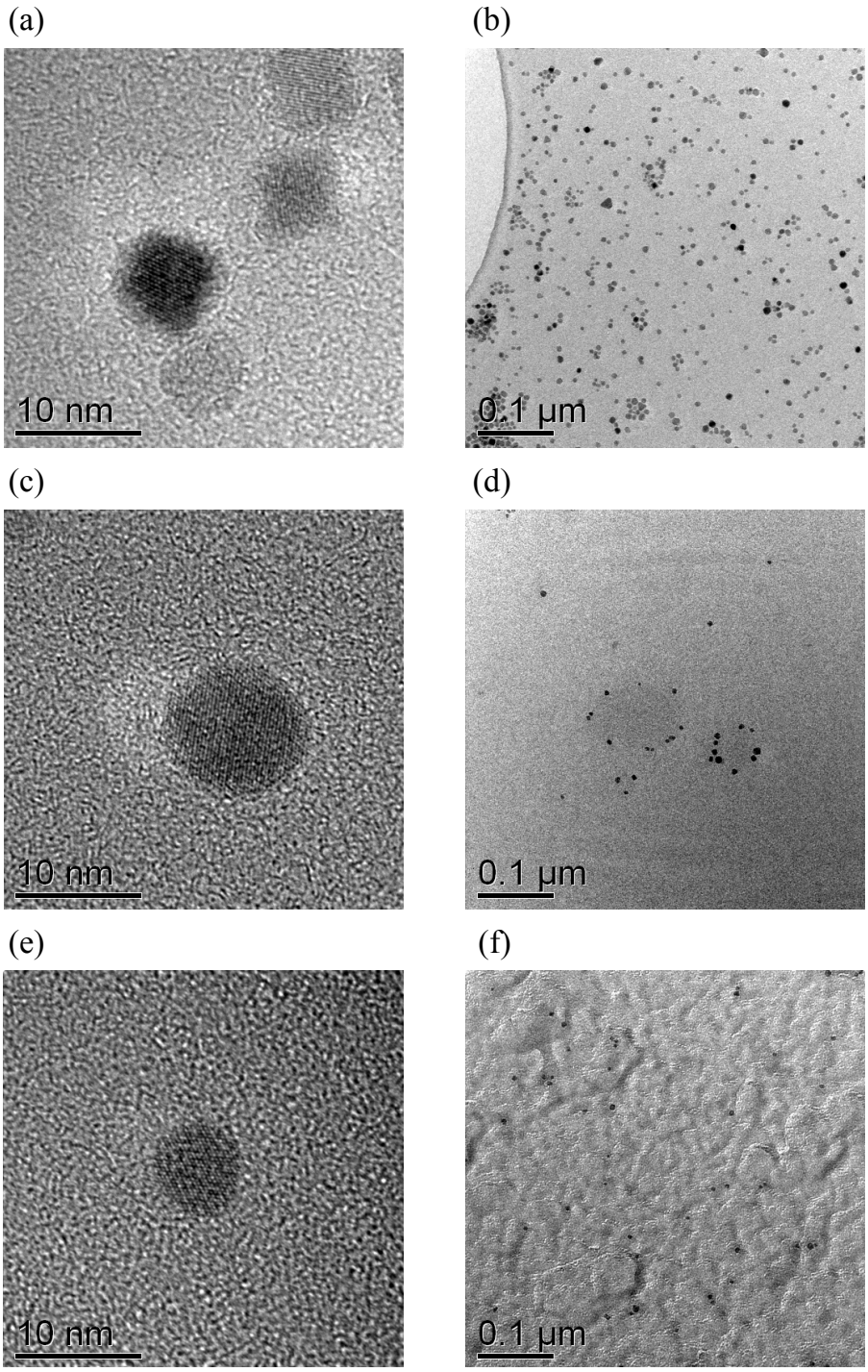

Figure 3.5: HRTEM images showing Fe_3O_4 particles at three stages of coating: uncoated particles (a & b), polymer coated Fe_3O_4 (c & d) and silica-over-polymer coated Fe_3O_4 (e & f)

3.4.2 DLS

DLS measurements were performed before coating, after addition of polymer and after silica formation. The nanocrystals before coating and with polymer were measured in chloroform. The final coated particles are in their respective solvents. Figure 3.6 shows Fe_3O_4 and InP@ZnS during the coating process.

The InP@ZnS increase in size slightly with the addition of the polymer. An increase in size is to be expected if the polymer has bound to the surface as expected. After addition of silane and transfer to NaOH (aq) there was a marked increase in size from approximately 10 to 20 nm in diameter. This is a strong indication that something has occurred on the surface of the particle.

A similar pattern is observed with the Fe_3O_4 nanocrystals. There was a larger size increase after the addition of the polymer than observed with InP@ZnS. Once the silane had reacted there was another size increase resulting in a hydrodynamic diameter of approximately 22 nm in dimethylformamide (DMF), again approximately doubling the initial size of the particles in chloroform.

The DLS results show a marked increase in size which along with the observed change in the solvent suggests that the surface of the nanocrystal has been altered. The lack of a detectable change using the TEM, in Section 3.4.1, does not support or contradict the DLS measurements.

It is important to remember that DLS size distributions are a measurement of the hydrodynamic radius of the particle and not the physical radius of the particle. For interpreting the DLS size distributions in Figure 3.6 this means that the measurements will appear as an overestimate of size when compared to TEM. Secondly, when comparing samples between solvents the solvation properties of the solvent will affect the observed size.

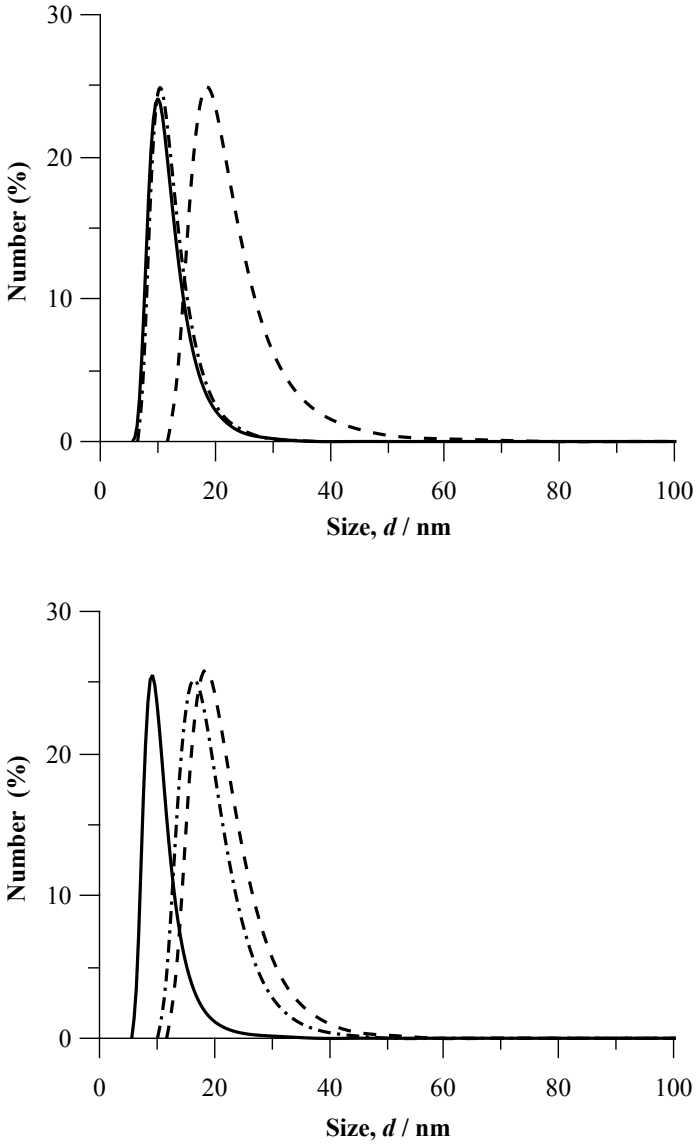

Figure 3.6: DLS size distributions for (top) InP@ZnS and (bottom) Fe_3O_4 at different stages in the coating process. The stages represented are before coating (full line), after polymer wrapping (dot and dashed line) and after silica growth (dashed line). After transfer the InP@ZnS are in 0.05 mol dm^{-3} NaOH (aq) and the Fe_3O_4 are in DMF. (d = particle diameter)

3.4.3 IR spectroscopy

Samples for ATR FT-IR spectrometer were prepared by precipitation from the solvent and 24 h drying on a Schlenk line. Once dry, the powder produced was then placed on the diamond crystal of the instrument. Figure 3.7 shows the infra-red spectra of the particles once coated in the silica-over-polymer layer. The envisaged hybrid layer contains many potential chemical functionalities which complicates characterisation. To elucidate more information the spectra of the precursors were also collected, Figure 3.8. Spectra of all remaining precursors and solvents were also collected but did not contribute toward the spectra of the products.

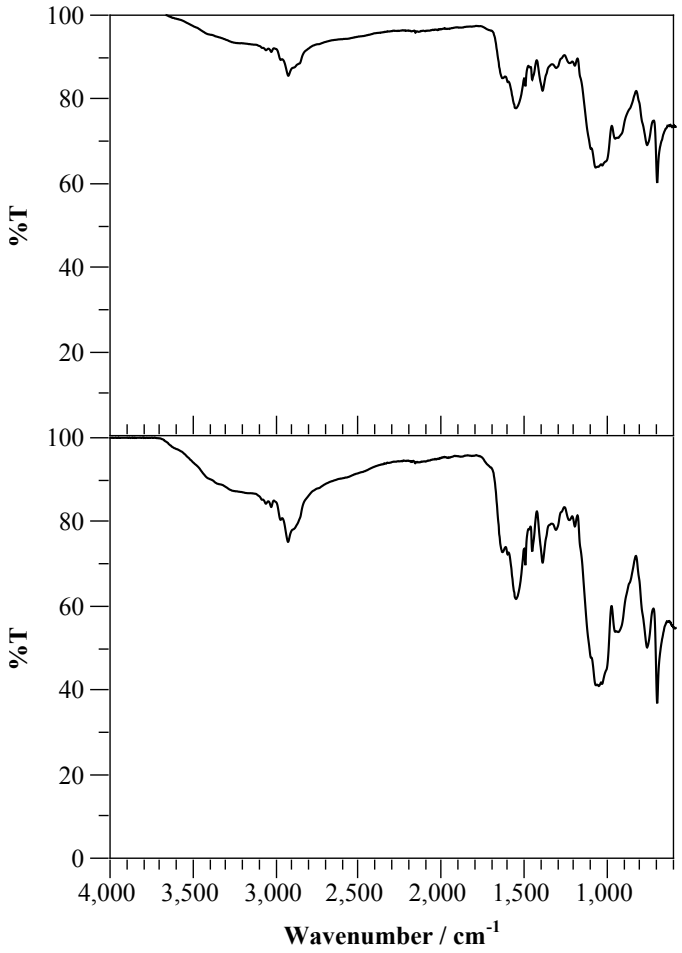

Figure 3.7: IR spectra of (top) InP@ZnS nanocrystals with the silica-over-polymer layer and (bottom) Fe_3O_4 nanocrystals with the silica-over-polymer layer.

The broad feature, in both spectra in Figure 3.7, between 3500 and 2500 cm^{-1} is typical of Si−O from silica. The rest of the spectrum is complicated and requires comparison against starting materials. Figure 3.8 shows the infra-red spectra for 3-aminopropyltriethoxysilane and poly(maleic anhydride-*co*-styrene) and their detailed analysis is in Tables 3.1 and 3.2. Superimposed on the broad Si−O feature are aryl and allyl C−H stretches from both 3-aminopropyltriethoxysilane and poly(maleic anhydride-*co*-styrene) implying these parts of the structure are unchanged from the precursors. The C−H

deformations that can be seen in the starting materials are hidden by strong features in the product.

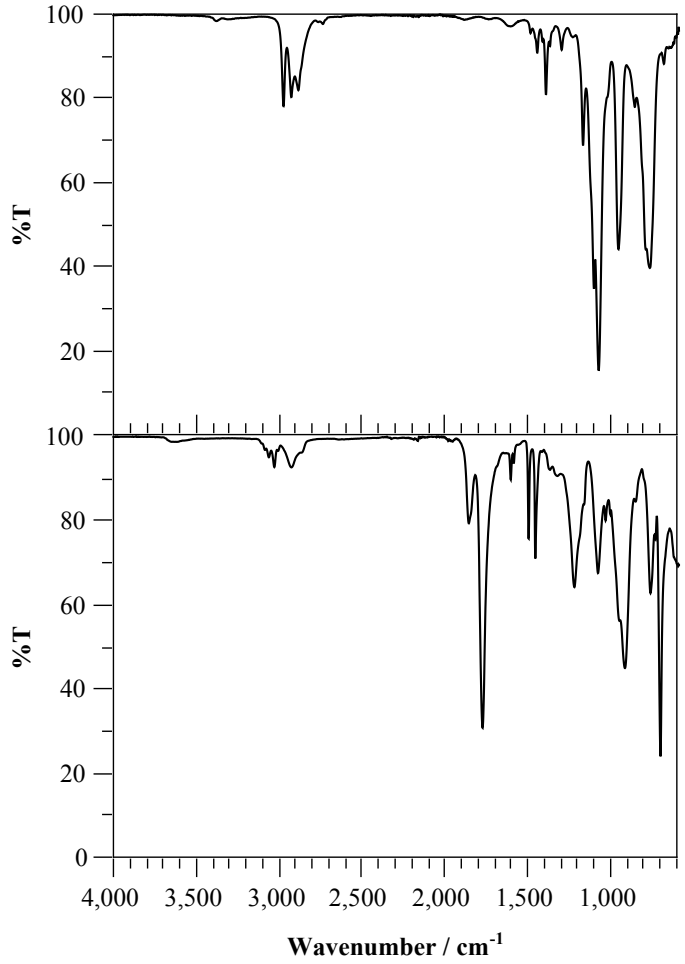

Figure 3.8: IR spectra of (top) 3-aminopropyltriethoxysilane and (bottom) poly(maleic anhydride-*co*-styrene).

Table 3.1: Infra-red band analysis for poly(maleic anhydride-*co*-styrene)

Structural Feature	**Vibrational Motion**	**Wavenumber / cm^{-1}**
Aryl	C−H stretch	3059, 3031
-CH_2-	C−H stretch	2929
-CO-O-CO-	C=O stretch	1855, 1775
Aryl		1602,1584,699
-CH_2-	C−H deformations	1495,1454
-C-O-C-		1217

Table 3.2: Infra-red band analysis for 3-aminopropyltriethoxysilane

Structural Feature	Vibrational Motion	Wavenumber / cm^{-1}
Amine	N−H stretch	3366 (very weak)
-CH_2- and -CH_3	C−H stretches	2973, 2972, 2886
Amine	N−H stretch	1600
-CH_2- and -CH_3	C−H deformations	1602,1584
-CH_3	CH_3 symmetrical deformations	1495,1454
Si−O		1067

3-Aminopropyltriethoxysilane has a sharp band for Si−O at 1067 cm^{-1}. This feature is still present in the product but is broader at 1068 cm^{-1} and is accompanied by a broad Si−O between 3500 and 2500 cm^{-1} which is characteristic of silica. The amine peak from the silane is observed as a very weak band at 1600 cm^{-1} and a very weak band at 3366 cm^{-1}. The 3366 cm^{-1} band is masked by the broad Si−O feature in the product and the 1600 cm^{-1} band is masked by a stronger feature.

Poly(maleic anhydride-*co*-styrene) has a very distinctive pair of peaks from the C=O stretches of the acid anhydride at 1855 cm^{-1} and 1755 cm^{-1}. In the spectra of the products this feature has disappeared and is replaced with a pair of peaks characteristic of a secondary amide (−CONH−) at 1634 cm^{-1} and 1556 cm^{-1}. This is a good indication that the reaction between the silane and polymer has taken place. The lack of remnant acid anhydride peaks suggests the reaction has gone to completion.

Table 3.3: Infra-red band analysis for silica-over-polymer coated particles

Structural Feature	Vibrational Motion	Wavenumber / cm^{-1}
Si−O from silica		3500 - 2500
Aryl	C−H stretch	3059, 3031 (partially masked by Si−O), 699
-CH_2-	C−H stretch	2929 (partially masked by Si−O)
Secondary amide -CONH-		1634,1556
Si−O from silica	C−H deformations	1068 (broad)

To summarise, the infra-red spectra of the product suggest that the reaction between the silane and the polymer has occurred due to the disappearance of the acid anhydride and the appearance of the secondary amide. The silane peak has been replaced with a pair of peaks characteristic of silica. Features which did not undergo reactions such as the rings from styrene, the polymer back bone and $-CH_2-$ in the silane appear in the spectra of the product. The assignment of the infra-red spectra for the silica-over-polymer coated nanocrystals, as shown in Figure 3.7, can be found in Table 3.3.

3.4.4 XPS

XPS allows the determination of which elements are in the sample and can indicate how many environments that element exists in. The process of identification depends strongly on the fitting of the peaks observed with Gaussians and requires care. Specra were collected at the three stages of coating: before polymer, after polymer addition and after silane reaction.

Figure 3.9 shows a survey spectrum for the sample and high resolution spectra for the Si 2p and N 1s electrons for Fe_3O_4 before the coating procedure. The survey spectrum shows all the expected peaks for Fe_3O_4 nanocrystals on a gold surface. An Si 2p signal is observed but is relatively small. The particles have not encountered silicon in any of the precursors so this is either an impurity or the sample has been contaminated. The N 1s peak is barely distinguishable from the baseline.

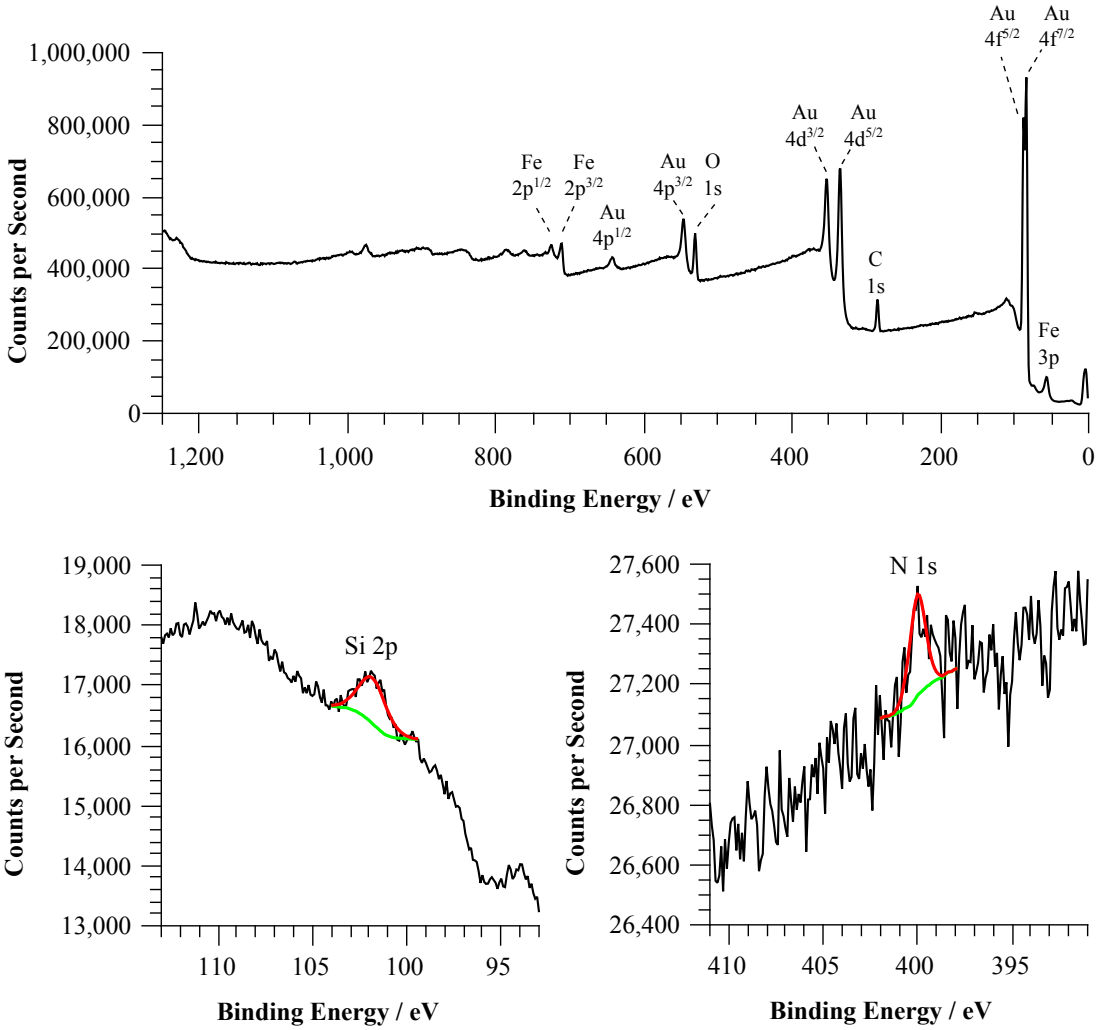

Figure 3.9: X-ray photoelectron spectra of Fe_3O_4 nanocrystals before coating. (top) A survey spectrum, (bottom left) a high resolution spectrum of the Si 2p and (bottom right) a high resolution spectrum of the N 1s.

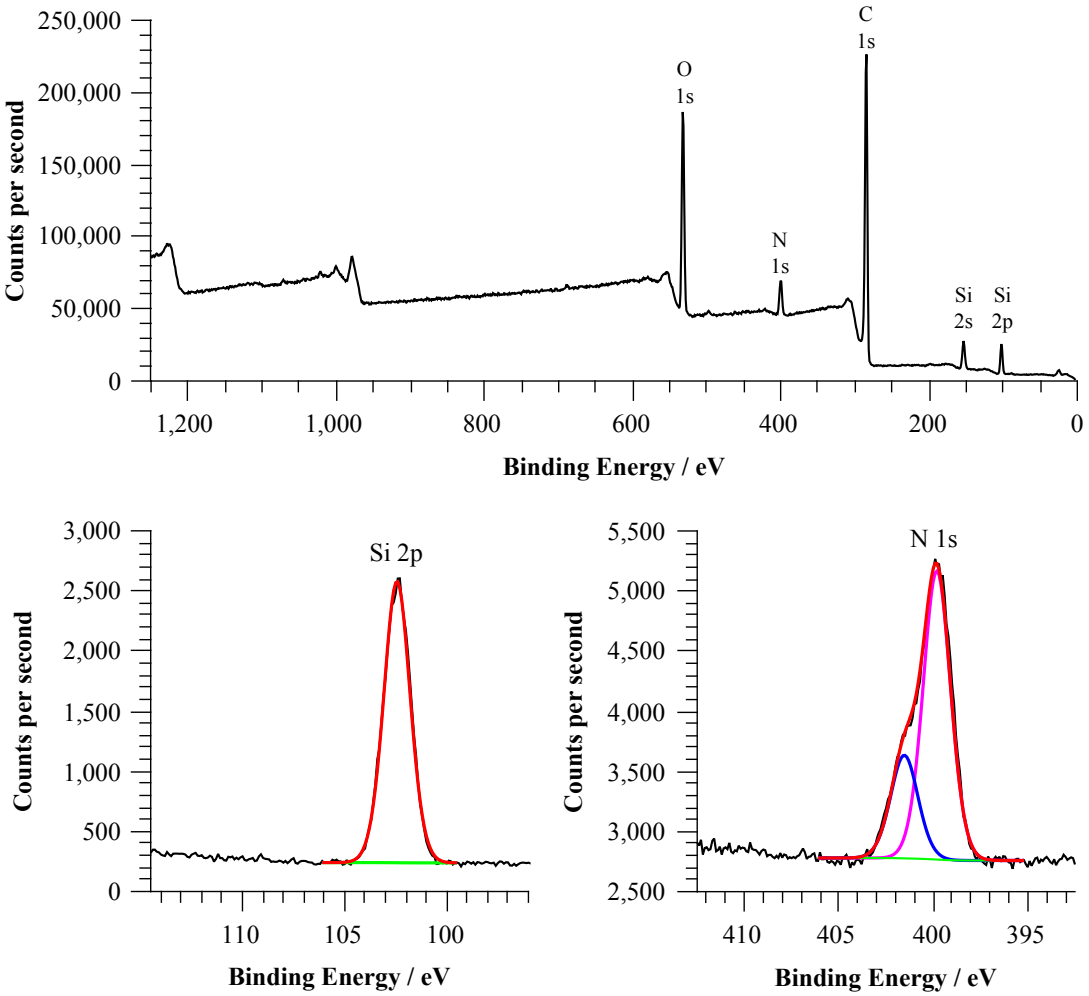

Figure 3.10: X-ray photoelectron spectra of Fe_3O_4 nanocrystals after coating with silica-over-polymer layer. (top) A survey spectrum, (bottom left) a high resolution spectrum of the Si 2p and (bottom right) a high resolution spectrum of the N 1s.

Figure 3.10 shows the same spectra but for the silica-over-polymer coated particles. The high resolution Si 2p spectrum shows a clear peak that is much more intense relative to the baseline when compared to the uncoated particles. The survey spectrum shows all the expected peaks from the sample. The N 1s peak shows an envelope which can't be described by a single Gaussian. There is a definite shoulder to the higher binding energy side. This was fitted with a pair of Guassians at 401.5 eV and 399.8 eV. This suggests that there are two different environments for the N 1s electron. The energies correspond to an amine and an amide. When comparing to the proposed reaction scheme, Figure 3.3, nitrogen can only come from the reactions of 3-aminopropyltriethoxysilane. It is either a secondary amide linking the silica to the polymer or as a primary amine as a part of the silica cage produced.

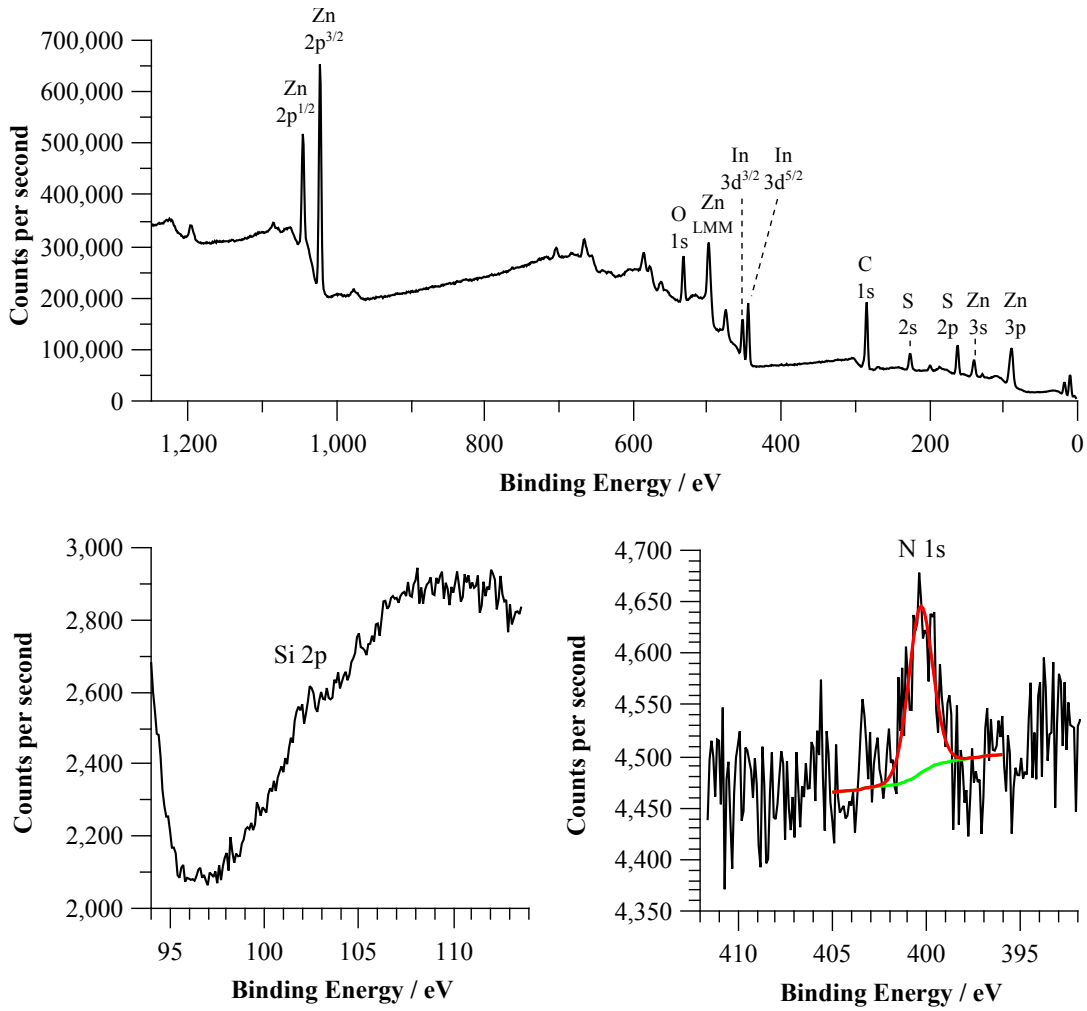

Figure 3.11: X-ray photoelectron spectra of InP@ZnS nanocrystals before coating. (Top) A survey spectrum, (bottom left) a high resolution spectrum of the Si 2p and (bottom right) a high resolution spectrum of the N 1s.

XPS measurements were also performed on InP@ZnS during the coating process. The uncoated nanocrystals are more complicated from an XPS perspective because they contain indium, phosphorous, zinc and sulphur. Complicating the measurement further, reagents used in the synthesis incorporate silicon, in the tris(trimethylsilyl)phosphine, and nitrogen, in hexadecylamine. As a consequence the survey spectrum is much more complicated but does show peaks from all the expected elements. As for silicon the potential contamination from tris(trimethylsilyl)phosphine has had a minimal impact on the high resolution spectrum for Si 2p, Figure 3.11 (bottom left). The contamination of nitrogen is only slightly worse than that of the Fe_3O_4, Figure 3.11 (bottom right). Both indicate that there is very little silicon or nitrogen in the raw particles.

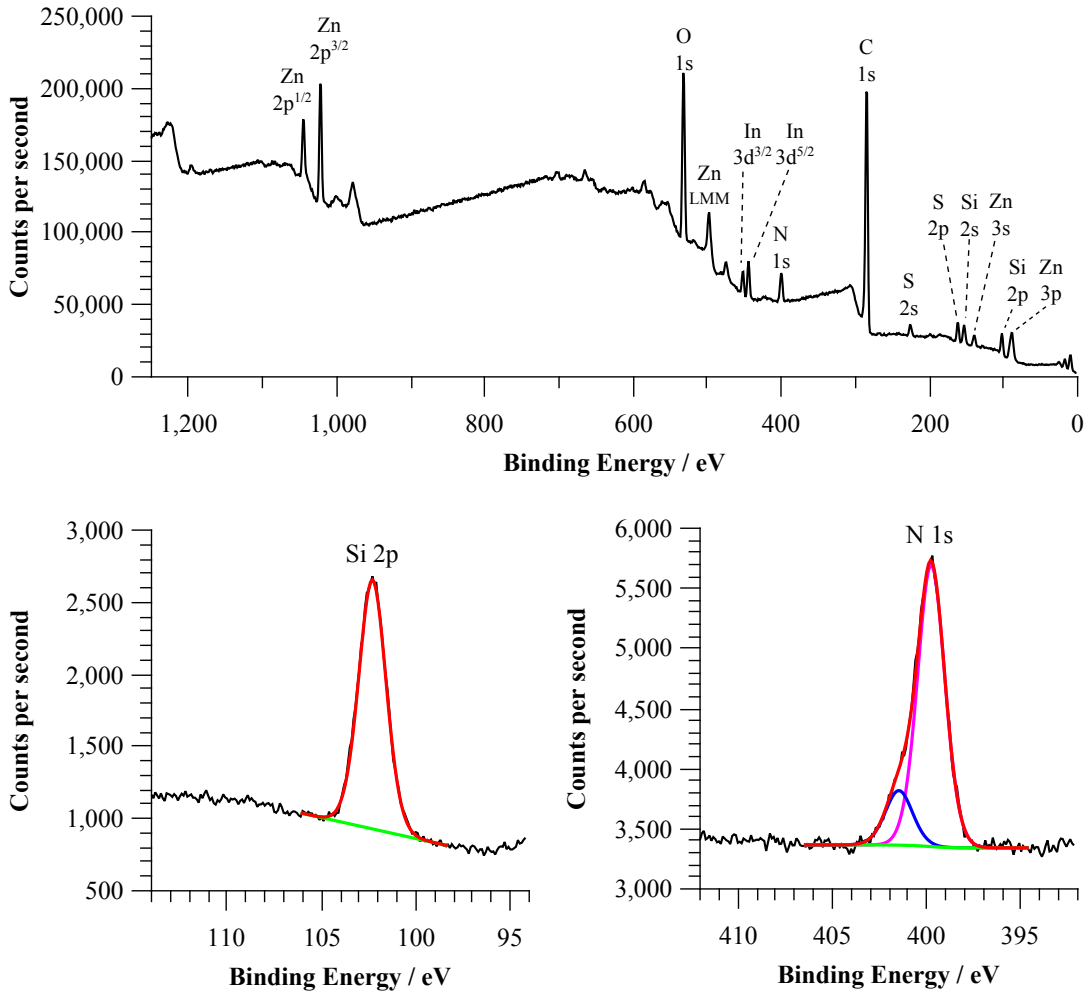

Figure 3.12: X-ray photoelectron spectra of InP@ZnS nanocrystals after coating with silica-over-polymer layer. (top) A survey spectrum, (bottom left) a high resolution spectrum of the Si 2p and (bottom right) a high resolution spectrum of the N 1s.

After coating the XPS spectrum is very similar to that of the coated Fe_3O_4, Figure 3.12. The survey spectrum shows the addition of peaks from nitrogen and silicon. The high resolution spectrum for the Si 2p electron region shows a clear peak from the Si 2p confirming the presence of silicon in the sample, Figure 3.12 (bottom left). An asymmetric peak for the N 1s is observed again showing a shoulder to higher energy. This was fitted using a pair of Gaussian distributions at 401.5 eV and 399.8 eV, identical positions as for the silica-over-polymer coated Fe_3O_4.

To summarise, the XPS proves that both silicon and nitrogen are introduced in the coating process. The most significant conclusion is that there are two N 1s environments which agree with the prediction that a secondary amide and an amine are formed.

3.4.5 EDX spectroscopy

EDX analysis was performed on the nanocrystals before coating, after introduction of polymer and after polymerisation of the silanes. This allows an elemental analysis to be performed on a relatively small area but is not sensitive to lighter elements, Section 2.3.1.3.

The EDX analysis for Fe_3O_4 are shown in Figure 3.13. The corresponding TEM images for the EDX measurements are included. In the case of Fe_3O_4 a sample region containing only one particle was used. Figure 3.13 (top) shows a number of peaks. The large signal at 0.30 keV for carbon originates from the the carbon film of the grid which is inevitably sampled. The copper peaks at 8.93 keV, 8.10 keV and 2.58 keV are from stray electrons interacting with copper in the grid. The iron peaks at 7.09 keV, 6.44 keV and 0.75 keV and oxygen peak at 0.56 keV are from the Fe_3O_4 nanocrystals and their oleic acid ligands.

Figure 3.13 (middle) shows the EDX result for the polymer coated particles. As the polymer is largely carbon and hydrogen the EDX spectrum changed very little from the uncoated nanocrystals as the film supporting the particles is carbon.

The coated particles are represented in Figure 3.13 (bottom). All the peaks from the particle and the grid are present as with the uncoated particles. The intensity of the oxygen peak at 0.56 keV has increased greatly in comparison to the neighbouring iron peak. A new peak has appeared at 1.78 keV which is characteristic of silicon. The combined appearance of silicon combined with the marked increase in the oxygen peak is a good indication that silica is present.

The measurements were repeated for InP@ZnS nanocrystals. In a similar fashion to XPS the InP@ZnS are more complicated to analyse due to the greater number of elements in the nanocrystal. The bare particles are shown in Figure 3.14 (top). Peaks from copper and carbon are present and are located in the same positions as for the Fe_3O_4 sample. The QD core is represented at 3.33 keV and 3.56 keV for indium and 2.04 keV for phosphorus. Zinc in the shell is at 9.65 keV, 8.67 keV and 1.06 keV. The peak at 2.35 keV is from the sulphur in the shell. As with the Fe_3O_4, the EDX analysis of the polymer coated particles, Figure 3.14 (middle), appears very similar to the bare particles. No new features are present for the same reasons as with Fe_3O_4. The nanocrystals once coated with the silica-over-polymer layer are represented in Figure 3.14 (bottom). The appearance of a silicon peak at 1.78 keV and the increase in intensity of the oxygen peak at 0.56 keV is again a good indication that silica is present.

To summarise, the results of the EDX analysis indicate that the nanocrystals contain the correct elements and that silicon and oxygen appear when the silica layer is grown. As the EDX analysis is over a small area this is a good indication that the silica is on the particles but does not absolutely identify the location of the silica.

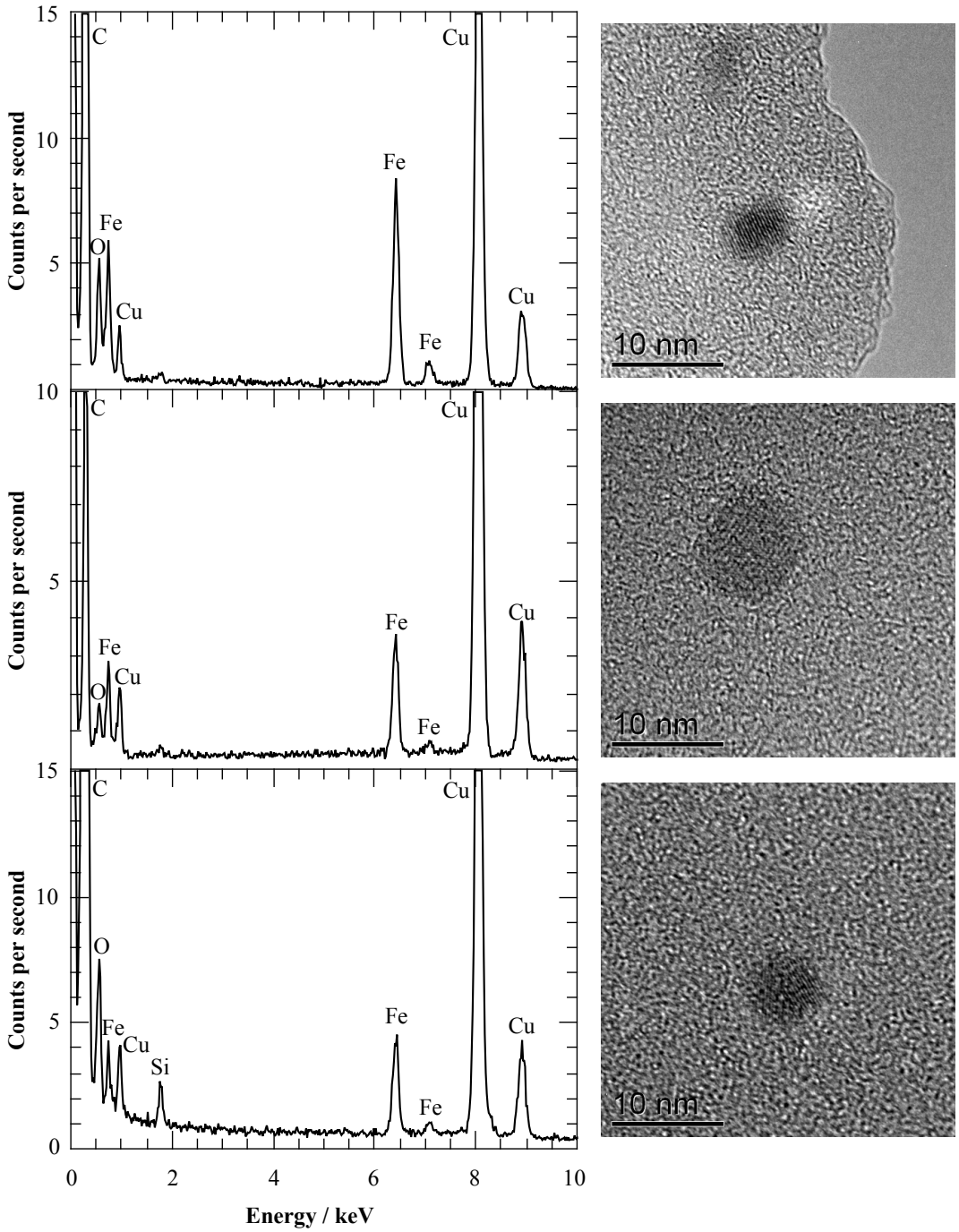

Figure 3.13: EDX analysis of Fe_3O_4 nanocrystals at different stages of coating and the corresponding HRTEM image. Fe_3O_4 particles before coating (top), Fe_3O_4 with polymer foundation (middle) and Fe_3O_4 with silica-over-polymer layer (bottom).

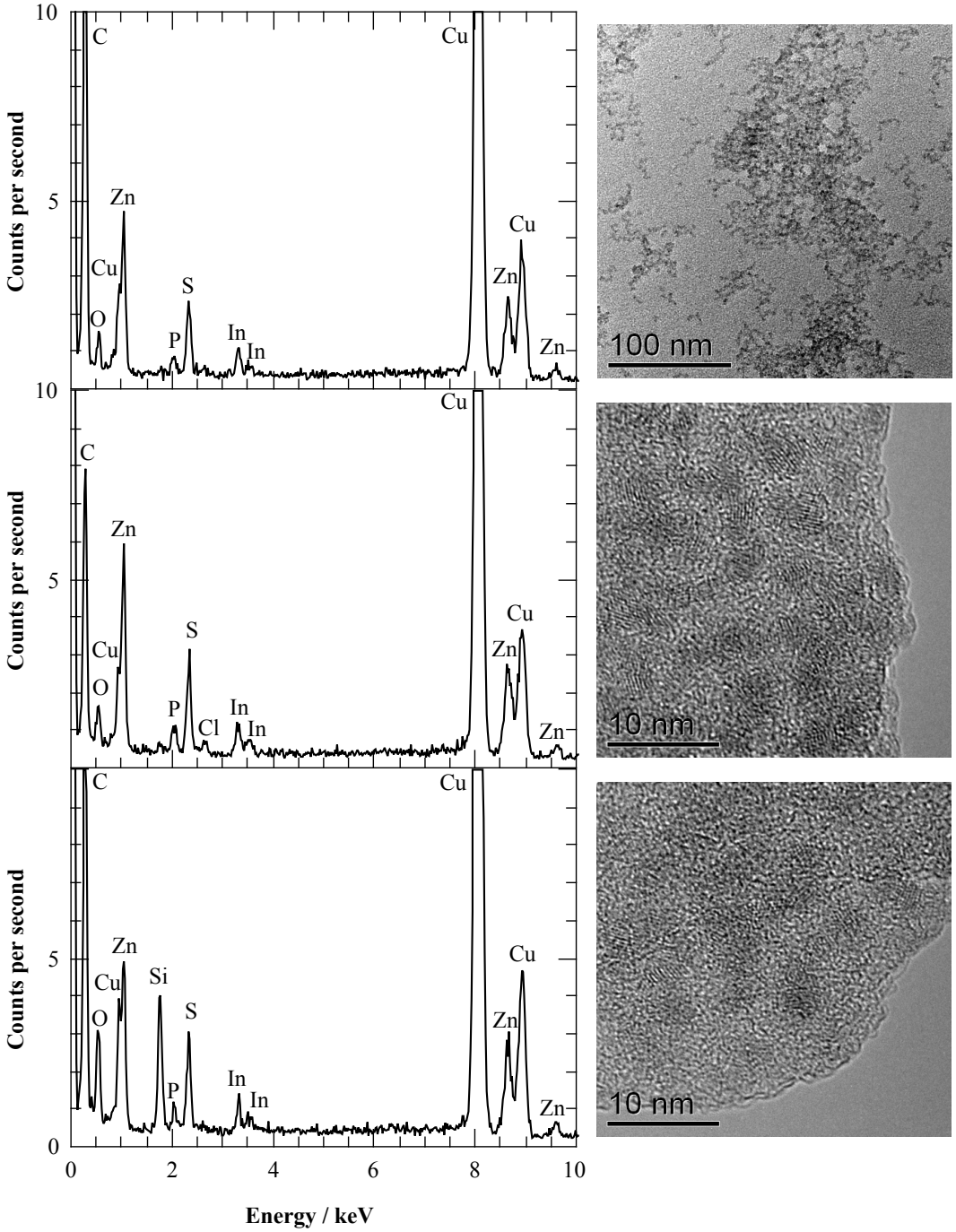

Figure 3.14: EDX analysis of InP@ZnS nanocrystals at different stages of coating and the corresponding HRTEM image. InP@ZnS particles before coating (top), InP@ZnS with polymer foundation (middle) and InP@ZnS with silica-over-polymer layer (bottom).

3.4.6 EFTEM images

Thus far the techniques used have largely looked at the chemical composition of the nanocrystals, EDX hints towards the location but does not prove it. EFTEM was employed to study the location of different elements within the structure. There are limits to what can be achieved with EFTEM as the elements that are observed have to be in a region of the EELS spectrum with no spectral overlap.

In the case of the Fe_3O_4 nanocrystals Fe and Si are observable without other elements contributing to the signal. The element specific maps along with the image from the zero-loss peak are shown in Figure 3.15. The light spots represent the element of interest in the energy filtered images. Comparing the Fe only image with the zero-loss image confirms that the Fe_3O_4 particles do indeed contain Fe. The particles on the zero-loss image match the Fe containing regions in the map. The Si map allows a similar conclusion to be drawn. Regions where silicon is found correspond to the iron regions and the zero-loss image. The regions of silicon look slightly larger than the particles in the zero-loss image although the difference is not measurable with any certainty from the images. The EFTEM images prove that the silica is around the surface of the particles as it is proven that the silicon is located around the particles.

Also, there are no Si containing particles which are not associated with an Fe containing particle. This is a good indication there are no low density silica structures which would have been invisible with TEM. This confirms that the signals in the EDX analysis are from coated nanocrystals and not free silica particles.

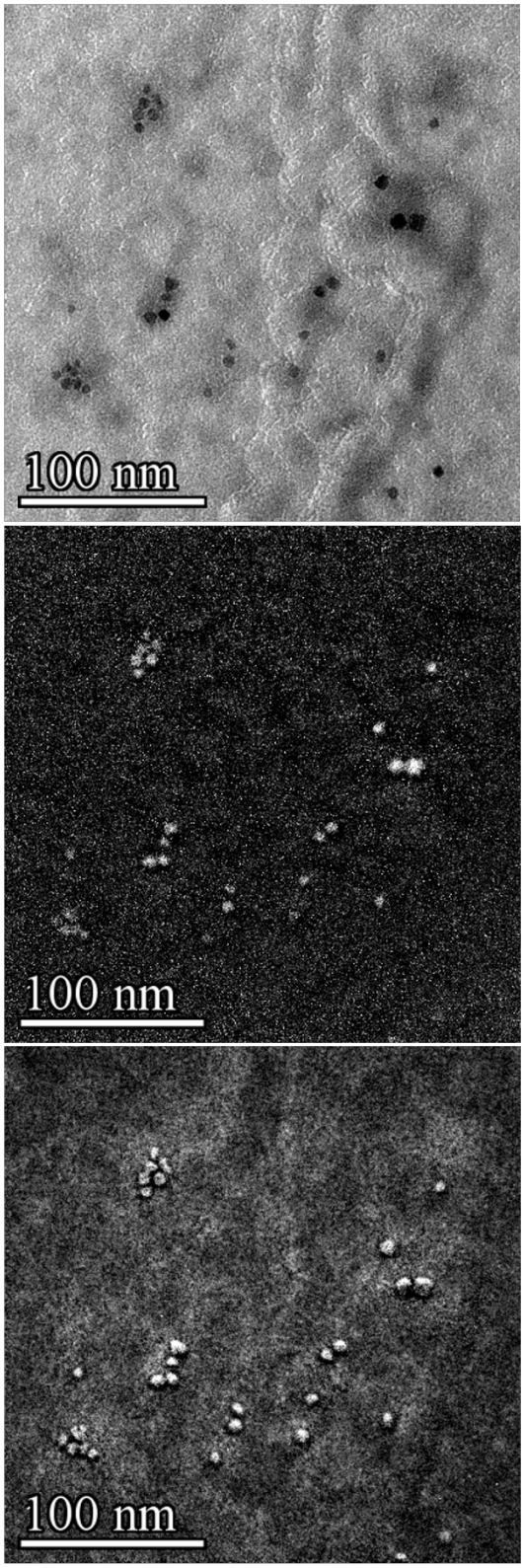

Figure 3.15: EFTEM maps of silica-over-polymer coated Fe_3O_4 nanocrystals. (top) EFTEM Zero-loss image, (middle) EFTEM image of Fe only and (bottom) EFTEM image of Si only.

3.4.7 Luminescence measurements

It is important that the nanocrystals do not lose their properties when modifying their surface. To monitor this the luminescence of the QDs were monitored during the coating process, Figure 3.16. Although a better measurement of this would be to measure the QY of the particles that is impractical due to the length of time required to make a measurement. The luminescence at a constant concentration is proportional to the QY and it is possible to measure this *in situ*.

The reaction was performed in a standard quartz luminescence cuvette and was monitored after addition of polymer, at twelve hour intervals after the silane was added and after transfer into the new solvent. The luminescence with and without polymer present were identical and the particles before polymer have been omitted. After 12 h reaction with silane the intensity had decreased by 21.3 % and the peak had red-shifted by 5 nm to 630 nm, Table 3.4. By the end of the period of growth the luminescence decreased by a total of 28.2 %. This is a good result as modification of surfaces can result in significant losses of photoluminescence intensity and is a crucial factor for success. Once transferred into DMF the photoluminescence decreased by a total of 68.9 %. The changing of solvent does affect the photoluminesence of a particle due to the change of the dielectric constant of the solvent, so this value cannot be directly related to previous measurements.

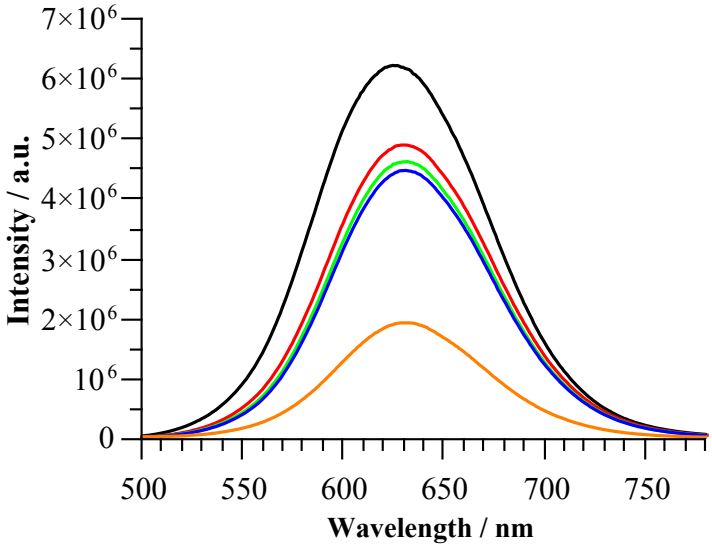

Figure 3.16: The luminescence profile for InP@ZnS coated with the silica-over-polymer layer. (black) InP@ZnS polymer coated, (red) after silane addition and 12 h, (green) after silane addition and 24 h, (blue) after silane addition and 36 h hours and (orange) in DMF after 37 h.

Table 3.4: Luminescence intensity and λ_{max} during layer growth

Stage	λ_{max} / nm	Intensity / a.u.
InP@ZnS & polymer	625	6,223,020
12 h after silane addition	630	4,897,750
24 h after silane addition	631	4,618,020
36 h after silane addition	630	4,470,950
After transfer to DMF	632	1,936,770

3.4.8 Zeta-potential

The zeta potential of InP@ZnS coated with the silica-over-polymer layer is shown in Figure 3.17. The negative ζ-potential is an indication that the surface of the particle is negative. Deprotonated silanol groups ($Si-O^-$) would give this signal. This also shows that the surface amine groups are deprotonated at pH 12.7 (0.05 mol dm^{-3} NaOH (aq)).

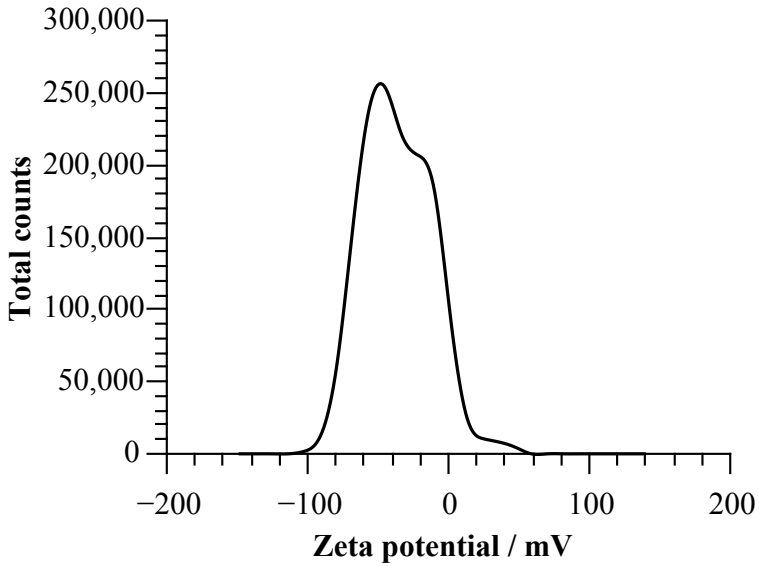

Figure 3.17: The zeta potential for InP@ZnS coated with the silica-over-polymer layer.

3.5 Conclusion

In this chapter a new method for developing a thin silica shell upon colloidal nanocrystals has been introduced and demonstrated through rigorous analytical characterisation. This method removes the need for surface specific chemistry to make a surface "vitreophilic" by use of an amphiphilic polymer as a foundation. The foundation can be reacted with a nucleophilic functional triethoxysilane allowing further reaction to occur with another functional triethoxysilane providing functionality to the surface of the coated nanocrystal. The chemical reactions have been followed using FT-IR spectroscopy and XPS demonstrating that the silane was tethered to the polymer and silane polymerisation had occurred. Changes in size of the colloid were followed by DLS showing that the size increased as the

coating procedure progressed. EDX analysis and EFTEM images gave information about the location of silicon with respect to the nanocrystal proving that it is wrapped around the crystals. The fluorescent properties of the InP@ZnS were monitored to ensure that the nanocrystals still had their size dependent properties. The publication which resulted from this chapter is included in Appendix B.

Consequently, this work has also demonstrated the location of adsorbed pro-amphiphilic polymer. Direct observation of amphiphilic polymers wrapped around particles has been restricted to polymer staining techniques for TEM. Using the tethered silicon as a marker the EFTEM measurements prove that the polymer is located at the surface of the nanocrystals.

This work could be expanded by introducing different trialkoxysilanes to impart nanocrystals with different functionalities, *i.e*. poly(ethylene glycol) (PEG), epoxy, phosphate, thiol, *etc*. This would give direct access to particles with better aqueous compatibility and presence of functional groups suitable for further elaboration or ligand attachment. Use of TEOS in combination with functional trialkoxysilanes could be used to control the thickness of the shell.

CHAPTER 4

Custom amphiphilic polymers for functionalising nanocrystals

4.1 Structural motifs of previous amphiphilic polymers

As described in Chapter 1, amphiphilic polymers provide a methodology for the functionalisation of colloidal nanocrystals stabilised with hyrophobic ligands. The polymers interact with the nanocrystals through hydrophobic interactions with the nanocrystal surface ligands in the same manner as standard amphiphilic molecules. *i.e*. the hydophobic ligands interdigit with the hydrophobic parts of the amphiphile, Figure 4.1. In the case of amphiphilic polymers there is a polymer backbone and from this there is pendant hydrophobic and hydrophilic functionality. Once wrapped around the nanocrystal, the resulting structure consists of a nanocrystal with hydrophobic bi-layer with a hydrophilic exterior. To date, the polymers used are either commercially-available, modifications of commercially-available polymers or are synthesised to heavily mimic the commercially-available polymers. Over the past decade the field has grown and a range of polymers, bioconjugation techniques and water transfer procedures involving amphiphilic polymers has ensued. These advances are largely covered in recent reviews by Zhang *et al.*[70] and Quarta *et al.*[71]

The polymers previously used have been either based on a poly(acrylic acid) or co-polymers of maleic anhydride. The first recorded use of an amphiphilic polymer for nanocrystal stabilisation was by Wu *et al.* using an octylamine modified poly(acrylic acid) stabilising CdSe@ZnS.[190] The methodology developed by Wu *et al.* involved the CdSe@ZnS nanocrystals being dispersed in chloroform with the octylamine modified poly(acrylic acid). The chloroform was removed by evaporation resulting in a dry film consisting of the polymer and the nanocrystals. Water was added and the particles dispersed in water. Excess polymer was removed using Size Exclusion Chromatography (SEC). This methodology is important as it became the foundation of the majority of water transfer procedures using amphiphilic and pro-amphiphilic polymers.

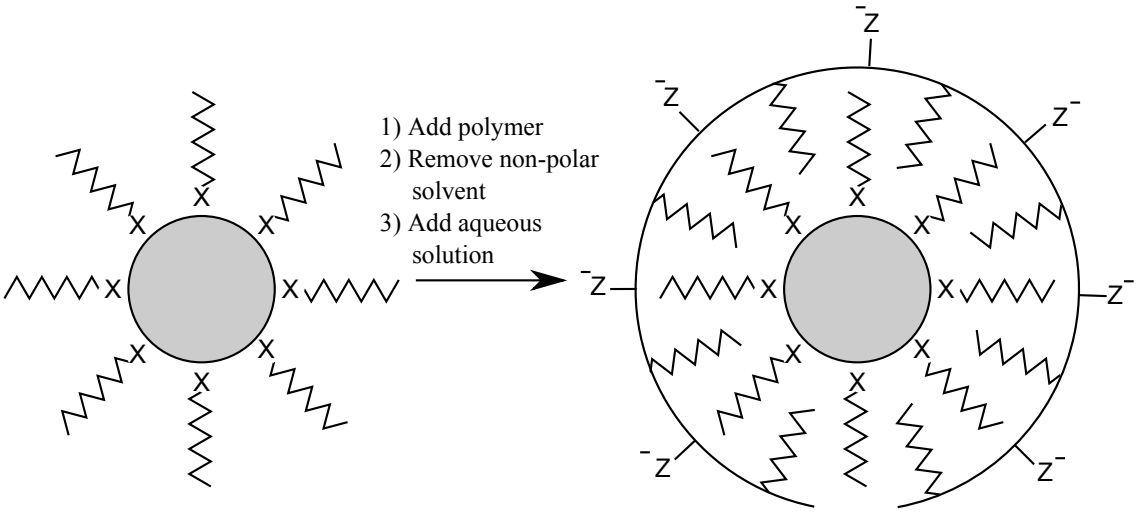

Figure 4.1: Ligand stabilised nanocrystals (left) are mixed with an amphiphilic polymer and the solvent is removed. A hydrophobic interaction occurs between the ligands and the hydrophobic subunits of the polymer resulting in a bilayer forming around the nanocrystal. After addition of aqueous media the nanocrystals redisperse (right).

In the case of maleic anhydride co-polymers, the other component is a non-polar subunit which allows the hydrophobic interaction with nanocrystal ligands to occur. The polymer is introduced to the nanocrystal in an organic solvent, typically chloroform, and the polymer forms a bi-layer with the ligands. After removal of the chloroform through evaporation the anhydride ring of maleic anhydride is opened by a hydrophilic nucleophile rendering the nanocrystal dispersible in aqueous media. Maleic anhydride co-polymers were first used by Pellegrino *et al.* using poly(maleic anhydride-*alt*-1-tetradecene).[191]

For the rest of this chapter the term amphiphilic polymer will be used to describe polymers with pendant hydrophilic and hydrophobic components. Many polymers used to date can not transfer the nanocrystals to the aqueous phase without reaction with a hydrophilic nucleophile. In the remainder of this work polymers requiring reaction with nucleophiles are termed "pro-amphiphilic" and polymers which require no further reaction are termed "amphiphilic". After the reaction pro-amphiphilic polymers become amphiphilic but in many of the water transfer procedures the properties of the pro-amphiphilic polymer is what governs the success of the water transfer.

It is worth stating that the use of amphiphilic polymers to make colloidal structures compatible with aqueous environments is not new. Tribet *et al.* water transferred hydrophobic membrane proteins using poly(acylic acid) that had been modified with octylamine and isopropylamine.[192,193] They also postulated that these polymers could be used as a general method for the phase transfer of hydrophobic colloids.[193]

A review is provided covering: the structures of amphiphilic polymers used to date, functionalisation of the polymers and transfer procedures. This structurally-orientated review will not cover the *in vitro* and *in vivo* studies performed with nanocrystals stabilised with amphiphilic polymers but information on this can be found in recent reviews.[70,71]

4.1.1 Commercially-available polymers

4.1.1.1 Alkylamine modified poly(acrylic acid) polymers

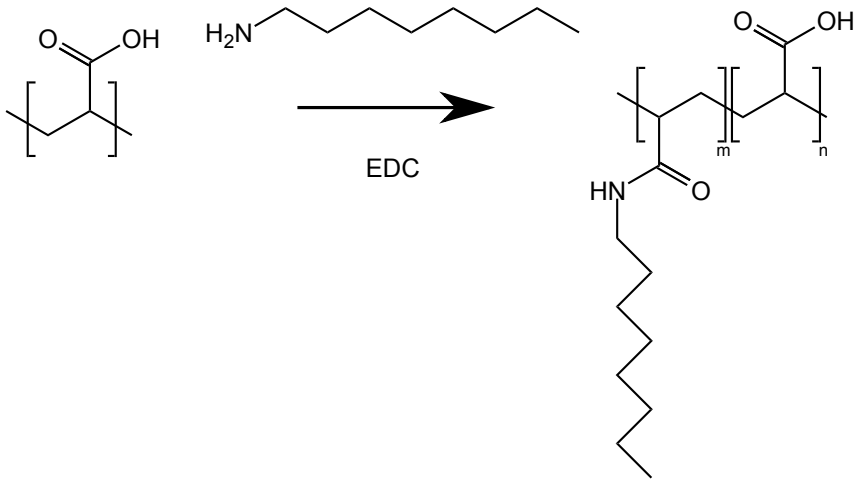

Figure 4.2: The reaction of poly(acrylic acid) with octylamine resulting in an amphiphilic polymer.

Poly(acrylic acid) modified with octylamine was first used by Wu *et al.* to transfer CdSe@ZnS.[190] 40 % of the carboxylic acid groups were coupled to octylamine to form an amphiphilic polymer, Figure 4.2. It was the first example of the slow removal of a common solvent for the nanocrystals and polymer. In the work a proportion of the stabilising -COOH groups provided by the polymer were used to couple the nanocrystal to streptavidin and antibodies using 1-ethyl-3-(3-diaminopropyl)carbodiimide (EDC).

The effect of the length of the amine used on the stabilising properties of modified poly(acrylic acid) on different size QDs was examined by Anderson and Chan.[194] It was found for CdSe@ZnS stabilised with trioctylphosphineoxide and hexadecylamine that the optimal amines attached to the polymer were octadecylamine and hexadecylamine. As the QDs got smaller a higher proportion of alkylamine substitution resulted in the highest transfer efficiencies.

Alkylamine modifed poly(acrylic acid) has been used to functionalise nanocrystals with lysine,[190,195] PEG-amine,[196] carboxy-PEG-amine,[196] aminopentanol tethered dye[197] and *N*-isopropylacryamide.[198] The amount of work published with alkylamine modified poly(acrylic acid) is quite limited as copolymers of maleic anhydride became more popular amongst the nanocrystal synthesis community.

4.1.1.2 Copolymers of maleic anhydride

Maleic anhydride containing polymers allow the modification of the polymer without carbodiimide coupling techniques. The acid anhydride group is an activated ester and requires no additional reagents to allow a nucleophile to attack and become attached to

the polymer. Unlike the modified poly(acrylic acid) polymers these polymers are not amphiphilic before reaction with a hydrophilic nucleophile.

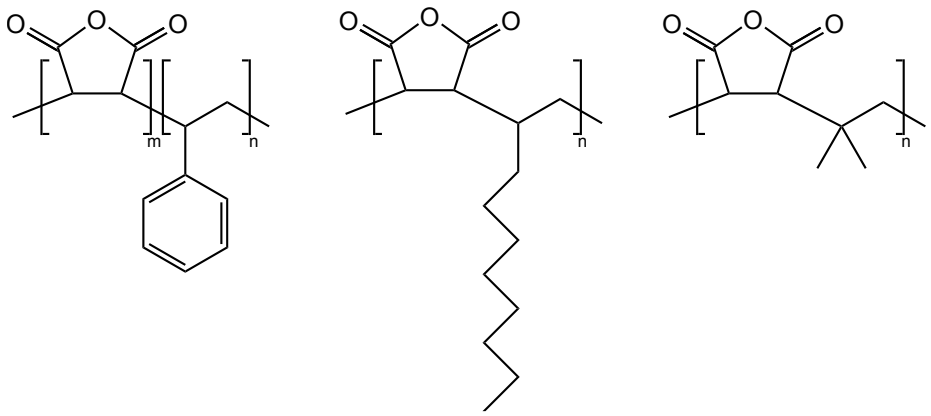

Figure 4.3: The three types of commercially-available maleic anhydride copolymers used. The polymers are (Left) poly(styrene-*co*-maleic anhydride), (Middle) poly(maleic anhydride-*alt*-1-alkene) and (Right) poly(isobutylene-*alt*-maleic anhydride).

If the nucleophile is hydroxide, HO^-, each acid anhydride will result in a pair of carboxylic acid groups. In the case of hydrophilic amines each reacted anhydride will produce a carboxylic acid and an amide. Strategies for bioconjugation can take advantage of any intentionally unreacted acid anhydrides or can use carbodiimide chemistry with carboxylic acid groups.

Poly(maleic anhydride-*alt*-1-alkene)

The most commonly used pro-amphiphilic polymers have the general structure of poly(maleic anhydride-*alt*-1-alkene). Pellegrino *et al.* pioneered the use of commercially available alternating copolymers of maleic anhydride by using poly(maleic anhydride-*alt*-1-tetradecene), $M_n \approx 7300$, opened with base to transfer a range of different nanocrystals, $CoPt_3$, Au, CdSe@ZnS and Fe_2O_3.[191] It was later demonstrated that the rings could be opened with $PEG-NH_2$ and furthermore the number of PEG chains per particle could be controlled through synthetic conditions and size separation.[199] *N*,*N*-dimethylethylenediamine was EDC coupled incrementally to adjust the ζ-potential to allow the surface of CdSe@ZnS to act as a buffer assisting delivery in biological systems.[200] Use of poly(maleic anhydride-*alt*-1-tetradecene) has been limited due to it no longer being commercially available.

As a consequence of the supply issues of poly(maleic anhydride-*alt*-1-tetradecene) alternatives were sought. Poly(maleic anhydride-*alt*-1-octadecene) was first demonstrated to transfer Fe_3O_4 nanocrystals by the research group of Colvin.[201] The poly(maleic anhydride-*alt*-1-octadecene), $M_n = 30{,}000 - 50{,}000\,\mathrm{g\,mol^{-1}}$, was first reacted with $PEG-NH_2$, $M_w = 6000$, resulting in an amphiphilic polymer. The nanocrystals and polymer in chloroform have the chloroform removed in the presence of water resulting in phase transfer. This methodology was later extended to CdSe@ZnS QDs.[202]

Di Corato *et al.* also used poly(maleic anhydride-*alt*-1-octadecene) showing that it could be used to transfer Au, CdSe@CdS quantum rods, $\gamma-Fe_2O_3$ and $FePt-Fe_xO_y$

heterodimer nanocrystals.[203] It was also demonstrated that ultracentrifugation techniques could be used for separation of polymer coated nanocrystals from the excess of free polymer. Doped $NaYF_4$ have also been transferred using the same polymer and a similar methodology.[204]

Poly(maleic anhydride-*alt*-1-octadecene) has proven to be versatile as three different coating methodologies have been used successfully, Section 4.1.3.[189,201,203] The nucleophiles that have been used with poly(maleic anhydride-*alt*-1-octadecene) include ethanolamine,[189] Jeffamine M-1000,[189] amine terminated poly(*N*-isopropylacrylamide),[205] amine terminated poly(ethyleneglycol),[203,206–208] a range of alkyl compounds containing alcohol and amine groups[206,207] and 4-aminophenyl β-D-galactopyranoside.[208,209]

A pair of publications by Qi *et al.* have shown the use of poly(maleic anhydride-*alt*-1-decene), $M_n = 18{,}500\,\mathrm{g\,mol^{-1}}$.[210,211] Both papers use the Pellegrino *et al.*[191] coating methodology and attach dimethylamino propylamine to the surface for *in vitro* applications.

Modified poly(isobutylene-*alt*-maleic anhydride)

Poly(isobutylene-*alt*-maleic anhydride), $M_w \approx 6000$, is unable to intercalate with a nanocrystals surface ligands without modification. Functionalisation with amines in a fashion similar to that of poly(acrylic acid) has been used to provide intercalating groups to the polymer. Unlike poly(acrylic acid) polymers, carbodiimide coupling techniques are not required as the acid anhydride is a form of activated ester. Just as in the case of poly(acrylic acid), the proportion of hydrophobic and hydrophilic groups is controllable. This was first used by Fernández-Argüelles *et al.* to impart water dispersability upon CdSe@ZnS using poly(isobutylene-*alt*-maleic anhydride) modified by reacting 75 % of the anhydride rings with dodecylamine.[212] Additionally, a hydrophobic dye was incorporated into the bi-layer. The pro-amphiphilic polymer was wrapped by mixing the polymer with the nanocrystals in chloroform and slowly removing the solvent. The particles were rendered hydrophilic by either opening the remaining acid anhydride groups with base or $PEG{-}NH_2$. This work was followed up by Lin *et al.* with a paper demonstrating successful water transfers for Au, CdSe@ZnS and Fe_3O_4.[213] The polymer has also successfully transferred FePt.[214,215]

A detailed description, for tutorial purposes, of the water transfer process with poly(isobutylene-*alt*-maleic anhydride) has been detailed in a recent publication by Jańczewski *et al.*[216] Although this method appears simple, the solubility of poly(isobutylene-*alt*-maleic anhydride) is an issue. Ideally, a common solvent for both the polymer and the alkylamine would be used as the medium for reaction but poly(isobutylene-*alt*-maleic anhydride) is insoluble in common laboratory solvents. All methods are based upon the reaction of powdered poly(isobutylene-*alt*-maleic anhydride) with an alkylamine in THF. Within minutes the powder has reacted with the alkylamine and the newly created pro-amphiphilic polymer is dissolved. Consequently, the amine will have only reacted with the exposed surface of the powder meaning there will be regions with widely differing degrees of amine attachment along the resulting polymer chains.

A wide range of nucleophiles have been successfully attached using the pro-amphiphilic polymer created from poly(isobutylene-*alt*-maleic anhydride) polymer including allylamine,[217] aminoethylacrylamide,[217] 2-hydroxyethyl acrylate,[217,218] 2-aminoethyl methacrylate,[219] proparlgyl amine,[220] 11-azido-3,6,9-trioxaundecan-1-amine,[220] amine terminated poly(*N*-isopropylacrylamide),[221] amine functionalised dyes,[212,213,215] amine terminated poly(ethyleneglycol),[212,213] biotin-PEG-amine[213] and 4-aminophenyl β-D-galactopyranoside.[213]

poly(styrene-*co*-maleic anhydride) based

Lees *et al.* demonstrated that poly(styrene-*co*-maleic anhydride) could also be used as a pro-amphiphilic polymer for the transfer of CdSe@ZnS from chloroform to water.[189] This work differs from previous attempts by use of an aryl group as the hydrophobic subunit for the amphiphile and this polymer is a random copolymer as opposed to the alternating polymers previously used. The molecular weight of the polymer is also comparatively short at $M_n = 1700\,\mathrm{g\,mol^{-1}}$.

4.1.2 Custom-synthesised polymers

Attempts have been made to synthesise pro-amphiphilic and amphiphilic polymers that improve upon the water transfer abilities of the commercial polymers or broaden the library of available polymers. In a similar fashion to the commercial polymers, the synthesised polymers fall into three categories: synthesised backbones without initial pendant functionality, polymers with pendant alkyl functionality and polymers with pendant phenyl functionality. Radical polymerisation, either uncontrolled or controlled by Reversible Addition-Fragmentation Chain Transfer (RAFT), has been used to synthesise all the polymers described in this section.

Polymers without pendant hydrophobic groups

Custom-synthesised poly(acrylic acid) of various lengths has been synthesised by RAFT. 40 % of the acrylic acid groups were reacted with octylamine, which allowed interaction with CdSe@ZnS, CdS@ZnS and Fe_2O_3 nanocrystals.[222] The polymers possessed a dithiocarbamate end group, which came from the RAFT agent, was reacted with a dye allowing it to be localised on the nanocrystal surface.

Poly(maleic anhydride) was synthesised in toluene using benzoylperoxide-initiated radical polymerisation. The polymer had pendant alkyl groups added by reaction of alkylamines of lengths between butylamine and hexadecylamine.[223] The proportion of reacted maleic anhydride groups ranged from 16 to 50 % of the monomers in the polymer backbone. Au and Ag nanocrystals were transferred using the polymers by evaporating the $CHCl_3$ in the presence of water.

Pendant alkyl groups

Poly(maleic anhydride-*alt*-1-octadecene) with a length shorter than that of the commercially available version was synthesised using RAFT.[207] It was found that with a molecular weight of 6480 g mol^{-1} the polymer was not as efficient as the commercially-available version (M_n = 30,000 to 50,000 g mol^{-1}) at transferring Fe_3O_4 nanocrystals.

Poly(methacrylic acid-*co*-stearyl methacrylate) was synthesised by radical polymerisation using ammonium persulphate. The pendant octadecyl chain intercalates with the surface ligands allowing the phase transfer of CdSe@ZnS.[224] Polymers with 7 to 33 % of stearyl methacrylate subunits were used to transfer the nanocrystals successfully.

Polymers with pendant dodecyl chains have been used to transfer nanocrystals. Park *et al.* synthesised poly(dodecylmethacrylate-*co*-poly(ethylene glycol)methylether methacrylate-*co*-methacrylic acid) using uncontrolled radical polymerisation.[225] This polymer has subunits containing poly(ethylene glycol) and carboxylic acid which allows a mixture of steric and electrostatic stabilisation. Oleic acid stabilised Fe_3O_4 nanocrystals were transferred to water using the polymer.

Parak and coworkers have synthesised a family of copolymers using lauryl methacrylate to transfer CdSe@ZnS and Au.[226] The polymers synthesised were poly(*N*,*N*,*N*-trimethylammonium-2-ethyl methacrylate iodide-*co*-lauryl methacrylate) and poly((dihydroxyphosphoryl)ethyl methacrylate-*co*-lauryl methacrylate) which provide positive and negative electrostatic stabilisation respectively. The *N*,*N*,*N*-trimethylammonium-2-ethyl methacrylate iodide copolymer is the first use of a positively stabilised polymer to transfer nanocrystals. It was concluded that the best transfers were achieved using a 1:1 monomer ratio. This methodology was extended to include propargyl methacrylate to allow further attachment to the particle surface *via* click chemistry.[227]

Poly(*n*-butyl vinyl ether-*co*-maleic anhydride) synthesised by RAFT has been reported to transfer Fe_3O_4 using a two phase transfer procedure.[207] This is the shortest alkyl chain reported to transfer nanocrystals in commercial and custom synthesised polymers. The polymer was synthesised by RAFT and had an M_n of 4900.

Pendant phenyl groups

The only example of styrene containing custom synthesised polymers are poly(styrene-*alt*-maleic anhydride).[207] Two different polymer lengths, 2000 & 6500 g mol^{-1}, were used and it was found that the shorter polymer gave better phase transfer efficiencies.

4.1.3 Water transfer procedures

The most common procedure for water transfer was first used by Wu *et al.* in 2003[190] for modified poly(acrylic acid) polymers and was later demonstrated on poly(maleic anhydride-*alt*-1-alkene)s by Lin *et al.*[213] and Di Corato *et al.*[203] In brief, the nanocrystals and amphiphilic or pro-amphiphilic polymer are mixed in chloroform. The chloroform is

slowly remove *in vacuo* resulting in a thin glassy film of polymer and nanocrystals. An aqueous solution of nucleophile is added and is stirred or sonicated for approximately 12 h resulting in the transfer of the nanocrystals. This method has been used on a wide range of nanocrystals but does introduce quite a large excess of unbound polymer, which must be removed.

In 2006, the Colvin group developed a two-phase water transfer procedure.[201] Briefly, the nanocrystals and amphiphilic polymer were mixed in chloroform. A water phase was added. The two phase mixture had the chloroform slowly evaporated and nanocrystals become soluble in the water.

Lees *et al.* developed a transfer procedure, which is a rare example as it does not depend on the slow removal of chloroform *in vacuo*.[189] The lower chloroform phase contains the QDs and poly(styrene-*co*-maleic anhydride) or poly(maleic anhydride-*alt*-1-octadecene). The upper aqueous phase contained the nucleophile required to open the acid anhydride and impart water dispersability. The lower phase was stirred and over 12 h the particles were transferred. This method is a more sensitive to the type of particle being transferred and the surface ligands than polymers which have pendant alkyl chains.

A slight variant of the Wu *et al.* solvent evaporation method by Moros *et al.* involved the drying of the polymer to make a glassy film and then the addition of a small amount of chloroform to make a concentrated solution of polymer and nanocrystals. An aqueous solution of base was added and the mixture was shaken until the chloroform had evaporated and the particles had transferred.[209]

Park *et al.* used their custom-synthesised amphiphilic polymer to transfer oleic acid stabilised Fe_3O_4 from hexane to water. An emulsion between the polymer in water and the nanocrystals in hexane was formed and the hexane was allowed to evaporate causing the transfer of the nanocrystals.[225]

4.1.4 Cross-linking between polymer chains

An appealing feature of alternative techniques such as silica coating is that the nanocrystal is trapped in a cross-linked cage. This means that, unlike simple ligand exchange and amphiphilic bi-layers, dynamic processes do not play a role in the stability of the nanocrystal. In the case of amphiphiles, assembly occurs over a critical concentration. Amphiphilic molecules are in exchange between the assemblies and the free molecule.

In an attempt to trap the polymer wrapped around the surface of the nanocrystal, cross-linkers in the form of diamines have been used. It has been reported to have been achieved with lysine[190] and bis(6-aminohexyl)amine.[191,204] With cross-linking comes a risk of linking between nanocrystals when using cross-linkers. This can be reduced by performing the cross-linking at low nanocrystal concentrations. There is some debate if cross-linkers are necessary with longer amphiphilic polymers.[228] As the polymer has multiple intercalated alkyl chains, it is very unlikely all of these hydrophobic interactions would allow the release of the polymer.

4.2 Polymerisation methods used

4.2.1 Controlled Radical Polymerisation

The development of anionic polymerisation by Michael Szwarc demonstrated polymerisations where chain transfer and termination reactions are removed from the chain growth.[229] This opened the door to control of polymer structure previously not achieved. In an ideal living polymerisation, all the chains are initiated together, *i.e*. the rate of initiation, k_i, is much greater than the rate of propagation, k_p. Also, the propagation rate is similar and other processes such as chain transfer and termination, with a rate of k_t, don't exist.[230] The polymerisation can only end by depletion of the monomer. The molecular weight distribution is very narrow and approaches a Poisson distribution.

Radical polymerisation struggles to meet these criteria due to the likelihood of radicals terminating in the presence of one another. In radical polymerisation the rate of termination, k_t, is proportional to $[P_n^{\bullet}]^2$ whereas the rate of propagation, k_p, is proportional to $[P_n^{\bullet}]$.[231] As a consequence, the concentration of the propagating species, $P_n^{\bullet}$, must be low for polymerisation to occur. Radical polymerisation has many positive characteristics such as a greater tolerance to moisture and oxygen, a wide range of compatible monomers and the ability to be used in dispersed media (emulsions, microemulsions and so on). The main weaknesses of radical polymerisation are poor stereoselectivity, due to the free radical species being sp^2, and a relatively large polydispersity of the resulting polymer molecular weight. In an effort to achieve similar levels of control in free radical polymerisation to living polymerisations a range of Controlled Radical Polymerisation (CRP) techniques have been developed.

There exist two mechanistic types of CRP: a deactivation/activation process or a degenerative exchange process, Figure 4.4. Deactivation/activation works due to the Persistant Radical Effect (PRE). The PRE relies on a stable, or persistent, radical ($X_S^{\bullet}$), which can only terminate with a propagating radical ($P_n^{\bullet}$) and not another persistent radical ($X_S^{\bullet}$).[232] Propagating radicals ($P_n^{\bullet}$) are trapped in a deactivated state by a persistent radical ($X_S^{\bullet}$) with a rate constant k_{deact}. The dormant chain is reactivated, with a rate constant k_{act}, by light, thermally or by a catalyst. Other than the deactivation pathway the growing chain can terminate (k_t) and propagate (k_p). Every termination event (the combination of a pair of $P_n^{\bullet}$) generates two unbound persistent radicals ($X_S^{\bullet}$), which can not terminate with each other due to the PRE. This causes the concentration of the persistent radical ($X_S^{\bullet}$) to increase with time, following a $\frac{1}{3}$ power law. As the concentration of the persistent radical ($X_S^{\bullet}$) increases the probability of a propagating radical finding another propagating radical decreases and the probability of termination also decreases. Consequently a steady state of growing radicals is achieved through the activation/deactivation process.[233]

Degenerative exchange process-based CRP are not based on the PRE and instead rely on a transfer agent, Figure 4.4. Unlike deactivation/activation processes, initiation and termination processes establish a steady state concentration of radicals in the same manner

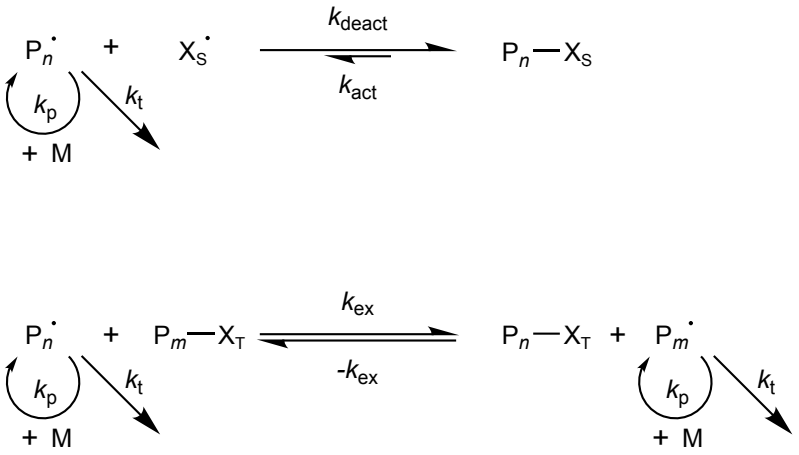

Figure 4.4: The two types of CRP mechanisms: deactivation/activation (top) and degenerative transfer (bottom). Where $X_S^{\bullet}$ is a stable radical and $X_T^{\bullet}$ is a transfer agent. Adapted from [233] Copyright (2007), with permission from Elsevier.

as conventional radical polymerisation. The degenerative exchange process depends on a thermodynamically-neutral transfer of one radical to the deactivated species and the release of another radical. Consequently, the equilibrium constant between the activated polymer chain and the deactivated chain should be 1. Typically, the concentration of the transfer agent is 100 times greater than that of the initiator resulting in the dormant chain transfer agent based species being dominant. At any one time, a small amount of propagating radicals undergo degenerative exchange with the dormant chain transfer based species. A short lived intermediate is formed during the exchange which plays an important role in the structure of the resulting polymer. The best control is achieved when the rate of propagation (k_p) is small compared to the rate of the exchange (k_{ex}), $k_p < k_{ex}$. If this is not the case, the transfer agent can retard the polymerisation, trap the radical or initiate growth of new chains.[233]

4.2.2 RAFT

The most widely used form of degenerative exchange-based CRP is RAFT.[234–236] The control is achieved using a RAFT agent, which is a carefully designed compound that deactivates the growing species. Figure 4.5 shows the general structure of a RAFT agent. A RAFT agent contains a double bond, which can readily react with the propagating radical, a weak A−R single bond, which releases $R^{\bullet}$, an alkyl radical, and a Z group, which allows control of addition and fragmentation rates to and from X and A. In most RAFT agents X and A are the same group of element, typically sulphur. This reduces differences in addition and fragmentation rates on both sides of the RAFT agent.

The process of RAFT polymerisation is shown in detail in Figure 4.6. RAFT is initiated by a standard radical initiator such as azobisisobutyronitrile (AIBN) resulting in $I^{\bullet}$. The radical propagates briefly, $P_n^{\bullet}$ and then reacts with the double bond of a RAFT agent forming an unstable intermediate with the radical located on the central carbon. At this stage the radical can be released in two ways. It can either release $P_n^{\bullet}$ once more or the R

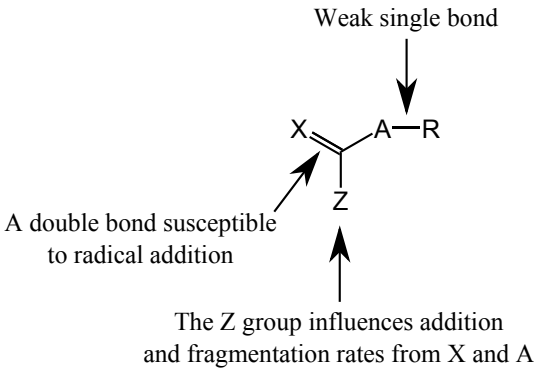

Figure 4.5: The general structure of a RAFT agent.

group can be released as a radical, $R^{\bullet}$. For RAFT to work, the probability of these two events occurring needs to be similar. $R^{\bullet}$ can propagate to form another propagating chain, $P_m{}^{\bullet}$. The most important stage for the growth of low molecular weight dispersity polymers is the chain equilibration. During chain equilibration, the polymer chains interchange on the RAFT agent, effectively taking turns to briefly polymerise monomers. When the monomers run out the likelihood of termination processes increases and propagating chains can terminate with one another.

Figure 4.6 gives the impression that there is an equal amount of growing species, P_n and dormant species attached to the RAFT agent. This is misleading since for successful RAFT the concentration of radicals needs to be kept very low so as to avoid termination processes. The dormant species is dominant and the final polymers have a high proportion of dormant RAFT agent at one chain end. At any one time the number of propagating species is small in comparison to the number of dormant chains.

Polymers made using RAFT have the R group of the RAFT agent used at the α-end and the dithiocarbamate and Z group at the ω-end. The R group is typically a branched alkane but the dithiocarbamate can undergo further chemistry. This can be useful if end functionalised polymers are required but can be a problem if sulphur containing functionalities are a concern. A range of techniques have been developed for RAFT agent ω-end group removal and modification and have recently been reviewed by Willcock and O'Reilly.[237]

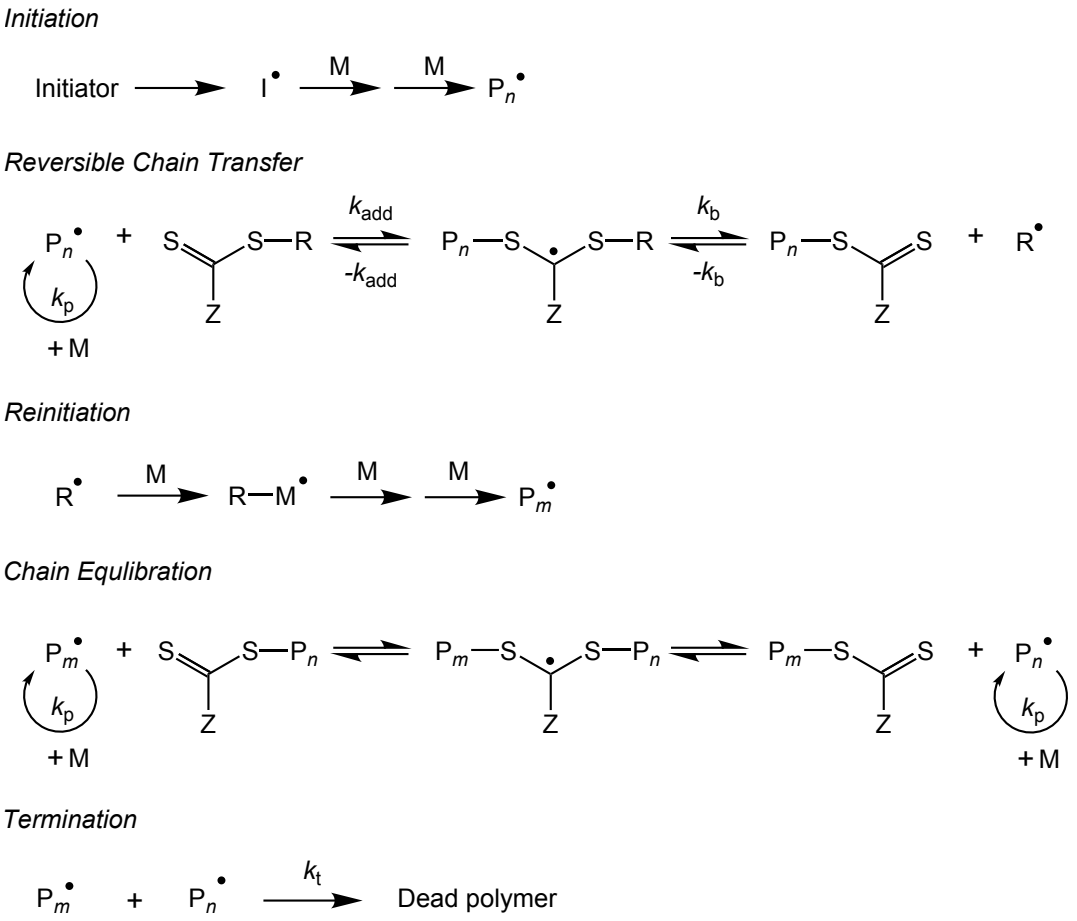

Figure 4.6: The key reactions that occur during RAFT polymerisation. Reprinted from [236] Copyright (2008), with permission from Wiley.

4.3 Proposed pro-amphiphilic and amphiphilic copolymers for nanocrystal stabilisation

In this work new families of amphiphilic and pro-amphiphilic polymers for the aqueous stabilisation of nanocrystals with hydrophobic ligands are proposed, Figure 4.7. The pro-amphiphilic polymers will contain active ester functionalities based upon readily reactive *N*-(hydroxy)succinimide leaving groups and the hydrophobic subunit is an alkyl acrylate. These groups allow total control of the method of stabilisation. If reacted with a poly(ethylene glycol) mono amine the particle would have steric stabilisation whereas base would bestow electrostatic stabilisation. A proportion of the active esters could be reacted with dyes, biomolecules or introduce many desired functionalities.

Current methodologies using maleic anhydride copolymers have an acid anhydride, also a form of activated ester. When this reacts with an amine an amide and a carboxylic acid is formed. If this carboxylic acid is to be removed reactions using carbodiimide chemistry are required. This method avoids the generation of a carboxylic acid and allows the user to control all of the surface functionality.

Also investigated are custom amphiphilc polymers that have poly(ethylene glycol) containing subunits, Figure 4.8. The copolymers of poly(ethylene glycol) containing monomers with alkylacrylates result in polymers that are amphiphilic before wrapping around the particle occurs. This is similar to octylamine modified poly(acrylic acid) in the sense that it is an amphiphilic polymer that requires no modification during the transfer process. A surface functionalised purely with poly(ethylene glycol) would have no potential sites of attachment for biomolecules. Bi-functional PEGs with leaving groups for further attachment are available but are expensive. It is envisaged that introducing a small proportion of active ester containing monomers would allow attachment of biomolecules.

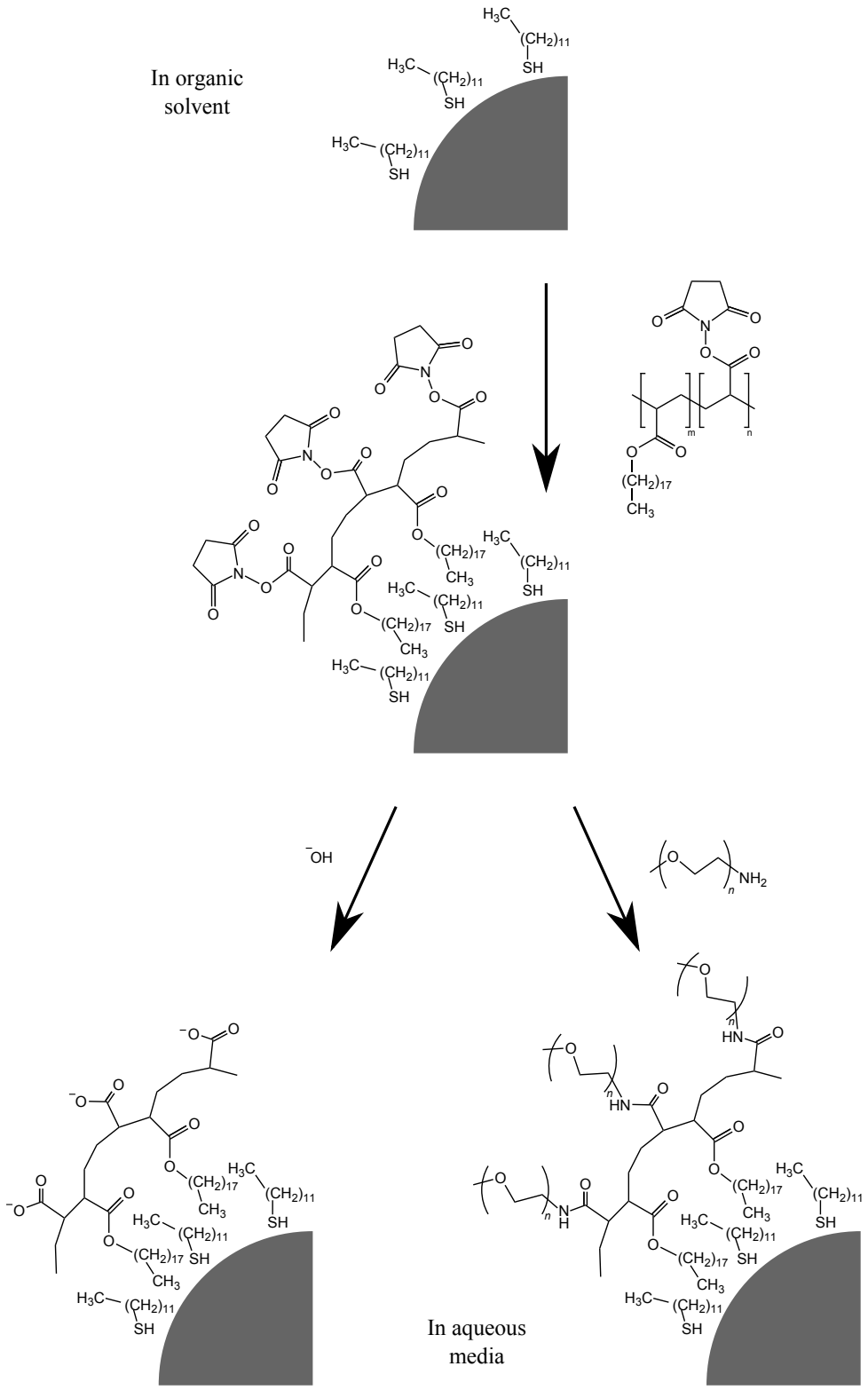

Figure 4.7: The proposed coating function of active ester copolymers. The routes to electrostatic (left) and steric (right) stabilisation are shown.

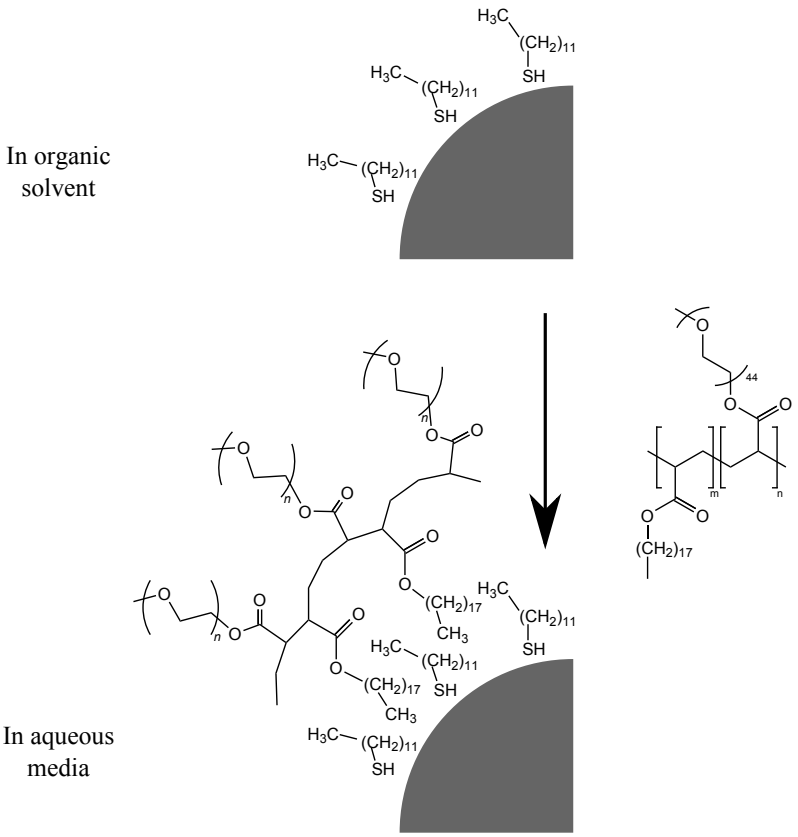

Figure 4.8: The proposed poly(ethyleneglycol) copolymer wrapping a dodacanethiol stabilised nanocrystal.

4.4 Polymer characterisation techniques

4.4.1 Nuclear magnetic resonance spectroscopy

Nuclear Magnetic Resonance (NMR) spectroscopy allows structural determination of compounds that contain NMR active nuclei. The nuclei are NMR active if they possess a non-zero spin. Commonly probed elements are ^{1}H and ^{13}C, although isotopes of elements such as nitrogen, fluorine, silicon, phosphorous can also be used.

In a permanent magnetic field, NMR active nuclei absorb radio waves at values characteristic to the isotope probed. Subtle variations in the frequency absorbed are caused by changes in the local environment experienced by nuclei, causing the element to become shielded or deshielded and are known as chemical shifts. Nuclei that are close, to one another in space, experience spin - spin coupling, specifically J-coupling, giving rise to a resonance peak being split. Splitting patterns are characteristic of which elements are coupled and the number of elements and are a powerful tool to elucidate structural information.

In this work only one-dimensional spectra are used to confirm the structure of synthesised monomers and to analyse the composition of the polymers produced. The ^{1}H spectra of copolymers are used to determine the ratio of monomers incorporated.

The measurements were performed on two different spectrometers. The copolymers

of *N*-(acryloyloxy)succinimide were measured using a Varian UNITY plus 400 MHz spectrometer with a 5 mm inverse detect broad band z-gradient probe. The copolymers of acryloyloxy poly(ethylene glycol) monomethyl ether were measured using a Bruker Avance III 500 MHz spectrometer with a 5 mm broad band observe BBFO plus smart probe™ fitted with an actively shielded z-gradient coil.

4.4.2 Gel permeation chromatography

Gel Permeation Chromatography (GPC) is used to characterise the molecular weight of polymers. The technique is a variant of high pressure liquid chromatography where the column contains a porous packing material, the stationary phase. The polymer in a suitable solvent, the mobile phase, is passed through the column. Shorter polymers are able to penetrate the porous stationary phase to a greater extent than longer polymers. This results in shorter polymers being retained for longer due to the larger accessible volume. A chromatogram will typically contain a series of peaks with the longest polymer being the first peak and the shortest being the last.

In this work the detector used observes changes in refractive index and is not capable of measuring absolute molecular weights. As a consequence, polymer standards are used to allow molecular weights relative to the standard to be determined. A range of poly(styrene) molecular weights are used.

The instrument used was a Polymer Labs GPC 220 with a refractive index detector. The column used was a 300×7.5 mm Mixed-C Pigel 5 µm.

4.5 Monomer synthesis

4.5.1 *N*-(Acryloyloxy)succinimide

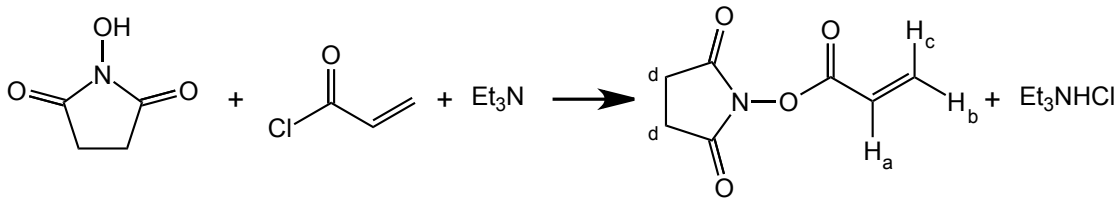

Figure 4.9: The reaction to produce *N*-(acryloyloxy)succinimide.

The following procedure was adapted from the work of G. M. Whitesides research group.[238,239] *N*-(Hydroxy)succinimide (10.19 g, 88.6 mmol, Aldrich, 98 %) and triethylamine (9.86 g, 97.5 mmol, Aldrich, 99.5 %) were dissolved in chloroform (200 ml, Fisher Scientific, >99 %). The solution was cooled to 0 °C and acryloyl chloride (8.02 g, 88.6 mmol, Aldrich, ≥97 %) in chloroform (60 ml) was added drop wise over 20 min to the stirred chloroform solution. The reaction was left to complete overnight whilst slowly being allowed to warm to room temperature. The solution was washed twice with water (300 ml

per wash) and once with brine (300 ml). The chloroform reaction mixture was dried over $MgSO_4$. The dried solution had the chloroform removed by rotary evaporator leaving a pale yellow solution. A 1:1 mixture of ethyl acetate and hexane (30 ml) was added to the yellow solution. Nucleation was started by the addition of hexane and the mixture was chilled overnight resulting in colourless crystals of *N*-(acryloyloxy)succinimide (NAS). The crystals were filtered, washed with an ice cold 4:1 mixture of *n*-hexane and ethylacetate (100 ml) and again with a 9:1 mixture of *n*-hexane and ethylacetate (100 ml). Finally, the crystals were washed with two portions of *n*-hexane (100 ml) and dried *in vacuo*. yield: 9.6 g colourless crystals (56.8 mmol, 64.1 %). ^{1}H-NMR (400 MHz, $CDCl_3$): δ (ppm) = 6.71 (H_c, dd, 1 H, $^3J(ac) = 17.29$ Hz, $^2J(bc) = 0.93$ Hz), 6.33 (H_a, dd, 1 H, $^3J(ac) = 17.29$ Hz, $^3J(ab) = 10.69$ Hz), 6.17 (H_b, dd, 1 H, $^3J(ab) = 10.69$ Hz, $^2J(bc) = 0.93$ Hz). 2.86 (H_d, s, 4 H).

4.5.2 Acryloyloxy poly(ethylene glycol) monomethyl ether, n = 44

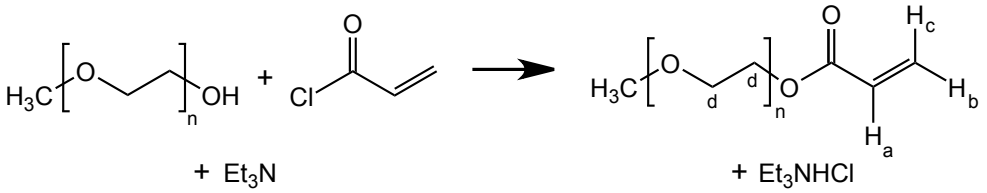

Figure 4.10: The reaction to produce acryloyloxy poly(ethylene glycol) monomethyl ether.

Poly(ethylene glycol) monomethylether (19.43 g, 9.73 mmol, $M_w = 2000\,\mathrm{g\,mol^{-1}}$, Fluka) and triethylamine (1.63 g, 16.07 mmol, Aldrich, 99.5 %) were dissolved in dichloromethane (200 ml). The solution was cooled to 0 °C and a solution of acryloyl chloride (1.32 g, 14.60 mmol, Aldrich, $\geq$97 %) in dichloromethane (20 ml) was added drop wise over 20 min to the stirred dichloromethane solution over 20 min. The reaction was left to complete overnight whilst slowly being allowed to warm to room temperature. The chloroform was removed by rotary evaporation and the compound was further dried using a Schlenk line and an in-line trap until the weight became constant.

The ratio of moles of poly(ethylene glycol) to acryloyl chloride and triethylamine was 1:1.5:1.65. An increased excess of acryloyl chloride and triethylamine was used to encourage a higher amount of successful reactions as it is difficult to separate unreacted poly(ethylene glycol) monomethyl ether and acryloyloxy poly(ethylene glycol) monomethyl ether (APEGm). Any unreacted acryloyl chloride and triethylamine is removed during the drying stage. yield: 15.13 g colourless powder (7.36 mmol, 75.7 %). ^{1}H-NMR (400 MHz, $CDCl_3$): δ (ppm) = 6.44 (H_c, dd, 1 H, $^3J(ac) = 17.34$ Hz, $^2J(bc) = 1.47$ Hz), 6.15 (H_a, dd, 1 H, $^3J(ac) = 17.34$ Hz, $^3J(ab) = 10.42$ Hz), 5.83 (H_b, dd, 1 H, $^3J(ab) = 10.42$ Hz, $^2J(bc) = 1.48$ Hz), 3.64 (H_d, s).

4.6 *N*-(acryloyloxy)succinimide copolymers

4.6.1 Poly(*N*-(acryloyloxy)succinimide-*co*-styrene)

4.6.1.1 RAFT polymerisation

In a typical polymerisation *N*-(acryloyloxy)succinimide (0.4 g, 0.2 mmol) and styrene (Sty) (170.4 µl, 1.47 mmol, Sigma-Aldrich, ≥99 %, were dissolved in 1,4-dioxane (4 ml, Sigma-Aldrich, ≤99 %), dried with molecular sieves. 2-cyano-2-propyl dodecyl trithiocarbamate (27.4 µl, 0.08 mmol, Aldrich, 97 %) and 1,1'-azobis(cyclohexanecarbonitrile) (2.17 mg, 0.008 mmol, Aldrich, 98 %) were added to the solution. The solution was degassed by passing argon through for 8 min and a reservoir was filled with argon to maintain a slight positive pressure in the reaction vessel. The solution was stirred and heated at 90 °C for 7 h. The solution was allowed to cool and the product was precipitated using 40–60 °C petroleum ether (20 ml, Sigma-Aldrich). The precipitate was collected by centrifugation and the 1,4-dioxane discarded. To remove any unreacted monomer, the precipitate was redissolved in THF and precipitated with petroleum ether. The precipitate was collected by centrifugation at 2800 × *g* for 5 min. The supernatent was discarded and residual solvent left to evaporate.

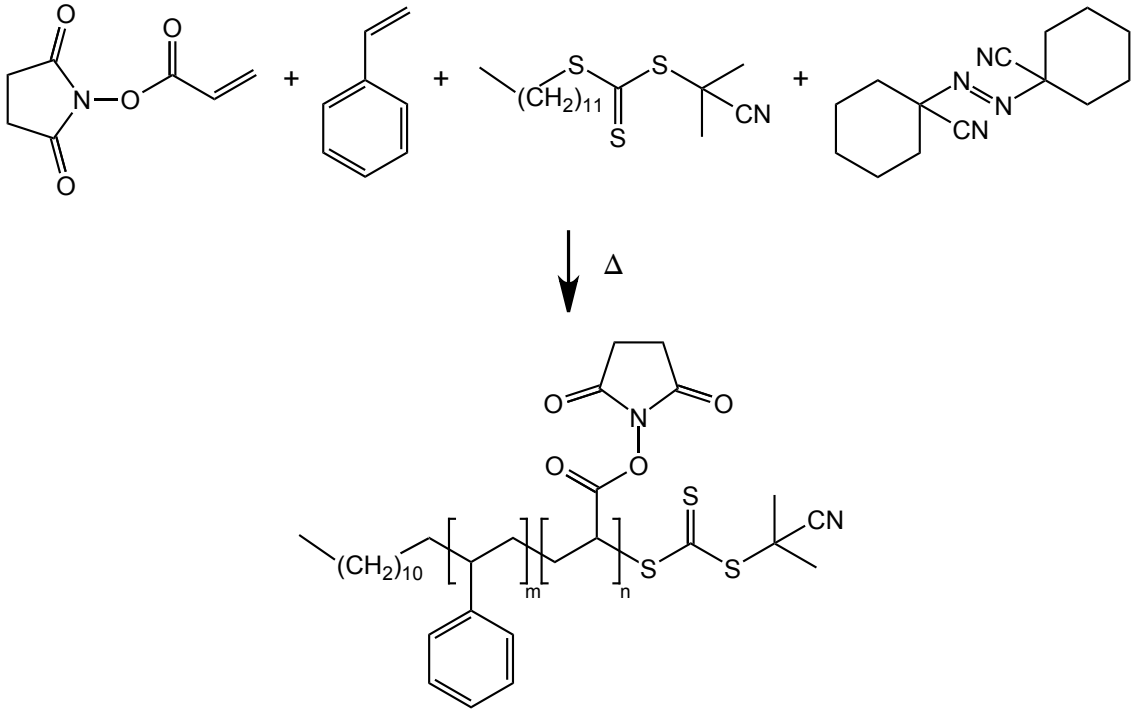

Figure 4.11: The reaction to produce poly(*N*-(acryloyloxy)succinimide-*co*-styrene)

The molecular weight was controlled by variation of the amount of RAFT agent used as documented in Tables 4.1 to 4.3. Increasing the amount of RAFT agent decreased the length of the resulting polymer. poly(*N*-(acryloyloxy)succinimide-*co*-styrene) polymers were synthesised with three target monomer ratios of styrene to *N*-(acryloyloxy)succinimide: 1:1, 2:1 and 3:1. Exploring different monomer ratios is a response to the commercial

polymers having varying monomer compositions. The majority of commercial polymers used are alternating copolymers and hence have a 1:1 monomer ratio. Poly(styrene-*co*-maleic anhydride) is the only commercial random copolymer that has been used to transfer nanocrystals and has a monomer ratio of approximately 2:1 styrene to maleic anhydride. Hence a range of monomer ratios have been explored for the copolymers of styrene. The target polymer lengths varied from 2000 to 50,000 g mol^{-1} to cover the range of poly(styrene-*co*-maleic anhydride) ($M_n = 1700\,\mathrm{g\,mol^{-1}}$) and poly(maleic anhydride-*alt*-1-octadecene) ($M_n = 30{,}000 - 50{,}000\,\mathrm{g\,mol^{-1}}$) that has been shown to transfer nanocrystals.

Table 4.1: Amounts of reagents used to control the molecular weight of the poly(*N*-(acryloyloxy)succinimide-*co*-styrene) polymers produced for a 1:1 monomer ratio.

Target molecular weight / g mol^{-1}	**Amount of reagents used**			
	NAS / µmol	**Sty / µmol**	**RAFT agent / µmol**	**Initiator / µmol**
2000	998	1336	196	22
5000	1109	1337	79	9
10,000	1146	1337	39	7
15,000	1159	1337	26	3
20,000	1164	1337	20	2
50,000	1176	1336	8	1

Table 4.2: Amounts of reagents used to control the molecular weight of the poly(*N*-(acryloyloxy)succinimide-*co*-styrene) polymers produced for a 2:1 monomer ratio.

Target molecular weight / g mol^{-1}	**Amount of reagents used**			
	NAS / µmol	**Sty / µmol**	**RAFT agent / µmol**	**Initiator / µmol**
2000	665	1778	196	22
5000	739	1976	79	9
10,000	764	2043	39	5
15,000	772	2064	26	3
20,000	778	2076	20	2
50,000	784	2095	8	1

Table 4.3: Amounts of reagents used to control the molecular weight of the poly(*N*-(acryloyloxy)succinimide-*co*-styrene) polymers produced for a 3:1 monomer ratio.

Target molecular weight / g mol^{-1}	Amount of reagents used			
	NAS / µmol	Sty / µmol	RAFT agent / µmol	Initiator / µmol
2000	499	2001	196	22
5000	554	2223	79	9
10,000	573	2297	39	5
15,000	579	2323	26	3
20,000	582	2335	20	2
50,000	588	2357	8	1

4.6.1.2 Polymer characterisation

Polymers were characterised using GPC and NMR and the results are shown for the 1:1 monomer ratio in Table 4.4. The polymerisations performed delivered polymers that were all below the target molecular weight but still in the range of the commercial polymers used. The use of RAFT produced polymers with small polydispersity index (PDI) values between 1.07 and 1.31. Monomer ratios, as characterised by NMR, are close to the intended values and the NMR spectrum had characteristic broad peaks associated with protons in macromolecules, Figure 4.12. The polymer lengths were much shorter than expected. As the GPC standards were poly(styrene), the values are a good indication that the polymers are much below their target values.

Similar conclusions about polydispersity can be drawn from the characterisation of the 2:1 series of polymers as were found with the 1:1 series as shown in Table 4.5. Again the polymer lengths are shorter than expected although they are marginally closer than the 1:1 series. The most notable result is that the monomer ratios are distinctly different from the 2:1 target with a final ratio of approximately 1.4:1 across the series.

The results from the 3:1 series are shown in Table 4.6 have the same qualities as the 2:1 series. Once more the monomer ratio and length fall short of the targets. The final monomer ratio was approximately 1.88:1 which indicates that the *N*-(acryloyloxy)succinimide and styrene don't react at the same rates with one another.

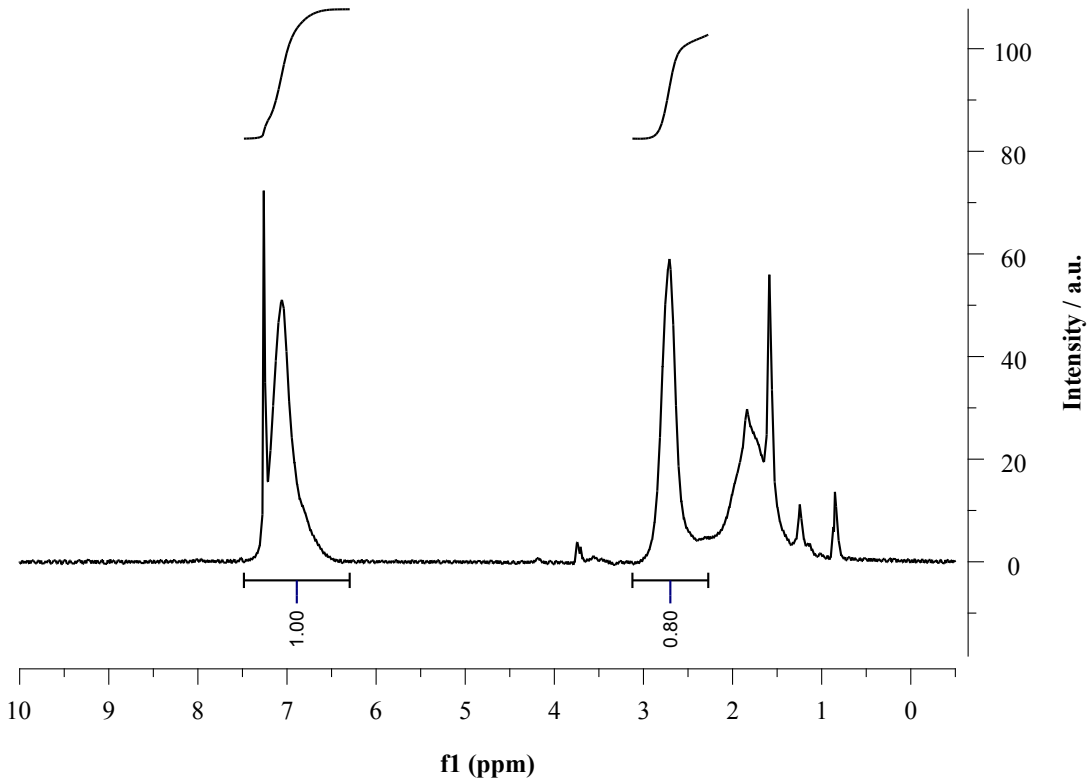

Figure 4.12: An example NMR spectrum of a poly(*N*-(acryloyloxy)succinimide-*co*-styrene) 1:1 target monomer ratio. The regions integrated to determine the monomer ratio are shown.

Table 4.4: Data for the poly(*N*-(acryloyloxy)succinimide-*co*-styrene) polymers with a 1:1 target monomer ratio.

Target molecular weight / g mol^{-1}	M_n / g mol^{-1}	M_w / g mol^{-1}	PDI	Monomer ratio NAS:Sty	Yield (%)
2000	1110	1190	1.07	1:1.11	18.8
5000	2700	3120	1.16	1:1.01	70.3
10,000	4480	5510	1.23	1:0.99	68.1
15,000	5580	6970	1.25	1:1.00	64.3
20,000	5570	7280	1.31	1:0.99	68.2
50,000	6990	8980	1.28	1:0.96	57.8

Table 4.5: Data for the poly(*N*-(acryloyloxy)succinimide-*co*-styrene) polymers with a 2:1 target monomer ratio.

Target molecular weight / g mol^{-1}	M_n / g mol^{-1}	M_w / g mol^{-1}	PDI	Monomer ratio NAS:Sty	Yield (%)
2000	1120	1240	1.11	1:1.29	8.6
5000	2650	3060	1.15	1:1.15	50.9
10,000	3740	4510	1.21	1:1.36	52.7
15,000	5530	6860	1.24	1:1.51	55.9
20,000	6210	8380	1.35	1:1.48	48.3
50,000	8360	11,600	1.39	1:1.45	57.6

Table 4.6: Data for the poly(*N*-(acryloyloxy)succinimide-*co*-styrene) polymers with a 3:1 target monomer ratio.

Target molecular weight / g mol^{-1}	M_n / g mol^{-1}	M_w / g mol^{-1}	PDI	Monomer ratio NAS:Sty	Yield (%)
5000	2320	2610	1.13	1:1.78	-
10,000	3790	4630	1.22	1:1.82	46.7
15,000	5360	6710	1.25	1:1.95	47.1
20,000	5960	7850	1.32	1:1.90	45.8
50,000	7350	10,200	1.39	1:1.86	48.1

4.6.1.3 Phase transfer testing

Water transfer testing was performed using the method of mixing the hydrophobic nanocrystals and the pro-amphiphilic polymer in a common solvent and the solvents slow removal to form a film. An aqueous solution of nucleophile was added and the film slowly reacted releasing the amphiphilic polymer coated nanocrystals. A given batch of Fe_3O_4 was water-transferred using poly(maleic anhydride-*alt*-1-octadecene) to determine the amount of poly(*N*-(acryloyloxy)succinimide-*co*-styrene) used.

In a typical water transfer test, 200 µl of a stock solution of oleic acid stabilised Fe_3O_4, as synthesised in Section 2.2.2, were precipitated using an excess of ethanol (Sigma-Aldrich, $\geq$99.8 %) and were redispersed in $CHCl_3$ (1 ml, Fisher Scientific, >99 %). A solution of the polymer being tested was made using 20 mg of the polymer dissolved in $CHCl_3$. The polymer was stirred in $CHCl_3$ for 20 min to allow it to solvate completely. The nanocrystal and polymer solutions were combined and allowed to mix for 5 min. By rotary evaporation, the $CHCl_3$ was slowly removed over the course of 30 min. To ensure maximum removal of $CHCl_3$ the sample was further dried using a Schlenk line under vacuum for 30 min. A solution of tetramethylammonium hydroxide pentahydrate (5 ml, 0.044 mol dm^{-3}, Sigma-Aldrich, $\geq$97 %) was added to the dry film. The solution was left overnight and the nanocrystals water transfer was assessed.

The procedure is the same for all poly(*N*-(acryloyloxy)succinimide-*co*-styrene) tested in this section. All particles were tested with the same batch of nanocrystals. Fe_3O_4 was chosen as the nanocrystal to transfer because the RAFT agent end group will not bind to the surface as with AuNPs or QDs. The end group would be removed before use with AuNPs or QDs but for the purpose of testing many polymers this was deemed unnecessary.

Table 4.7 shows the phase transfer results for the 1:1 monomer ratio poly(*N*-(acryloyloxy)succinimide-*co*-styrene) with Fe_3O_4. The longer polymers were unable to transfer the nanocrystals and below a target length of 5000 g mol^{-1} partial transfers were achieved, Figure 4.13. Undispersed nanocrystals had a sand-like appearance forming small grains. A measure of particle transfer completion was made by comparing the absorbance in the UV-visible region against particles fully transferred with poly(maleic anhydride-*alt*-1-octadecene) showing both of the low molecular weight polymers transferred over 65 %. The

results from DLS measurements showed multiple peaks, which is normal for commercial polymers before purification, as can be seen in Figure 4.14. The peaks between 30 and 50 nm are likely to be from individual coated nanocrystals. The remaining peaks are suspected to be from unbound polymer in assemblies or single chains. DLS measurements of multi-modal samples are difficult to extract information from and absolute numbers are not trustworthy. If the assumption of some peaks being from structures consisting purely of polymer is correct the refractive index used for the nanocrystal will not be suitable for analysing these regions.

Table 4.7: Water transfer results for iron oxide nanocrystals transferred using poly(*N*-(acryloyloxy)succinimide-*co*-styrene) with a 1:1 target monomer ratio, where N represents no transfer, P represents a partial transfer and F represents a full transfer.

Target molecular weight / g mol^{-1}	**Transfer**	**Percentage Transfer Using A at 470 nm (%)**	**Z-average diameter, *d* / nm**	***d* values from CONTIN / nm**
2000	P	65	59.9	5.6, 32.6, 164.2
5000	P	81	160.9	43.8, 295.3
10,000	N	-	-	-
15,000	N	-	-	-
20,000	N	-	-	-
50,000	N	-	-	-

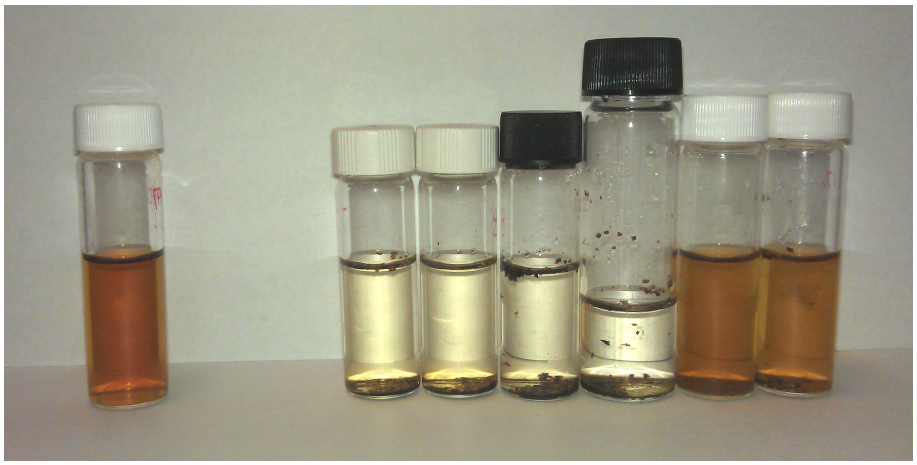

Figure 4.13: A photo showing a complete transfer poly(maleic anhydride-*alt*-1-octadecene) (left) and the attempted water transfers using poly(*N*-(acryloyloxy)succinimide-*co*-styrene) with a 1:1 target monomer ratio (right). The series increases in molecular weight from right to left.

The 2:1 poly(*N*-(acryloyloxy)succinimide-*co*-styrene) based transfers followed a similar pattern to the 1:1 polymers, Table 4.8. Shorter polymers transferred nanocrystals better but did not achieve complete transfer, Figure 4.15. The DLS results for the 2000 g mol^{-1} target polymers had a promising size profile with a peak with a diameter of 18.2 nm and a transfer of 75 %. An example DLS profile is shown in Figure 4.16.

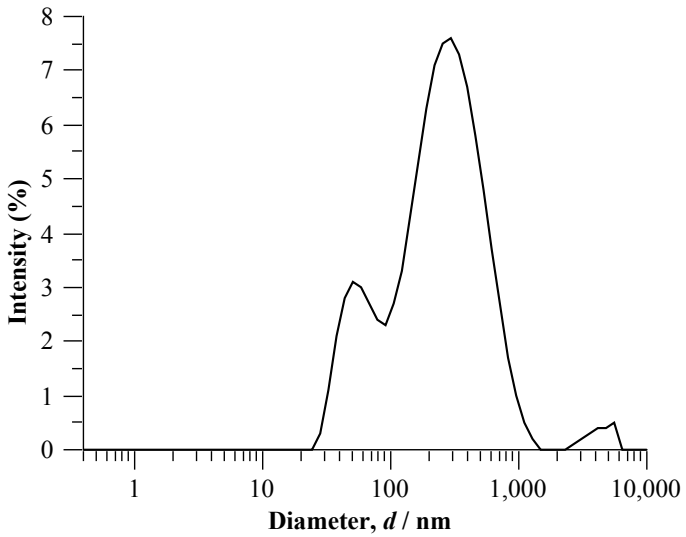

Figure 4.14: The DLS profile of transferred Fe_3O_4 using poly(*N*-(acryloyloxy)succinimide-*co*-styrene) with a 1:1 target monomer ratio and target molecular weight of 5000 g mol^{-1}.

Table 4.8: Water transfer results for iron oxide nanocrystals transferred using poly(*N*-(acryloyloxy)succinimide-*co*-styrene) with a 1:2 target monomer ratio, where N represents no transfer, P represents a partial transfer and F represents a full transfer.

Target molecular weight / g mol^{-1}	Transfer	Percentage Transfer Using A at 470 nm (%)	Z-average diameter, *d* / nm	*d* values from CONTIN / nm
2000	P	75	154.1	18.2, 58.8
5000	P	12	88.1	91.3
10,000	N	-	-	-
15,000	N	-	-	-
20,000	N	-	-	-
50,000	N	-	-	-

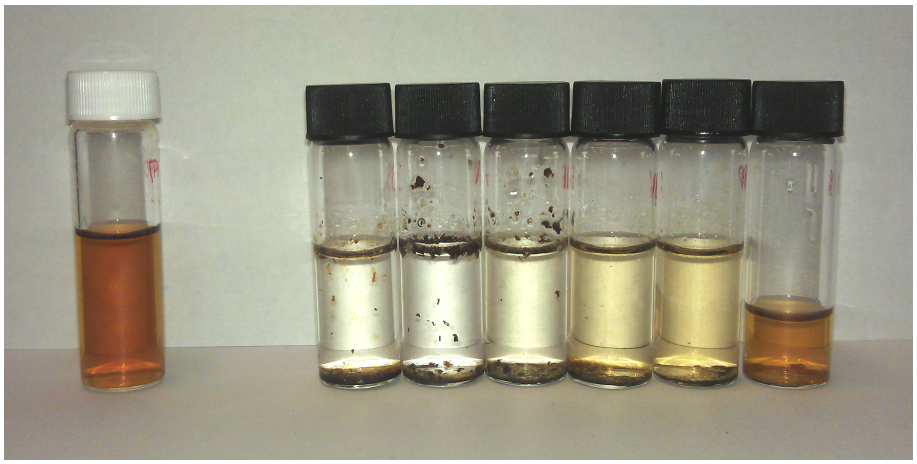

Figure 4.15: A photo showing a complete transfer poly(maleic anhydride-*alt*-1-octadecene) (left) and the attempted water transfers using poly(*N*-(acryloyloxy)succinimide-*co*-styrene) with a 2:1 target monomer ratio (right). The series increases in molecular weight from right to left.

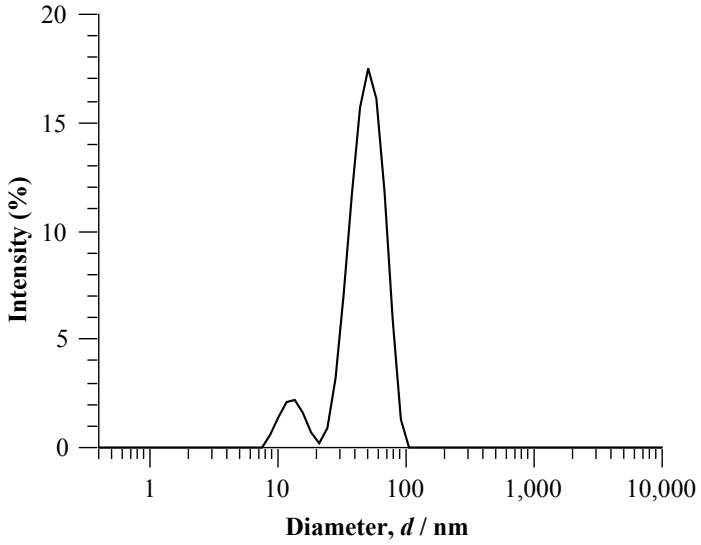

Figure 4.16: The DLS profile of transferred Fe_3O_4 using poly(*N*-(acryloyloxy)succinimide-*co*-styrene) with a 1:2 target monomer ratio and target molecular weight of 2000 g mol^{-1}.

The transfer abilities of the polymers follow a similar pattern to the other monomer ratios as shown in Table 4.9 and Figures 4.17 and 4.18. In the case of 3:1 poly(*N*-(acryloyloxy)succinimide-*co*-styrene) the 2000 g mol^{-1} target polymer was not possible to collect after synthesis. As a consequence this series of polymers appears worse than the other ratios.

Table 4.9: Water transfer results for iron oxide nanocrystals transferred using poly(*N*-(acryloyloxy)succinimide-*co*-styrene) with a 1:3 target monomer ratio, where N represents no transfer, P represents a partial transfer and F represents a full transfer.

Target molecular weight / g mol^{-1}	**Transfer**	**Percentage Transfer Using A at 470 nm (%)**	**Z-average diameter, *d* / nm**	***d* values from CONTIN / nm**
5000	P	40	44.9	50.75
10,000	P	5	110.2	18.17, 68.06
15,000	N	-	-	-
20,000	N	-	-	-
50,000	N	-	-	-

Partial transfers have been achieved with poly(*N*-(acryloyloxy)succinimide-*co*-styrene). The transfer abilities improve with decreasing polymer length. In the case of the 2000 g mol^{-1} target polymers the actual molecular weight is 1120 g mol^{-1}, which corresponds to an average of 6.7 monomers per chain. This means that the polymers are so short they could be thought of as being sophisticated surfactants and not polymers. As the majority of successful commercial polymers use alkyl chains for the hydrophobic interaction with the nanocrystal ligands, polymers containing *N*-(acryloyloxy)succinimide and pendant alkyl functionality were explored next in an attempt to have a complete transfer.

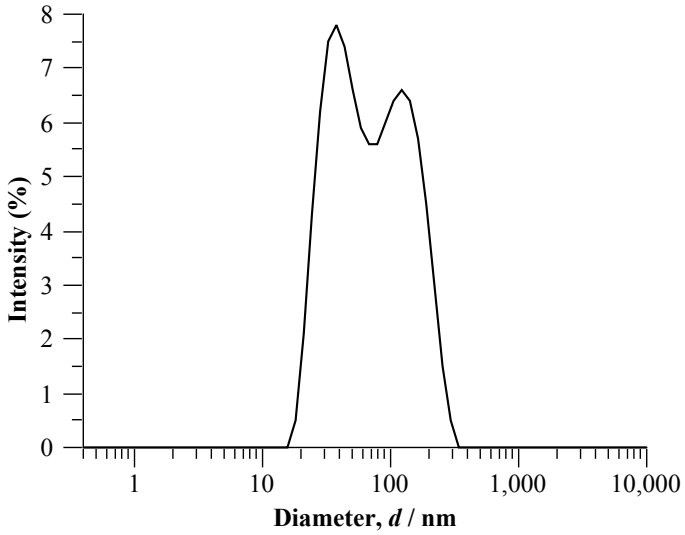

Figure 4.17: The DLS profile of transferred Fe_3O_4 using poly(*N*-(acryloyloxy)succinimide-*co*-styrene) with a 1:3 target monomer ratio and target molecular weight of 10,000 g mol^{-1}.

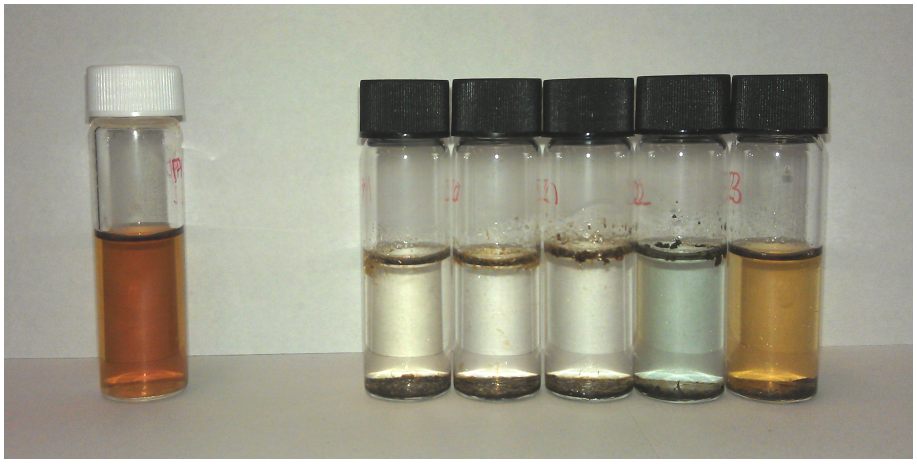

Figure 4.18: A photo showing a complete transfer poly(maleic anhydride-*alt*-1-octadecene) (left) and the attempted water transfers using poly(*N*-(acryloyloxy)succinimide-*co*-styrene) with a 3:1 target monomer ratio (right). The series increases in molecular weight from right to left.

4.6.2 Poly(*N*-(acryloyloxy)succinimide-*co*-octadecyl acrylate)

4.6.2.1 RAFT polymerisation

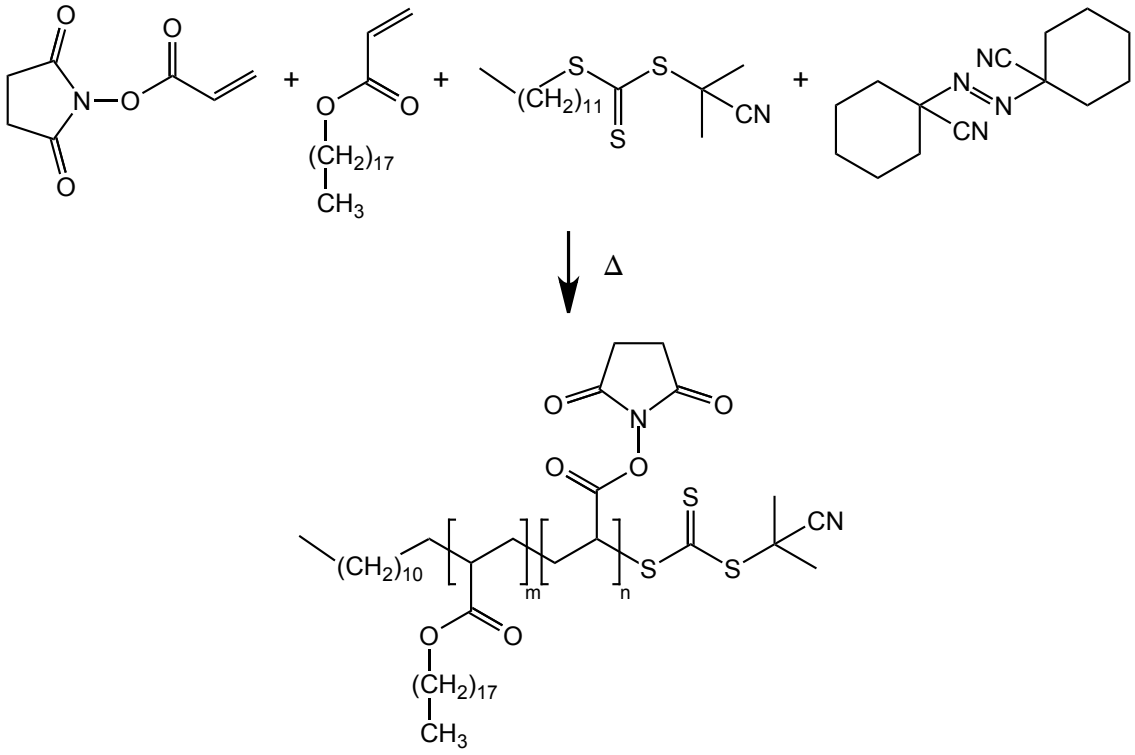

Figure 4.19: The reaction to produce poly(*N*-(acryloyloxy)succinimide-*co*-octadecyl acrylate)

In a typical polymerisation *N*-(acryloyloxy)succinimide (168.7 mg, 998.1 µmol) and octadecylacrylate (ODA) (168.7 mg, 519.8 µmol, Aldrich, 97 %, were dissolved in 1,4-dioxane (5 ml, Sigma-Aldrich, $\leq$ 99 %) , dried with molecular sieves. 2-cyano-2-propyl dodecyl trithiocarbamate (68.5 µl, 196.4 µmol, Aldrich, 97 %) and 1,1'-azobis(cyclohexanecarbonitrile) (5.4 mg, 22.1 µmol, Aldrich, 98 %) were added to the solution. The solution was degassed by passing argon through for 8 min and a reservoir was filled with argon to maintain a slight positive pressure in the reaction vessel. The solution was stirred and heated at 93 °C for 7 h.

The solution was allowed to cool and the product precipitated using acetonitrile (40 ml, Sigma-Aldrich). The precipitate was collected by centrifugation and the supernatant was discarded. To remove any unreacted monomer the precipitate was redisolved in THF and reprecipitated with acetonitrile. The precipitate was collected by centrifugation, the solvent was discarded and residual solvent was left to evaporate.

The molecular weight was controlled by variation of the amount of RAFT agent used, Table 4.10. A greater amount of RAFT agent resulted in shorter polymers. Due to the similarities of water transfer abilities of the poly(*N*-(acryloyloxy)succinimide-*co*-styrene) polymers of various ratios in Section 4.6.1.3 a single monomer ratio of 1:1 was chosen. All of the commercial maleic anhydride copolymers have a 1:1 monomer ratio, which also suggests it is a sensible ratio to use. The actual monomer ratio used was 1:0.53

N-(acryloyloxy)succinimide to octadecylacrylate due to an calculation error.

Table 4.10: Amounts of reagents used to control the molecular weight of the poly(*N*-(acryloyloxy)succinimide-*co*-octadecyl acrylate) polymers produced.

Target molecular weight / g mol^{-1}	Amount of reagents used			
	NAS / µmol	ODA / µmol	RAFT agent / µmol	Initiator / µmol
5000	1109	596	79	9
10,000	1146	615	39	4
20,000	1165	625	20	2
50,000	1176	631	8	1
75,000	1178	633	5	0.6
100,000	1180	633	4	0.4

4.6.2.2 Polymer characterisation

The properties of the poly(*N*-(acryloyloxy)succinimide-*co*-octadecyl acrylate) polymers synthesised are collected in Table 4.11. The NMR spectra showed broadened peaks from the monomers with an example spectrum in Figure 4.20. In light of the target ratio of 1:0.53 the reported values are reasonably close to the target suggesting the monomers react similarly with each other. The molecular weights are far short of the target values. As these polymers do not contain styrene the use of polystyrene standards when performing GPC means that the molecular weights collected allow relative comparison but not absolute. Even taking this into account the discrepancy between target and reported values is still large suggesting too much RAFT agent or initiator was used. This is commonly encountered with RAFT polymerisations, however, and the technique is generally used to produce low molecular weight polymers and blocks, where molecular weight and PDI remain well controlled.

Table 4.11: Data for the poly(*N*-(acryloyloxy)succinimide-*co*-octadecyl acrylate) polymers.

Target molecular weight / g mol^{-1}	M_n / g mol^{-1}	M_w / g mol^{-1}	PDI	Monomer ratio NAS:ODA	Yield (%)
5000	4500	5570	1.24	1:0.67	32.6
10,000	6370	8340	1.31	1:0.60	47.7
20,000	7810	10,900	1.39	1:0.62	46.5
50,000	8810	12,800	1.45	1:0.60	49.7
75,000	7370	10,100	1.38	1:0.59	42.0
100,000	8220	12,100	1.47	1:0.57	45.8

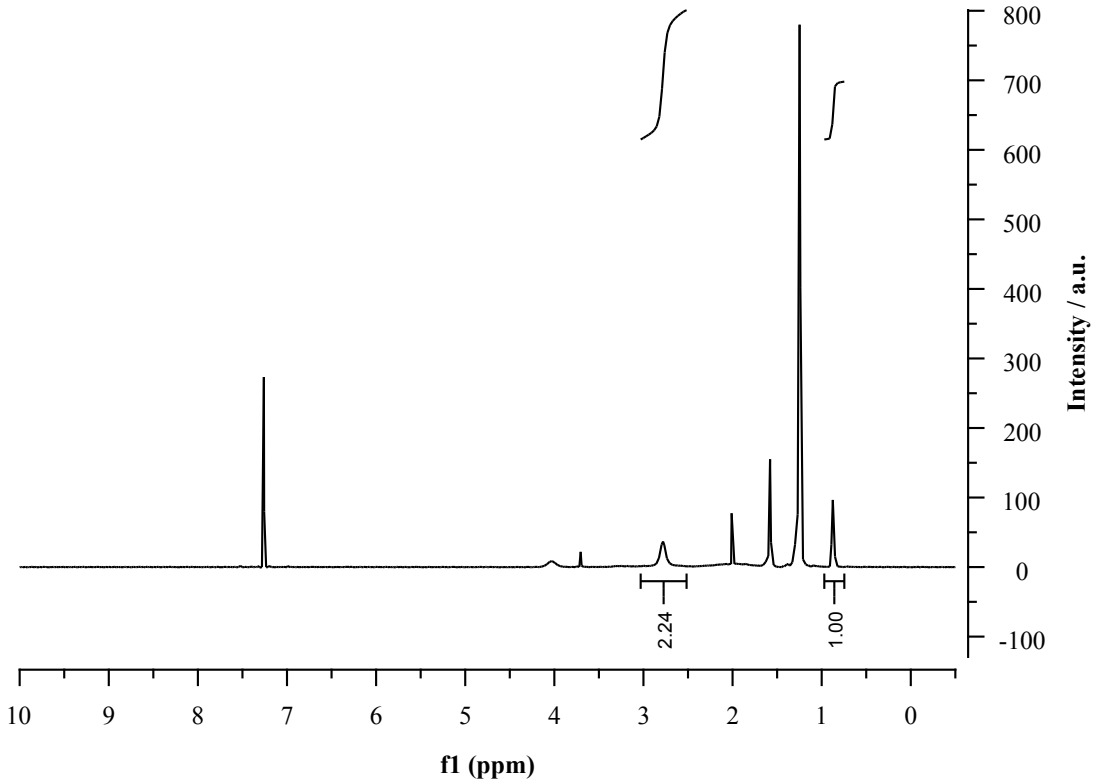

Figure 4.20: An example NMR spectrum of a poly(*N*-(acryloyloxy)succinimide-*co*-octadecylacrylate) with a 1:1 target monomer ratio. The regions integrated to determine the monomer ratio are shown.

4.6.2.3 Phase transfer testing

The method for testing the ability of the synthesised poly(*N*-(acryloyloxy)succinimide-*co*-octadecyl acrylate) polymers was identical to that for poly(*N*-(acryloyloxy)succinimide-*co*-styrene) in Section 4.6.1.3. The amount to use was identical to poly(*N*-(acryloyloxy)succinimide-*co*-styrene) as the same batch of particles was used. None of the poly(*N*-(acryloyloxy)succinimide-*co*-octadecyl acrylate) polymers resulted in any transfer, Table 4.18. The dried mixture of polymer and nanocrystal did not form a thin glass like film as with poly(maleic anhydride-*alt*-1-octadecene). A thicker layer was formed, which did not appear to undergo any change after being introduced to the nucleophile solution.

The polymers did not transfer the nanocrystals. Possible reasoning could be due to using a pendant alkyl chain that is too long, the commercial octadecene copolymer has a pendant alkyl chain with 16 carbons. The ratio of octadecylacrylate could also be too low relative to the poly(*N*-(acryloyloxy)succinimide, resulting in not enough alkyl groups to interact with the nanocrystal ligands.

Table 4.12: Water transfer results for iron oxide nanocrystals transferred using poly(*N*-(acryloyloxy)succinimide-*co*-octadecylacrylate) with a 1:1 target monomer ratio, where N represents no transfer, P represents a partial transfer and F represents a full transfer.

Target molecular weight / g mol^{-1}	Transfer
5000	N
10,000	N
20,000	N
50,000	N
75,000	N
100,000	N

4.7 Acryloyloxy poly(ethylene glycol) monomethyl ether copolymers

4.7.1 Poly(acryloyloxy poly(ethylene glycol) monomethyl ether-*co*-octadecyl acrylate), n = 44

When designing the experiments for the acryloyloxy poly(ethylene glycol) monomethyl ether copolymers, the length of the backbone of commercially-available polymers was the target length. The largest number of reports of water transfer show the use of poly(maleic anhydride-*alt*-1-octadecene) with a molecular weight between 30,000 and 50,000 g mol^{-1}. A chain with a molecular weight of 40,000 g mol^{-1} will have approximately 114 pairs of monomers in the backbone. The shortest polymer reported to successfully transfer nanocrystals is poly(styrene-*co*-maleic anhydride) with a molecular weight of 1700 g mol^{-1}. This translates into approximately 10 monomer units. In this section polymers are referred to in terms of their monomers per backbone.

4.7.1.1 RAFT polymerisation

In a typical polymerisation, acryloyloxy poly(ethylene glycol) monomethyl ether (2.58 g, 1.26 mmol, $M_n = 2054.11$ g mol^{-1}) was dissolved with octadecylacrylate (0.41 g, 1.26 mmol, Aldrich, 97 %, were dissolved in warm 1,4-dioxane (70 ml, Sigma-Aldrich, $\leq$99 %), dried using sodium. 4-cyano-4-[(dodecylsulphanylthiocarbonyl)sulphanyl]pentanoic acid (8.3 mg, 22.8 µmol, Aldrich, 97 %) and 1,1'-azobis(cyclohexanecarbonitrile) (0.8 mg, 3.4 µmol, Aldrich, 98 %) were dissolved in dried 1,4-dioxane (1.5 ml) and added to the monomer solution. The solution was degassed by passing argon through for 15 min and a reservoir was filled with argon to maintain a slight positive pressure in the reaction vessel. The solution was stirred and heated at 96 °C for 14 h. The viscosity of the reaction mixture underwent a marked increase.

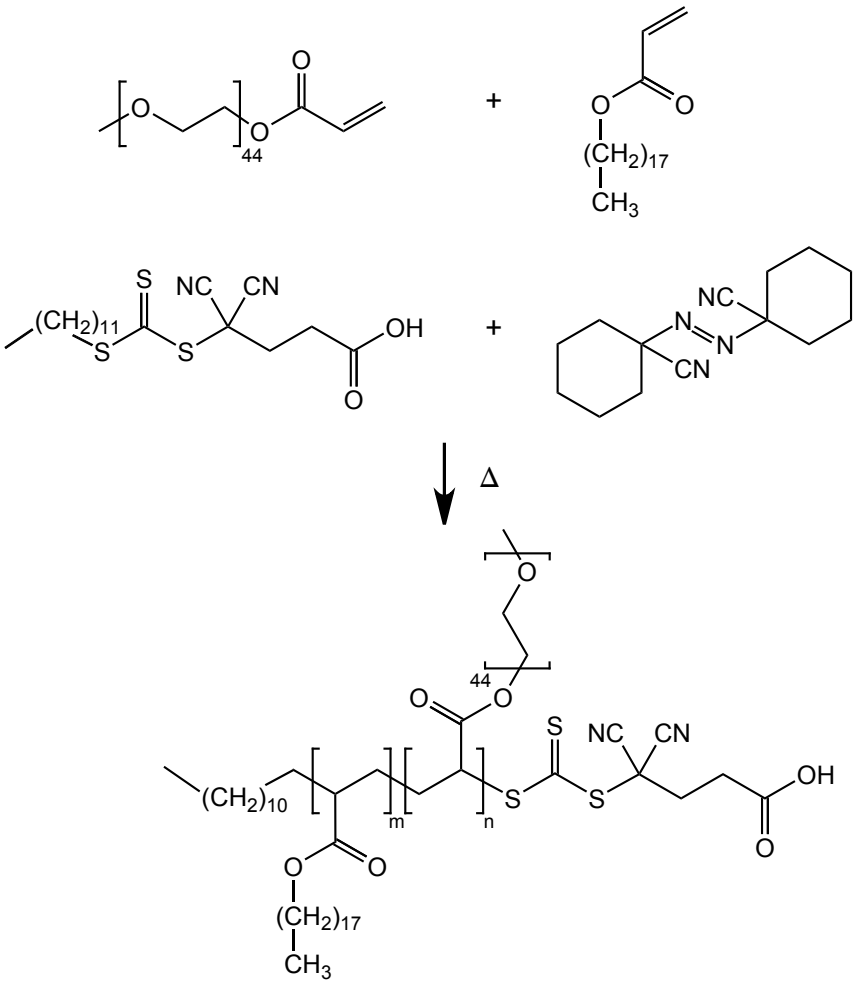

Figure 4.21: The reaction to produce poly(acryloyloxy poly(ethylene glycol) monomethyl ether-*co*-octadecyl acrylate), n = 44.

The 1,4-dioxane was removed using rotary evaporation (55 °C, 100 mbar. To encourage further removal of 1,4-dioxane the sample was heated to 65 °C whilst using the Schlenk line for 4 h. The polymer was redissolved in dichloromethane (5 ml) and precipitated using cold 40–60 °C petroleum ether (40 ml, Sigma-Aldrich). The precipitate was collected by centrifugation at 2800 × *g* for 1 min. The supernatant was discarded and the collected polymer was dried under vacuum provided by the Schlenk line.

Table 4.13: Amounts of reagents used to control the molecular weight of the poly(acryloyloxy poly(ethylene glycol) monomethyl ether-*co*-octadecyl acrylate), n = 44, polymers produced. Both polymers had a target backbone length of 110 monomers.

Target monomer ratio	Target molecular weight / g mol^{-1}	Amount of reagents used			
		APEGm / mmol	ODA / mmol	RAFT agent / µmol	Initiator / µmol
1:1	131,190	1.26	1.26	22.8	3

4.7.1.2 Polymer characterisation

The NMR spectrum, Figure 4.22, showed that acryloyloxy poly(ethylene glycol) monomethyl ether and octadecylacrylate did not copolymerise readily and resulted in a monomer ratio of 1:0.39. GPC results showed a molecular weight approximately the same as an individual acryloyloxy poly(ethylene glycol) monomethyl ether monomer, Table 4.14. This polymer is significantly different to the polystyrene standards and the significance of this number is hard to estimate. It is possible that interaction with the GPC stationary phase may have retarded elution, leading to an erroneous underestimate of the molecular weight. This would also cause band-broadening, which would lead to a larger estimate of PDI. The NMR suggested that a polymer had been formed due to broadening of the peaks from octadecylacrylate.

Table 4.14: Data for the poly(acryloyloxy poly(ethylene glycol) monomethyl ether-*co*-octadecyl acrylate), n = 44, polymers.

Target monomer ratio APEGm:ODA	Target molecular weight / g mol^{-1}	M_n / g mol^{-1}	M_w / g mol^{-1}	PDI	Monomer ratio APEGm:ODA	Yield (%)
1:1	131,190	804	2280	2.84	1:0.39	62.6

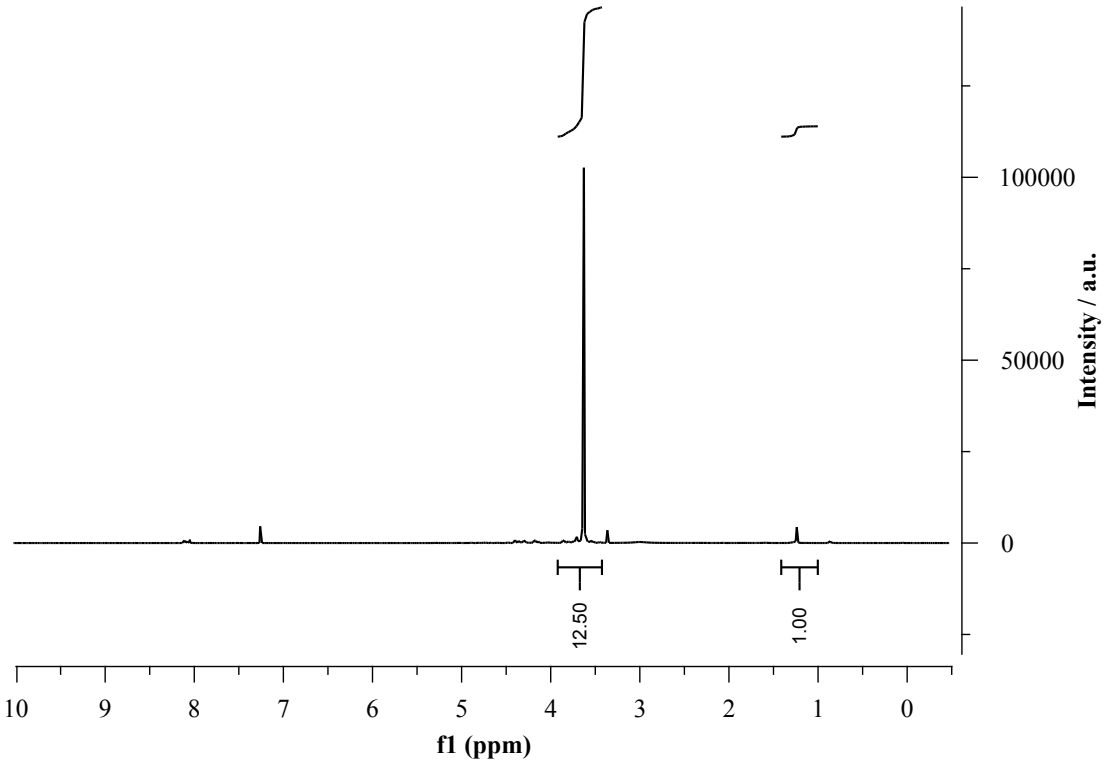

Figure 4.22: An example NMR spectrum of poly(acryloyloxy poly(ethylene glycol) monomethyl ether-*co*-octadecyl acrylate), n =44, with a 1:1 target monomer ratio. The regions integrated to determine the monomer ratio are shown. The molecular weight of the poly(ethylene glycol) used was M_n =2054 g mol^{-1}

4.7.1.3 Testing

The method for testing poly(acryloyloxy poly(ethylene glycol) monomethyl ether-*co*-octadecyl acrylate) was slightly different to the protocol described in Section 4.6.1.3, but the same reasoning applies.

In a typical water transfer test, 200 µl of a stock solution of oleic acid stabilised Fe_3O_4, as synthesised in Section 2.2.2, was precipitated using an excess of ethanol (Sigma-Aldrich, $\geq$99.8 %) and were redispersed in $CHCl_3$ (1 ml, Fisher Scientific, >99 %). A solution of the polymer being tested was made using 30 mg of the polymer dissolved in $CHCl_3$. The polymer was stirred in $CHCl_3$ for 20 min to allow it to fully solvate. The nanocrystal and polymer solutions were combined and allowed to mix for 5 min. By rotary evaporation, the $CHCl_3$ was slowly removed over the course of 30 min. To ensure maximum removal of $CHCl_3$ the sample was further dried using a Schlenk line under vacuum for 90 min. 5 ml of water was added to the dry film and left overnight.

The nanocrystals did not transfer with the poly(acryloyloxy poly(ethylene glycol) monomethyl ether-*co*-octadecyl acrylate), n = 44, polymer. Removal of $CHCl_3$ resulted in a waxy brown solid. The thickness of the solid was irregular and not a thinly spread film. After addition of water the polymer-nanocrystal layer did not show any signs of redispersing.

The poor polymerisation and absence of any water transfer caused the consideration of using monomers containing shorter poly(ethylene glycol) chains. Shorter chains will

diffuse more readily and the monomer end will be more accessible for reaction with other monomers.

Table 4.15: Water transfer results for iron oxide nanocrystals transferred using poly(acryloyloxy poly(ethylene glycol) monomethyl ether-*co*-octadecyl acrylate), n = 44, where N represents no transfer, P represents a partial transfer and F represents a full transfer.

Target molecular weight / g mol^{-1}	Transfer
131,190	N

4.7.2 Poly(acryloyloxy poly(ethylene glycol) monomethyl ether-*co*-octadecyl acrylate), n = 9

Having poor water transfers and incorporation of monomers into the polymer, a monomer containing a shorter poly(ethylene glycol) chain was investigated. The synthesised acryloyloxy poly(ethylene glycol) monomethyl ether had a molecular weight of 2054.11 g mol^{-1} which contains on average 44 repeating subunits in the poly(ethylene glycol) chain. In this series of polymers a shorter and commercially available acryloyloxy poly(ethylene glycol) monomethyl ether, with a molecular weight of 480 g mol^{-1} was incorporated. This contains 9 repeating subunits in the poly(ethylene glycol) chain on average. This was hoped to balance the target amphiphilic polymer so the hydrophilic groups do not dominate the product and allow polymerisations to proceed more easily.

4.7.2.1 RAFT polymerisation

In a typical polymerisation, acryloyloxy poly(ethylene glycol) monomethyl ether (2.98 g, 6.21 mmol, Aldrich, $M_n = 480\,\mathrm{g\,mol^{-1}}$) was dissolved with octadecylacrylate (2.02 g, 6.21 mmol, Aldrich, 97 %), in 1,4-dioxane (20 ml, Sigma-Aldrich, $\leq$99 %), dried using sodium. 4-cyano-4-[(dodecylsulphanylthiocarbonyl)sulphanyl]pentanoic acid (41.1 mg, 113 µmol, Aldrch, 97 %) and 1,1'-azobis(cyclohexanecarbonitrile) (2.0 mg, 8.2 µmol, Aldrich, 98 %) were dissolved in dried 1,4-dioxane (1 ml) and added to the monomer solution. The solution was degassed by passing argon through for 10 min and a reservoir was filled with argon to maintain a slight positive pressure in the reaction vessel. The solution was stirred and heated at 96 °C for 18 h. The viscosity of the reaction mixture underwent a marked increase and the solution became cloudy.

The 1,4-dioxane was removed using rotary evaporation (55 °C, 100 mbar). To encourage further removal of dioxane the sample was heated to 65 °C whilst using the Schlenk line for 4 h. The polymer was redissolved in THF (5 ml) and precipitated using cold 40–60 °C petroleum ether (40 ml, Sigma-Aldrich). The precipitate was collected by centrifugation at

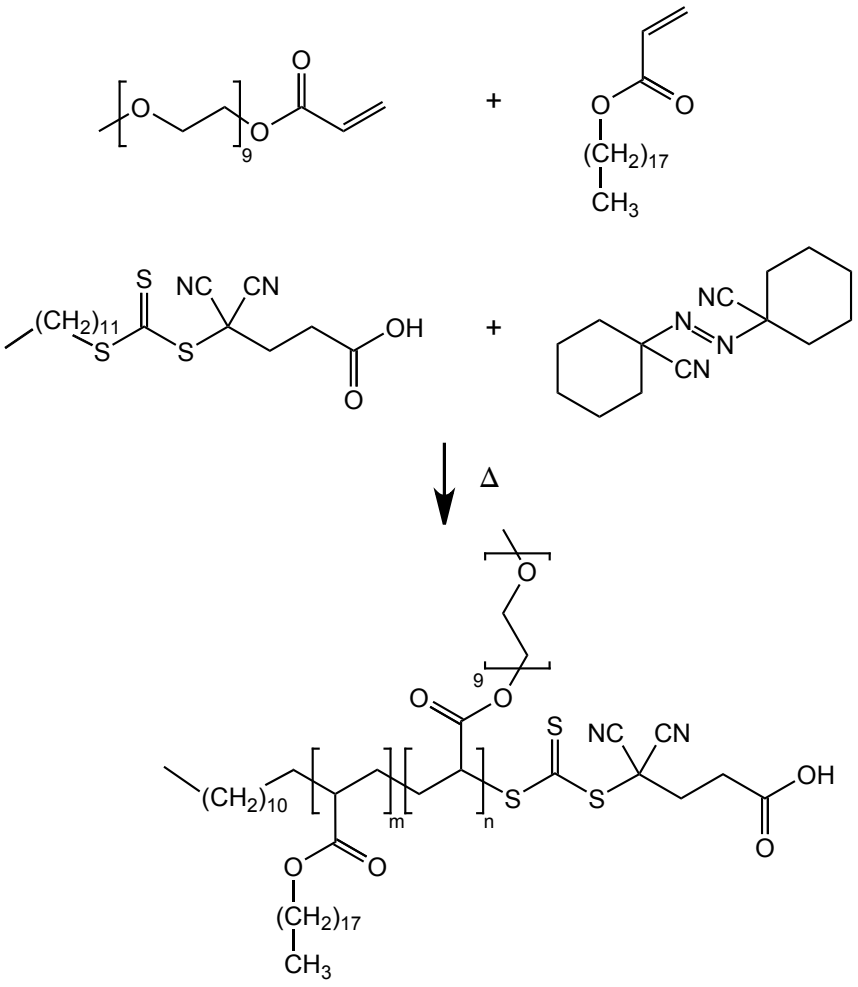

Figure 4.23: The reaction to produce poly(acryloyloxy poly(ethylene glycol) monomethyl ether-*co*-octadecyl acrylate), n = 44.

2800 × *g* for 1 min. The supernatant was discarded and the collected polymer was dried under vacuum provided by the Schlenk line.

Table 4.16: Amounts of reagents used to control the molecular weight of the poly(acryloyloxy poly(ethylene glycol) monomethyl ether-*co*-octadecyl acrylate), n = 9, polymers produced.

Target number of monomers per chain	Target monomer ratio APEGm:ODA	Target molecular weight / g mol^{-1}	Amount of reagents used			
			APEGm / mmol	ODA / mmol	RAFT agent / µmol	Initiator / µmol
55	1:1	22,490	6.21	6.21	225	16
55	1:2.33	20,780	4.03	9.42	239	18
110	1:1	44,610	6.21	6.21	113	8
110	1:2.33	41,190	4.03	9.42	239	2

4.7.2.2 Polymer characterisation

The NMR spectra for the poly(acryloyloxy poly(ethylene glycol) monomethyl ether-*co*-octadecyl acrylate), n = 9, polymers showed broad signals from octadecylacrylate subunits suggesting polymerisation had occured; Figure 4.24. The corresponding ratios from the NMR spectra showed that the monomers reacted well with each other and were near the target values, Table 4.17. The molecular weights from GPC were much closer to their target values than the n = 44 monomer. The values were still approximately half of the target but the polystyrene standard is not suitable for these polymers.

Table 4.17: Data for the poly(acryloyloxy poly(ethylene glycol) monomethyl ether-*co*-octadecyl acrylate), n = 9, polymers.

Target number of monomers per chain	Target monomer ratio APEGm:ODA	M_n / g mol^{-1}	M_w / g mol^{-1}	PDI	Monomer ratio APEGm:ODA	Yield (%)
55	1:1	10,100	13,200	1.30	1:0.87	62.2
55	1:2.33	9780	12,200	1.24	1:2.70	-
110	1:1	15,100	19,600	1.30	1:0.88	62.1
100	1:2.33	20,400	27,000	1.32	1:2.78	63.3

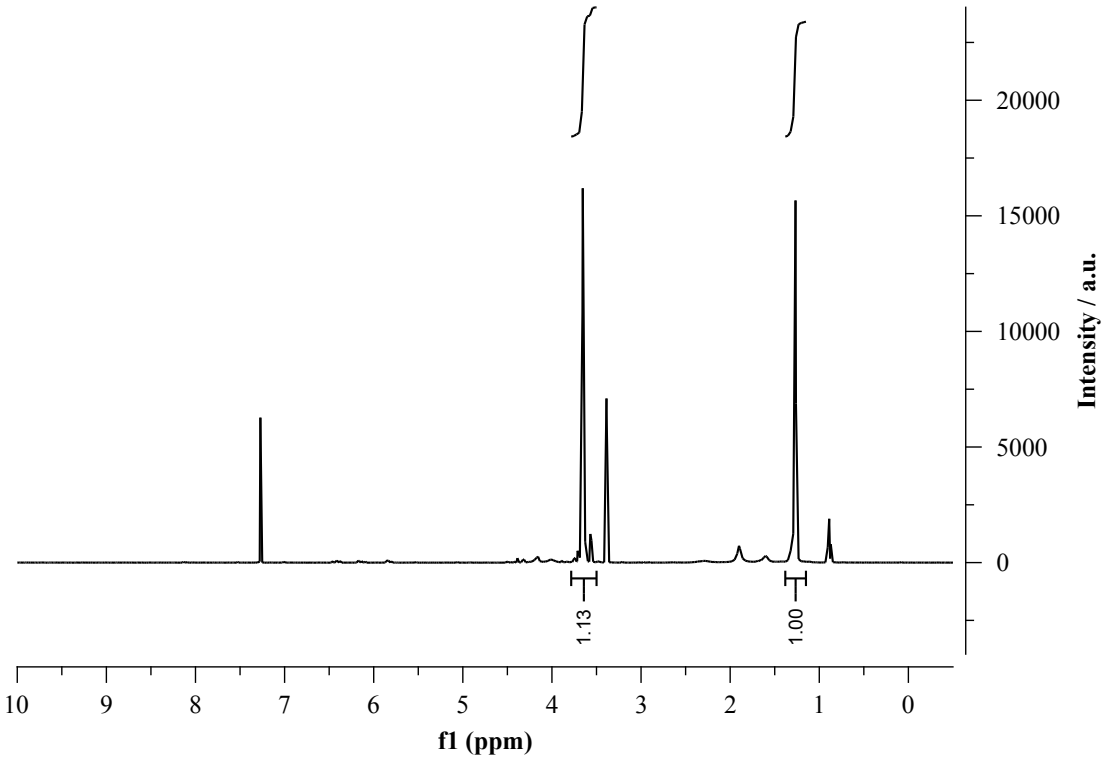

Figure 4.24: An example NMR spectrum of poly(acryloyloxy poly(ethylene glycol) monomethyl ether-*co*-octadecyl acrylate), n = 9, with a 1:1 target monomer ratio. The regions integrated to determine the monomer ratio are shown. The molecular weight of the poly(ethylene glycol) used was M_n =480 g mol^{-1}

4.7.2.3 Testing

The testing procedure used for poly(acryloyloxy poly(ethylene glycol) monomethyl ether-*co*-octadecyl acrylate) was identical to Section 4.6.1.3. Water transfer tests did not result in a transfer. Upon removal of the solvent a waxy brown layer was left. The layer did not show any signs of dispersing in water after 12 h.

Table 4.18: Water transfer results for iron oxide nanocrystals transferred using poly(acryloyloxy poly(ethylene glycol) monomethyl ether-*co*-octadecyl acrylate), n = 9, where N represents no transfer, P represents a partial transfer and F represents a full transfer.

Target number of monomers per chain	Target monomer ratio APEGm:ODA	Transfer
55	1:1	N
55	1:2.33	N
110	1:1	N
110	1:2.33	N

4.8 Conclusions

In this chapter a range of random copolymers containing activated esters have been synthesised. This was an attempt to structurally mimic the commercially-available pro-amphiphilic polymers which are known to perform successful transfers. A family of amphiphilic random copolymers with inbuilt pendant poly(ethylene glycol) functionality were also synthesised. All of the copolymers were synthesised, characterised and their water transfer ability was tested.

Of the copolymers of *N*-(acryloyloxy)succinimide, partial transfers to water were achieved using styrene based copolymers. It was found that the shorter polymers transferred the nanocrystals better than the longer polymers, although none allowed a total transfer. The ratio of monomers in the poly(*N*-(acryloyloxy)succinimide-*co*-styrene) polymer made no difference to the water transfer ability over the range tested.

The family of poly(*N*-(acryloyloxy)succinimide-*co*-octadecyl acrylate) polymers did not cause any nanocrystal water transfers. This family would benefit from further investigation. For instance, varying monomer ratios and pendant alkyl chain length may improve the ability of the polymer to perform water transfers.

The poly(acryloyloxy poly(ethylene glycol) monomethyl ether-*co*-octadecyl acrylate) polymers proved to be unable to perform water transfers using the water transfer methodology used for poly(maleic anhydride-*alt*-1-octadecene). These polymers are unlike the commercially-used polymers as they are strongly amphiphilic without further reaction with a water-liking nucleophile. As a consequence it is likely that their properties in chloroform are significantly different to pro-amphiphilic polymers. The water transfer method used depends on how the polymer interacts with the nanocrystal ligands as $CHCl_3$ is slowly removed. Poly(ethylene glycol) is soluble in solvents of a wide range of polarities, *e.g.* toluene through to water. As such both "sides" of the polymer are soluble in $CHCl_3$ and it is unlikely the same processes occur as the solvent is removed.

CHAPTER 5

Protein corona formation on nanocrystals & model systems

5.1 Protein-nanoparticle interactions

As described in Chapter 1, there are a wide range of potential applications for nanocrystals and nanomaterials within biological systems. Successful use of nanomaterials in biological systems requires knowledge of how materials interact with the biological system it will encounter. The nanomaterials need to be introduced to the system and typically will migrate to the site where their intended function will be performed. During the migration, the nanomaterial will encounter a range of environments, each potentially with unique interactions with the nanomaterial. An understanding of how the nanomaterial interacts with the components of the biological medium and the machinery of cells is crucial to the material performing its envisaged task.

5.1.1 Corona formation on nanoparticles

It has long been established that, when introduced to a solution of biomolecules, that surfaces acquire a coating formed from a selection of the biomolecules, *i.e*. proteins, lipids, carbohydrates *etc*.[240] Once coated in the biomolecules, the material has a new "biological identity" from the perspective of the biological system with which it is in contact. In turn, this identity governs the responses from cells and tissues towards the material.

Nanomaterials are not exempt from these interactions and may, due to their high surface to volume ratio, experience interactions distinct from their bulk counterparts. As a consequence of the high surface to volume ratio, nanoparticle surfaces possess a free energy higher than that of the bulk material, as shown in Figure 2.1. When introduced to biological fluids, the nanoparticles attempt to minimise the surface free energy by adsorbing biomolecules to the surface.[241–243] The resulting "corona" of biomolecules

masks the surface of the particle from the surrounding environment.

Early studies into the interaction of proteins with the surfaces of spherical nanoparticles were performed in the 1990s. In these studies, Rainer H. Müller and coworkers used two-dimensional polyacrylamide gel electrophoresis to examine the proteins adsorbed to the surface of a range of nanoparticles.[244] The nanoparticles were incubated in human blood serum and then the unbound and weakly bound proteins were removed with centrifugal washing cycles. The objective of early work looking into protein nanoparticle interactions was concerned with increasing the lifespan of nanoparticles in the blood system and the relationship between the protein coating and cellular uptake. It became clear that the properties of the nanoparticle surface dictated the identity and quantity of the proteins adsorbed.[245] Studies were conducted with polystyrene-based particles, with different surface charges and hydrophobicities, which showed "*a remarkable differentiation in amount and type of proteins adsorbed*".[246] In the following reports, Müller and coworkers investigated the effect of the particle material, surface charge density and surface hydrophobicity on protein adsorption using two-dimensional polyacrylamide gel electrophoresis.[247–251] The studies clearly demonstrated that surface properties influenced the composition of the protein layer and that it had consequences with cellular uptake and retention time in the blood although a detailed rationale for this was not reached.

During the late 1990s and the 2000s the discovery and rapid development of nanoscale materials with size dependent properties, such as QDs, increased interest in nanomaterial-protein interactions. The two driving forces were the understanding of how protein interactions would influence the performance of the envisaged nanomaterial and also the assessment of any potential toxic properties of these new materials.

Protein-nanoparticle interactions were later studied in more detail by the group of Prof. Kenneth A. Dawson. Early work investigated copolymer nanoparticles of *N*-*iso*-propylacrylamide and *N*-*tert*-butylacrylamide allowing control over surface hydrophobicity and surface curvature.[252,253] It was found when using SEC the nanoparticles eluted first and were followed by proteins that had disassociated from the corona. The protein elution was in order of affinity to the nanoparticles which allowed identification and relative affinities of proteins to be determined.[253] Commercially available nanoparticles of controlled sizes and surface functionalities were studied by Dawson and coworkers.[242,243,254] The work focussed on the corona formed on polystyrene[241,255–259] and silica nanoparticles.[241,256,257] These studies shaped the current descriptions of the protein corona in the field and some of the concepts are discussed in this review.

The corona upon nanoparticles is dynamic, *i.e*. the proteins are in exchange with the surrounding medium.[258] In a typical human biological fluid, there are several thousand proteins which vary in abundance and have differing affinities for nanopartcle surfaces. The corona that is initially formed will be dominated by the more abundant proteins, even if their affinity for the surface is low, and with time the corona evolves through the exchange of proteins.[260] The proteins with the highest affinity eventually dominate the composition

of the corona as they are less likely to desorb once on the surface.[257]

The adsorption of a protein to the surface of a nanoparticle is in itself non-trivial. During adsorption, the protein can undergo conformational change resulting in a difference in the expressed function of the protein. The effect on proteins due to interactions with nanoparticles is the subject of a recent review by Shemetov *et al.*[261]

5.1.1.1 Hard and soft coronas

If a protein has a high affinity for the nanopaticle surface, a strongly bound layer of protein can form. This layer will stay on the surface after the concentration of free protein has been significantly lowered after removal of free protein. This layer has been described as a "hard corona", which is distinct from the rest of the corona which is in faster exchange with the unbound proteins.[258] The "hard corona" is bound tightly to the surface forming a near-monolayer. The rest of the corona which undergoes faster exchange with free biomolecules is more loosely bound and is called the "soft" corona.[243] The hard and soft corona are depicted in Figure 5.1.

There are approximately 3700 proteins in human blood plasma,[262] although typically less than a hundred of these are found in protein coronas. The proteins which are typically in the hard corona rarely have high abundances in serum and do not necessarily have the highest affinities to the surface.[263–265] The high stability of the hard corona has consequences as the particle moves between environments. A new environment will have a different composition of proteins which will in turn begin to exchange with the corona. Any biomolecules which were from the first environment and do not exchange can act as a molecular memory of the previous environment.[257] The composition of a hard protein corona would be the consequence of all the environments encountered by the nanoparticle.

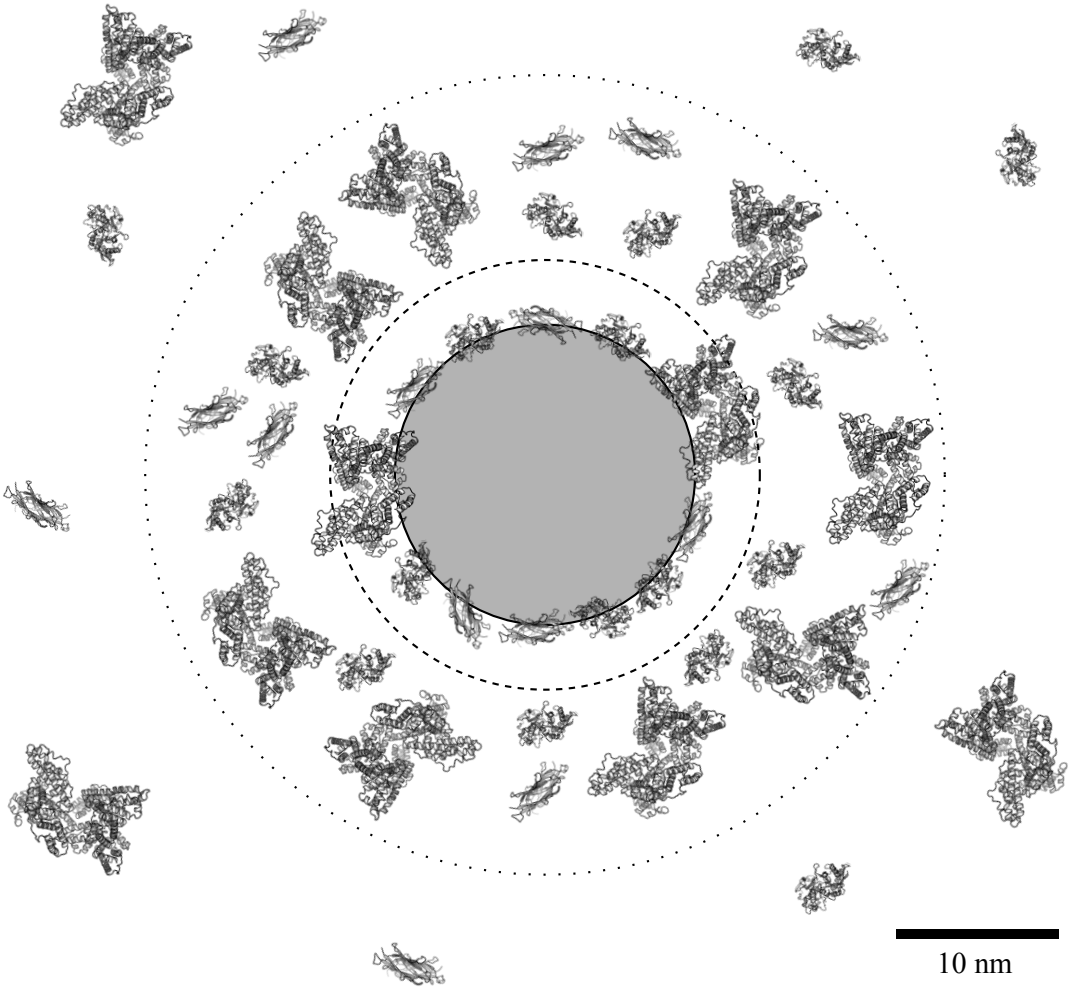

Figure 5.1: An illustration of the protein corona surrounding a nanoparticle. The approximate boundaries of the "hard" and "soft" corona are illustrated. The hard corona is between the nanoparticle and the dashed line and the soft corona is between the dashed and dotted lines. In this illustration human serum albumin, the largest protein is less prevalent in the hard corona and more in the soft, illustrating an affinity to the surface. The protein structures used were entries 1BM0, 1A8E and 2P9R from the protein data base.

5.1.1.2 The perception of nanoparticles in biological systems

Nanomaterials often display size dependent properties in a size range that potentially allows movement through biological systems. These *intrinsic* properties of the nanomaterial are what makes them interesting at first, but once a protein layer has formed upon their surface the particles will exhibit *extrinsic* properties in biological systems. These extrinsic properties are as much linked to the size of the particle and the material as the intrinsic properties. The study of the intrinsic properties has been the subject of a large number of studies over the past fifteen years. Even though a vast range of bioanalytical and theraputic nanoscale devices have been envisaged and developed, the study of the extrinsic biological properties of nanomaterials followed much later.

A recent publication by Salvati *et al.* demonstrates transferrin functionalised nanoparticles losing their targeting ability due to the protein corona formed on their surface.[266] In another study, the ability of a particle to undergo click chemistry has been demonstrated to significantly reduce the yield of the reaction when coated with a protein corona.[267] These observations are beginning to guide strategies for particle functionalisation to circumvent this effect. The two approaches involve the minimisation of protein absorption of the surface or the use of the protein corona to perform targeting.[268]

5.1.1.3 The structure of the protein corona

It has been been demonstrated that isolated nanoparticles with protein coronas are representative of the corona in biological media.[241] The structure of the corona has not been studied to the same level as the composition of the corona. This may be due to the complexity of the structure formed or the ease of identifying proteins which form the corona. The structure of the corona has been studied using techniques from colloid and interface science such as DLS[241] and fluorescence correlation spectroscopy.[215,258] Both of these techniques determine the hydrodynamic radius and result in a size distribution. As DLS and fluorescence correlation spectroscopy both observe the Brownian motion of the corona coated nanoparticles, the structural information is derived from dynamic information. These techniques will not contain detailed structural information that static techniques, such as SANS, can deliver.

5.1.2 Protein-nanoparticle interactions upon nanocrystals

The studies of corona formation upon nanocrystals are complicated by the wide range of materials from which nanocrystals can be formed. The size of a typical nanocrystal is $\leq$15 nm which is significantly smaller than the majority of studies on silica and polystyrene particles and places nanocrystals in a similar size domain to large proteins. With particles in this size range, a small change in radius results in a large change in surface curvature, a factor which is thought to influence which proteins can bind. Not all nanocrystals with envisaged biological applications are spherical, such as AuNRs, adding further

complexity to nanocrystal studies. Studies of coronas upon inorganic nanocrystals have recently been reviewed by Casals and Puntes.[269] To date the nanocrystals that have had protein layers studied on their surface include Au,[227,260,263,270–274] Ag,[274] FePt,[215,275] Fe_3O_4,[274,276] CoO,[274] CeO_2,[274,277] CdTe[278] and CdSe@ZnS.[215] The studies suffer from being fragmented by the wide range of materials and surface functionalities available and a clear trend in the structure and composition of the corona is in the early stages.

Casals *et al.* have studied the formation of a protein corona on AuNPs from 4 to 40 nm.[260] Positive or negative surface charges were created by ligand exchange with aminoundecanethiol or mercaptoundecanoic acid respectively. Negatively charged AuNP were found to form only a soft corona whereas positively charged AuNP formed a hard corona. It was found that albumin rich protein coronas formed although albumin was not observed on the smallest, 4 nm, AuNP. Casals *et al.* studied a range of electrostatically stabilised nanocrystals. Au, Ag, Fe_3O_4, CoO and CeO_2 of similar sizes with negative surfaces were exposed to protein containing media. It was found that coronas formed on the surfaces but the proteins would desorb after time once removed from serum. This suggests the corona was entirely soft and a hard corona did not form.[274]

The binding of Human serum albumin (HSA)[215] and transferrin[275] has been investigated upon the surface of nanocrystals stabilised with a poly(isobutylene-*alt*-maleic anhydride)-based amphiphilic polymer. The polymer coated FePt and CdSe@ZnS nanocrystals are stabilised by the carboxylic groups the amphiphilic polymer provides, as discussed in Chapter 4. Röcker *et al.* used fluorescence correlation spectroscopy to determine that HSA formed a 3.3 nm thick monolayer upon the nanocrystal surface.[215] Time-resolved fluorescence quenching experiments found that HSA resided on the surface for approximately 100 s. A similar study with amphiphilic polymer coated FePt showed transferrin formed a monolayer on the surface with a thickness of 7 nm.[275] This work was expanded to investigate the effect of surface charge provided by custom-synthesised amphiphilic polymers by Hühn *et al.*[227] Poly(*N*,*N*,*N*-trimethylammonium-2-ethyl methacrylate iodide-*co*-lauryl methacrylate) and poly((dihydroxyphosphoryl)ethyl methacrylate-*co*-lauryl methacrylate) were used to transfer AuNP. It was found that the thickness of the corona formed was similar regardless of the sign of the charge but the cellular uptake varied. The corona coated nanocrystals with a positively charged amphiphilic polymer coating exhibited a higher rate of cellular uptake.

5.2 Proposed protein-nanoparticle systems for study with SANS

In this chapter, SANS techniques for the investigation of the structure of the protein corona formed upon nanocrystals and silica nanoparticles are developed. SANS is a static scattering technique, which allows structural elucidation through the analysis of scattering profiles. Materials containing protons, *i.e*. polymers and biomaterials, are often studied with SANS. The difference in scattering length of hydrogen and deuterium allows experiments to be performed where different parts of the structure can be investigated independently through contast variation. As discussed in Section 2.3.2.1, the analysis of scattering profiles is dependent on the fitting of form factors, which are derived from simple geometric systems, *i.e*. spheres, cylinders *etc*. The protein corona formed upon the surface of a spherical nanocrystal could be first approximated as a shell upon a core which allows use of the established core-shell model.

In the envisaged experiment, polymer coated nanocrystals would be measured in the absence of protein to determine the bi-layer thickness, shown as A in Figure 5.2. The nanocrystals with protein corona would subsequently be measured. The neutrons would be scattered by both the bi-layer and the protein corona resulting in a profile from region C in Figure 5.2. The fitted parameters determined from the nanocrystals without corona would be used to decipher the profile, allowing information of region B to be extracted.

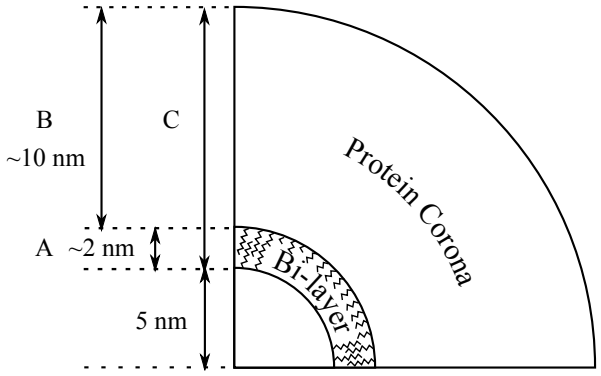

Figure 5.2: Schematic showing the approximate radius of the particle core and the thickness of the ligand-polymer bi-layer and the "hard" protein corona, where A is the thickness of the bi-layer, B is the thickness of the protein corona and C is the total thickness of organic content.

As an alternative system, silica nanoparticles are also investigated. These offer the advantage of not having an additional organic layer, which simplifies the fitting process when compared to the polymer coated nanocrystal system. Silica nanoparticles are commercially available with a range of surface functionalities and sizes, allowing ready measurement of the corona. The ability to contrast match silica using a mixture of D_2O and H_2O is advantageous as complementary data for fitting purposes can be generated.

Development of the methods to produce aqueous nanocrystal dispersions at the required concentration for SANS is discussed. Preliminary SANS results for nanocrystal systems

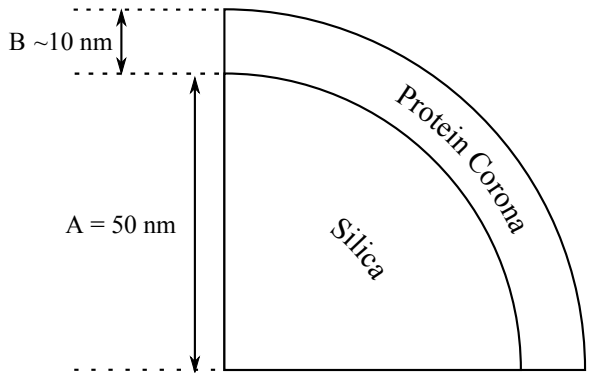

Figure 5.3: Schematic showing the approximate radius of the particle and the thickness of the "hard" protein corona, where A is the radius of the silica nanoparticle and B is the thickness of the protein corona.

are demonstrated for Fe_3O_4 and AuNPs. This is followed by SANS measurements for the silica particles with soft and hard coronas.

5.3 Studies of the corona upon nanocrystals

5.3.1 Purification of nanocrystal samples

The nanocrystals examined using SANS were stabilised in aqueous environments using the amphiphilic polymer technique discussed in Chapter 4. In particular, poly(maleic anhydride-*alt*-1-octadecene) was used due to the well established literature precedent. Briefly, in the water transfer procedure, a mixture of nanocrystals and polymer in chloroform had the solvent slowly removed until a film was produced. An aqueous solution of nucleophile was added and the nanocrystals became stable in an aqueous solution. In this transfer an excess of polymer was used and after the nanocrystals had transferred the excess is also transferred in aqueous solution. In this transfer an excess of polymer was used, which transferred into the aqueous phase with the polymer coated nanocrystals.

This is shown in Figure 5.4, where the number weighted DLS profile (top) only shows a peak at approximately 10 nm, which is the polymer transferred nanocrystals. Figure 5.4 (bottom) shows the DLS profile by intensity, where a second structure can be seen at 70 nm. This structure is an assembly of amphiphilic polymer. In a SANS experiment the larger structure will cause scattering, which will complicate the scattering profile.

To remove the larger structure and excess free amphiphilic polymer, a cleaning protocol using SEC was developed. A column containing Sephacryl S-1000 SF which was 98 cm long and 2.5 cm in diameter was found to separate the particles from the polymer. Figure 5.5 shows the separation of the polymer-coated nanocrystals from the polymer aggregates using a flow rate of 170 µl min^{-1}. Figure 5.5 (top) shows that, as the collection tube number increases, the population of the larger peak decreases relative to the smaller peak. As more mobile phase passes, the nanocrystals become separated from the large material and size separation amongst the isolated nanocrystals is observed, Figure 5.5

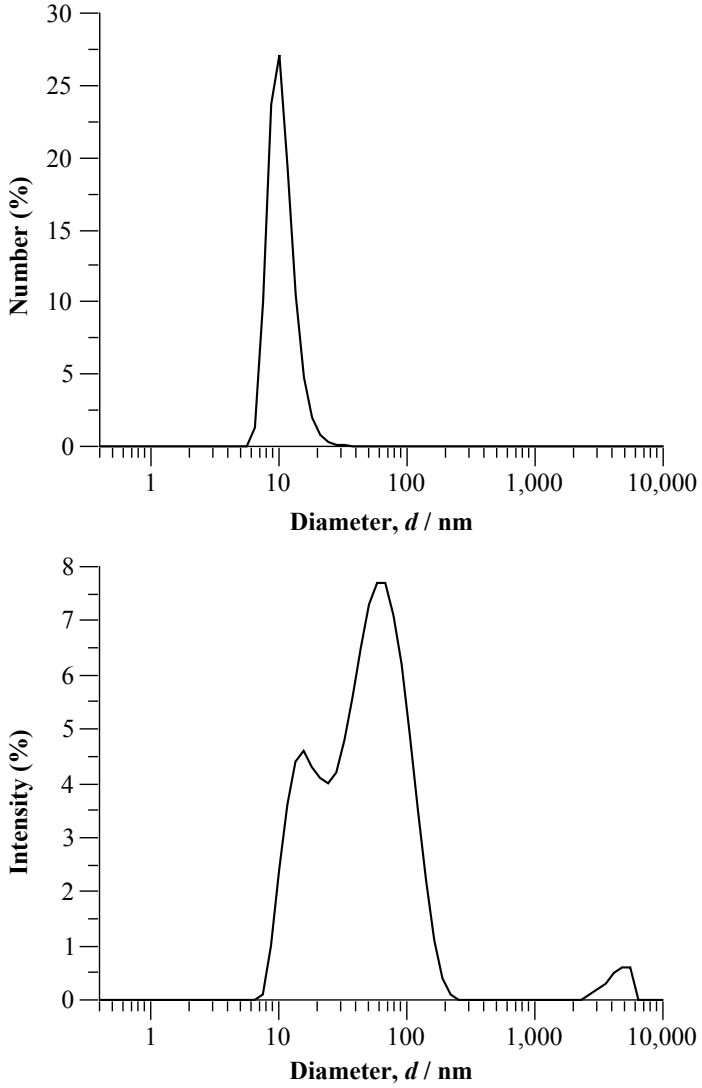

Figure 5.4: DLS profiles of Fe_3O_4 transferred using poly(maleic anhydride-*alt*-1-octadecene). The profile is represented weighted by number (top) and the intensity profile (bottom).

(middle). To give perspective on the amount of nanocrystals passing through the column the absorbance at $\lambda = 320\,\text{nm}$ is followed, Figure 5.5 (bottom). This shows that the majority of the nanocrystals are passing through when separated from the large material.

As the process of SEC dilutes the nanocrystals, centrifugal filters (Amicon ultra centrifugal filters, 50,000 molecular weight cut off, $2200 \times g$) were used to make more concentrated dispersions. Following concentration of the samples, the DLS profiles were collected. There is a possibility that the polymer aggregate had not been removed but the dilution of the sample may have caused it to disassemble. After concentrating the particles the second peak did not return, as shown in Figure 5.6, which suggests this is unlikely.

The SEC process was scaled up to allow the production of samples for SANS. A 1 m long column with a diameter of 5 cm was built and packed with Sephacryl S-1000 SF. This would allow the separation of approximately 10 times more material per run. Samples were prepared by scaling up the water transfer procedure 40 times as in Section 5.3.2.1. When added to the column the sample caused the disruption of the packing material through the osmotic potential of the sample. The narrow band of particles was distorted over $\approx$15 cm and the separation abilities of the column were compromised. SEC was not able to deliver separated nanocrystals at the scale demanded by SANS, but works well on smaller and more dilute samples, both to remove large structures and to fractionate the population to give samples with lower polydispersity.

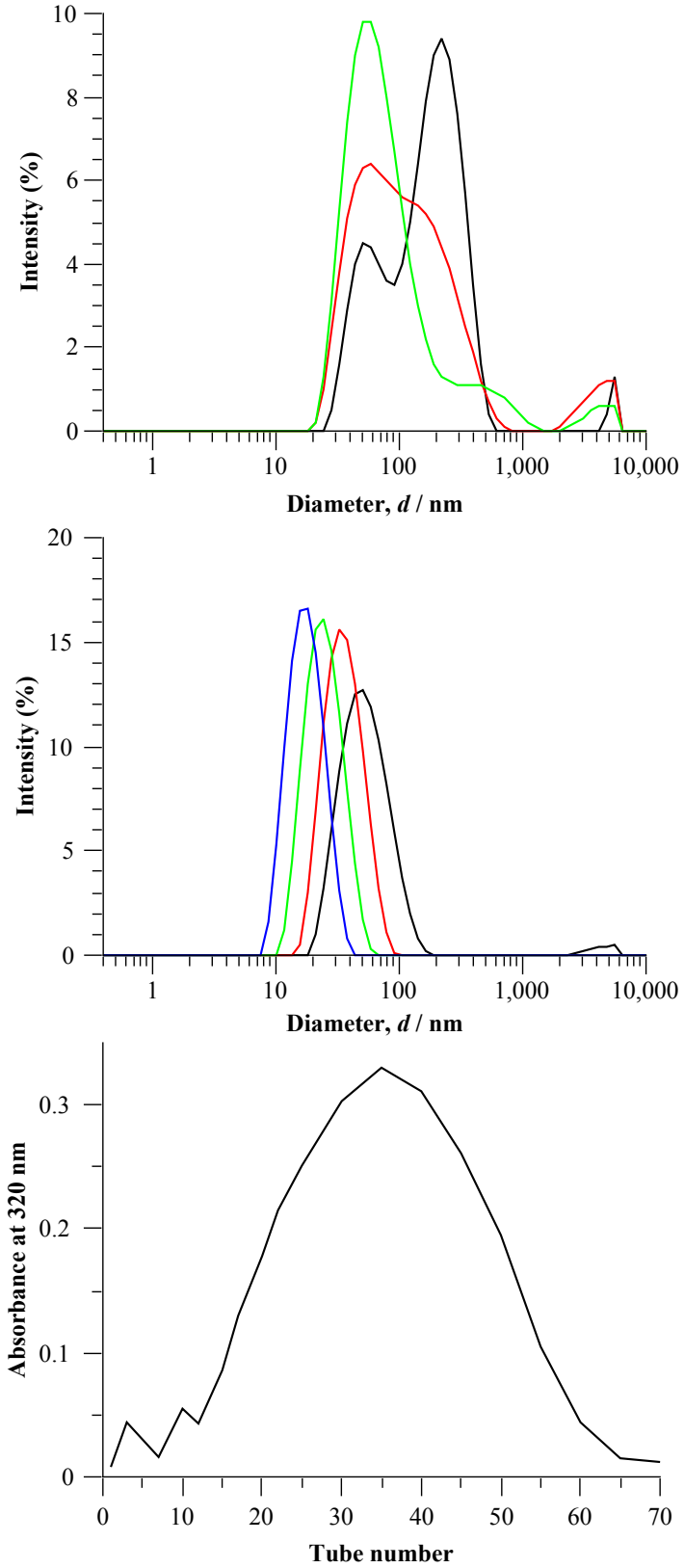

Figure 5.5: DLS profiles of Fe_3O_4 separated by SEC. (Top) Tubes 1 (black), 7 (red) and 12 (green) show the large polymer aggregate. (Middle) Tubes 20 (black), 30 (red), 40 (green) and 50 (blue) show the size separation of pure nanocrystals. (Bottom) Absorbance against tube number.

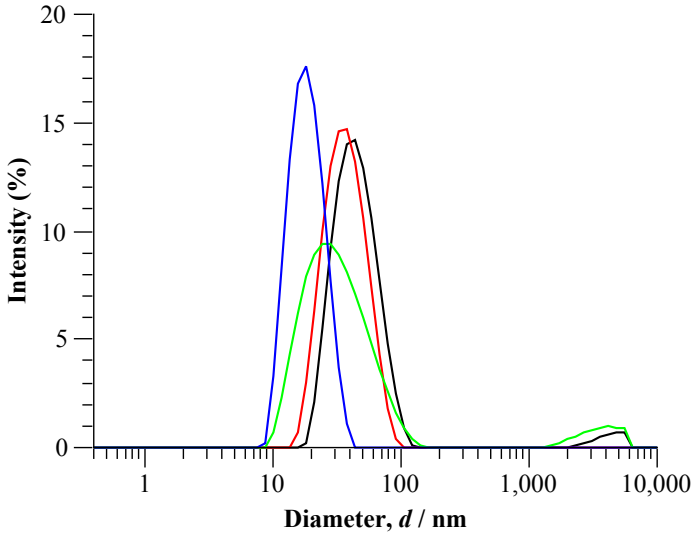

Figure 5.6: DLS profiles of reconcentrated Fe_3O_4 nanocrystals stabilised with poly(maleic anhydride-*alt*-1-octadecene). The curves represent tubes 17 to 25 (black), 26 to 35 (red), 36 to 45 (green) and 46 to 55 (blue).

5.3.2 SANS studies of nanocrystals

5.3.2.1 Sample preparation

The Au and Fe_3O_4 nanocrystals were synthesised according to the protocols described in Sections 2.2.2 and 2.2.3. 350 µl of nanocrystals in organic solvent were precipitated using ethanol (14 ml, Sigma-Aldrich, $\geq$99.8 %) and centrifuged at 2220 $\times$ *g* for 10 min. The samples were resuspended in 350 µl of either H8-toluene (Sigma-Aldrich, $\geq$99.9 %) or D8-toluene ($>$ 99.50 atom %D, Apollo Scientific) to achieve the required contrast. TEM images for AuNP and Fe_3O_4 in toluene are shown in Figures 5.7 and 5.8.

Polymer coated nanocrystal samples were prepared in a similar manner to previous chapters except the quantities were scaled by 40 to deliver quantities required for SANS. In a scaled-up water transfer, 4 ml of a stock solution of nanocrystals was precipitated using ethanol (45 ml) and resuspended in chloroform (10 ml, Fisher Scientific, $>$99 %). A solution of poly(maleic anhydride-*alt*-1-octadecene) (8 g, 30,000 – 50,000 g mol^{-1} Aldrich) in chloroform (200 ml) was stirred for 30 min. The poly(maleic anhydride-*alt*-1-octadecene) and nanocrystal solutions were mixed and the solvent was slowly removed by rotary evaporation over 4 h. This was further dried by use of a Schlenk line for 2 h. A solution of tetramethylammonium hydroxide (16 g, Sigma, $\geq$97 %) in distilled water (200 ml) was added to the dried film and swirled overnight resulting in the particles dispersing in the aqueous phase. Once transferred, the solution was buffer exchanged using a 42 ml Sephadex G-25 column into Phosphate Buffered Saline (PBS). This was concentrated using ultrafiltration (Amicon polyethersulphone 5000 MWCO membrane, 5 cm, 2.5 bar) until a paste was formed. The particles were resuspended into 10 ml of distilled water.

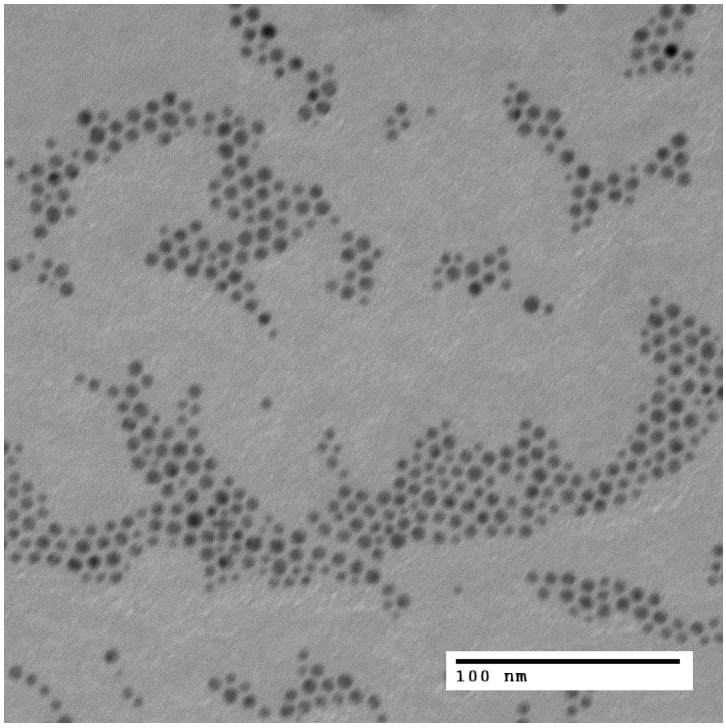

Figure 5.7: TEM micrograph of the AuNP used

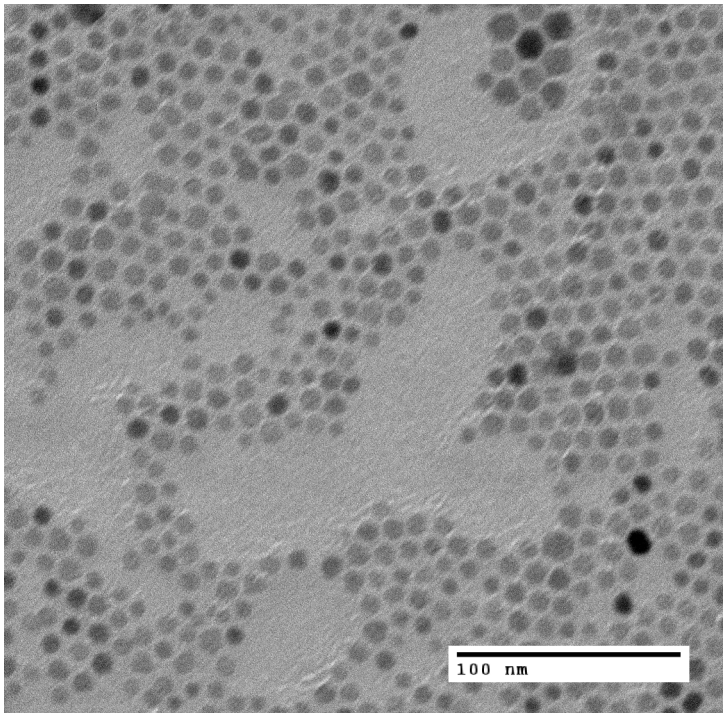

Figure 5.8: TEM micrograph of the Fe_3O_4 nanocrystals used

5.3.2.2 Neutron scattering profiles

The nanocrystals in organic solvents can be studied to observe the behaviour of the stabilising ligands. Information about ligand packing is in itself interesting and may shed light on how the amphiphilic polymers interact with a particular ligand. In this section, Fe_3O_4 stabilised with oleic acid and AuNP stabilised with dodecanethiol were studied. The SLDs of materials frequently used in this section are listed in Table 5.1.

Table 5.1: SLDs of solvents and nanocrystal materials

Material	SLD / Å^{-2}
Fe_3O_4	7.03×10^{-6}
Au	4.67×10^{-6}
dodecanethiol	-3.68×10^{-7}
oleic acid	3.67×10^{-7}
H-toluene	9.39×10^{-7}
D-toluene	5.66×10^{-6}
H_2O	-5.61×10^{-7}
D_2O	6.39×10^{-6}

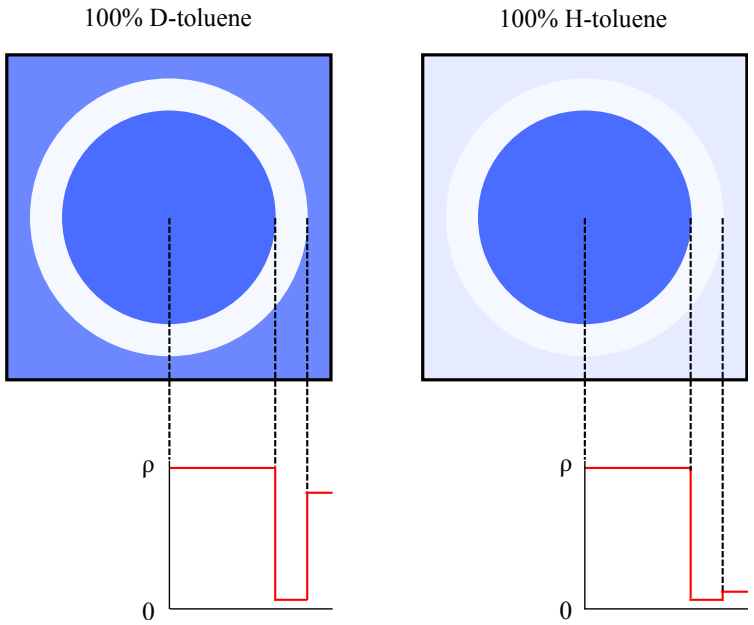

Figure 5.9: The contrast schemes for Fe_3O_4 in D-toluene (left) and H-toluene (right). The ligand SLD is assumed to be equal to the pure ligand in these schemes.

A simultaneous fit was performed on Fe_3O_4 in H-toluene and D-toluene. In this parameters from the form factors applied were locked to one another. This constraint enhances the quality of the fit as the likelihood of both fits being incorrect is smaller than an individual fit.

In H-toluene the oleic acid layer is almost contrast matched and the layer is assumed to not contribute to the scattering profile. Consequently, a spherical form factor has been used to model just the Fe_3O_4 core in H-toluene. The Fe_3O_4 sample in D-toluene has no

contrast matching as the SLD of the solvent is not near that of the ligand shell nor the nanocrystal core. In the fitting process, the radius and polydispersity associated with the sphere, in the H-toluene case, and the core, in the D-toluene case, were locked together. The SLD of the solvents and Fe_3O_4 were fixed and the remaining values were allowed to float. The resulting profiles are shown in Figure 5.10 and parameters in Table 5.2.

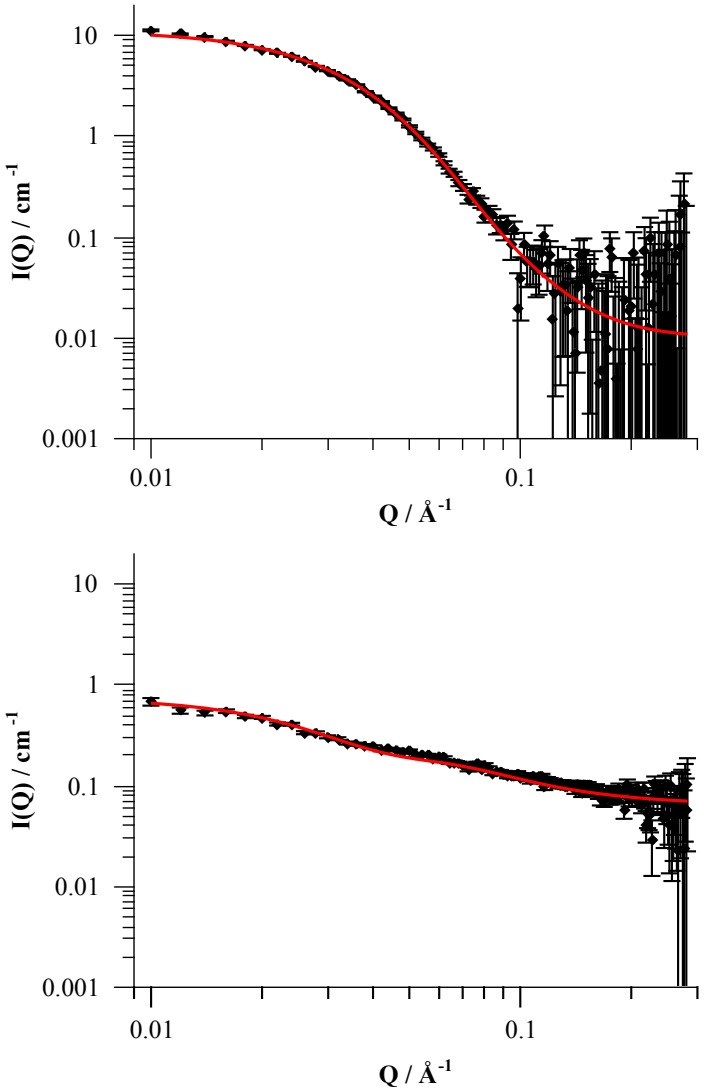

Figure 5.10: The scattering profiles for Fe_3O_4 in H-toluene (top) and D-toluene (bottom). The profiles were fitted using a simultaneous fit where the dimensions of the Fe_3O_4 core were linked in the two fits.

The shell thickness was determined to be 8.2 Å. This value contains information on the adopted packing of the ligand layer stabilising the nanocrystal. Oleic acid is an alkyl chain possessing eighteen carbon atoms. If the chain were to be extended to form the longest structure possible it would extend for 24 Å. The determined value of 8.2 Å is much smaller than the maximum the ligand can reach. This could be indicative of either the ligand layer laying tightly on the surface, which is a possibility as the double bond in oleic acid may cause a bend in the molecule encouraging the formation of a thin layer. Alternatively, the apparently thin layer could be a consequence of ligand solvation. As the distance from the

Table 5.2: Parameters of the Fe_3O_4 simultaneous fit. Parameters with a star were fitted. A double star signifies the parameter was locked to the counterpart in a simultaneous fit.

Fe_3O_4 in H-toluene Sphere Form Factor		**Fe_3O_4 in D-toluene Core-Shell Form Factor**	
Parameter	**Value**	**Parameter**	**Value**
Background*	$0.0100\,cm^{-1}$	Background*	$0.0681\,cm^{-1}$
Volume fraction*	0.0036	Volume fraction*	0.0075
Sphere radius**	36.0 Å	Core radius**	36.0 Å
SLD of sphere	7.03×10^{-6} Å^{-2}	SLD of core	7.03×10^{-6} Å^{-2}
SLD of solvent	9.39×10^{-7} Å^{-2}	SLD of solvent	5.66×10^{-6} Å^{-2}
		SLD of shell*	6.19×10^{-7} Å^{-2}
		Shell thickness*	8.2 Å
Polydispersity* *	0.39	Polydispersity* *	0.39

nanocrystal surface increases the average distance between ligands may increase, due to the high curvature of the nanocrystals. The volume available for solvent to reside between ligands would increase, causing the SLD to approach that of the solvent. In this case, the shell modelled would be closer to an effective ligand length, *i.e.* the ligand length visible to the neutrons. The SLD of the ligands has moved from the value for pure oleic acid, of 3.67×10^{-7} Å^{-2}, towards the value of the solvent as expected with ligand solvation.

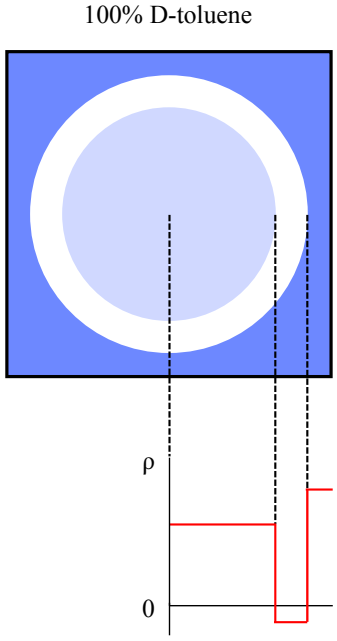

Figure 5.11: The contrast scheme for AuNP in D-toluene. The ligand SLD is assumed to be equal to the pure ligand.

In the case of AuNP, a core shell model was applied due to the core and ligand not being contrast matched by D-toluene, Figure 5.11. The AuNP were fitted using a core-shell model as shown in Figure 5.12. Table 5.3 shows that the SLD of the ligand shell floated towards that of D-toluene which is expected. The ligand shell thickness is much thinner

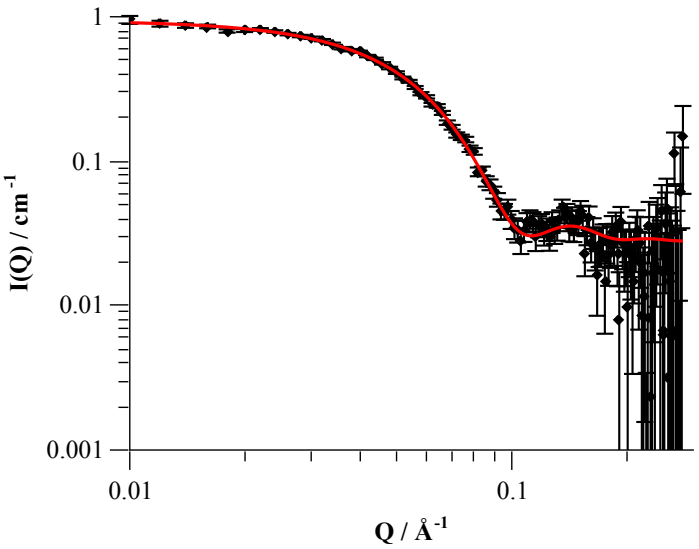

Figure 5.12: The scattering profile for AuNP in D-toluene.

for dodecanethiol stabilised AuNP than was observed for oleic acid stabilised Fe_3O_4. This could be due to differences in ligand density, the absence of the double bond as in oleic acid or the higher surface curvature. The higher surface curvature would cause the spacing between ligands to increase more rapidly with distance from the nanocrystal surface. Dodecanethiol ligands can potentially point straight away from the surface, unlike oleic acid with a double bond. This could result in a less dense layer causing the SLD to decrease faster from the surface and cause a smaller effective ligand length than oleic acid. A more detailed study with particles of varying particle size and ligand would be required to determine the nature of the ligand layer. Time on the SANS2D instrument was applied for at ISIS to perform this study but beam time was not awarded.

Table 5.3: Parameters of the AuNP fit. Parameters with a star were fitted.

Au in D-toluene **Core-Shell Form Factor**	
Parameter	**Value**
Background*	$0.0274\,\mathrm{cm}^{-1}$
Volume fraction*	0.0221
Core radius*	33.9 Å
SLD of core	4.67×10^{-6} Å^{-2}
SLD of solvent	5.66×10^{-6} Å^{-2}
SLD of shell*	7.89×10^{-7} Å^{-2}
Shell thickness*	1.4 Å
Polydispersity*	0.10

5.3.2.3 Polymer coated nanocrystals

The AuNP were stabilised in aqueous solution using poly(maleic anhydride-*alt*-1-octadecene), which had been reacted to produce pendant carboxylic acid or poly(ethylene oxide)-poly(propylene oxide) functionality. The profile for the carboxylic acid stabilised AuNP is shown in Figure 5.13. An attempt at fitting a core-shell form factor to the experimentally observed scattering is also shown in Figure 5.13. Parameters for the core from the fit in D-toluene, Table 5.3, were used as fixed values in the fit. A shell thickness of 20 Å has been used in order to create a curve similar to the expected hydrophobic bilayer. The SLD of the shell and the volume fraction were allowed to float and the parameters of the fitted core-shell form factor are shown in Table 5.4.

The fitted curve in Figure 5.13 is not the correct shape to model the observed scattering profile. The high Q features of a core shell form factor are absent in the observed scattering profile. The fitting software has increased the difference in SLDs and the volume fraction to scale the form factor to the observed profile. What can be concluded is that the collected curve is not a product of a core-shell form factor. The volume fraction of the scattering material is much higher than that of the stock solution of AuNP in toluene. The scattering is likely to be from an excess of polymer which is not wrapped around the nanocrystal surface and the contribution from wrapped nanocrystals is negligible in comparison.

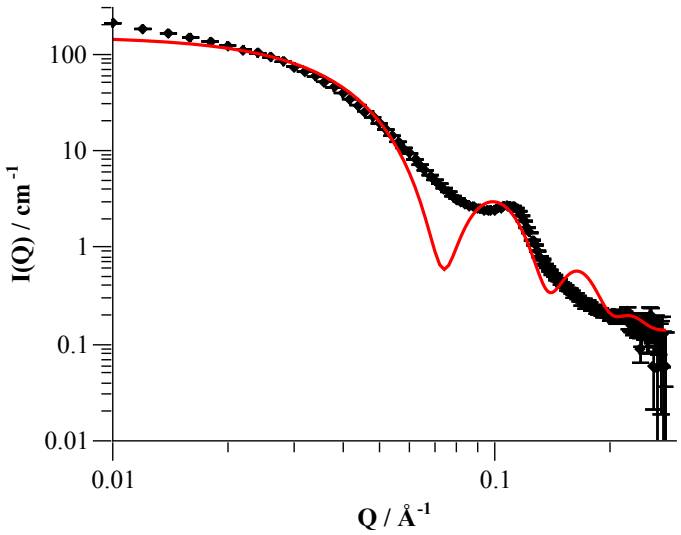

Figure 5.13: The scattering profile for AuNP coated with poly(maleic anhydride-*alt*-1-octadecene) with pendant carboxylic acid groups in D-PBS. The fitted curve represents an approximation of the profile expected for AuNP with a 2 nm hydrophobic bilayer.

Figure 5.14 shows an equivalent sample transferred using poly(maleic anhydride-*alt*-1-octadecene) opened with Jeffamine M-1000. This also shows strong features which are responsible from a large contribution from structure factor which is thought to arise from excess unbound polymer. It is also clear that the shape of the structure factor from a polymer with pendant poly(ethylene oxide)-poly(propylene oxide) chains is significantly different to that of the same polymer with pendant carboxylic acid groups. In the case of

Table 5.4: Parameters used to simulate an approximation of polymer coated AuNPs using a core-shell form factor. Parameters with a star were fitted.

AuNP in Deuterated-PBS Core-Shell Form Factor	
Parameter	**Value**
Background	$0.13\,\mathrm{cm}^{-1}$
Volume fraction*	0.109
Core radius	33.9 Å
SLD of core	4.67×10^{-6} Å^{-2}
SLD of solvent	6.39×10^{-6} Å^{-2}
SLD of shell*	9.42×10^{-7} Å^{-2}
Shell thickness*	20 Å
Polydispersity	0.10

the scattering profile from the pendant Jeffamine M-1000 poly(maleic anhydride-*alt*-1-octadecene) it is clearer that a core-shell, similar to the fitted profile in Figure 5.13, could not fit the observed curve. The conclusion is that there is a concentration of excess polymer which is high enough to create the observed profile and the contribution from polymer coated nanocrystals is small.

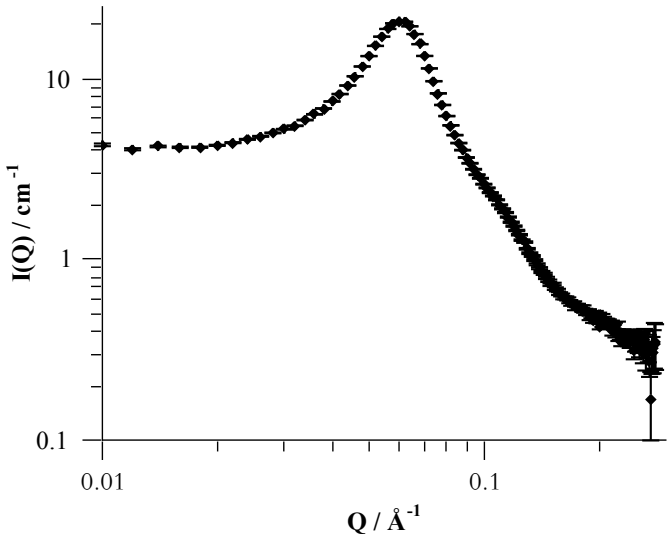

Figure 5.14: The scattering profile for AuNP coated with poly(maleic anhydride-*alt*-1-octadecene) with pendant Jeffamine M-1000 in deuterated PBS.

5.3.2.4 Conclusion

It was concluded that the scaling up of the polymer coating of nanocrystals resulted in an excess of free polymer, which could not to be removed using SEC. As a consequence silica nanoparticles were studied at the next allocation of beam time. This has two advantages: the particles require no elaborate preparation and the sizes of silica nanoparticles fall into the middle of the Q-range available which means they are easier to measure due to increased scattering.

The ligand layers of AuNP and Fe_3O_4 were studied in toluene of different contrasts. It was possible to model the nanocrystals using sphere and core shell form factors to elucidate information about their ligand layers. The oleic acid stabilised Fe_3O_4 had a shell thickness, at 8.2 Å, compared to the dodecanethiol stabilised AuNP, at 1.4 Å. There are many factors which could be contributing to the difference, such as surface curvature, ligand packing density, ligand length and the presence of unsaturation. This would warrant further investigation as it is in itself interesting and could explain bilayer thicknesses of polymer coated nanocrystals after the scale up issue is solved.

5.4 Studies of the corona upon silica nanoparticles

5.4.1 Corona formation methodology

Uncoated SiO_2-COOH nanoparticles (50 nm diameter, Micromod, 25 mg ml^{-1}) were exchanged into D_2O using centrifugal filters (Amicon ultra centrifugal filters, 50,000 molecular weight cut off). 1 ml of SiO_2-COOH nanoparticles was diluted with 14 ml of deuterium oxide ($>$ 99.92 atom %D, Apollo Scientific). The volume was reduced to 1 ml by centrifugation at $2200 \times g$ for 12 min. The process of dilution to 15 ml and centrifugation to 1 ml was repeated two more times to create a stock solution of SiO_2-COOH in D_2O. Solutions of mixed solvent were prepared by mixing nanoparticles in H_2O and D_2O to get the required ratio.

Silica nanoparticles with carboxylic acid surfaces and protein coronas were prepared as follows. 50 µl of the 25 mg ml^{-1} stock solution in H_2O of silica nanoparticles were mixed with 400 µl of serum (Foetal bovine serum, Fisher Scientific, Batch RVJ35882) and 50 µl of D-PBS (tablets, Sigma), *i.e.* a 90 % serum solution. The mixture of particles and serum was incubated at room temperature for 1 h. The protein coated particles were collected by centrifugation at $9500 \times g$ for 15 min resulting in a colourless pellet. The supernatant containing unbound protein was discarded and the pellet resuspended in 1 ml of D-PBS through agitation by pipette. This resulted in a 1.25 mg ml^{-1} dispersion of silica nanoparticles coated with a soft protein corona.

The process of centrifugation at $9500 \times g$ for 15 min and resuspension was repeated twice more, a total of three times, to isolate silica nanoparticles coated with only a hard protein corona. Resuspension became more difficult with each centrifugation. Contrast matched samples were prepared in the same manner except the PBS solution contained a mixture, by volume, of 60 % D_2O and 40 % H_2O.

5.4.2 Characterisation of the corona

5.4.2.1 Characterisation of the uncoated particles

The scattering profiles generated require as much information about the sample as possible to be acquired to strengthen the fitting procedure. In this experiment the structure of the corona is the unknown quantity. If the corona upon a nanoparticle is modelled using a core-shell form factor the properties which can be determined are the thickness and SLD of the corona. The silica nanoparticle at the core can be characterised completely. This generates values which are used as knowns when fitting the corona coated nanoparticles.

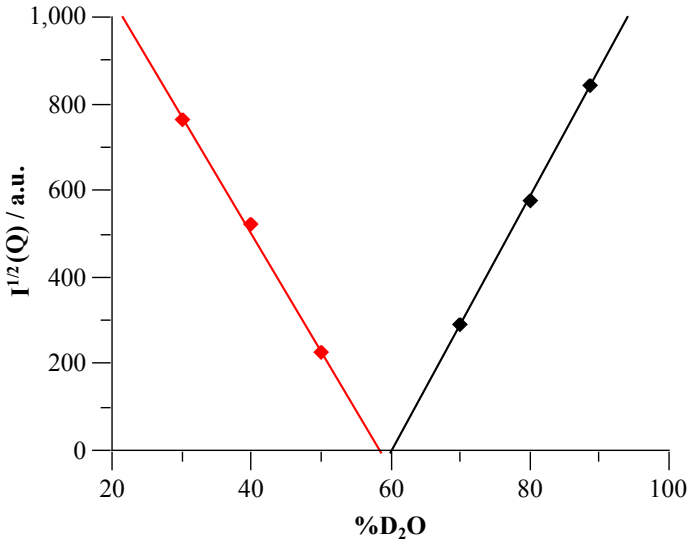

Figure 5.15: Experimental determination of the contrast of SiO_2 particles by variation of the proportion of deuterated solvent.

The density of the silica nanoparticles is quoted by the manufacturer as 1.8 g ml^{-1} which results in an SLD of 2.84×10^{-6} Å^{-2}. The SLD of the silica particles was determined experimentally by performing measurements of the particles in mixtures of D_2O and H_2O. At the point $I^{1/2}(Q)$ is equal to zero, the contrast of the solvent is matched with that of the dispersed object. The plot of $I^{1/2}(Q)$ against the percentage of D_2O is shown in Figure 5.15. The percentage of D_2O required to achieve $I^{1/2}(Q)$ equal to zero was determined to be 59 %. Taking into account the SLDs of H_2O and D_2O, as shown in Table 5.5, the SLD of the silica particles was determined to be 3.54×10^{-6} Å^{-2}. When performing contrast matching experiments a mixture of D_2O and H_2O containing 60 % by volume of D_2O is used. The experimentally determined value is used for the fitting of the corona samples. The higher value may be attributed to solvent penetration of the nanoparticles.

Table 5.5: SLDs of solvents and silica

Material	SLD / Å^{-2}
SiO_2	3.54×10^{-6}
H_2O	-5.61×10^{-7}
D_2O	6.39×10^{-6}

A TEM was used to capture images of the carboxylic acid functionalised silica nanoparticles (SiO_2-COOH) as shown in Figure 5.16. This allowed a mean size and a polydispersity to be determined. These values serve as the starting values for the fitting of the particles without corona. 300 nanoparticles were measured to determine the radius and polydispersity. The radius was found to be 234.4 Å with a polydispersity of 0.13.

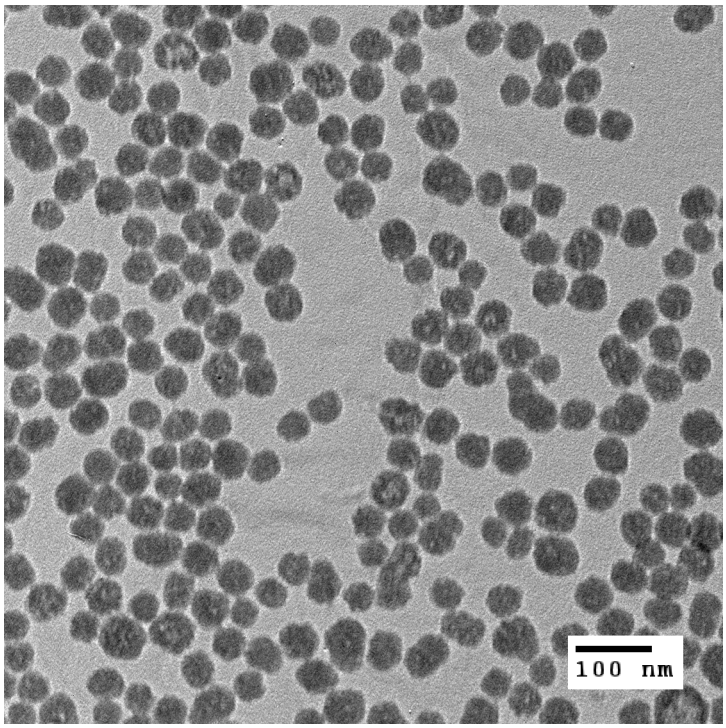

Figure 5.16: TEM micrograph for SiO_2-COOH.

The scattering profile for the SiO_2-COOH was fitted using a spherical form factor. The starting values for the radius and the polydispersity were taken from the TEM measurement. These values were allowed to find the optimal value as the average particle as perceived by the neutrons is not necessarily the same as that of the electrons. Figure 5.17 shows the fitted scattering profile and Table 5.6 lists the final values for the parameters. The solvent and nanoparticle SLDs were fixed and the remaining values were left to float. A value of 201.1 Å was determined for the radius, which is smaller than the value measured by TEM. This implies that there is a degree of solvent penetration at the surface lowering the effective nanoparticle diameter seen by the neutrons. The polydispersity was also slightly higher than that of the TEM at 0.16. The values for the SLD, radius and polydispersity of

the bare particles are used in the fitting of the corona coated particles as fixed values due to their determination in this section.

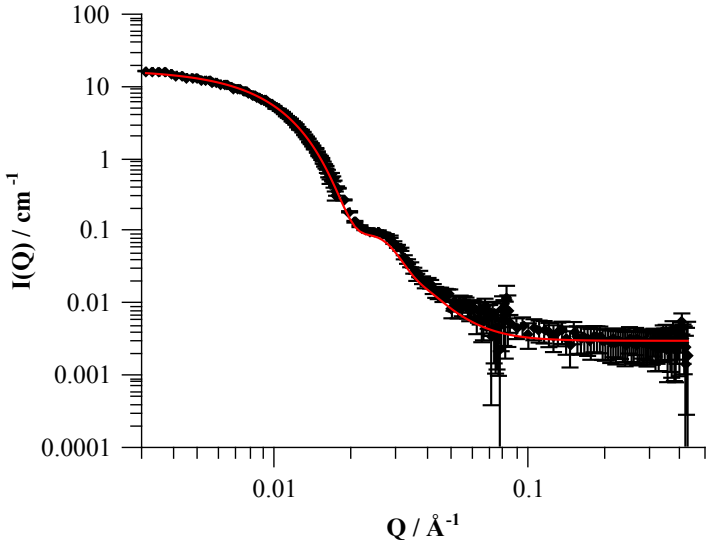

Figure 5.17: The scattering profile for SiO_2-COOH in D_2O. The red curve is the fitted profile for a sphere.

Table 5.6: Parameters of the SiO_2-COOH fit. Parameters with a star were allowed to float and those without were fixed.

SiO_2-COOH in D_2O Sphere Form Factor	
Parameter	**Value**
Background*	$0.003\ cm^{-1}$
Volume fraction*	0.0000459
Sphere radius*	201.1 Å
SLD of sphere	3.54×10^{-6} Å^{-2}
SLD of solvent	6.37×10^{-6} Å^{-2}
Polydispersity*	0.16

5.4.2.2 Corona coated silica nanoparticles

The SLD of proteins typically fall between 1.8 and 3 $Å^{-2}$. With the experimentally determined SLD for the silica nanoparticles and the known value for D_2O, an approximate scheme for a silica core with a protein shell in D_2O can be made, Figure 5.18. As the contrast condition for silica has been determined in Figure 5.15, a scheme for the contrast matched core is also presented.

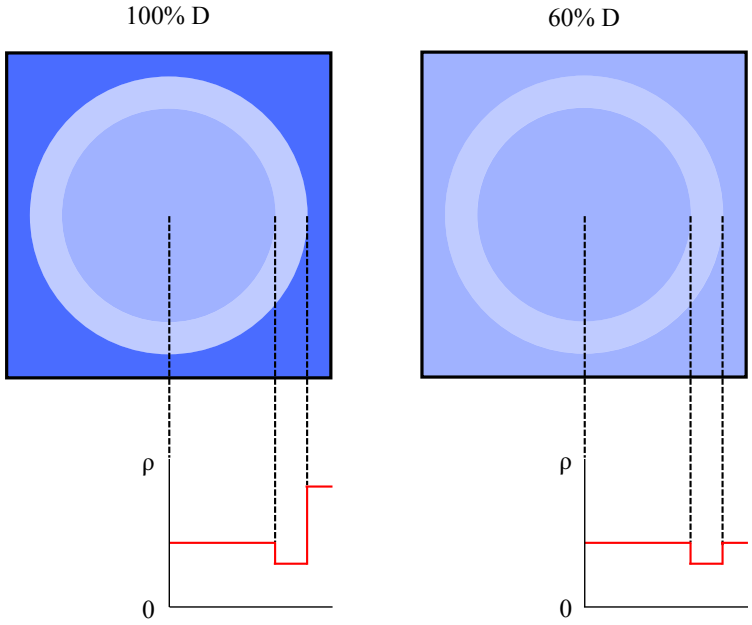

Figure 5.18: The contrast matching scheme used for corona coated SiO_2 particles (left) in 100 % D-PBS with no contrast matching and (right) in 60 % the core is contrast matched against the solvent.

Silica nanoparticles were incubated in serum and washed to produce nanoparticles with either a soft corona or a hard corona, as described in Section 5.4.1. The four samples discussed are the hard and soft corona coated particles in 100 % D-PBS and 60 % D-PBS. The profiles from the two contrasts are complementary to each other as the dimensions of the structure are the same. Using a simultaneous fit between the 100 % and 60 % D samples strengthens the fitted curve as the parameters that are locked to one another produce curves for both samples. In the case of the contrast matched hard and soft coronas, the only parameter that was locked for the simultaneous fit was the thickness of the shell. The SLD of the shell has not been locked as solvation of the proteins will move the SLD of the corona towards that of the solvent used.

The DLS size distributions of the hard and soft corona coated nanoparticles are shown in Figure 5.19. SiO_2-COOH with a soft corona have a hydrodynamic radius of 56.1 nm and a single peak. This is as expected as the corona coated nanoparticle is larger than the uncoated particles. The hard corona coated SiO_2-COOH has a maximum hydrodynamic radius at 74.5 nm although the size distribution has a tail to higher radius. This may indicate the presence of an artefact from the centrifugal washing process. The hard corona having a larger hydrodynamic radius than the soft corona is the opposite of what would be

expected to be observed and suggests that some degree of particle aggregation has occured.

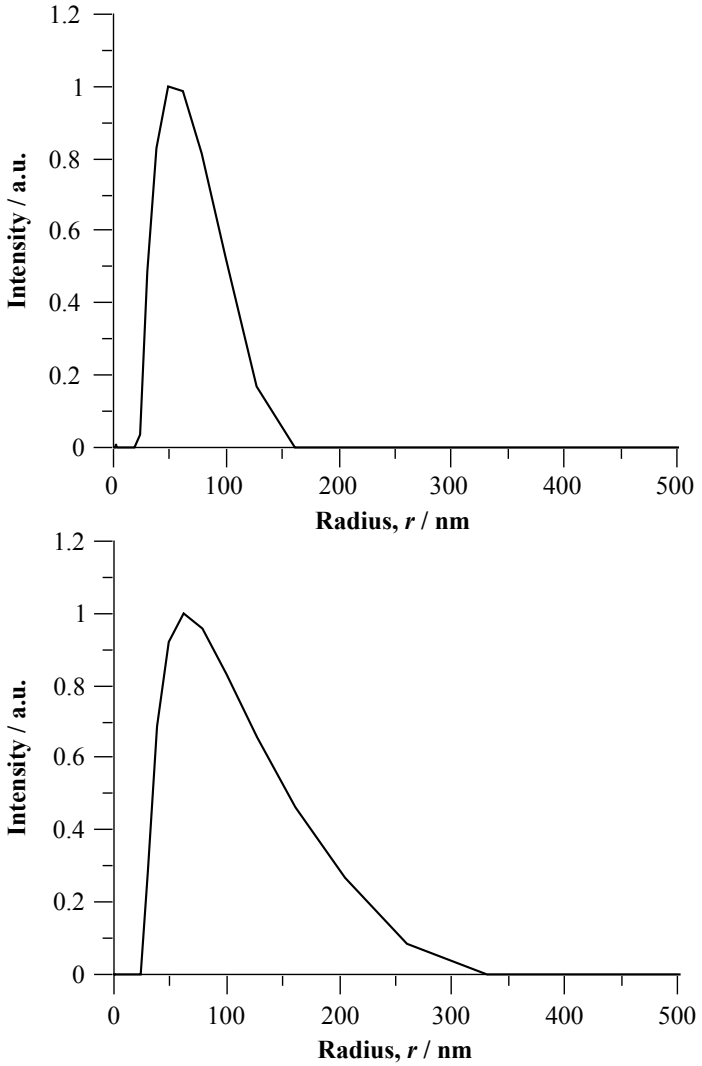

Figure 5.19: DLS profiles for SiO_2-COOH with a soft corona (top) and hard corona (bottom).

The fitted scattering profiles for the hard protein corona are shown in Figure 5.20. The soft corona profiles with the two contrasts were fitted using a simultaneous fit where the thickness of the shell was locked. Scattering from the nanoparticle and the corona causes the 100 % profile in Figure 5.20 (top). There are three features in the profile at Q values of 0.008, 0.02 and 0.06 $Å^{-1}$. A fitted profile for a core shell is superimposed. The fitted profile does not agree with the observed profile but does share some features. The 0.008 $Å^{-1}$ feature is much smoother than the fitted core shell profile. The smooth feature at low Q is an indication of a large polydisperse structure which is not from a single nanoparticle with a corona. The polydispersity of the core is the main contributor to the polydispersity of the corona coated nanoparticle and this is well characterised suggesting another structure must be contributing to the observed polydispersity. The 60 % D system has larger associated error bars due to the scattering only coming from the corona and the difference in SLD of the corona and the solvent/core being small. The three features as observed in the 100 % D system are not there. This is a good indication that the features seen in the 100 % system are from the nanoparticle and not the corona. The 60 % D profile

shows a smooth curve with no additional features, although the error bars are large enough for features to be hidden, hence caution is required in fitting the results.

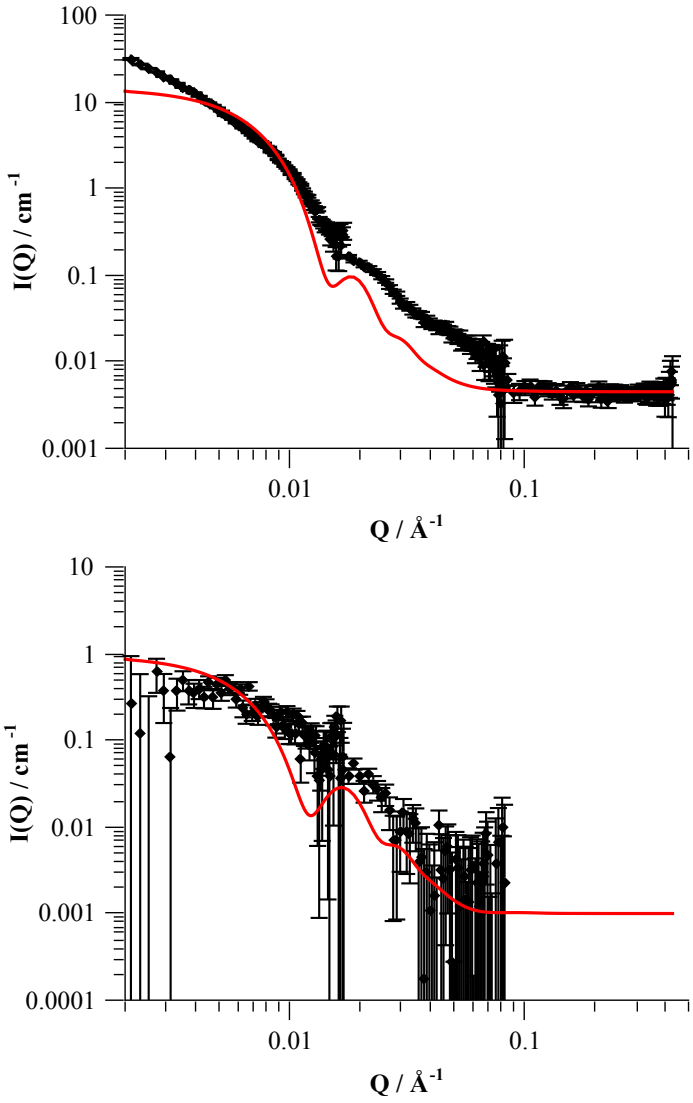

Figure 5.20: The scattering profiles for SiO_2-COOH with a hard protein corona in 100 % D-PBS (top) and 60 % D-PBS (bottom).

The parameters of the fit are displayed in Table 5.7. Parameters from the fitting of the bare particle were used as fixed values and parameters from the corona were allowed to float. The SLD of the shell was started at 3×10^{-6} Å^{-2}, which is the average value of a protein in D_2O, and allowed to float. With the 100 % D sample, the SLD of the shell would float to the lowest value possible if unconstrained. This is surprising as the SLD might be expected to tend to that of the solvent, due to solvent filling spaces in the corona. The fitting software attempting to reach a low value for the corona SLD is an attempt to increase the difference in SLD between the shell and the solvent. As shown in Equation 2.15 a larger difference in solvent and shell SLD increases the contribution from the shell in the resulting core shell form factor. This is unlikely to be representative of the system being observed and is just an attempt of the fitting software to make the curve fit.

As a consequence, the SLD reported in Table 5.7 is fixed at 3×10^{-6} Å^{-2}. The SLD of the corona in the 60 % fit was found to be 1.05×10^{-6} Å^{-2}. This has also moved away from the value of the solvent but has found a sensible value.

Table 5.7: Parameters of the simultaneous fit for the SiO_2-COOH with hard corona. Parameters with a star were fitted. A double star signifies the parameter was locked to the counterpart in a simultaneous fit.

SiO_2-COOH with hard corona in 60 % D-PBS Core-Shell Form Factor		**SiO_2-COOH with hard corona in 100 % D-PBS Core-Shell Form Factor**	
Parameter	**Value**	**Parameter**	**Value**
Background	0.002,80 cm^{-1}	Background*	0.01 cm^{-1}
Volume fraction*	0.000106	Volume fraction*	0.000237
Core radius	201.1 Å	Core radius	201.1 Å
SLD of core	3.54×10^{-6} Å^{-2}	SLD of core	3.54×10^{-6} Å^{-2}
SLD of solvent	3.54×10^{-6} Å^{-2}	SLD of solvent	6.37×10^{-6} Å^{-2}
SLD of shell*	1.05×10^{-6} Å^{-2}	SLD of shell*	3×10^{-6} Å^{-2}
Shell thickness**	72.9 Å	Shell thickness**	72.9 Å
Polydispersity of core	0.16	Polydispersity of core	0.16
Polydispersity of shell	0.15	Polydispersity of shell	0.15

The thickness of the hard corona was found to be 72.9 Å. This value is within the sensible range as Bovine serum albumin (BSA), which is a relatively large plasma protein, is 80 Å long. This implies that the hard corona is about one or two monolayers thick, though much caution is required in interpretation as the fit is not optimal. The fitted curves do not fit the acquired curve and the values can not be treated as absolutely correct but rather as an indication of the potential structures that could contribute towards the total curve. Both curves for the hard corona appear more polydisperse than the well characterised polydispersity for the core suggests should be possible, again suggesting other structures are contributing. Polydispersity of the core is the major contributor to the smoothing of a core shell form factor. The polydispersity of the silica nanoparticles is well characterised and is not responsible for the curves acquired.

The acquired scattering profiles for SiO_2-COOH coated with a soft protein corona are shown in Figure 5.21. The scattering profile of the soft corona coated SiO_2-COOH in 100 % D-PBS, Figure 5.21 (top), shares all the key features with the hard corona coated SiO_2-COOH D-PBS. In the region at low Q, *i.e.* below 0.01 Å^{-1}, the soft corona-coated SiO_2-COOH has a higher degree of curvature, which is closer to a typical core shell form factor. The scattering profile in 60 % D, Figure 5.21 (bottom), shows at least two features at 0.006 and 0.02 Å^{-1}. These features appear to line up with the fitted core-shell form factor but the intensities of the features differ.

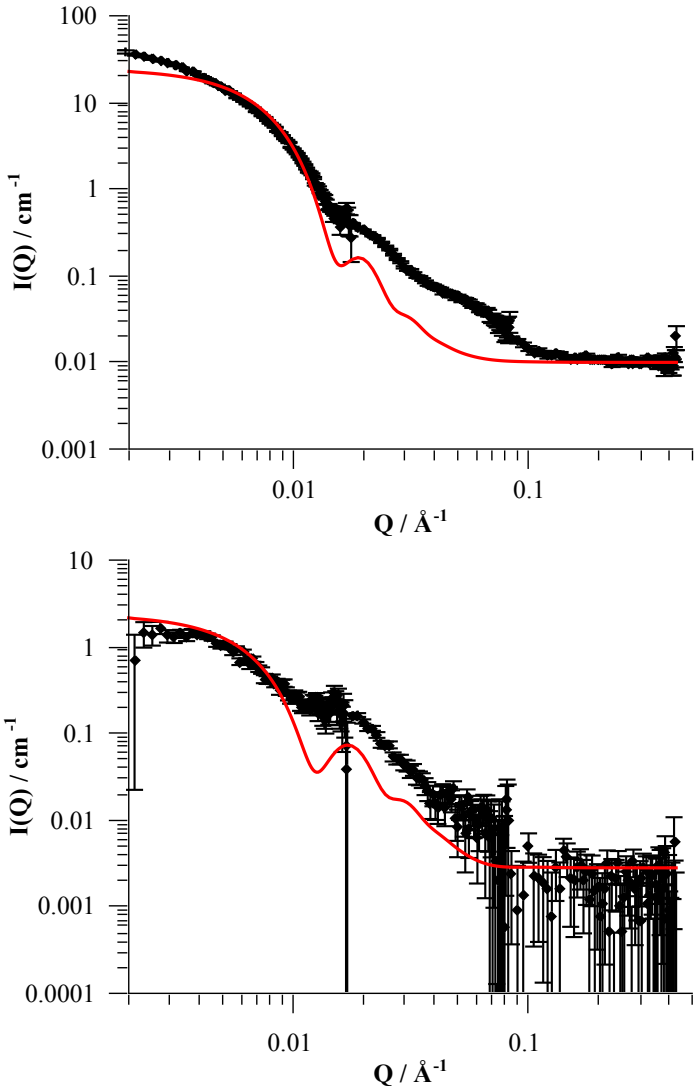

Figure 5.21: The scattering profiles for SiO_2-COOH with a soft protein corona in 100 % D-PBS (top) and 60 % D-PBS (bottom).

The soft corona-coated SiO_2-COOH was fitted in an identical way to the hard corona-coated particles and the parameters of the fitted curves are shown in Table 5.8. The parameters of the silica nanoparticle were taken from the fit of the bare particle and fixed at these values. As with the soft corona coated nanoparticles in 100 % D-PBS the SLD of the shell had a tendency to move to values lower than sensible to increase the difference between SLDs. Consequently, the SLD was fixed at 3×10^{-6} Å^{-2}. The shell SLD was allowed to float in the 60 % D-PBS fit. The result was the movement towards the value of the solvent. The shell thickness was the locked parameter in the simultaneous fit and was given as 85.4 Å, which is a realistic value when compared to larger serum proteins. This value is very similar to that of the hard corona, which was 72.9 Å.

Table 5.8: Parameters of the simultaneous fit for SiO_2-COOH with soft corona. Parameters with a star were fitted. A double star signifies the parameter was locked to the counterpart in a simultaneous fit.

SiO_2-COOH with soft corona in 60 % D-PBS Core-Shell Form Factor		**SiO_2-COOH with soft corona in 100 % D-PBS Core-Shell Form Factor**	
Parameter	**Value**	**Parameter**	**Value**
Background*	$0.001\ cm^{-1}$	Background*	$0.0045\ cm^{-1}$
Volume fraction*	0.00345	Volume fraction*	0.000122
Core radius	201.1 Å	Core radius	201.1 Å
SLD of core	3.54×10^{-6} Å^{-2}	SLD of core	3.54×10^{-6} Å^{-2}
SLD of solvent	3.54×10^{-6} Å^{-2}	SLD of solvent	6.37×10^{-6} Å^{-2}
SLD of shell*	3.30×10^{-6} Å^{-2}	SLD of shell	3×10^{-6} Å^{-2}
Shell thickness**	84.4 Å	Shell thickness**	84.4 Å
Polydispersity of core	0.16	Polydispersity of core	0.16
Polydispersity of shell	0.15	Polydispersity of shell	0.15

5.4.3 Conclusion

The scattering profiles acquired using D11 were too complicated to fit using simple geometric form factors. It is likely that there is another structure which is contributing towards the observed profile. The existence of multiple particles coated with a corona, identified as dimers and trimers, has been demonstrated when preparation of samples when using centrifugal preparations has been demonstrated by Walczyk *et al.*[241] The DLS of the hard corona coated SiO_2-COOH studied suggested that an artefact was introduced during the cleaning process. This reduces the confidence in the outcomes of the fitting.

There is also a strong possibility that a core-shell model is an over-simplification of the system. For instance, defining the end of the soft corona may be a similar situation to defining edge of the atmosphere or an electrostatic double-layer. In this case the core-shell model would be inappropriate. Moving too far from simple models requires more detailed knowledge of the system. Fitting programs contain many models but the majority of non-simple models available on fitting software have been developed with particular systems in mind. Simplification of the profiles may also be achieved by studying more refined systems such as single protein studies or a more focussed study on the hard corona.

5.5 Conclusions

The study of the protein corona formed upon amphiphilic polymer coated nanocrystals using SANS was attempted. Scaling the synthesis of the polymer coated nanocrystals to the concentrations required by SANS was hindered by the removal of the excess polymer

which is a consequence of the water transfer procedure used. Separation of the polymer coated nanocrystals from excess unbound polymer was performed on a small scale but could not be scaled up to concentrations required for SANS.

The first set of SANS experiments demonstrated that the organic ligands on nanocrystals can be used with a core-shell form factor to determine an effective ligand shell thickness. Although the set of results was small the differences in the ligand shell thickness modelled were interesting and warrant further study. Information of ligand packing could be useful in future modelling of the amphiphilic bilayer on different particles. Once the removal of excess polymer is achieved, this can be extended to determine the thickness of the polymer bilayer. The polymer coated nanocrystals showed scattering profiles which were dominated by free polymer producing profiles which could not be modelled using a core-shell form factors with approximate expected dimensions. The profile generated by the excess of free polymer dominated the observed profile preventing observation of the polymer coated nanocrystals.

The second set of SANS experiments examined the protein corona formed on silica nanoparticles as an alternative to polymer coated nanocrystals. The acquired scattering profiles for protein coated silica nanoparticles showed a distinct difference from the bare nanoparticles. An attempt to fit the scattering profiles was performed using core shell form factors. The fitted profiles showed characteristics that mimicked parts of the acquired profiles but did not explain the features fully. A possibility is that there is a mixture of structures, which increases the complexity of the fitting. Another possibility is that the use of a core-shell form factor is not suitable to model the corona, in particular the soft corona.

CHAPTER 6

Conclusion and future work

6.1 Conclusion to the thesis

In Chapter 3 a method for functionalising nanocrystals with a thin silica layer over an amphiphilic polymer foundation was presented. A foundation of poly(styrene-*co*-maleic anhydride) was formed upon the particle by the hydrophobic interaction between the pendant phenyl groups and the nanocrystal ligands. The anhydride rings were then reacted with (3-aminopropyl)triethoxy silane which subsequently polymerised to form a silica shell.

The layer was characterised with a wide selection of techniques, which allowed the chemical composition of the layer to be identified and the product was identified as containing both the amphiphilic polymer foundation and silica. The location of the layer was proven using EDX and EFTEM proving that the silica was situated on the nanocystals.

In Chapter 4 families of pro-amphiphilic polymers containing the activated ester monomer *N*-(acryloyloxy)succinimide and amphiphilic polymers containing acryloyloxy poly(ethylene glycol) monomethyl ether were synthesised, characterised and had their ability to water transfer nanocrystals tested. It was found that poly(*N*-(acryloyloxy)-succinimide-*co*-styrene) polymers could perform a partial transfer of the nanocrystals tested. The ability to transfer particles increased with decreasing polymer chain length, an observation similar to that of with their synthesised poly(styrene-*alt*-maleic anhydride).[207]

The poly(*N*-(acryloyloxy)succinimide-*co*-octadecylacrylate) polymers were found to be ineffective at transferring nanocrystals. No partial transfers were observed. This may be attributed to poor choice of the pendant alkyl chain. A possible reason for incompatibility is poor interactions between ligand and polymer due to size differences. This may explain the difference between synthesised octadecylacylate and styrene copolymers.

Both types of poly(acryloyloxy poly(ethylene glycol) monomethyl ether-*co*-octadecyl acrylate) were unable to achieve any transfer of the Fe_3O_4 nanocrystals. This could be due

to poor choice of the pendant alkyl chains as with the poly(*N*-(acryloyloxy)succinimide-*co*-octadecylacrylate) polymer or how the polymer behaves in chloroform as the solvent is removed. It is likely that the acryloyloxy poly(ethylene glycol) monomethyl ether has significantly different properties in solution in comparison to the commercially available polymers that have been used successfully.

In Chapter 5, the study of the protein corona formed upon nanocrystals and silica nanoparticles was attempted using SANS. The first experiment on amphiphilic polymer systems revealed that the polymer coated nanocrystals contained an excess of unbound polymer. The excess could be removed using SEC when working on a small scale but became an issue after scaling up the particle concentration to the concentrations required for SANS.

The second experiment focussed on the corona formed on silica nanoparticles. The information from this would provide valuable information on the structure of the corona and allow the development of fitting processes to interpret the scattering profiles obtained. Soft and hard coronas were observed using SANS but could not be fitted due to the samples being too complex for simple SANS models. It is not clear if the complexity arises from the corona around a particle or if other species exist contributing to the observed scattering patterns.

6.2 Future work

To expand the work conducted in Chapter 3, the layer synthesised could be increased in thickness by introducing TEOS into the layer growth phase. The ability to deliver controlled shell thicknesses would be an attractive extension to this work. The poor reproducibility of the silica coating methods discussed in Section 3.1.2.3 is suspected to be due to the water content of the organic solvents in which the reactions are performed. In this work the reproducibility was improved by controlling the temperature and slowing the reaction further by use of triethoxysilanes and not trimethoxysilanes, although the question of water content has not been addressed. Control over water could be addressed by using solvents containing defined water content by salt hydrate pairs to buffer the water content.

The polymers synthesised in Chapter 4 were unable to perform complete transfers of Fe_3O_4 nanocrystals. An extension of this work would be to synthesise a series of polymers where the length of the pendant alkyl chain decreases to see if this has any influence on transfer ability. There are other activated ester containing monomers which could potentially be explored, such as pentafluorophenyl acrylate, although the partial transfers observed do not suggest (*N*-(acryloyloxy)succinimide is the source of the poor transfers observed.

Investigation of monomers containing shorter poly(ethylene glycol) chains could improve transfer. Pendent poly(ethylene glycol) chains which are longer than the amphiphilic polymer backbone are likely to dominate the properties of the resulting polymer. Although,

the use of shorter poly(ethylene glycol) chains could compromise colloidal stability of the coated nanocrystals.

The studies of corona formation upon nanocrystals and model nanoparticle systems did not yield any reliable information on the dimensions of the coronas formed. The corona is a complex system made from a large potential range of proteins, which have different affinities, packing abilities, sizes and solvations. Studying a single protein system, in particular the hard corona, may allow the development of the fitting process which can be expanded for the more sophisticated corona formed at media which resembles *in vivo* systems more closely. For instance, a study of HSA on silica particles of different surface funtionalisations could allow the use of existing form factors or the development of a custom form factor for the protein corona. If sample preparation is introducing artefacts, SANS measurements of the corona-nanoparticle system *in situ* would allow comparisons to be made to the isolated corona-nanoparticle system.

References

(1) R. P. Feynman, 'There's plenty of room at the bottom', *J. Microelectromech. S.*, 1992, **1**, 60–66, DOI: 10.1109/84.128057 (cit. on p. 1).

(2) M. Faraday, 'The Bakerian lecture: Experimental relations of gold (and other metals) to light', *Phil. Trans. R. Soc. Lond.*, 1857, **147**, 145–181, DOI: 10.1098/rstl.1857.0011 (cit. on pp. 2, 22).

(3) R. Zsigmondy, *Colloids and the ultramicroscope: A manual of colloid chemistry and ultramicroscopy*, trans. by J. Alexander, J. Wiley, 1909 (cit. on p. 2).

(4) H. W. Kroto, J. R. Heath, S. C. O'Brien, R. F. Curl and R. E. Smalley, 'C_{60}: Buckminsterfullerene', *Nature*, 1985, **318**, 162–163, DOI: 10.1038/318162a0 (cit. on p. 2).

(5) C. N. R. Rao, P. J. Thomas and G. U. Kulkarni, *Nanocrystals: Synthesis, properties and applications*, Springer Berlin, Heidelberg, 2007, ISBN: 3-540-68751-3 (cit. on pp. 2, 6, 21).

(6) S. Eustis and M. A. El-Sayed, 'Why gold nanoparticles are more precious than pretty gold: Noble metal surface plasmon resonance and its enhancement of the radiative and nonradiative properties of nanocrystals of different shapes', *Chem. Soc. Rev.*, 2006, **35**, 209–217, DOI: 10.1039/b514191e (cit. on p. 3).

(7) G. Mie, 'Beiträge zur Optik trüber Medien, speziell kolloidaler Metallösungen', *Ann. Physik*, 1908, **330**, 377–445, DOI: 10.1002/andp.19083300302 (cit. on p. 3).

(8) S. Link and M. A. El-Sayed, 'Spectral properties and relaxation dynamics of surface plasmon electronic oscillations in gold and silver nanodots and nanorods', *J. Phys. Chem. B*, 1999, **103**, 8410–8426, DOI: 10.1021/jp9917648 (cit. on p. 3).

(9) K. A. Willets and R. P. Van Duyne, 'Localized surface plasmon resonance spectroscopy and sensing', *Annu. Rev. Phys. Chem.*, 2007, **58**, 267–297, DOI: 10.1146/annurev.physchem.58.032806.104607 (cit. on p. 3).

(10) R. Philip, P. Chantharasupawong, H. Qian, R. Jin and J. Thomas, 'Evolution of nonlinear optical properties: From gold atomic clusters to plasmonic nanocrystals', *Nano Lett.*, 2012, **12**, 4661–4667, DOI: 10.1021/nl301988v (cit. on p. 3).

(11) L. E. Brus, 'A simple model for the ionization potential, electron affinity, and aqueous redox potentials of small semiconductor crystallites', *J. Chem. Phys.*, 1983, **79**, 5566–5571, DOI: 10.1063/1.445676 (cit. on p. 4).

(12) L. E. Brus, 'Electron-electron and electron-hole interactions in small semiconductor crystallites: The size dependence of the lowest excited electronic state', *J. Chem. Phys.*, 1984, **80**, 4403–4409, DOI: 10.1063/1.447218 (cit. on p. 4).

(13) T. Kippeny, L. A. Swafford and S. J. Rosenthal, 'Semiconductor nanocrystals: A powerful visual aid for introducing the particle in a box', *J. Chem. Educ.*, 2002, **79**, 1094, DOI: 10.1021/ed079p1094 (cit. on p. 4).

(14) S. P. Gubin, N. A. Kataeva and G. B. Khomutov, 'Promising avenues of research in nanoscience: Chemistry of semiconductor nanoparticles', *Russ. Chem. Bull., Int. Ed.*, 2005, **54**, 827–852, DOI: 10.1007/s11172-005-0331-3 (cit. on p. 4).

(15) A. M. Smith and S. Nie, 'Semiconductor nanocrystals: Structure, properties, and band gap engineering', *Acc. Chem. Res.*, 2009, **43**, 190–200, DOI: 10.1021/ar9001069 (cit. on p. 4).

(16) U. Resch-Genger, M. Grabolle, S. Cavaliere-Jaricot, R. Nitschke and T. Nann, 'Quantum dots versus organic dyes as fluorescent labels', *Nat. Methods*, 2008, **5**, 763–775, DOI: 10.1038/nmeth.1248 (cit. on pp. 4, 15).

(17) P. Reiss, M. Protière and L. Li, 'Core/shell semiconductor nanocrystals', *Small*, 2009, **5**, 154–168, DOI: 10.1002/smll.200800841 (cit. on p. 5).

(18) R. M. Cornell and U. Schwertmann, *The iron oxides: Structure, properties, reactions, occurrences and uses*, Wiley VCH, 2nd edn., 2003, ISBN: 3-527-30274-3 (cit. on p. 5).

(19) S. Laurent, D. Forge, M. Port, A. Roch, C. Robic, L. Vander Elst and R. N. Muller, 'Magnetic iron oxide nanoparticles: Synthesis, stabilization, vectorization, physicochemical characterizations, and biological applications', *Chem. Rev.*, 2008, **108**, 2064–2110, DOI: 10.1021/cr068445e (cit. on p. 5).

(20) D. S. Mathew and R.-S. Juang, 'An overview of the structure and magnetism of spinel ferrite nanoparticles and their synthesis in microemulsions', *Chem. Eng. J.*, 2007, **129**, 51–65, DOI: 10.1016/j.cej.2006.11.001 (cit. on p. 6).

(21) R. Qiao, C. Yang and M. Gao, 'Superparamagnetic iron oxide nanoparticles: From preparations to *in vivo* MRI applications', *J. Mater. Chem.*, 2009, **19**, 6274–6293, DOI: 10.1039/b902394a (cit. on pp. 6, 16).

(22) R. A. Sperling and W. J. Parak, 'Surface modification, functionalization and bioconjugation of colloidal inorganic nanoparticles', *Phil. Trans. R. Soc. A*, 2010, **368**, 1333–1383, DOI: 10.1098/rsta.2009.0273 (cit. on p. 7).

(23) D. Shaw, *Introduction to colloid and surface chemistry*, Butterworth-Heinemann, 4th edn., 1992, ISBN: 0750611820 (cit. on pp. 7, 17).

(24) J. Turkevich, P. C. Stevenson and J. Hillier, 'A study of the nucleation and growth processes in the synthesis of colloidal gold', *Discuss. Faraday Soc.*, 1951, **11**, 55–75, DOI: 10.1039/df9511100055 (cit. on p. 9).

(25) A. C. Templeton, W. P. Wuelfing and R. W. Murray, 'Monolayer-protected cluster molecules', *Acc. Chem. Res.*, 2000, **33**, 27–36, DOI: 10.1021/ar9602664 (cit. on p. 9).

(26) M. Brust, M. Walker, D. Bethell, D. J. Schiffrin and R. Whyman, 'Synthesis of thiol-derivatised gold nanoparticles in a two-phase Liquid-Liquid system', *J. Chem. Soc., Chem. Commun.*, 1994, 801, DOI: 10.1039/c39940000801 (cit. on pp. 9, 22, 24).

(27) M. Brust, J. Fink, D. Bethell, D. J. Schiffrin and C. Kiely, 'Synthesis and reactions of functionalised gold nanoparticles', *J. Chem. Soc., Chem. Commun.*, 1995, 1655, DOI: 10.1039/c39950001655 (cit. on pp. 9, 22).

(28) M. J. Hostetler, A. C. Templeton and R. W. Murray, 'Dynamics of place-exchange reactions on monolayer-protected gold cluster molecules', *Langmuir*, 1999, **15**, 3782–3789, DOI: 10.1021/la981598f (cit. on p. 9).

(29) M. Green, 'The nature of quantum dot capping ligands', *J. Mater. Chem.*, 2010, **20**, 5797–5809, DOI: 10.1039/c0jm00007h (cit. on p. 9).

(30) H. Döllefeld, K. Hoppe, J. Kolny, K. Schilling, H. Weller and A. Eychmüller, 'Investigations on the stability of thiol stabilized semiconductor nanoparticles', *Phys. Chem. Chem. Phys.*, 2002, **4**, 4747–4753, DOI: 10.1039/b202101c (cit. on p. 9).

(31) Y. Zhang and A. Clapp, 'Overview of stabilizing ligands for biocompatible quantum dot nanocrystals', *Sensors*, 2011, **11**, 11036–11055, DOI: 10.3390/s111211036 (cit. on p. 9).

(32) C. Bullen and P. Mulvaney, 'The effects of chemisorption on the luminescence of CdSe quantum dots', *Langmuir*, 2006, **22**, 3007–3013, DOI: 10.1021/la051898e (cit. on p. 9).

(33) G. Kalyuzhny and R. W. Murray, 'Ligand effects on optical properties of CdSe nanocrystals', *J. Phys. Chem. B*, 2005, **109**, 7012–7021, DOI: 10.1021/jp045352x (cit. on p. 9).

(34) F. Dubois, B. Mahler, B. Dubertret, E. Doris and C. Mioskowski, 'A versatile strategy for quantum dot ligand exchange', *J. Am. Chem. Soc.*, 2006, **129**, 482–483, DOI: 10.1021/ja067742y (cit. on p. 9).

(35) I. Potapova, R. Mruk, S. Prehl, R. Zentel, T. Basché and A. Mews, 'Semiconductor nanocrystals with multifunctional polymer ligands', *J. Am. Chem. Soc.*, 2002, **125**, 320–321, DOI: 10.1021/ja028641c (cit. on p. 9).

(36) A. M. Smith and S. Nie, 'Minimizing the hydrodynamic size of quantum dots with multifunctional multidentate polymer ligands', *J. Am. Chem. Soc.*, 2008, **130**, 11278–11279, DOI: 10.1021/ja804306c (cit. on p. 9).

(37) K. Susumu, H. T. Uyeda, I. L. Medintz, T. Pons, J. B. Delehanty and H. Mattoussi, 'Enhancing the stability and biological functionalities of quantum dots *via* compact multifunctional ligands', *J. Am. Chem. Soc.*, 2007, **129**, 13987–13996, DOI: 10.1021/ja0749744 (cit. on p. 9).

(38) K. Susumu, B. C. Mei and H. Mattoussi, 'Multifunctional ligands based on dihydrolipoic acid and polyethylene glycol to promote biocompatibility of quantum dots', *Nat. Protocols*, 2009, **4**, 424–436, DOI: 10.1038/nprot.2008.247 (cit. on p. 9).

(39) M.-A. Neouze and U. Schubert, 'Surface modification and functionalization of metal and metal oxide nanoparticles by organic ligands', *Monatsh. Chem.*, 2008, **139**, 183–195, DOI: 10.1007/s00706-007-0775-2 (cit. on p. 10).

(40) E. Amstad, M. Textor and E. Reimhult, 'Stabilization and functionalization of iron oxide nanoparticles for biomedical applications', *Nanoscale*, 2011, **3**, 2819–2843, DOI: 10.1039/c1nr10173k (cit. on p. 10).

(41) M. Lattuada and T. A. Hatton, 'Functionalization of monodisperse magnetic nanoparticles', *Langmuir*, 2007, **23**, 2158–2168, DOI: 10.1021/la062092x (cit. on pp. 10, 24).

(42) H.-T. Song, J.-S. Choi, Y.-M. Huh, S. Kim, Y.-W. Jun, J.-S. Suh and J. Cheon, 'Surface modulation of magnetic nanocrystals in the development of highly efficient magnetic resonance probes for intracellular labeling', *J. Am. Chem. Soc.*, 2005, **127**, 9992–9993, DOI: 10.1021/ja051833y (cit. on p. 10).

(43) M. A. White, J. A. Johnson, J. T. Koberstein and N. J. Turro, 'Toward the syntheses of universal ligands for metal oxide surfaces: Controlling surface functionality through click chemistry', *J. Am. Chem. Soc.*, 2006, **128**, 11356–11357, DOI: 10.1021/ja064041s (cit. on p. 10).

(44) C. Xu, K. Xu, H. Gu, R. Zheng, H. Liu, X. Zhang, Z. Guo and B. Xu, 'Dopamine as a robust anchor to immobilize functional molecules on the iron oxide shell of magnetic nanoparticles', *J. Am. Chem. Soc.*, 2004, **126**, 9938–9939, DOI: 10.1021/ja0464802 (cit. on p. 10).

(45) J. Xie, C. Xu, Z. Xu, Y. Hou, K. L. Young, S. X. Wang, N. Pourmand and S. Sun, 'Linking hydrophilic macromolecules to monodisperse magnetite (Fe_3O_4) nanoparticles *via* trichloro-*s*-triazine', *Chem. Mater.*, 2006, **18**, 5401–5403, DOI: 10.1021/cm061793c (cit. on p. 10).

(46) E. Amstad, T. Gillich, I. Bilecka, M. Textor and E. Reimhult, 'Ultrastable iron oxide nanoparticle colloidal suspensions using dispersants with catechol-derived anchor groups', *Nano Lett.*, 2009, **9**, 4042–4048, DOI: 10.1021/nl902212q (cit. on p. 10).

(47) E. Amstad, S. Zurcher, A. Mashaghi, J. Y. Wong, M. Textor and E. Reimhult, 'Surface functionalization of single superparamagnetic iron oxide nanoparticles for targeted magnetic resonance imaging', *Small*, 2009, **5**, 1334–1342, DOI: 10.1002/smll.200801328 (cit. on p. 10).

(48) Y. Lalatonne, C. Paris, J. M. Serfaty, P. Weinmann, M. Lecouvey and L. Motte, 'Bis-phosphonates-ultra small superparamagnetic iron oxide nanoparticles: A platform towards diagnosis and therapy', *Chem. Commun.*, 2008, 2553–2555, DOI: 10.1039/b801911h (cit. on p. 10).

(49) R. De Palma, S. Peeters, M. J. Van Bael, H. Van den Rul, K. Bonroy, W. Laureyn, J. Mullens, G. Borghs and G. Maes, 'Silane ligand exchange to make hydrophobic superparamagnetic nanoparticles water-dispersible', *Chem. Mater.*, 2007, **19**, 1821–1831, DOI: 10.1021/cm0628000 (cit. on p. 10).

(50) J. A. Kloepfer, S. E. Bradforth and J. L. Nadeau, 'Photophysical properties of biologically compatible CdSe quantum dot structures', *J. Phys. Chem. B*, 2005, **109**, 9996–10003, DOI: 10.1021/jp044581g (cit. on p. 10).

(51) J. Aldana, Y. A. Wang and X. Peng, 'Photochemical instability of CdSe nanocrystals coated by hydrophilic thiols', *J. Am. Chem. Soc.*, 2001, **123**, 8844–8850, DOI: 10.1021/ja016424q (cit. on p. 10).

(52) H. Fan, 'Nanocrystal-micelle: synthesis, self-assembly and application', *Chem. Commun.*, 2008, 1383–1394, DOI: 10.1039/b711251n (cit. on p. 10).

(53) J. Shimoiizaka, K. Nakatsuka, T. Fujita and A. Kounosu, 'Sink-float separators using permanent magnets and water based magnetic fluid', *IEEE T. Magn.*, 1980, **16**, 368–371, DOI: 10.1109/tmag.1980.1060588 (cit. on p. 11).

(54) V. Patil, K. S. Mayya, S. D. Pradhan and M. Sastry, 'Evidence for novel interdigitated bilayer formation of fatty acids during three-dimensional self-assembly on silver colloidal particles', *J. Am. Chem. Soc.*, 1997, **119**, 9281–9282, DOI: 10.1021/ja971161e (cit. on p. 11).

(55) L. Shen, P. E. Laibinis and T. A. Hatton, 'Bilayer surfactant stabilized magnetic fluids: Synthesis and interactions at interfaces', *Langmuir*, 1999, **15**, 447–453, DOI: 10.1021/la9807661 (cit. on p. 11).

(56) A. Prakash, H. Zhu, C. J. Jones, D. N. Benoit, A. Z. Ellsworth, E. L. Bryant and V. L. Colvin, 'Bilayers as phase transfer agents for nanocrystals prepared in nonpolar solvents', *ACS Nano*, 2009, **3**, 2139–2146, DOI: 10.1021/nn900373b (cit. on p. 11).

(57) B. Nikoobakht and M. A. El-Sayed, 'Evidence for bilayer assembly of cationic surfactants on the surface of gold nanorods', *Langmuir*, 2001, **17**, 6368–6374, DOI: 10.1021/la010530o (cit. on p. 11).

(58) A. Swami, A. Kumar and M. Sastry, 'Formation of water-dispersible gold nanoparticles using a technique based on surface-bound interdigitated bilayers', *Langmuir*, 2003, **19**, 1168–1172, DOI: 10.1021/la026523x (cit. on p. 11).

(59) H. Fan, K. Yang, D. M. Boye, T. Sigmon, K. J. Malloy, H. Xu, G. P. López and C. J. Brinker, 'Self-assembly of ordered, robust, three-dimensional gold nanocrystal/silica arrays', *Science*, 2004, **304**, 567–571, DOI: 10.1126/science.1095140 (cit. on pp. 11, 45).

(60) H. Fan, E. Leve, J. Gabaldon, A. Wright, R. E. Haddad and C. J. Brinker, 'Ordered two- and three-dimensional arrays self-assembled from water-soluble nanocrystal-micelles', *Adv. Mater.*, 2005, **17**, 2587–2590, DOI: 10.1002/adma.200501088 (cit. on p. 11).

(61) H. Fan, A. Wright, J. Gabaldon, A. Rodriguez, C. J. Brinker and Y.-B. Jiang, 'Three-dimensionally ordered gold nanocrystal/silica superlattice thin films synthesized *via* sol–gel self-assembly', *Adv. Funct. Mater.*, 2006, **16**, 891–895, DOI: 10.1002/adfm.200500603 (cit. on pp. 11, 45).

(62) B. Dubertret, P. Skourides, D. J. Norris, V. Noireaux, A. H. Brivanlou and A. Libchaber, '*In vivo* imaging of quantum dots encapsulated in phospholipid micelles', *Science*, 2002, **298**, 1759–1762, DOI: 10.1126/science.1077194 (cit. on p. 11).

(63) H. Fan, E. W. Leve, C. Scullin, J. Gabaldon, D. Tallant, S. Bunge, T. Boyle, M. C. Wilson and C. J. Brinker, 'Surfactant-assisted synthesis of water-soluble and biocompatible semiconductor quantum dot micelles', *Nano Lett.*, 2005, **5**, 645–648, DOI: 10.1021/nl0500171 (cit. on p. 11).

(64) O. Carion, B. Mahler, T. Pons and B. Dubertret, 'Synthesis, encapsulation, purification and coupling of single quantum dots in phospholipid micelles for their use in cellular and *in vivo* imaging', *Nat. Protocols*, 2007, **2**, 2383–2390, DOI: 10.1038/nprot.2007.351 (cit. on p. 11).

(65) H. Li, X. Wang, Z. Gao and Z. He, 'Gemini surfactant for fluorescent and stable quantum dots in aqueous solution', *Nanotechnology*, 2007, **18**, 205603, DOI: 10.1088/0957-4484/18/20/205603 (cit. on p. 11).

(66) H. Li and X. Wang, 'Single quantum dot-micelles coated with gemini surfactant for selective recognition of a cation and an anion in aqueous solutions', *Sensor. Actuat. B: Chem.*, 2008, **134**, 238–244, DOI: 10.1016/j.snb.2008.04.041 (cit. on p. 11).

(67) J. Rubio, M. A. Izquierdo, M. I. Burguete, F. Galindo and S. V. Luis, 'Photoluminescence of CdSe/ZnS core-shell quantum dots stabilized in water with a pseudopeptidic gemini surfactant', *Nanoscale*, 2011, **3**, 3613–3615, DOI: 10.1039/c1nr10680e (cit. on p. 11).

(68) H. Fan, Z. Chen, C. J. Brinker, J. Clawson and T. Alam, 'Synthesis of organo-silane functionalized nanocrystal micelles and their self-assembly', *J. Am. Chem. Soc.*, 2005, **127**, 13746–13747, DOI: 10.1021/ja053795o (cit. on pp. 11, 45).

(69) M. Gonzales and K. M. Krishnan, 'Phase transfer of highly monodisperse iron oxide nanocrystals with Pluronic F127 for biomedical applications', *J. Magn. Magn. Mater.*, 2007, **311**, 59–62, DOI: 10.1016/j.jmmm.2006.10.1150 (cit. on p. 11).

(70) F. Zhang, E. Lees, F. Amin, P. Rivera Gil, F. Yang, P. Mulvaney and W. J. Parak, 'Polymer-coated nanoparticles: A universal tool for biolabelling experiments', *Small*, 2011, **7**, 3113–3127, DOI: 10.1002/smll.201100608 (cit. on pp. 11, 70, 71).

(71) A. Quarta, A. Curcio, H. Kakwere and T. Pellegrino, 'Polymer coated inorganic nanoparticles: Tailoring the nanocrystal surface for designing nanoprobes with biological implications', *Nanoscale*, 2012, **4**, 3319–3334, DOI: 10.1039/c2nr30271c (cit. on pp. 11, 70, 71).

(72) N. Lala, S. P. Lalbegi, S. D. Adyanthaya and M. Sastry, 'Phase transfer of aqueous gold colloidal particles capped with inclusion complexes of cyclodextrin and alkanethiol molecules into chloroform', *Langmuir*, 2001, **17**, 3766–3768, DOI: 10.1021/la0015765 (cit. on p. 12).

(73) Y. Wang, J. F. Wong, X. Teng, X. Z. Lin and H. Yang, '"Pulling" nanoparticles into water: Phase transfer of oleic acid stabilized monodisperse nanoparticles into aqueous solutions of α-cyclodextrin', *Nano Lett.*, 2003, **3**, 1555–1559, DOI: 10.1021/nl034731j (cit. on p. 12).

(74) J. M. McMahon and S. R. Emory, 'Phase transfer of large gold nanoparticles to organic solvents with increased stability', *Langmuir*, 2006, **23**, 1414–1418, DOI: 10.1021/la0617560 (cit. on p. 12).

(75) W. Stöber, A. Fink and E. Bohn, 'Controlled growth of monodisperse silica spheres in the micron size range', *J. Colloid Interf. Sci.*, 1968, **26**, 62–69, DOI: 10.1016/0021-9797(68)90272-5 (cit. on pp. 13, 41).

(76) K. Osseo-Asare and F. Arriagada, 'Preparation of SiO_2 nanoparticles in a non-ionic reverse micellar system', *Colloid Surface.*, 1990, **50**, 321–339, DOI: 10.1016/0166-6622(90)80273-7 (cit. on pp. 13, 41, 43).

(77) D. Li, Q. He and J. Li, 'Smart core/shell nanocomposites: Intelligent polymers modified gold nanoparticles', *Adv. Colloid Interfac.*, 2009, **149**, 28–38, DOI: 10.1016/j.cis.2008.12.007 (cit. on p. 13).

(78) A. M. Smith, H. Duan, M. N. Rhyner, G. Ruan and S. Nie, 'A systematic examination of surface coatings on the optical and chemical properties of semiconductor quantum dots', *Phys. Chem. Chem. Phys.*, 2006, **8**, 3895–3903, DOI: 10.1039/b606572b (cit. on p. 13).

(79) C. Kirchner, T. Liedl, S. Kudera, T. Pellegrino, A. Muñoz Javier, H. E. Gaub, S. Stölzle, N. Fertig and W. J. Parak, 'Cytotoxicity of colloidal CdSe and CdSe/ZnS nanoparticles', *Nano Lett.*, 2004, **5**, 331–338, DOI: 10.1021/nl047996m (cit. on pp. 13, 40).

(80) J. Bear, G. Charron, M. T. Fernández-Argüelles, S. Massadeh, P. McNaughter and T. Nann, *In vivo* applications of inorganic nanoparticles, in *BetaSys: Systems biology of regulated exocytosis in pancreatic β-cells*, ed. B. Booß-Bavnbek, B. Klösgen, J. Larsen, F. Pociot and E. Renström, Springer New York, New York, NY, 2011, pp. 185–220, ISBN: 978-1-4419-6955-2, DOI: 10.1007/978-1-4419-6956-9_9 (cit. on pp. 14, 174).

(81) G. Han, P. Ghosh, M. De and V. M. Rotello, 'Drug and gene delivery using gold nanoparticles', *Nanobiotechnol.*, 2007, **3**, 40–45, DOI: 10.1007/s12030-007-0005-3 (cit. on p. 14).

(82) P. Ghosh, G. Han, M. De, C. K. Kim and V. M. Rotello, 'Gold nanoparticles in delivery applications', *Adv. Drug Deliver. Rev.*, 2008, **60**, 1307–1315, DOI: 10.1016/j.addr.2008.03.016 (cit. on p. 14).

(83) M. Mahmoudi, S. Sant, B. Wang, S. Laurent and T. Sen, 'Superparamagnetic iron oxide nanoparticles (SPIONs): Development, surface modification and applications in chemotherapy', *Adv. Drug Deliver. Rev.*, 2011, **63**, 24–46, DOI: 10.1016/j.addr.2010.05.006 (cit. on p. 14).

(84) S. Laurent, S. Dutz, U. O. Häfeli and M. Mahmoudi, 'Magnetic fluid hyperthermia: Focus on superparamagnetic iron oxide nanoparticles', *Adv. Colloid Interfac.*, 2011, **166**, 8–23, DOI: 10.1016/j.cis.2011.04.003 (cit. on pp. 14, 15).

(85) E. B. Dickerson, E. C. Dreaden, X. Huang, I. H. El-Sayed, H. Chu, S. Pushpanketh, J. F. McDonald and M. A. El-Sayed, 'Gold nanorod assisted near-infrared plasmonic photothermal therapy (PPTT) of squamous cell carcinoma in mice', *Cancer Lett.*, 2008, **269**, 57–66, DOI: 10.1016/j.canlet.2008.04.026 (cit. on p. 15).

(86) G. Charron, T. Stuchinskaya, D. R. Edwards, D. A. Russell and T. Nann, 'Insights into the mechanism of quantum dot-sensitized singlet oxygen production for photodynamic therapy', *J. Phys. Chem. C*, 2012, **116**, 9334–9342, DOI: 10.1021/jp301103f (cit. on p. 15).

(87) J. M. Tsay, M. Trzoss, L. Shi, X. Kong, M. Selke, M. E. Jung and S. Weiss, 'Singlet oxygen production by peptide-coated quantum dot-photosensitizer conjugates', *J. Am. Chem. Soc.*, 2007, **129**, 6865–6871, DOI: 10.1021/ja070713i (cit. on p. 15).

(88) D. K. Chatterjee, L. S. Fong and Y. Zhang, 'Nanoparticles in photodynamic therapy: An emerging paradigm', *Adv. Drug Deliver. Rev.*, 2008, **60**, 1627–1637, DOI: 10.1016/j.addr.2008.08.003 (cit. on p. 15).

(89) F. Wang, D. Banerjee, Y. Liu, X. Chen and X. Liu, 'Upconversion nanoparticles in biological labeling, imaging and therapy', *Analyst*, 2010, **135**, 1839–1854, DOI: 10.1039/c0an00144a (cit. on pp. 15, 16).

(90) T. Stuchinskaya, M. Moreno, M. J. Cook, D. R. Edwards and D. A. Russell, 'Targeted photodynamic therapy of breast cancer cells using antibody-phthalocyanine-gold nanoparticle conjugates', *Photochem. Photobiol. Sci.*, 2011, **10**, 822–831, DOI: 10.1039/c1pp05014a (cit. on p. 15).

(91) X. Michalet, F. F. Pinaud, L. A. Bentolila, J. M. Tsay, S. Doose, J. J. Li, G. Sundaresan, A. M. Wu, S. S. Gambhir and S. Weiss, 'Quantum dots for live cells, *in vivo* imaging, and diagnostics', *Science*, 2005, **307**, 538–544, DOI: 10.1126/science.1104274 (cit. on p. 15).

(92) S. Jiang, M. K. Gnanasammandhan and Y. Zhang, 'Optical imaging-guided cancer therapy with fluorescent nanoparticles', *J. R. Soc. Interface*, 2010, **7**, 3–18, DOI: 10.1098/rsif.2009.0243 (cit. on pp. 15, 16).

(93) L. Tong, Q. Wei, A. Wei and J.-X. Cheng, 'Gold nanorods as contrast agents for biological imaging: Optical properties, surface conjugation and photothermal effects', *Photochem. Photobiol.*, 2009, **85**, 21–32, DOI: 10.1111/j.1751-1097.2008.00507.x (cit. on p. 16).

(94) Q. Zhang, N. Iwakuma, P. Sharma, B. M. Moudgil, C. Wu, J. McNeill and S. R. Grobmyer, 'Gold nanoparticles as a contrast agent for *in vivo* tumor imaging with photoacoustic tomography', *Nanotechnology*, 2009, **20**, 395102, DOI: 10.1088/0957-4484/20/39/395102 (cit. on p. 16).

(95) P. V. Kamat, 'Quantum dot solar cells. Semiconductor nanocrystals as light harvesters', *J. Phys. Chem. C*, 2008, **112**, 18737–18753, DOI: 10.1021/jp806791s (cit. on p. 16).

(96) F. Hetsch, X. Xu, H. Wang, S. V. Kershaw and A. L. Rogach, 'Semiconductor nanocrystal quantum dots as solar cell components and photosensitizers: Material, charge transfer, and separation aspects of some device topologies', *J. Phys. Chem. Lett.*, 2011, **2**, 1879–1887, DOI: 10.1021/jz200802j (cit. on p. 16).

(97) T. Nann, S. K. Ibrahim, P.-M. Woi, S. Xu, J. Ziegler and C. J. Pickett, 'Water splitting by visible light: A nanophotocathode for hydrogen production', *Angew. Chem. Int. Ed.*, 2010, **49**, 1574–1577, DOI: 10.1002/anie.200906262 (cit. on p. 16).

(98) V. Wood and V. Bulović, 'Colloidal quantum dot light-emitting devices', *Nano Rev.*, 2010, **1**, 5202, DOI: 10.3402/nano.v1i0.5202 (cit. on p. 16).

(99) P. O. Anikeeva, J. E. Halpert, M. G. Bawendi and V. Bulović, 'Quantum dot light-emitting devices with electroluminescence tunable over the entire visible spectrum', *Nano Lett.*, 2009, **9**, 2532–2536, DOI: 10.1021/nl9002969 (cit. on p. 16).

(100) J. Park, J. Joo, S. G. Kwon, Y. Jang and T. Hyeon, 'Synthesis of monodisperse spherical nanocrystals', *Angew. Chem. Int. Ed.*, 2007, **46**, 4630–4660, DOI: 10.1002/anie.200603148 (cit. on pp. 17, 20).

(101) V. A. Hackley and C. F. Ferraris, *NIST recommended practice guide: The use of nomenclature in dispersion science and technology*, Special Publication 960-3, National Institute of Standards and Technology, 2001 (cit. on p. 17).

(102) E. E. Finney and R. G. Finke, 'Nanocluster nucleation and growth kinetic and mechanistic studies: A review emphasizing transition-metal nanoclusters', *J. Colloid Interf. Sci.*, 2008, **317**, 351–374, DOI: 10.1016/j.jcis.2007.05.092 (cit. on pp. 18–20).

(103) D. W. Oxtoby, 'Nucleation of first-order phase transitions', *Acc. Chem. Rev.*, 1998, **31**, 91–97, DOI: 10.1021/ar9702278 (cit. on p. 18).

(104) V. K. LaMer and R. H. Dinegar, 'Theory, production and mechanism of formation of monodispersed hydrosols', *J. Am. Chem. Soc.*, 1950, **72**, 4847–4854, DOI: 10.1021/ja01167a001 (cit. on pp. 18, 19).

(105) S. G. Kwon and T. Hyeon, 'Formation mechanisms of uniform nanocrystals *via* hot-injection and heat-up methods', *Small*, 2011, **7**, 2685–2702, DOI: 10.1002/smll.201002022 (cit. on pp. 19, 22, 23).

(106) J. van Embden, J. E. Sader, M. Davidson and P. Mulvaney, 'Evolution of colloidal nanocrystals: Theory and modeling of their nucleation and growth', *J. Phys. Chem. C*, 2009, **113**, 16342–16355, DOI: 10.1021/jp9027673 (cit. on p. 20).

(107) B. V. Enüstün and J. Turkevich, 'Coagulation of colloidal gold', *J. Am. Chem. Soc.*, 1963, **85**, 3317–3328, DOI: 10.1021/ja00904a001 (cit. on p. 22).

(108) C. B. Murray, D. J. Norris and M. G. Bawendi, 'Synthesis and characterization of nearly monodisperse CdE (E = sulfur, selenium, tellurium) semiconductor nanocrystallites', *J. Am. Chem. Soc.*, 1993, **115**, 8706–8715, DOI: 10.1021/ja00072a025 (cit. on p. 22).

(109) C. de Mello Donegá, P. Liljeroth and D. Vanmaekelbergh, 'Physicochemical evaluation of the hot-injection method, a synthesis route for monodisperse nanocrystals', *Small*, 2005, **1**, 1152–1162, DOI: 10.1002/smll.200500239 (cit. on p. 23).

(110) S. Xu, J. Ziegler and T. Nann, 'Rapid synthesis of highly luminescent InP and InP/ZnS nanocrystals', *J. Mater. Chem.*, 2008, **18**, 2653–2656, DOI: 10.1039/b803263g (cit. on p. 23).

(111) T. Hyeon, S. S. Lee, J. Park, Y. Chung and H. B. Na, 'Synthesis of highly crystalline and monodisperse maghemite nanocrystallites without a size-selection process', *J. Am. Chem. Soc.*, 2001, **123**, 12798–12801, DOI: 10.1021/ja016812s (cit. on p. 23).

(112) S. Sun and H. Zeng, 'Size-controlled synthesis of magnetite nanoparticles', *J. Am. Chem. Soc.*, 2002, **124**, 8204–8205, DOI: 10.1021/ja026501x (cit. on p. 23).

(113) J. Park, K. An, Y. Hwang, J.-G. Park, H.-J. Noh, J.-Y. Kim, J.-H. Park, N.-M. Hwang and T. Hyeon, 'Ultra-large-scale syntheses of monodisperse nanocrystals', *Nat. Mater.*, 2004, **3**, 891–895, DOI: 10.1038/nmat1251 (cit. on p. 23).

(114) S. Xu, S. Kumar and T. Nann, 'Rapid synthesis of high-quality InP nanocrystals', *J. Am. Chem. Soc.*, 2006, **128**, 1054–1055, DOI: 10.1021/ja057676k (cit. on p. 23).

(115) S. Xu, 'Synthesis of high quality low-toxic semiconductor nanocrystals', Ph.D. Thesis, University of East Anglia, UK, 2008 (cit. on p. 23).

(116) C. N. R. Rao and K. Biswas, 'Characterization of nanomaterials by physical methods', *Annu. Rev. Anal. Chem.*, 2009, **2**, 435–462, DOI: 10.1146/annurev-anchem-060908-155236 (cit. on p. 25).

(117) *Nanocharacterisation*, ed. J. Hutchison and A. Kirkland, The Royal Society of Chemistry, 2008, ISBN: 978-0-85404-241-8, DOI: 10.1039/9781847557926 (cit. on p. 25).

(118) D. B. Williams and C. B. Carter, *Transmission electron microscopy: A textbook for materials science*, Springer, 2nd edn., 2009, ISBN: 0387765026 (cit. on pp. 26–29).

(119) A. Abragam, 'Louis Victor Pierre Raymond de Broglie. 15 August 1892-19 March 1987', *Biogr. Mems Fell. R. Soc.*, 1988, **34**, 22–41, DOI: 10.1098/rsbm.1988.0002 (cit. on p. 26).

(120) A. J. Garratt-Reed and D. C. Bell, *Energy-dispersive X-ray analysis in the electron microscope*, BIOS Scientific Publishers Ltd, Oxford, 1st edn., 2003, ISBN: 1-85996-109-6 (cit. on p. 30).

(121) R. F. Egerton, *Electron energy-loss spectroscopy in the electron microscope*, Springer, 3rd edn., 2011, ISBN: 978-1-4419-9582-7, DOI: 10.1007/978-1-4419-9583-4 (cit. on p. 30).

(122) P. N. Pusey, Introduction to Scattering Experiments, in *Neutrons, X-rays and light: Scattering methods applied to soft condensed matter*, ed. P. Lindner and T. Zemb, North-Holland, 2002, ch. 1, ISBN: 0-444-51122-9 (cit. on p. 31).

(123) *Neutron scattering in biology: Techniques and applications*, ed. J. Fitter, T. Gutberlet and J. Katsaras, Springer, 2006, ISBN: 3-540-29108-3 (cit. on p. 32).

(124) *Neutron, X-rays and light: Scattering methods applied to soft condensed matter*, ed. P. Lindner and T. Zemb, North-Holland, 2002, ISBN: 0-444-51122-9 (cit. on p. 34).

(125) L. Rayleigh, 'The incidence of light upon a transparent sphere of dimensions comparable with the wave-length', *Proc. R. Soc. Lond. A.*, 1910, **84**, 25–46, DOI: 10.1098/rspa.1910.0054 (cit. on p. 34).

(126) *SasView for small angle scattering analysis*, http://www.sasview.org (visited on 22/01/2013) (cit. on p. 35).

(127) R. Pecora, 'Dynamic light scattering measurement of nanometer particles in liquids', *J. Nanopart. Res.*, 2000, **2**, 123–131, DOI: 10.1023/a:1010067107182 (cit. on p. 36).

(128) F. Rouessac and A. Rouessac, *Chemical analysis: Modern instrumentation, methods and techniques*, Wiley, 2nd edn., 2007, ISBN: 978-0-470-85903-2 (cit. on pp. 37, 39).

(129) J. R. Lakowicz, *Principles of fluorescence spectroscopy*, English, Kluwer Academic/Plenum Publishers, New York, 2nd edn., 1999, ISBN: 0-306-460093-9 (cit. on p. 38).

(130) D. H. Williams and I. Fleming, *Spectroscopic methods in organic chemistry*, McGraw-Hill Book Company Europe, 5th edn., 1995, ISBN: 0-07-709147-7 (cit. on p. 38).

(131) J. Nölte, *ICP emission spectrometry: A practical guide*, Wiley VCH, 2003, ISBN: 3-527-30672-2 (cit. on p. 39).

(132) J. F. Watts and J. Wolstenholme, *An introduction to surface analysis by XPS and AES*, Wiley, 2003, ISBN: 0-470-84713-1 (cit. on p. 39).

(133) J. Yan, M. C. Estévez, J. E. Smith, K. Wang, X. He, L. Wang and W. Tan, 'Dye-doped nanoparticles for bioanalysis', *Nano Today*, 2007, **2**, 44–50, DOI: 10.1016/s1748-0132(07)70086-5 (cit. on p. 40).

(134) A. M. Derfus, W. C. W. Chan and S. N. Bhatia, 'Probing the cytotoxicity of semiconductor quantum dots', *Nano Lett.*, 2004, **4**, 11–18, DOI: 10.1021/nl0347334 (cit. on p. 40).

(135) P. V. Der Voort and E. F. Vansant, 'Silylation of the silica surface: A review', *J. Liq. Chromatogr. R. T.*, 1996, **19**, 2723–2752, DOI: 10.1080/10826079608015107 (cit. on p. 41).

(136) J.-W. Park, Y. J. Park and C.-H. Jun, 'Post-grafting of silica surfaces with pre-functionalized organosilanes: New synthetic equivalents of conventional trialkoxysilanes', *Chem. Commun.*, 2011, **47**, 4860–4871, DOI: 10.1039/c1cc00038a (cit. on p. 41).

(137) F. Arriagada and K. Osseo-Asare, 'Synthesis of nanosize silica in a nonionic water-in-oil microemulsion: Effects of the water/surfactant molar ratio and ammonia concentration', *J. Colloid Interf. Sci.*, 1999, **211**, 210–220, DOI: 10.1006/jcis.1998.5985 (cit. on pp. 41, 43).

(138) P. Mulvaney, L. M. Liz-Marzán, M. Giersig and T. Ung, 'Silica encapsulation of quantum dots and metal clusters', *J. Mater. Chem.*, 2000, **10**, 1259–1270, DOI: 10.1039/b000136h (cit. on p. 42).

(139) A. Guerrero-Martínez, J. Pérez-Juste and L. M. Liz-Marzán, 'Recent progress on silica coating of nanoparticles and related nanomaterials', *Adv. Mater.*, 2010, **22**, 1182–1195, DOI: 10.1002/adma.200901263 (cit. on p. 42).

(140) S. Liu and M.-Y. Han, 'Silica-coated metal nanoparticles', *Chem. Asian J.*, 2010, **5**, 36–45, DOI: 10.1002/asia.200900228 (cit. on p. 42).

(141) L. M. Liz-Marzán and A. P. Philipse, 'Synthesis and optical properties of gold-labeled silica particles', *J. Colloid Interf. Sci.*, 1995, **176**, 459–466, DOI: 10.1006/jcis.1995.9945 (cit. on p. 42).

(142) L. M. Liz-Marzán, M. Giersig and P. Mulvaney, 'Homogeneous silica coating of vitreophobic colloids', *Chem. Commun.*, 1996, 731–732, DOI: 10.1039/cc9960000731 (cit. on p. 42).

(143) I. Pastoriza-Santos and L. M. Liz-Marzán, 'Formation and stabilization of silver nanoparticles through reduction by *N*,*N*-dimethylformamide', *Langmuir*, 1999, **15**, 948–951, DOI: 10.1021/la980984u (cit. on pp. 42, 44).

(144) P. A. Buining, B. M. Humbel, A. P. Philipse and A. J. Verkleij, 'Preparation of functional silane-stabilized gold colloids in the (sub)nanometer size range', *Langmuir*, 1997, **13**, 3921–3926, DOI: 10.1021/la962071a (cit. on pp. 42, 44).

(145) A. P. Philipse, M. P. B. van Bruggen and C. Pathmamanoharan, 'Magnetic silica dispersions: Preparation and stability of surface-modified silica particles with a magnetic core', *Langmuir*, 1994, **10**, 92–99, DOI: 10.1021/la00013a014 (cit. on p. 42).

(146) L. M. Liz-Marzán, M. Giersig and P. Mulvaney, 'Synthesis of nanosized gold-silica core-shell particles', *Langmuir*, 1996, **12**, 4329–4335, DOI: 10.1021/la9601871 (cit. on p. 42).

(147) M. A. Correa-Duarte, M. Giersig and L. M. Liz-Marzán, 'Stabilization of CdS semiconductor nanoparticles against photodegradation by a silica coating procedure', *Chem. Phys. Lett.*, 1998, **286**, 497–501, DOI: 10.1016/s0009-2614(98)00012-8 (cit. on p. 43).

(148) T. Ung, L. M. Liz-Marzán and P. Mulvaney, 'Controlled method for silica coating of silver colloids. Influence of coating on the rate of chemical reactions', *Langmuir*, 1998, **14**, 3740–3748, DOI: 10.1021/la980047m (cit. on p. 43).

(149) S.-Y. Chang, L. Liu and S. A. Asher, 'Preparation and properties of tailored morphology, monodisperse colloidal silica-cadmium sulfide nanocomposites', *J. Am. Chem. Soc.*, 1994, **116**, 6739–6744, DOI: 10.1021/ja00094a032 (cit. on p. 43).

(150) H. Yang, S. Santra, G. A. Walter and P. H. Holloway, 'Gd^{III}-functionalized fluorescent quantum dots as multimodal imaging probes', *Adv. Mater.*, 2006, **18**, 2890–2894, DOI: 10.1002/adma.200502665 (cit. on p. 43).

(151) H. Wang, K. Schaefer and M. Moeller, '*In situ* immobilization of gold nanoparticle dimers in silica nanoshell by microemulsion coalescence', *J. Phys. Chem. C*, 2008, **112**, 3175–3178, DOI: 10.1021/jp7113658 (cit. on p. 43).

(152) T. Li, J. Moon, A. A. Morrone, J. J. Mecholsky, D. R. Talham and J. H. Adair, 'Preparation of Ag/SiO_2 nanosize composites by a reverse micelle and sol-gel technique', *Langmuir*, 1999, **15**, 4328–4334, DOI: 10.1021/la970801o (cit. on p. 43).

(153) D.-S. Bae, K.-S. Han and J. H. Adair, 'Synthesis and microstructure of Pd/SiO_2 nanosized particles by reverse micelle and sol-gel processing', *J. Mater. Chem.*, 2002, **12**, 3117–3120, DOI: 10.1039/b203203c (cit. on p. 43).

(154) J.-N. Park, A. J. Forman, W. Tang, J. Cheng, Y.-S. Hu, H. Lin and E. W. McFarland, 'Highly active and sinter-resistant Pd-nanoparticle catalysts encapsulated in silica', *Small*, 2008, **4**, 1694–1697, DOI: 10.1002/smll.200800895 (cit. on p. 43).

(155) Y. Yang and M. Y. Gao, 'Preparation of fluorescent SiO_2 particles with single CdTe nanocrystal cores by the reverse microemulsion method', *Adv. Mater.*, 2005, **17**, 2354–2357, DOI: 10.1002/adma.200500403 (cit. on p. 43).

(156) S. Santra, R. Tapec, N. Theodoropoulou, J. Dobson, A. Hebard and W. Tan, 'Synthesis and characterization of silica-coated iron oxide nanoparticles in microemulsion: The effect of nonionic surfactants', *Langmuir*, 2001, **17**, 2900–2906, DOI: 10.1021/la0008636 (cit. on p. 43).

(157) J. Lee, Y. Lee, J. K. Youn, H. B. Na, T. Yu, H. Kim, S.-M. Lee, Y.-M. Koo, J. H. Kwak, H. G. Park, H. N. Chang, M. Hwang, J.-G. Park, J. Kim and T. Hyeon, 'Simple synthesis of functionalized superparamagnetic magnetite/silica core/shell nanoparticles and their application as magnetically separable high-performance biocatalysts', *Small*, 2008, **4**, 143–152, DOI: 10.1002/smll.200700456 (cit. on p. 43).

(158) Q. Yan, A. Purkayastha, T. Kim, R. Kröger, A. Bose and G. Ramanath, 'Synthesis and assembly of monodisperse high-coercivity silica-capped FePt nanomagnets of tunable size, composition, and thermal stability from microemulsions', *Adv. Mater.*, 2006, **18**, 2569–2573, DOI: 10.1002/adma.200502607 (cit. on p. 43).

(159) Y. Yang, L. Jing, X. Yu, D. Yan and M. Gao, 'Coating aqueous quantum dots with silica *via* reverse microemulsion method: Toward size-controllable and robust fluorescent nanoparticles', *Chem. Mater.*, 2007, **19**, 4123–4128, DOI: 10.1021/cm070798m (cit. on p. 43).

(160) S. T. Selvan, T. T. Tan and J. Y. Ying, 'Robust, non-cytotoxic, silica-coated CdSe quantum dots with efficient photoluminescence', *Adv. Mater.*, 2005, **17**, 1620–1625, DOI: 10.1002/adma.200401960 (cit. on p. 43).

(161) T. T. Tan, S. T. Selvan, L. Zhao, S. Gao and J. Y. Ying, 'Size control, shape evolution, and silica coating of near-infrared-emitting PbSe quantum dots', *Chem. Mater.*, 2007, **19**, 3112–3117, DOI: 10.1021/cm061974e (cit. on p. 43).

(162) S. T. Selvan, P. K. Patra, C. Y. Ang and J. Y. Ying, 'Synthesis of silica-coated semiconductor and magnetic quantum dots and their use in the imaging of live cells', *Angew. Chem. Int. Ed.*, 2007, **46**, 2448–2452, DOI: 10.1002/anie.200604245 (cit. on pp. 43, 45).

(163) M. Darbandi, R. Thomann and T. Nann, 'Single quantum dots in silica spheres by microemulsion synthesis', *Chem. Mater.*, 2005, **17**, 5720–5725, DOI: 10.1021/cm051467h (cit. on pp. 43, 50).

(164) M. Darbandi, 'Silica coated nanocomposites', Ph.D. Thesis, University of Freiburg, Germany, 2007 (cit. on p. 43).

(165) M. Darbandi, W. Lu, J. Fang and T. Nann, 'Silica encapsulation of hydrophobically ligated PbSe nanocrystals', *Langmuir*, 2006, **22**, 4371–4375, DOI: 10.1021/la0529658 (cit. on p. 43).

(166) J. Ziegler, S. Xu, E. Kucur, F. Meister, M. Batentschuk, F. Gindele and T. Nann, 'Silica-coated InP/ZnS nanocrystals as converter material in white LEDs', *Adv. Mater.*, 2008, **20**, 4068–4073, DOI: 10.1002/adma.200800724 (cit. on p. 43).

(167) M. Darbandi and T. Nann, 'One-pot synthesis of YF_3@silica core/shell nanoparticles', *Chem. Commun.*, 2006, 776–778, DOI: 10.1039/b516171a (cit. on p. 43).

(168) O. Ehlert, R. Thomann, M. Darbandi and T. Nann, 'A four-color colloidal multiplexing nanoparticle system', *ACS Nano*, 2008, **2**, 120–124, DOI: 10.1021/nn7002458 (cit. on p. 43).

(169) R. Koole, M. M. van Schooneveld, J. Hilhorst, C. de Mello Donegá, D. C. 't Hart, A. van Blaaderen, D. Vanmaekelbergh and A. Meijerink, 'On the incorporation mechanism of hydrophobic quantum dots in silica spheres by a reverse microemulsion method', *Chem. Mater.*, 2008, **20**, 2503–2512, DOI: 10.1021/cm703348y (cit. on pp. 43, 44).

(170) D. K. Yi, S. T. Selvan, S. S. Lee, G. C. Papaefthymiou, D. Kundaliya and J. Y. Ying, 'Silica-coated nanocomposites of magnetic nanoparticles and quantum dots', *J. Am. Chem. Soc.*, 2005, **127**, 4990–4991, DOI: 10.1021/ja0428863 (cit. on p. 44).

(171) D. K. Yi, S. S. Lee, G. C. Papaefthymiou and J. Y. Ying, 'Nanoparticle architectures templated by SiO_2/Fe_2O_3 nanocomposites', *Chem. Mater.*, 2006, **18**, 614–619, DOI: 10.1021/cm0512979 (cit. on p. 44).

(172) Y. Han, J. Jiang, S. S. Lee and J. Y. Ying, 'Reverse microemulsion-mediated synthesis of silica-coated gold and silver nanoparticles', *Langmuir*, 2008, **24**, 5842–5848, DOI: 10.1021/la703440p (cit. on p. 44).

(173) H. L. Ding, Y. X. Zhang, S. Wang, J. M. Xu, S. C. Xu and G. H. Li, 'Fe_3O_4@SiO_2 core/shell nanoparticles: The silica coating regulations with a single core for different core sizes and shell thicknesses', *Chem. Mater.*, 2012, **24**, 4572–4580, DOI: 10.1021/cm302828d (cit. on p. 44).

(174) M. Darbandi, G. Urban and M. Krüger, 'A facile synthesis method to silica coated CdSe/ZnS nanocomposites with tuneable size and optical properties', *J. Colloid Interf. Sci.*, 2010, **351**, 30–34, DOI: 10.1016/j.jcis.2010.07.043 (cit. on p. 44).

(175) M. Bruchez, M. Moronne, P. Gin, S. Weiss and A. P. Alivisatos, 'Semiconductor nanocrystals as fluorescent biological labels', *Science*, 1998, **281**, 2013–2016, DOI: 10.1126/science.281.5385.2013 (cit. on p. 44).

(176) D. Gerion, F. Pinaud, S. C. Williams, W. J. Parak, D. Zanchet, S. Weiss and A. P. Alivisatos, 'Synthesis and properties of biocompatible water-soluble silica-coated CdSe/ZnS semiconductor quantum dots', *J. Phys. Chem. B*, 2001, **105**, 8861–8871, DOI: 10.1021/jp0105488 (cit. on p. 44).

(177) W. J. Parak, D. Gerion, D. Zanchet, A. S. Woerz, T. Pellegrino, C. Micheel, S. C. Williams, M. Seitz, R. E. Bruehl, Z. Bryant, C. Bustamante, C. R. Bertozzi and A. P. Alivisatos, 'Conjugation of DNA to silanized colloidal semiconductor nanocrystalline quantum dots', *Chem. Mater.*, 2002, **14**, 2113–2119, DOI: 10.1021/cm0107878 (cit. on p. 44).

(178) A. Schroedter and H. Weller, 'Ligand design and bioconjugation of colloidal gold nanoparticles', *Angew. Chem. Int. Ed.*, 2002, **41**, 3218–3221, DOI: 10.1002/1521-3773(20020902)41:17<3218::aid-anie3218>3.0.co;2-p (cit. on p. 44).

(179) A. Schroedter, H. Weller, R. Eritja, W. E. Ford and J. M. Wessels, 'Biofunctionalization of silica-coated CdTe and gold nanocrystals', *Nano Lett.*, 2002, **2**, 1363–1367, DOI: 10.1021/nl025779k (cit. on p. 44).

(180) N. R. Jana, C. Earhart and J. Y. Ying, 'Synthesis of water-soluble and functionalized nanoparticles by silica coating', *Chem. Mater.*, 2007, **19**, 5074–5082, DOI: 10.1021/cm071368z (cit. on p. 45).

(181) N. R. Jana, H.-h. Yu, E. M. Ali, Y. Zheng and J. Y. Ying, 'Controlled photostability of luminescent nanocrystalline ZnO solution for selective detection of aldehydes', *Chem. Commun.*, 2007, 1406–1408, DOI: 10.1039/b613043g (cit. on p. 45).

(182) C. Earhart, N. R. Jana, N. Erathodiyil and J. Y. Ying, 'Synthesis of carbohydrate-conjugated nanoparticles and quantum dots', *Langmuir*, 2008, **24**, 6215–6219, DOI: 10.1021/la800066g (cit. on p. 45).

(183) J. Kim, J. E. Lee, J. Lee, J. H. Yu, B. C. Kim, K. An, Y. Hwang, C.-H. Shin, J.-G. Park, J. Kim and T. Hyeon, 'Magnetic fluorescent delivery vehicle using uniform mesoporous silica spheres embedded with monodisperse magnetic and semiconductor nanocrystals', *J. Am. Chem. Soc.*, 2005, **128**, 688–689, DOI: 10.1021/ja0565875 (cit. on p. 45).

(184) H. Fan, J. Gabaldon, C. J. Brinker and Y.-B. Jiang, 'Ordered nanocrystal/silica particles self-assembled from nanocrystal micelles and silicate', *Chem. Commun.*, 2006, 2323–2325, DOI: 10.1039/b600923a (cit. on p. 45).

(185) I. Gorelikov and N. Matsuura, 'Single-step coating of mesoporous silica on cetyltrimethyl ammonium bromide-capped nanoparticles', *Nano Lett.*, 2007, **8**, 369–373, DOI: 10.1021/nl0727415 (cit. on p. 45).

(186) Z. Zhelev, H. Ohba and R. Bakalova, 'Single quantum dot-micelles coated with silica shell as potentially non-cytotoxic fluorescent cell tracers', *J. Am. Chem. Soc.*, 2006, **128**, 6324–6325, DOI: 10.1021/ja061137d (cit. on p. 45).

(187) C. Graf, D. L. J. Vossen, A. Imhof and A. van Blaaderen, 'A general method to coat colloidal particles with silica', *Langmuir*, 2003, **19**, 6693–6700, DOI: 10.1021/la0347859 (cit. on p. 45).

(188) I. Pastoriza-Santos, J. Pérez-Juste and L. M. Liz-Marzán, 'Silica-coating and hydrophobation of CTAB-stabilized gold nanorods', *Chem. Mater.*, 2006, **18**, 2465–2467, DOI: 10.1021/cm060293g (cit. on p. 45).

(189) E. E. Lees, T.-L. Nguyen, A. H. A. Clayton and P. Mulvaney, 'The preparation of colloidally stable, water-soluble, biocompatible, semiconductor nanocrystals with a small hydrodynamic diameter', *ACS Nano*, 2009, **3**, 1121–1128, DOI: 10.1021/nn900144n (cit. on pp. 48, 74, 75, 77).

(190) X. Wu, H. Liu, J. Liu, K. N. Haley, J. A. Treadway, J. P. Larson, N. Ge, F. Peale and M. P. Bruchez, 'Immunofluorescent labeling of cancer marker Her2 and other cellular targets with semiconductor quantum dots', *Nat. Biotechnol.*, 2003, **21**, 41–46, DOI: 10.1038/nbt764 (cit. on pp. 70, 72, 76, 77).

(191) T. Pellegrino, L. Manna, S. Kudera, T. Liedl, D. Koktysh, A. Rogach, S. Keller, J. Rädler, G. Natile and W. Parak, 'Hydrophobic nanocrystals coated with an amphiphilic polymer shell: A general route to water soluble nanocrystals', *Nano Lett.*, 2004, **4**, 703–707, DOI: 10.1021/nl035172j (cit. on pp. 71, 73, 74, 77).

(192) C. Tribet, R. Audebert and J.-L. Popot, 'Amphipols: Polymers that keep membrane proteins soluble in aqueous solutions', *Proc. Natl. Acad. Sci. USA*, 1996, **93**, 15047–15050 (cit. on p. 71).

(193) C. Tribet, R. Audebert and J.-L. Popot, 'Stabilization of hydrophobic colloidal dispersions in water with amphiphilic polymers: Application to integral membrane proteins', *Langmuir*, 1997, **13**, 5570–5576, DOI: 10.1021/la970136j (cit. on p. 71).

(194) R. Anderson and W. Chan, 'Systematic investigation of preparing biocompatible, single, and small ZnS-capped CdSe quantum dots with amphiphilic polymers', *ACS Nano*, 2008, **2**, 1341–1352, DOI: 10.1021/nn700450g (cit. on p. 72).

(195) L. C. Mattheakis, J. M. Dias, Y.-J. Choi, J. Gong, M. P. Bruchez, J. Liu and E. Wang, 'Optical coding of mammalian cells using semiconductor quantum dots', *Anal. Biochem.*, 2004, **327**, 200–208, DOI: 10.1016/j.ab.2004.01.031 (cit. on p. 72).

(196) B. Ballou, B. C. Lagerholm, L. A. Ernst, M. P. Bruchez and A. S. Waggoner, 'Noninvasive imaging of quantum dots in mice', *Bioconjugate Chem.*, 2004, **15**, 79–86, DOI: 10.1021/bc034153y (cit. on p. 72).

(197) R. C. Somers, P. T. Snee, M. G. Bawendi and D. G. Nocera, 'Energy transfer of CdSe/ZnS nanocrystals encapsulated with rhodamine-dye functionalized poly(acrylic acid)', *J. Photoch. Photobio. A*, 2012, **248**, 24–29, DOI: 10.1016/j.jphotochem.2012.07.012 (cit. on p. 72).

(198) C. Luccardini, C. Tribet, F. Vial, V. Marchi-Artzner and M. Dahan, 'Size, charge, and interactions with giant lipid vesicles of quantum dots coated with an amphiphilic macromolecule', *Langmuir*, 2006, **22**, 2304–2310, DOI: 10.1021/la052704y (cit. on p. 72).

(199) R. A. Sperling, T. Pellegrino, J. K. Li, W. H. Chang and W. J. Parak, 'Electrophoretic separation of nanoparticles with a discrete number of functional groups', en, *Adv. Funct. Mater.*, 2006, **16**, 943–948, DOI: 10.1002/adfm.200500589 (cit. on p. 73).

(200) M. V. Yezhelyev, L. Qi, R. M. O'Regan, S. Nie and X. Gao, 'Proton-sponge coated quantum dots for siRNA delivery and intracellular imaging', *J. Am. Chem. Soc.*, 2008, **130**, 9006–9012, DOI: 10.1021/ja800086u (cit. on p. 73).

(201) W. W. Yu, E. Chang, C. M. Sayes, R. Drezek and V. L. Colvin, 'Aqueous dispersion of monodisperse magnetic iron oxide nanocrystals through phase transfer', *Nanotechnology*, 2006, **17**, 4483–4487, DOI: 10.1088/0957-4484/17/17/033 (cit. on pp. 73, 74, 77).

(202) W. W. Yu, E. Chang, J. C. Falkner, J. Zhang, A. M. Al-Somali, C. M. Sayes, J. Johns, R. Drezek and V. L. Colvin, 'Forming biocompatible and nonaggregated nanocrystals in water using amphiphilic polymers', *J. Am. Chem. Soc.*, 2007, **129**, 2871–2879, DOI: 10.1021/ja067184n (cit. on p. 73).

(203) R. Di Corato, A. Quarta, P. Piacenza, A. Ragusa, A. Figuerola, R. Buonsanti, R. Cingolani, L. Manna and T. Pellegrino, 'Water solubilization of hydrophobic nanocrystals by means of poly(maleic anhydride-*alt*-1-octadecene)', *J. Mater. Chem.*, 2008, **18**, 1991–1996, DOI: 10.1039/b717801h (cit. on pp. 73, 74, 76).

(204) G. Jiang, J. Pichaandi, N. J. Johnson, R. D. Burke and F. C. van Veggel, 'An effective polymer crosslinking strategy to obtain stable dispersions of upconverting $NaYF_4$ nanoparticles in buffers and biological growth media for biolabeling applications', *Langmuir*, 2012, DOI: 10.1021/la204020m (cit. on pp. 74, 77).

(205) J. Qin, Y. S. Jo and M. Muhammed, 'Coating nanocrystals with amphiphilic thermosensitive copolymers', *Angew. Chem. Int. Ed.*, 2009, **48**, 7845–7849, DOI: 10.1002/anie.200900489 (cit. on p. 74).

(206) L. M. Bronstein, E. V. Shtykova, A. Malyutin, J. C. Dyke, E. Gunn, X. Gao, B. Stein, P. V. Konarev, B. Dragnea and D. I. Svergun, 'Hydrophilization of magnetic nanoparticles with modified alternating copolymers. Part 1: The influence of the grafting', *J. Phys. Chem. C*, 2010, **114**, 21900–21907, DOI: 10.1021/jp107283w (cit. on p. 74).

(207) B. W. Muir, B. A. Moffat, P. Harbour, G. Coia, G. Zhen, L. Waddington, J. Scoble, D. Krah, S. H. Thang, Y. K. Chong, P. Mulvaney and P. Hartley, 'Combinatorial discovery of novel amphiphilic polymers for the phase transfer of magnetic nanoparticles', *J. Phys. Chem. C*, 2009, **113**, 16615–16624, DOI: 10.1021/jp904846e (cit. on pp. 74, 76, 138).

(208) M. Moros, B. Hernáez, E. Garet, J. T. Dias, B. Sáez, V. Grazú, Á. González-Fernández, C. Alonso and J. M. de la Fuente, 'Monosaccharides versus PEG-functionalized NPs: Influence in the cellular uptake', *ACS Nano*, 2012, **6**, 1565–1577, DOI: 10.1021/nn204543c (cit. on p. 74).

(209) M. Moros, B. Pelaz, P. Lopez-Larrubia, M. L. Garcia-Martin, V. Grazu and J. M. de la Fuente, 'Engineering biofunctional magnetic nanoparticles for biotechnological applications', *Nanoscale*, 2010, **2**, 1746–1755, DOI: 10.1039/c0nr00104j (cit. on pp. 74, 77).

(210) L. Qi, L. Wu, S. Zheng, Y. Wang, H. Fu and D. Cui, 'Cell-penetrating magnetic nanoparticles for highly efficient delivery and intracellular imaging of siRNA', *Biomacromolecules*, 2012, **13**, 2723–2730, DOI: 10.1021/bm3006903 (cit. on p. 74).

(211) L. Qi and X. Gao, 'Quantum dot-amphipol nanocomplex for intracellular delivery and real-time imaging of siRNA', *ACS Nano*, 2008, **2**, 1403–1410, DOI: 10.1021/nn800280r (cit. on p. 74).

(212) M. T. Fernández-Argüelles, A. Yakovlev, R. A. Sperling, C. Luccardini, S. Gaillard, A. Sanz Medel, J.-M. Mallet, J.-C. Brochon, A. Feltz, M. Oheim and W. J. Parak, 'Synthesis and characterization of polymer-coated quantum dots with integrated acceptor dyes as FRET-Based nanoprobes', *Nano Lett.*, 2007, **7**, 2613–2617, DOI: 10.1021/nl070971d (cit. on pp. 74, 75).

(213) C.-A. J. Lin, R. A. Sperling, J. K. Li, T.-Y. Yang, P.-Y. Li, M. Zanella, W. H. Chang and W. J. Parak, 'Design of an amphiphilic polymer for nanoparticle coating and functionalization', *Small*, 2008, **4**, 334–341, DOI: 10.1002/smll.200700654 (cit. on pp. 74–76).

(214) M. P. Morales, M. F. Bedard, A. G. Roca, P. d. l. Presa, A. Hernando, F. Zhang, M. Zanella, A. A. Zahoor, G. B. Sukhorukov, L. L. del Mercato and W. J. Parak, 'Relaxation times of colloidal iron platinum in polymer matrixes', *J. Mater. Chem.*, 2009, **19**, 6381–6386, DOI: 10.1039/b906455a (cit. on p. 74).

(215) C. Röcker, M. Potzl, F. Zhang, W. J. Parak and G. U. Nienhaus, 'A quantitative fluorescence study of protein monolayer formation on colloidal nanoparticles', *Nat. Nanotechnol.*, 2009, **4**, 577–580, DOI: 10.1038/nnano.2009.195 (cit. on pp. 74, 75, 112, 113).

(216) D. Jańczewski, N. Tomczak, M.-Y. Han and G. J. Vancso, 'Synthesis of functionalized amphiphilic polymers for coating quantum dots', *Nat. Protocols*, 2011, **6**, 1546–1553, DOI: 10.1038/nprot.2011.381 (cit. on p. 74).

(217) D. Jańczewski, N. Tomczak, M.-Y. Han and G. J. Vancso, 'Introduction of quantum dots into PNIPAM microspheres by precipitation polymerization above LCST', *Eur. Polym. J.*, 2009, **45**, 1912–1917, DOI: 10.1016/j.eurpolymj.2009.04.005 (cit. on p. 75).

(218) D. Jańczewski, N. Tomczak, M.-Y. Han and G. J. Vancso, 'Stimulus responsive PNIPAM/QD hybrid microspheres by copolymerization with surface engineered QDs', *Macromolecules*, 2009, **42**, 1801–1804, DOI: 10.1021/ma802521a (cit. on p. 75).

(219) D. Jańczewski, N. Tomczak, J. Song, H. Long, M.-Y. Han and G. J. Vancso, 'Fabrication and responsive behaviour of quantum dot/PNIPAM micropatterns obtained by template copolymerization in water', *J. Mater. Chem.*, 2011, **21**, 6487–6490, DOI: 10.1039/c1jm10351b (cit. on p. 75).

(220) D. Jańczewski, N. Tomczak, S. Liu, M.-Y. Han and G. J. Vancso, 'Covalent assembly of functional inorganic nanoparticles by "click" chemistry in water', *Chem. Commun.*, 2010, **46**, 3253–3255, DOI: 10.1039/b921848c (cit. on p. 75).

(221) O. Tagit, D. Jańczewski, N. Tomczak, M. Y. Han, J. L. Herek and G. J. Vancso, 'Nanostructured thermoresponsive quantum dot/PNIPAM assemblies', *Eur. Polym. J.*, 2010, **46**, 1397–1403, DOI: 10.1016/j.eurpolymj.2010.04.026 (cit. on p. 75).

(222) Y. Chen, R. Thakar and P. T. Snee, 'Imparting nanoparticle function with size-controlled amphiphilic polymers', *J. Am. Chem. Soc.*, 2008, **130**, 3744–3745, DOI: 10.1021/ja711252n (cit. on p. 75).

(223) C. Zhou, W. Xu, S. Lou, Z. Zhang, L. S. Li and J. Chen, 'Formation of water-soluble gold and silver nanocrystals using a phase transfer method based on surface-bound interactions', *Colloid. Surface. A*, 2010, **355**, 139–145, DOI: 10.1016/j.colsurfa.2009.12.006 (cit. on p. 75).

(224) Z. Wu, Y. Zhao, F. Qiu, Y. Li, S. Wang, B. Yang, L. Chen, J. Sun and J. Wang, 'Forming water-soluble CdSe/ZnS QDs using amphiphilic polymers, stearyl methacrylate/methylacrylate copolymers with different hydrophobic moiety ratios and their optical properties and stability', *Colloid. Surface. A*, 2009, **350**, 121–129, DOI: 10.1016/j.colsurfa.2009.09.014 (cit. on p. 76).

(225) J. Park, M. K. Yu, Y. Y. Jeong, J. W. Kim, K. Lee, V. N. Phan and S. Jon, 'Antibiofouling amphiphilic polymer-coated superparamagnetic iron oxide nanoparticles: Synthesis, characterization, and use in cancer imaging *in vivo*', *J. Mater. Chem.*, 2009, **19**, 6412–6417, DOI: 10.1039/b902445j (cit. on pp. 76, 77).

(226) C. Geidel, S. Schmachtel, A. Riedinger, C. Pfeiffer, K. Müllen, M. Klapper and W. J. Parak, 'A general synthetic approach for obtaining cationic and anionic inorganic nanoparticles *via* encapsulation in amphiphilic copolymers', *Small*, 2011, **7**, 2929–2934, DOI: 10.1002/smll.201100509 (cit. on p. 76).

(227) D. Hühn, K. Kantner, C. Geidel, S. Brandholt, I. De Cock, S. J. H. Soenen, P. Rivera Gil, J.-M. Montenegro, K. Braeckmans, K. Müllen, G. U. Nienhaus, M. Klapper and W. J. Parak, 'Polymer-coated nanoparticles interacting with proteins and cells: Focusing on the sign of the net charge', *ACS Nano*, 2013, ASAP, DOI: 10.1021/nn3059295 (cit. on pp. 76, 113).

(228) E. V. Shtykova, X. Huang, X. Gao, J. C. Dyke, A. L. Schmucker, B. Dragnea, N. Remmes, D. V. Baxter, B. Stein, P. V. Konarev, D. I. Svergun and L. M. Bronstein, 'Hydrophilic monodisperse magnetic nanoparticles protected by an amphiphilic alternating copolymer', *J. Phys. Chem. C*, 2008, **112**, 16809–16817, DOI: 10.1021/jp8053636 (cit. on p. 77).

(229) M. Szwarc, ''Living' polymers', *Nature*, 1956, **178**, 1168–1169, DOI: 10.1038/1781168a0 (cit. on p. 78).

(230) Definition of living polymerization, in *IUPAC. Compendium of Chemical Terminology, 2nd ed. (the "Gold Book")*, ed. A. D. McNaught and A. Wilkinson, XML on-line corrected version: http://goldbook.iupac.org (2006-) created by M. Nic, J. Jirat and B. Kosata; updates compiled by A. Jenkins., Blackwell Scientific Publications, Oxford, 1997, ISBN: 0-9678550-9-8, DOI: 10.1351/goldbook.L03597 (cit. on p. 78).

(231) G. Odian, *Principles of polymerization*, Wiley-Blackwell, 4th edn., 2004, ISBN: 0471274003 (cit. on p. 78).

(232) H. Fischer, 'The persistent radical effect: A principle for selective radical reactions and living radical polymerizations', *Chem. Rev.*, 2001, **101**, 3581–3610, DOI: 10.1021/cr990124y (cit. on p. 78).

(233) W. A. Braunecker and K. Matyjaszewski, 'Controlled/living radical polymerization: Features, developments, and perspectives', *Prog. Polym. Sci.*, 2007, **32**, 93–146, DOI: 10.1016/j.progpolymsci.2006.11.002 (cit. on pp. 78, 79).

(234) G. Moad, E. Rizzardo and S. H. Thang, 'Radical addition-fragmentation chemistry in polymer synthesis', *Polymer*, 2008, **49**, 1079–1131, DOI: 10.1016/j.polymer.2007.11.020 (cit. on p. 79).

(235) G. Moad, E. Rizzardo and S. H. Thang, 'Toward living radical polymerization', *Acc. Chem. Rev.*, 2008, **41**, 1133–1142, DOI: 10.1021/ar800075n (cit. on p. 79).

(236) *Handbook of RAFT polymerization*, ed. C. Barner-Kowollik, Wiley-VCH, 2008, ISBN: 978-3-527-31924-4 (cit. on pp. 79, 81).

(237) H. Willcock and R. K. O'Reilly, 'End group removal and modification of RAFT polymers', *Polym. Chem.*, 2010, **1**, DOI: 10.1039/b9py00340a (cit. on p. 80).

(238) A. Pollak, H. Blumenfeld, M. Wax, R. L. Baughn and G. M. Whitesides, 'Enzyme immobilization by condensation copolymerization into crosslinked polyacrylamide gels', *J. Am. Chem. Soc.*, 1980, **102**, 6324–6336, DOI: 10.1021/ja00540a026 (cit. on p. 85).

(239) M. Mammen, G. Dahmann and G. M. Whitesides, 'Effective inhibitors of hemagglutination by influenza virus synthesized from polymers having active ester groups. Insight into mechanism of inhibition', *J. Med. Chem.*, 1995, **38**, 4179–4190, DOI: 10.1021/jm00021a007 (cit. on p. 85).

(240) J. J. Gray, 'The interaction of proteins with solid surfaces', *Curr. Opin. Struc. Biol.*, 2004, **14**, 110–115, DOI: 10.1016/j.sbi.2003.12.001 (cit. on p. 108).

(241) D. Walczyk, F. Baldelli Bombelli, M. P. Monopoli, I. Lynch and K. A. Dawson, 'What the cell "sees" in bionanoscience', *J. Am. Chem. Soc.*, 2010, **132**, 5761–5768, DOI: 10.1021/ja910675v (cit. on pp. 108, 109, 112, 136).

(242) I. Lynch and K. A. Dawson, 'Protein-nanoparticle interactions', *Nano Today*, 2008, **3**, 40–47, DOI: 10.1016/s1748-0132(08)70014-8 (cit. on pp. 108, 109).

(243) M. P. Monopoli, C. Aberg, A. Salvati and K. A. Dawson, 'Biomolecular coronas provide the biological identity of nanosized materials', *Nat. Nanotechnol.*, 2012, **7**, 779–786, DOI: 10.1038/nnano.2012.207 (cit. on pp. 108–110).

(244) T. Blunk, D. F. Hochstrasser, J.-C. Sanchez, B. W. Müller and R. H. Müller, 'Colloidal carriers for intravenous drug targeting: Plasma protein adsorption patterns on surface-modified latex particles evaluated by two-dimensional polyacrylamide gel electrophoresis', *Electrophoresis*, 1993, **14**, 1382–1387, DOI: 10.1002/elps.11501401214 (cit. on p. 109).

(245) R. H. Müller, D. Rühl, M. Lück and B.-R. Paulke, 'Influence of fluorescent labelling of polystyrene particles on phagocytic uptake, surface hydrophobicity, and plasma protein adsorption', *Pharm. Res.*, 1997, **14**, 18–24, DOI: 10.1023/a:1012043131081 (cit. on p. 109).

(246) M. Lück, B.-R. Paulke, W. Schröder, T. Blunk and R. H. Müller, 'Analysis of plasma protein adsorption on polymeric nanoparticles with different surface characteristics', *J. Biomed. Mater. Res.*, 1998, **39**, 478–485, DOI: 10.1002/(sici)1097-4636(19980305)39:3<478::aid-jbm19>3.0.co;2-6 (cit. on p. 109).

(247) K. Thode, M. Lück, W. Semmler, R. H. Müller and M. Kresse, 'Determination of plasma protein adsorption on magnetic iron oxides: Sample preparation', *Pharm. Res.*, 1997, **14**, 905–910, DOI: 10.1023/a:1012104017761 (cit. on p. 109).

(248) M. Lück, K.-F. Pistel, Y.-X. Li, T. Blunk, R. H. Müller and T. Kissel, 'Plasma protein adsorption on biodegradable microspheres consisting of poly(D,L-lactide-*co*-glycolide), poly(L-lactide) or ABA triblock copolymers containing poly(oxyethylene): Influence of production method and polymer composition', *J. Control. Release*, 1998, **55**, 107–120, DOI: 10.1016/s0168-3659(98)00030-3 (cit. on p. 109).

(249) A. Gessner, R. Waicz, A. Lieske, B.-R. Paulke, K. Mäder and R. H. Müller, 'Nanoparticles with decreasing surface hydrophobicities: Influence on plasma protein adsorption', *Int. J. Pharm.*, 2000, **196**, 245–249, DOI: 10.1016/s0378-5173(99)00432-9 (cit. on p. 109).

(250) A. Gessner, A. Lieske, B.-R. Paulke and R. H. Müller, 'Influence of surface charge density on protein adsorption on polymeric nanoparticles: Analysis by two-dimensional electrophoresis', *Eur. J. Pharm. Biopharm.*, 2002, **54**, 165–170, DOI: 10.1016/s0939-6411(02)00081-4 (cit. on p. 109).

(251) A. Gessner, A. Lieske, B.-R. Paulke and R. H. Müller, 'Functional groups on polystyrene model nanoparticles: Influence on protein adsorption', *J. Biomed. Mater. Res. A*, 2003, **65A**, 319–326, DOI: 10.1002/jbm.a.10371 (cit. on p. 109).

(252) T. Cedervall, I. Lynch, M. Foy, T. Berggård, S. C. Donnelly, G. Cagney, S. Linse and K. A. Dawson, 'Detailed identification of plasma proteins adsorbed on copolymer nanoparticles', *Angew. Chem. Int. Ed.*, 2007, **46**, 5754–5756, DOI: 10.1002/anie.200700465 (cit. on p. 109).

(253) T. Cedervall, I. Lynch, S. Lindman, T. Berggård, E. Thulin, H. Nilsson, K. A. Dawson and S. Linse, 'Understanding the nanoparticle-protein corona using methods to quantify exchange rates and affinities of proteins for nanoparticles', *Proc. Natl. Acad. Sci. U.S.A.*, 2007, **104**, 2050–2055, DOI: 10.1073/pnas.0608582104 (cit. on p. 109).

(254) I. Lynch, A. Salvati and K. A. Dawson, 'Protein-nanoparticle interactions: What does the cell see?', *Nat. Nanotechnol.*, 2009, **4**, 546–547, DOI: 10.1038/nnano.2009.248 (cit. on p. 109).

(255) M. Lundqvist, J. Stigler, G. Elia, I. Lynch, T. Cedervall and K. A. Dawson, 'Nanoparticle size and surface properties determine the protein corona with possible implications for biological impacts', *Proc. Natl. Acad. Sci. U.S.A.*, 2008, **105**, 14265–14270, DOI: 10.1073/pnas.0805135105 (cit. on p. 109).

(256) M. P. Monopoli, D. Walczyk, A. Campbell, G. Elia, I. Lynch, F. Baldelli Bombelli and K. A. Dawson, 'Physical-chemical aspects of protein corona: Relevance to *in vitro* and *in vivo* biological impacts of nanoparticles', *J. Am. Chem. Soc.*, 2011, **133**, 2525–2534, DOI: 10.1021/ja107583h (cit. on p. 109).

(257) M. Lundqvist, J. Stigler, T. Cedervall, T. Berggård, M. B. Flanagan, I. Lynch, G. Elia and K. Dawson, 'The evolution of the protein corona around nanoparticles: A test study', *ACS Nano*, 2011, **5**, 7503–7509, DOI: 10.1021/nn202458g (cit. on pp. 109, 110).

(258) S. Milani, F. Baldelli Bombelli, A. S. Pitek, K. A. Dawson and J. Rädler, 'Reversible versus irreversible binding of transferrin to polystyrene nanoparticles: Soft and hard corona', *ACS Nano*, 2012, **6**, 2532–2541, DOI: 10.1021/nn204951s (cit. on pp. 109, 110, 112).

(259) A. S. Pitek, D. O'Connell, E. Mahon, M. P. Monopoli, F. Baldelli Bombelli and K. A. Dawson, 'Transferrin coated nanoparticles: Study of the bionano interface in human plasma', *PLoS ONE*, 2012, **7**, e40685, DOI: 10.1371/journal.pone.0040685 (cit. on p. 109).

(260) E. Casals, T. Pfaller, A. Duschl, G. J. Oostingh and V. Puntes, 'Time evolution of the nanoparticle protein corona', *ACS Nano*, 2010, **4**, 3623–3632, DOI: 10.1021/nn901372t (cit. on pp. 109, 113).

(261) A. A. Shemetov, I. Nabiev and A. Sukhanova, 'Molecular interaction of proteins and peptides with nanoparticles', *ACS Nano*, 2012, **6**, 4585–4602, DOI: 10.1021/nn300415x (cit. on p. 110).

(262) N. L. Anderson and N. G. Anderson, 'The human plasma proteome: History, character, and diagnostic prospects', *Mol. Cell. Proteomics*, 2002, **1**, 845–867, DOI: 10.1074/mcp.r200007-mcp200 (cit. on p. 110).

(263) M. A. Dobrovolskaia, A. K. Patri, J. Zheng, J. D. Clogston, N. Ayub, P. Aggarwal, B. W. Neun, J. B. Hall and S. E. McNeil, 'Interaction of colloidal gold nanoparticles with human blood: effects on particle size and analysis of plasma protein binding profiles', *Nanomed. Nanotechnol. Biol. Med.*, 2009, **5**, 106–117, DOI: 10.1016/j.nano.2008.08.001 (cit. on pp. 110, 113).

(264) S. Tenzer, D. Docter, S. Rosfa, A. Wlodarski, J. Kuharev, A. Rekik, S. K. Knauer, C. Bantz, T. Nawroth, C. Bier, J. Sirirattanapan, W. Mann, L. Treuel, R. Zellner, M. Maskos, H. Schild and R. H. Stauber, 'Nanoparticle size is a critical physicochemical determinant of the human blood plasma corona: A comprehensive quantitative proteomic analysis', *ACS Nano*, 2011, **5**, 7155–7167, DOI: 10.1021/nn201950e (cit. on p. 110).

(265) H. Zhang, K. E. Burnum, M. L. Luna, B. O. Petritis, J.-S. Kim, W.-J. Qian, R. J. Moore, A. Heredia-Langner, B.-J. M. Webb-Robertson, B. D. Thrall, D. G. Camp, R. D. Smith, J. G. Pounds and T. Liu, 'Quantitative proteomics analysis of adsorbed plasma proteins classifies nanoparticles with different surface properties and size', *Proteomics*, 2011, **11**, 4569–4577, DOI: 10.1002/pmic.201100037 (cit. on p. 110).

(266) A. Salvati, A. S. Pitek, M. P. Monopoli, K. Prapainop, F. Baldelli Bombelli, D. R. Hristov, P. M. Kelly, C. Aberg, E. Mahon and K. A. Dawson, 'Transferrin-functionalized nanoparticles lose their targeting capabilities when a biomolecule corona adsorbs on the surface', *Nat. Nanotechnol.*, 2013, **8**, 137–143, DOI: 10.1038/nnano.2012.237 (cit. on p. 112).

(267) V. Mirshafiee, M. Mahmoudi, K. Lou, J. Cheng and M. L. Kraft, 'Protein corona significantly reduces active targeting yield', *Chem. Commun.*, 2013, **49**, 2557–2559, DOI: 10.1039/c3cc37307j (cit. on p. 112).

(268) E. Mahon, A. Salvati, F. Baldelli Bombelli, I. Lynch and K. A. Dawson, 'Designing the nanoparticle-biomolecule interface for "targeting and therapeutic delivery"', *J. Control. Release*, 2012, **161**, 164–174, DOI: 10.1016/j.jconrel.2012.04.009 (cit. on p. 112).

(269) E. Casals and V. F. Puntes, 'Inorganic nanoparticle biomolecular corona: Formation, evolution and biological impact', *Nanomedicine*, 2012, **7**, 1917–1930, DOI: 10.2217/nnm.12.169 (cit. on p. 113).

(270) S. H. De Paoli Lacerda, J. J. Park, C. Meuse, D. Pristinski, M. L. Becker, A. Karim and J. F. Douglas, 'Interaction of gold nanoparticles with common human blood proteins', *ACS Nano*, 2009, **4**, 365–379, DOI: 10.1021/nn9011187 (cit. on p. 113).

(271) L. Calzolai, F. Franchini, D. Gilliland and F. Rossi, 'Protein-nanoparticle interaction: Identification of the ubiquitin-gold nanoparticle interaction site', *Nano Lett.*, 2010, **10**, 3101–3105, DOI: 10.1021/nl101746v (cit. on p. 113).

(272) S. Goy-López, J. Juárez, M. Alatorre-Meda, E. Casals, V. F. Puntes, P. Taboada and V. Mosquera, 'Physicochemical characteristics of protein–NP bioconjugates: The role of particle curvature and solution conditions on human serum albumin conformation and fibrillogenesis inhibition', *Langmuir*, 2012, **28**, 9113–9126, DOI: 10.1021/la300402w (cit. on p. 113).

(273) K. Vangala, F. Ameer, G. Salomon, V. Le, E. Lewis, L. Yu, D. Liu and D. Zhang, 'Studying protein and gold nanoparticle interaction using organothiols as molecular probes', *J. Phys. Chem. C*, 2012, **116**, 3645–3652, DOI: 10.1021/jp2107318 (cit. on p. 113).

(274) E. Casals, T. Pfaller, A. Duschl, G. J. Oostingh and V. F. Puntes, 'Hardening of the nanoparticle–protein corona in metal (Au, Ag) and oxide (Fe_3O_4, CoO, and CeO_2) nanoparticles', *Small*, 2011, **7**, 3479–3486, DOI: 10.1002/smll.201101511 (cit. on p. 113).

(275) X. Jiang, S. Weise, M. Hafner, C. Röcker, F. Zhang, W. J. Parak and G. U. Nienhaus, 'Quantitative analysis of the protein corona on FePt nanoparticles formed by transferrin binding', *J. R. Soc. Interface*, 2010, **7**, S5–S13, DOI: 10.1098/rsif.2009.0272.focus (cit. on p. 113).

(276) M. Mahmoudi, F. Quinlan-Pluck, M. P. Monopoli, S. Sheibani, H. Vali, K. A. Dawson and I. Lynch, 'Influence of the physiochemical properties of superparamagnetic iron oxide nanoparticles on amyloid β protein fibrillation in solution', *ACS Chem. Neurosci.*, 2012, **4**, 475–485, DOI: 10.1021/cn300196n (cit. on p. 113).

(277) W. Liu, J. Rose, S. Plantevin, M. Auffan, J.-Y. Bottero and C. Vidaud, 'Protein corona formation for nanomaterials and proteins of a similar size: Hard or soft corona?', *Nanoscale*, 2013, **5**, 1658–1668, DOI: 10.1039/c2nr33611a (cit. on p. 113).

(278) L. Shao, C. Dong, F. Sang, H. Qian and J. Ren, 'Studies on interaction of CdTe quantum dots with bovine serum albumin using fluorescence correlation spectroscopy', *J. Fluoresc.*, 2009, **19**, 151–157, DOI: 10.1007/s10895-008-0396-0 (cit. on p. 113).

(279) P. D. McNaughter, J. C. Bear, D. C. Steytler, A. G. Mayes and T. Nann, 'A thin silica-polymer shell for functionalising colloidal inorganic nanoparticles', *Angew. Chem. Int. Ed.*, 2011, **50**, 10384–10387, DOI: 10.1002/anie.201103954 (cit. on p. 174).

APPENDIX A

Typical nanocrystal characterisation data

InP@ZnS characterisation

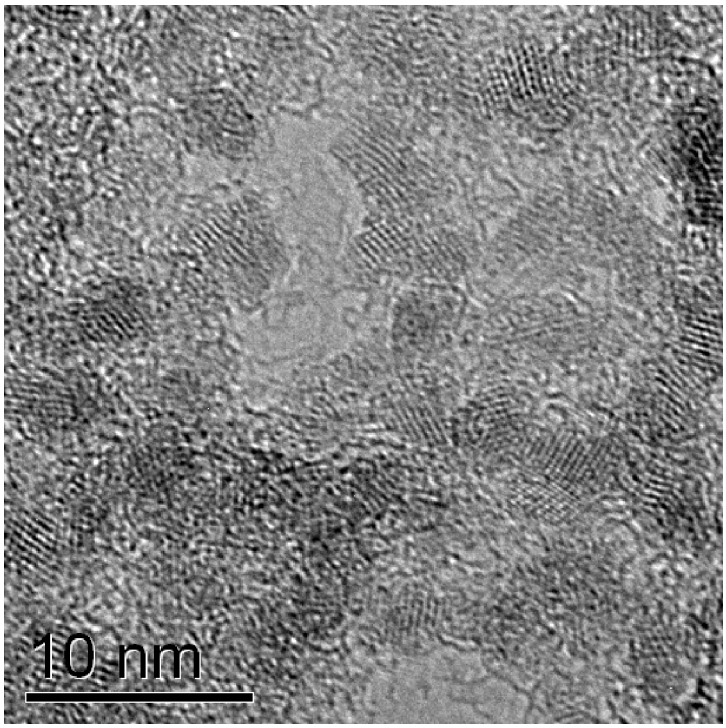

Figure A.1: An HRTEM micrograph of InP@ZnS nanocrystals.

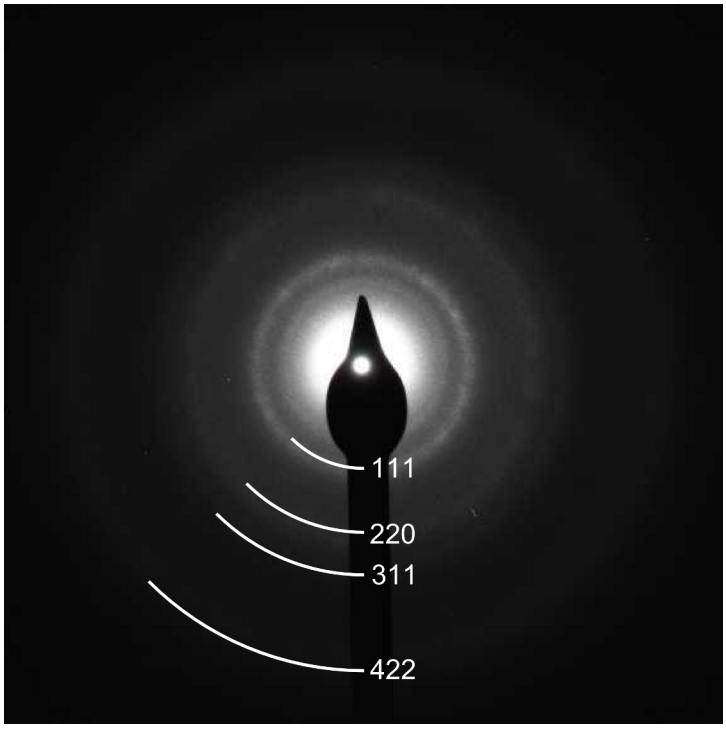

Figure A.2: An SAED pattern of InP@ZnS nanocrystals showing the hkl Miller indices for InP identified using PDF 00-032-0452.

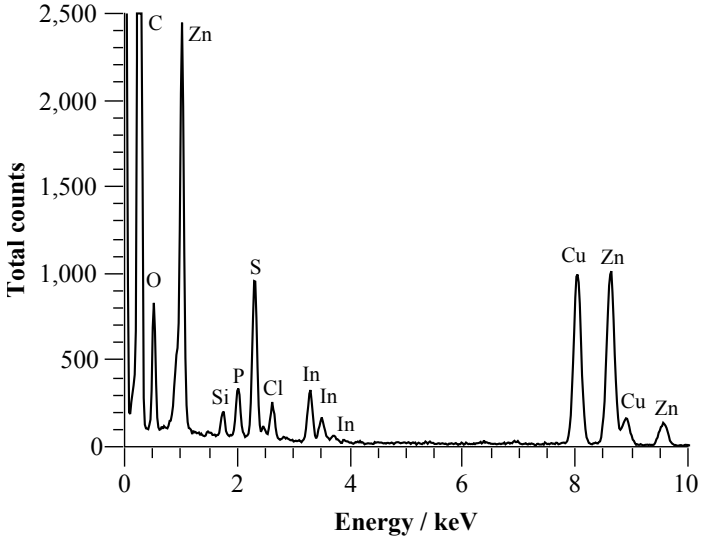

Figure A.3: An EDX spectrum for InP@ZnS

Fe_3O_4 characterisation

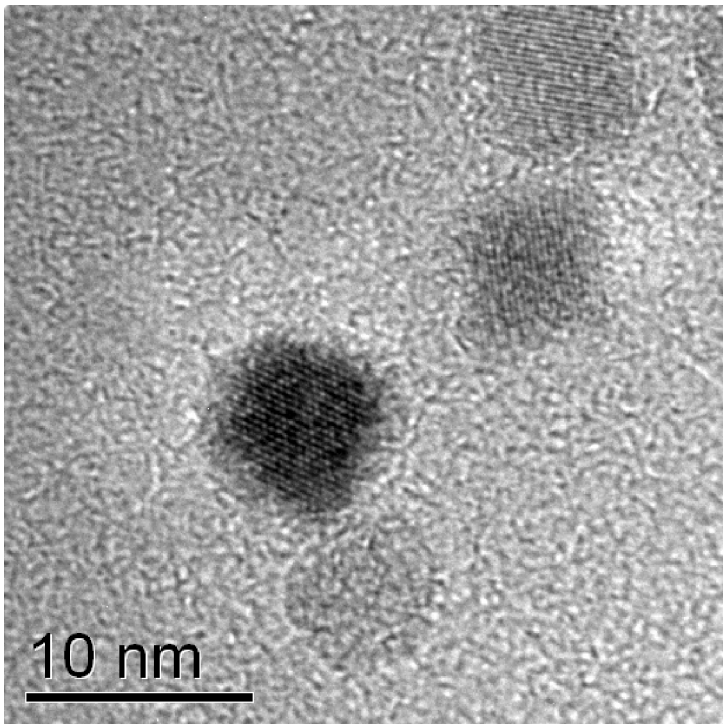

Figure A.4: An HRTEM micrograph of Fe_3O_4 nanocrystals.

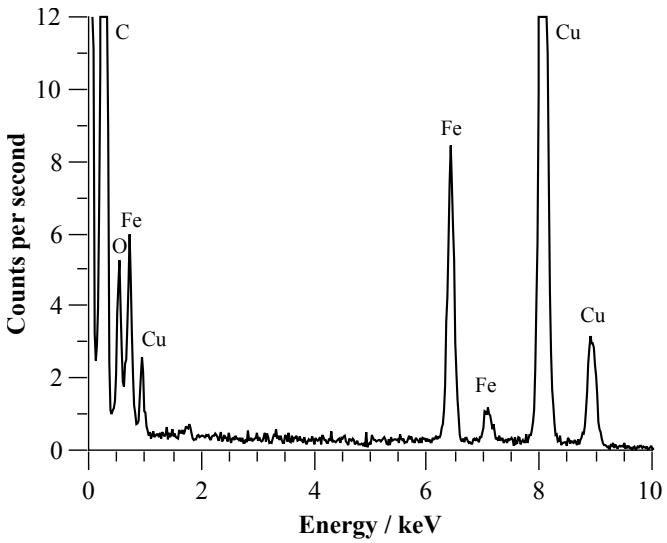

Figure A.5: An EDX spectrum for Fe_3O_4

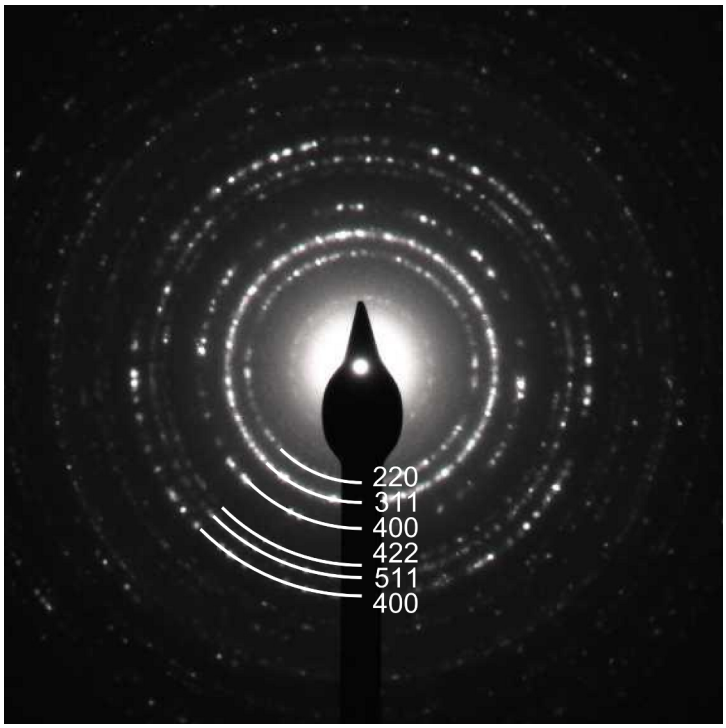

Figure A.6: An SAED pattern of Fe_3O_4 nanocrystals showing the hkl Miller indices for Fe_3O_4 identified using PDF 00-019-0629

AuNP characterisation

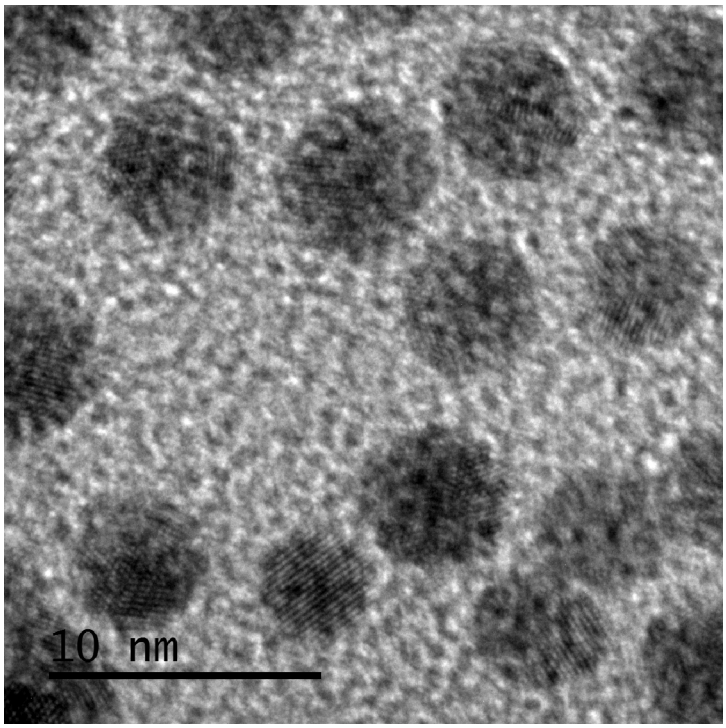

Figure A.7: An HRTEM micrograph of AuNP.

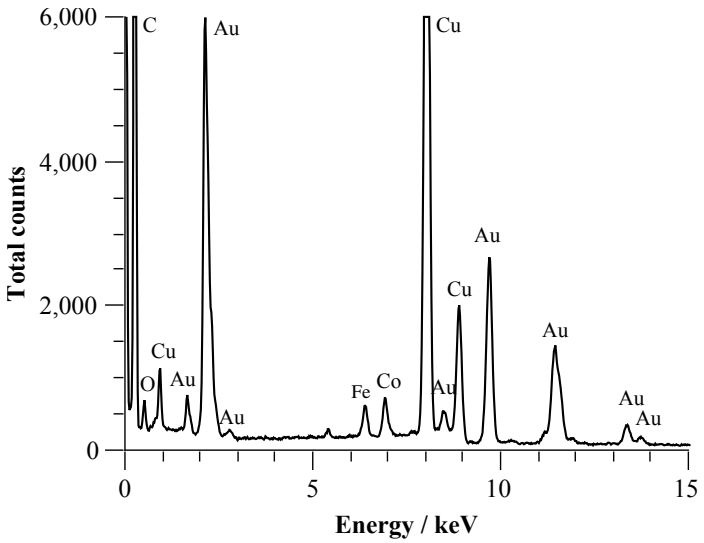

Figure A.8: An EDX spectrum for AuNP

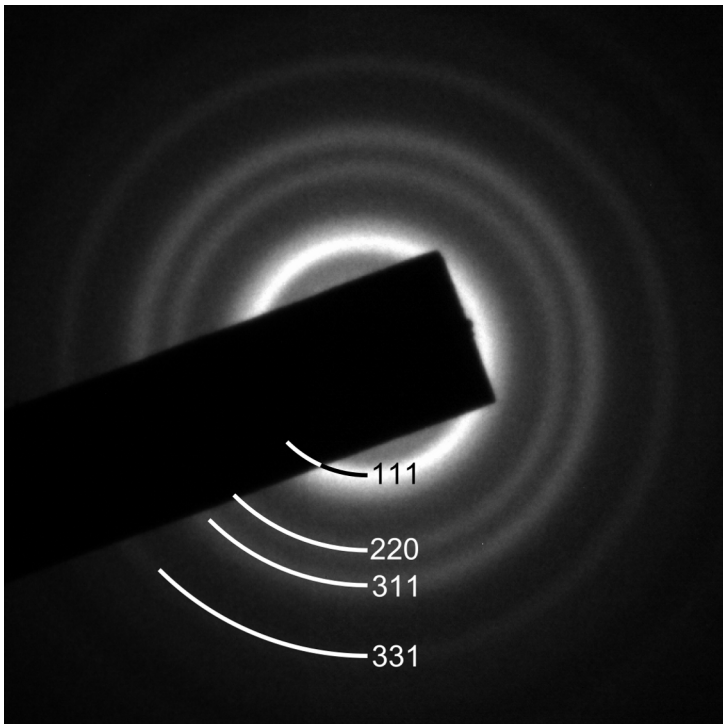

Figure A.9: An SAED pattern of AuNP showing the hkl Miller indices for Au identified using JCPDS 4-0784

APPENDIX B

Publications

The research paper by McNaughter *et al.*, detailed below, is included with permission from Wiley. Copyright (2011).

P. D. McNaughter *et al.*, 'A thin silica-polymer shell for functionalising colloidal inorganic nanoparticles', *Angew. Chem. Int. Ed.*, 2011, **50**, 10384–10387, DOI: 10.1002/anie.201103954

The title page of the book chapter by Bear *et al.*, detailed below, is included with kind permission of Springer Science+Business Media. Copyright Springer Science+Business Media, LCC (2011).

J. Bear *et al.*, *In vivo* applications of inorganic nanoparticles, in *BetaSys: Systems biology of regulated exocytosis in pancreatic β-cells*, ed. B. Booß-Bavnbek *et al.*, Springer New York, New York, NY, 2011, pp. 185–220, ISBN: 978-1-4419-6955-2, DOI: 10.1007/978-1-4419-6956-9_9

Organic–Inorganic Hybrid Composites

DOI: 10.1002/anie.201103954

A Thin Silica–Polymer Shell for Functionalizing Colloidal Inorganic Nanoparticles**

*Paul D. McNaughter, Joseph C. Bear, David C. Steytler, Andrew G. Mayes, and Thomas Nann**

Universally applicable, thin, and reproducible coatings for colloidal nanoparticles are a prerequisite for almost any of the wide-ranging applications of these exciting materials. Many techniques developed for coating and functionalization of nanoparticles have restrictions toward future applications with regard to key properties, such as solubility, size, and colloidal stability.[1] The greatest weakness of current methods, such as ligand exchange,[2] silica shells of various thicknesses,[3–5] and organic shells,[6,7] is the strong dependence of the chemistry on the inorganic core surface. Herein, InP/ZnS and Fe_3O_4 colloidal inorganic nanoparticles that have different surface properties are coated with a thin, cross-linked and functionalized shell containing organic and inorganic layers. Although not shown in this report, the method has also been applied to other colloidal particles, such as Au, $CuInS_2$ (CIS), CdSe/ZnS, and InP. This work expands nanoparticle coating techniques to develop a completely new type of hybrid coating technique. Using silicon as a marker, we conclusively prove that the underlying amphiphilic polymer foundation[8–12] is arranged on the particle surface as predicted in past reports.

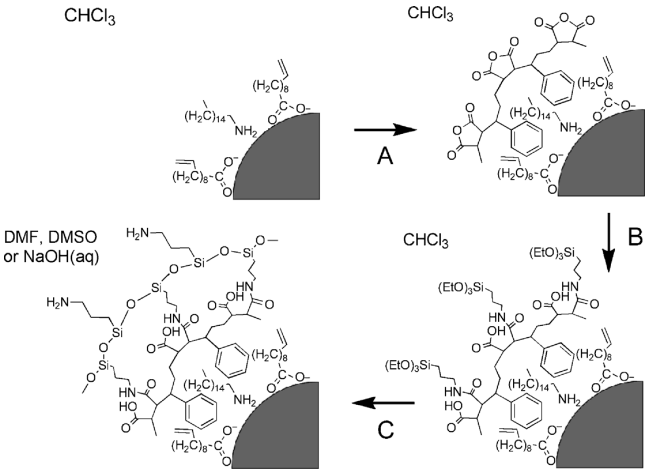

Scheme 1. Formation of the thin layer around the nanoparticle. A) The amphiphilic polymer, PSMA, wraps around the particle. B) The silica precursor, TEAPS, opens the anhydride ring on the polymer and attaches the silane to the polymer. C) Polymerization between the bound and free TEAPS to form a thin silica layer. The solvent used at each stage is noted above each structure.

The synthesis of the hybrid surface layer takes advantage of the adsorption of amphiphilic polymers to the hydrophobic stabilizing ligands on the colloidal nanoparticle surfaces. Commercial poly(styrene-*co*-maleic anhydride) (PSMA) was adsorbed as described by Mulvaney and coworkers (Scheme 1, step A).[8] The silica precursor, 3-aminopropyltriethoxysilane (TEAPS), was then reacted, resulting in a silane being tethered to the polymer (Scheme 1, step B). Generally, other methods for thin silica layers[3,4,13] use trimethoxysilanes as silica precursors. In an effort to separate the nucleophilic attack of the silica precursor to the polymer foundation and the polymerization to form silica the triethoxysilane equivalent was used, thus attempting to resolve steps B and C in Scheme 1. The temperature of the reaction mixture was also lowered to further aid this process. The polymerization of the tethered silica precursors occurs (Scheme 1, step C) resulting in particles that are soluble in dimethyl sulfoxide (DMSO), dimethylformamide (DMF), and 0.05 M NaOH (aq).

High-resolution transmission electron microscopy (HRTEM) and dynamic light scattering (DLS) measurements (Figure 1) both show that the particles were well-dispersed in solution. The DLS results show an increase in the hydrodynamic radius of the particles during the synthesis indicating that a layer has formed on the surface of the particles. The HRTEM image of a single hybrid-layer-coated particle (Figure 1b) showed no indication of a layer. This is unsurprising because the layer is amorphous and consists of elements that scatter electrons weakly. Once transferred to 0.05 M NaOH (aq) the zeta potential of the colloid was −37.1 mV indicating a good stability.

Retention of nanoparticle properties when coated with a hybrid layer is fundamental for their application. To investigate the retention of nanoparticle properties, the luminescence of InP/ZnS quantum dots was monitored during the formation of the layer. The luminescence decreased by approximately 33% between polymer coating and growth of the silica component of the layer. Once transferred to DMF the luminescence was still present although approximately

[*] Prof. T. Nann[+]
Ian Wark Research Institute, University of South Australia
Adelaide, SA 5095 (Australia)
E-mail: thomas.nann@unisa.edu.au
P. D. McNaughter, J. C. Bear, Dr. D. C. Steytler, Dr. A. G. Mayes[+]
School of Chemistry, University of East Anglia
Norwich Research Park, Norwich, Norfolk NR4 7TJ (UK)
[+] Joint last authors.

[**] We thank the Leeds EPSRC Nanoscience and Nanotechnology Facility for equipment access and the University of East Anglia for the PhD studentship awarded to P.D.McN.

Supporting information for this article is available on the WWW under http://dx.doi.org/10.1002/anie.201103954.

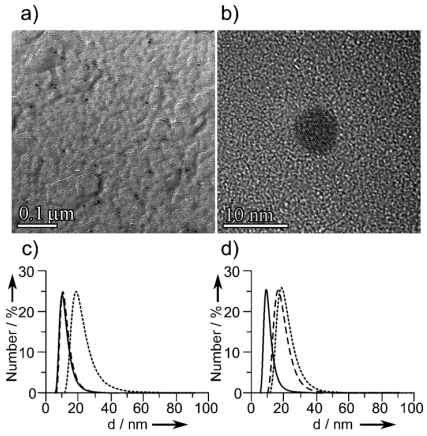

Figure 1. a) TEM image showing well-separated Fe_3O_4 particles coated with hybrid layer and b) HRTEM image of a single Fe_3O_4 particle coated with the hybrid layer. c) DLS size distribution showing InP/ZnS particles coated with the hybrid layer and transferred to 0.05 M NaOH (aq). d) DLS size distribution showing Fe_3O_4 particles coated with the hybrid layer, after transfer to DMF. In c) and d) the full lines represent the uncoated particles in $CHCl_3$, the dotted lines represent particles after coating in $CHCl_3$ and the dashed lines represent particles in the new respective solvent (d = particle size).

halved relative to the luminescence observed before the transfer to $CHCl_3$.

The IR spectrum of the hybrid-layer-coated particles was compared to that of the layer precursors (Figure 2). The hybrid layer contains many chemical functionalities (Scheme 1), which complicates the characterization, but the presence of an amide group (1556 and 1634 cm^{-1}; Figure 2, top), and the disappearance of the vibrational modes of acid anhydride from the original polymer (1775 and 1855 cm^{-1}, Figure 2, bottom), verify the successful reaction between silane and polymer on the particle surface. The hybrid layer IR spectrum shows a broad Si–O band (3500 cm^{-1}–2500 cm^{-1}; Figure 2, top), which is a characteristic feature of amorphous silica. The Si–O peak in the silane spectrum (1067 cm^{-1}) is still present in the hybrid layer spectrum but is widened (1068 cm^{-1}). Both signals indicate Si–O bonds from silica are present in the hybrid-layer-coated particle. Numerous bands from both silane and polymer can be seen superimposed on the coated particle spectrum, demonstrating retention of key functionalities. The weak amine peaks observed in the silane spectrum (1600 cm^{-1}, 3366 cm^{-1}) are masked by other features in the hybrid layer spectrum.

To confirm the presence of multiple nitrogen environments, X-ray photoelectron spectroscopy (XPS) was used. The spectrum for the N 1s electron from InP/ZnS with the hybrid layer (Figure 3) shows an asymmetric peak, not present in the XPS results of the untreated InP/ZnS and after addition of polymer. Fitting was achieved using a pair of Gaussian functions separated by 1.71 eV, which confirms two environments: an amine (lower energy) and an amide (higher energy) environment. Other peaks, such as the C 1s peak, contained too many potential environments for an accurate analysis and were not fitted.

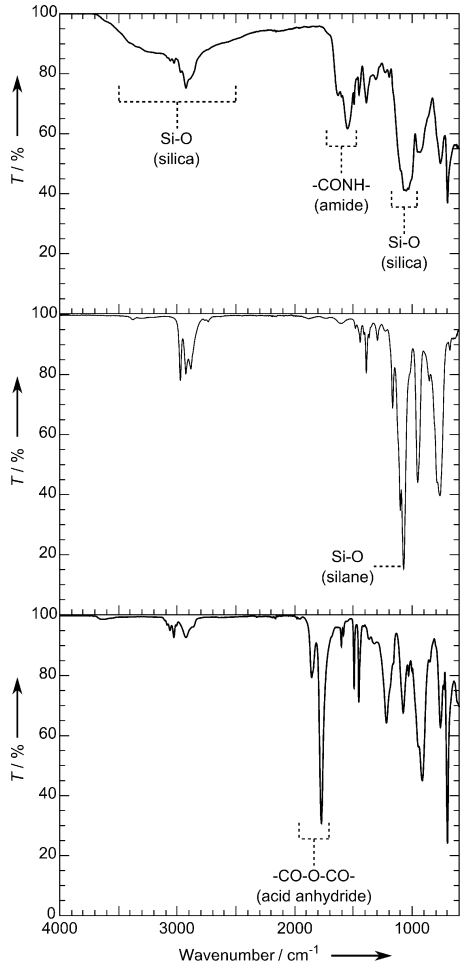

Figure 2. IR spectra (T = transmittance) with the key functionalities labeled for Fe_3O_4 coated with the hybrid layer (top), silane precursor (middle), and poly(styrene-*co*-maleic anhydride) (bottom).

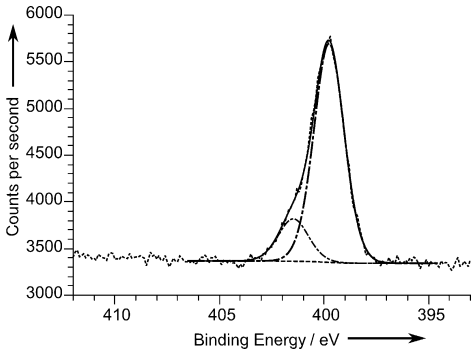

Figure 3. XPS spectrum observing the N 1s electron of InP/ZnS coated with hybrid layer. XPS spectrum (dots), baseline (dashed line), Gaussian function for the amide group (dotted and dashed line), Gaussian function for the amine group (dotted and long dashed line) and envelope formed from both Gaussian functions (full line).

Energy dispersive X-ray spectroscopy (EDXS) measurements were performed on individual Fe_3O_4 particles at the different stages of layer formation (Figure 4). As expected, polymer-coated particles showed no silicon signal. After reaction with silane and transfer to DMF a silicon peak was evident and the oxygen peak increased dramatically, confirming the presence of these elements in the outer coating. The large copper and carbon peaks originate from the TEM grid.

Electron energy loss spectroscopy (EELS) images were collected to locate electrons that had lost energy to selected elements. Figure 5 (left) shows the TEM image for Fe_3O_4 particles coated with the hybrid layer; as previously seen in Figure 1, the hybrid layer is not visible. The image was filtered to observe electrons that had lost energy to Fe and the particles are still visible (Figure 5, center). The image was again filtered to observe electrons interacting with Si (Figure 5, right). Si is clearly located on the surface of the Fe_3O_4 particles, which appear slightly larger in the Si-filtered image, indicating that the diameter of the hybrid-layer-coated particle is larger than the initial particle (consistent with the DLS data, Figure 1) and also that the coating is rather uniform.

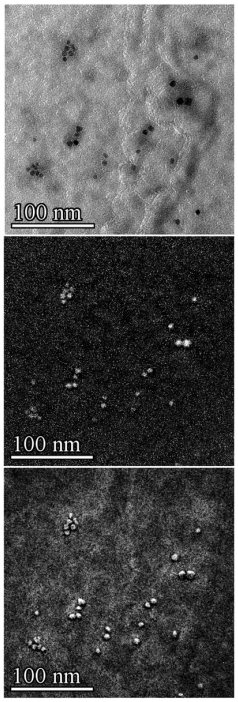

Figure 5. EELS images of Fe_3O_4 nanoparticles with hybrid layer. TEM image of Fe_3O_4 nanoparticles (top), EELS image showing Fe only (middle), and EELS image showing Si only (bottom).

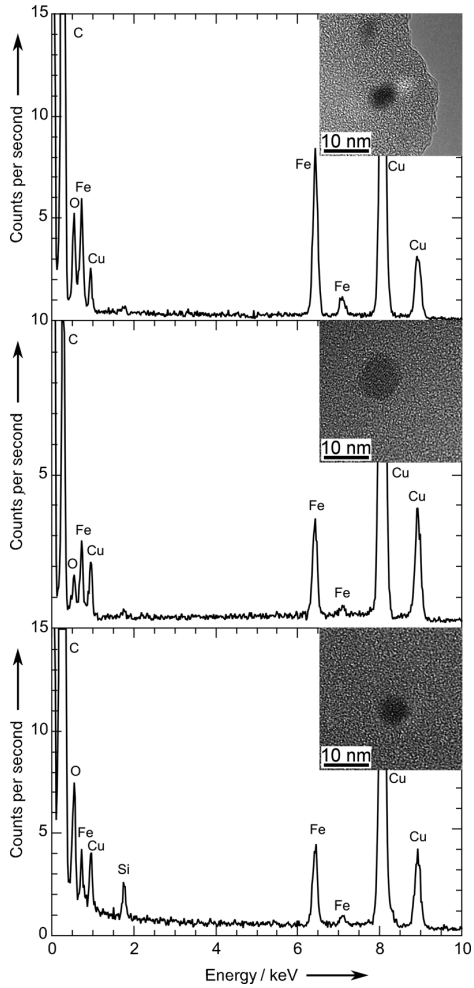

Figure 4. Energy dispersive X-ray spectroscopy (EDXS) measurements of Fe_3O_4 at each stage of hybrid layer formation with an inset TEM image depicting the region of the EDXS measurement. Top panel: Untreated Fe_3O_4 nanoparticles, middle panel: Fe_3O_4 particles coated with polymer foundation, and bottom panel: Fe_3O_4 with complete hybrid layer.

The use of amphiphilic polymers with colloidal inorganic nanoparticles has become increasingly popular but little direct proof exists as to the location or uniformity of the layer. Silicon in the silica layer provides a marker to locate the amphiphilic polymer foundation using EELS measurements. Figure 5 serves to prove that the amphiphilic polymer is located on the surface of individual particles and the layer is uniform across the surface. The EDX measurements (Figure 4) also support this conclusion though not as elegantly as the EELS.

In summary, a novel hybrid material consisting of organic and inorganic polymers has been successfully synthesized around the surface of two distinct types of colloidal inorganic nanoparticles forming a thin layer which results in non-aggregated colloidally stable particles. The layer was characterized using IR spectroscopy and XPS, confirming that the reaction had taken place by the presence of amide and amine groups and silica. The location of the hybrid material was confirmed using EDXS and EELS showing that the layer was formed on the surface of the particles. As a consequence silicon acts as a marker proving that the amphiphilic polymers

used are located on the surface of the colloidal inorganic particles thus supporting the work of Parak, Mulvaney, and others.[8,10,12] It is envisioned that this material can act as a foundation for further incorporation of colloidal inorganic particles into more complex materials.

Experimental Section

The procedure for the synthesis of InP/ZnS quantum dots was based on an earlier publication by Xu et al.[14] made up to 7 mL. The procedure for the synthesis of Fe_3O_4 particles used was described by Lattuada and Hatton[15] and the saturated particle in toluene solution was diluted 100-fold. An amount of 0.5 mL of this solution was used in a typical reaction.

To determine the quantity of poly(styrene-*co*-maleic anhydride) (Aldrich, $M_n = 1700$; PSMA) required, a series of water transfer experiments were undertaken where the amount of PSMA was varied using the method of Lees et al.[8] Typically, InP/ZnS (100 μL) redispersed in chloroform (1 mL) required 0.9 mg of PSMA in $CHCl_3$ to achieve a transfer when 0.5 mL of a 0.12 M aqueous solution of ethanolamine (Sigma–Aldrich, ≥ 99.9 %) was added.

Coating of colloidal inorganic particles with a thin hybrid organic–inorganic layer was achieved as follows:

Using InP/ZnS as an example, InP/ZnS (100 μL) were redispersed in chloroform (1 mL) and were stirred with PSMA (0.9 mg) overnight. 3-Aminopropyltriethoxysilane (7 μL, Sigma–Aldrich, 99 %) was added and stirred at 18 °C for 24 h. Toluene was added to precipitate the particles. The resulting precipitate was redispersed in tetrahydrofuran (1 mL, Sigma–Aldrich, ≥ 99.5 %), dimethylsulfoxide (1 mL, Sigma–Aldrich, ≥ 8.0 %) or 1 mL of 0.05 M NaOH (aq) (Fisher Scientific, ≥ 98.0 %).

Received: June 10, 2011
Revised: August 17, 2011
Published online: September 14, 2011

Keywords: amphiphilic polymers · iron oxide · organic–inorganic hybrid composites · quantum dots · silica

[1] R. A. Sperling, W. J. Parak, *Philos. Trans. R. Soc. London Ser. A* **2010**, *368*, 1333 – 1383.
[2] A. Saha, S. Basiruddin, N. Pradhan, N. R. Jana, *Langmuir* **2010**, *26*, 4351 – 4356.
[3] D. Gerion, F. Pinaud, S. C. Williams, W. J. Parak, D. Zanchet, S. Weiss, A. P. Alivisatos, *J. Phys. Chem. B* **2001**, *105*, 8861 – 8871.
[4] N. Jana, C. Earhart, J. Ying, *Chem. Mater.* **2007**, *19*, 5074 – 5082.
[5] M. Darbandi, R. Thomann, T. Nann, *Chem. Mater.* **2005**, *17*, 5720 – 5725.
[6] S. Carregal-Romero, N. J. Buurma, J. Pérez-Juste, L. M. Liz-Marzán, P. Hervés, *Chem. Mater.* **2010**, *22*, 3051 – 3059.
[7] Y. Wang, X. Teng, J. Wang, H. Yang, *Nano Lett.* **2003**, *3*, 789 – 793.
[8] E. E. Lees, T.-L. Nguyen, A. H. A. Clayton, P. Mulvaney, *ACS Nano* **2009**, *3*, 1121 – 1128.
[9] B. W. Muir, B. A. Moffat, P. Harbour, G. Coia, G. Zhen, L. Waddington, J. Scoble, D. Krah, S. H. Thang, Y. K. Chong, P. Mulvaney, P. Hartley, *J. Phys. Chem. C* **2009**, *113*, 16615 – 16624.
[10] C. Lin, R. Sperling, J. Li, T. Yang, P. Li, M. Zanella, W. H. Chang, W. J. Parak, *Small* **2008**, *4*, 334 – 341.
[11] M. T. Fernández-Argüelles, A. Yakovlev, R. A. Sperling, C. Luccardini, S. Gaillard, A. Sanz Medel, J.-M. Mallet, J.-C. Brochon, A. Feltz, M. Oheim, W. J. Parak, *Nano Lett.* **2007**, *7*, 2613 – 2617.
[12] T. Pellegrino, L. Manna, S. Kudera, T. Liedl, D. Koktysh, A. Rogach et al., *Nano Lett.* **2004**, *4*, 703 – 707.
[13] L. M. Liz-Marzán, M. Giersig, P. Mulvaney, *Langmuir* **1996**, *12*, 4329 – 4335.
[14] S. Xu, J. Ziegler, T. Nann, *J. Mater. Chem.* **2008**, *18*, 2653 – 2656.
[15] M. Lattuada, T. A. Hatton, *Langmuir* **2007**, *23*, 2158 – 2168.

Chapter 9
In Vivo Applications of Inorganic Nanoparticles

Joseph Bear, Gaëlle Charron, María Teresa Fernández-Argüelles, Salam Massadeh, Paul McNaughter, and Thomas Nann

Abstract Chapter 9 is primarily concerned with in vivo applications of nanoparticles. This very broad review includes aspects such as bioconjugation, which is a pre-requisite for any in vivo application, and nanotoxicity. We introduce the two main fields of in vivo applications of nanoparticles: bioimaging and therapy. In the field of imaging, magnetic resonance imaging and optical imaging are distinguished, and the latter is further subdivided into groups of luminophores. These groups include gold nanoparticles, semiconductor quantum dots and rare-earth-doped nanoparticles. In Section 9.4, we discuss the methods of hyperthermia, photodynamic therapy and magnetic targeting. The aim of this chapter is not to provide in-depth insights into the different applications but to give an overview of possibilities and limitations when nanoparticles are used within living organisms.

Keywords Imaging · In vivo · Nanoparticles · Therapy · Toxicity

Abbreviations

AC	Alternating current
AuNP	Gold nanoparticle
AuNR	Gold nanorod
BSA	Bovine serum albumin
DHLA	Dihydrolipoic acid
DNA	Deoxyribonucleic acid
DTPA	Diethylenetriaminepentaacetic acid
DTT	Dithiothreitol
EDC	1-Ethyl-3- (3-dimethylaminopropyl) carbodiimide
FRET	Förster or fluorescence resonance energy transfer
GPC	Glial progenitor cell
Hb	Haemoglobin

M.T. Fernández-Argüelles ( )
Faculty of Chemistry, University of Oviedo, Oviedo 33006, Spain
e-mail: fernandezteresa@uniovi.es

B. Booß-Bavnbek et al. (eds.), *BetaSys*, Systems Biology 2,
DOI 10.1007/978-1-4419-6956-9_9,